Revue of the ICSRI-Proceedings: N°2@2023, ISSN 2800 1362

Proceedings of the Second International Conference and School on Radiation Imaging and Nuclear Medicine (ICSRI-2023)

SETIF, JUNE 11-15, 2023

Ferhat Abbas-Setif1 University-UFAS1
Faculty of Sciences
In partnership with the Atomic Energy Commission-COMENA
ALGERIA

Edited by: Prof. Fayçal KHARFI (EIC)

Second International Conference and School on Radiation Imaging and Nuclear Medicine-ICSRI-2023

Setif, June 11-15, 2023

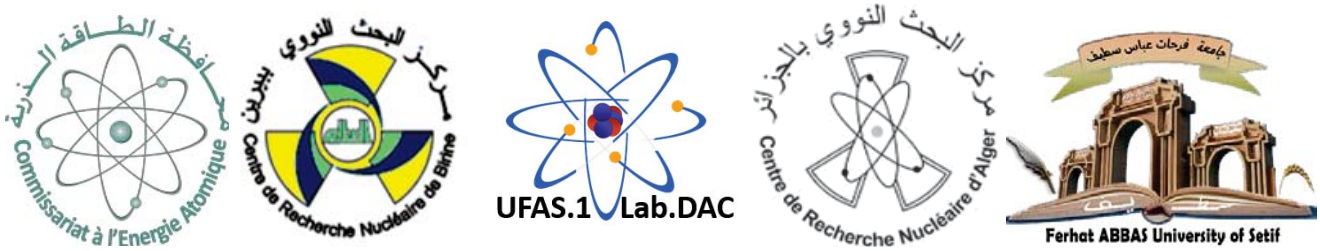

Proceedings of the ICSRI-2023

Edited by: Prof. Fayçal KHARFI (EIC)

Co-edited by:

Prof. Hacene AZIZI, Prof. Djemal Eddine Chouaib BELKHIAT, Prof. Abdelouahab MOUSSAOUI, Dr. Layachi BOUKERDJA, Dr. Seif Eddine Allah CHOUABA, Dr. Adouda ADJIRI, and Prof. Bilal SARI

Acknowledgments:

The proceedings of the ICSRI-2023 are printed in the framework of the socio-economic research project on "Control and improvement of radiotherapy treatment plans using thermoluminescence dosimetry" (Contract N° 07/2019, 15/12/2019). This project is supported by the Thematic Research Agency for Sciences and Technology (ATRST) of the Directorate-General for Scientific Research and Technological Development (DGRSDT). Editors and the principal investigator of the project are very grateful to ATRST and DGRSDT.

Proceedings of the Second International Conference and School on Radiation Imaging and Nuclear Medicine (ICSRI-2023)
Setif, Algeria
June 11-15, 2023
Edited by Prof. Fayçal KHARFI

2023 Ferhat Abbas-Setif1 University
Laboratory of Dosing, Analysis and Characterisation with high resolution
Campus El-Bèz, Setif-19000, Algeria

ISSN 2800-1362

Printed in Algeria by Founoune Printing Press

Local Organizing Committee

General Chair:

Prof. Fayçal Kharfi (Ferhat Abbas-Setif1 University, Algeria)

Deputy Chair:

Dr. Layachi Boukerdja (Nuclear Research Centre of Birine, Algeria)

Committee Members:

Prof. Hacene Azizi (Ferhat Abbas-Setif1 University, Algeria)
Prof. Djamel Edine Chouaib Belkhiat (Ferhat Abbas-Setif1 University, Algeria)
Prof. Abdelouahab Moussaoui (Ferhat Abbas-Setif1 University, Algeria)
Dr. Djilali Khelfi (Atomic Energy Commission, Algeria)
Dr. Seif Eddine Allah Chouaba (Ferhat Abbas-Setif1 University, Algeria)
Dr. Ammar Mosbah (Ferhat Abbas-Setif1 University, Algeria)
Prof. Sari Bilal (Ferhat Abbas-Setif1 University, Algeria)
Prof. Boudaoud Khadidja (CLCC-Setif, Dz)
Mrs. Lilia Benachour (Ferhat Abbas-Setif1 University, Algeria)
Mr. Nacim Benachour (Ferhat Abbas-Setif1 University, Algeria)

Conference Secretariat and Technical Staff :

Ms. Karima Bey (Ferhat Abbas-Setif1 University, Algeria)
Mr. Ilyas Sekhri (Ferhat Abbas-Setif1 University, Algeria)

Scientific Advisory Committee

Prof. Atef El-Taher (Al-Azhar University, Eg)
Prof. Amrani Naima (Ferhat Abbas-Setif1 University, Dz)
Prof. Azizi Hacene (Ferhat Abbas-Setif1 University, Dz)
Prof. Babahenini Mohamed Chaouki (Biskra University, Dz)
Prof. Benamrane Nacéra (Oran Sciences and Technology Univesity, Dz)
Prof. Boucenna Ahmed (Ferhat Abbas-Setif1 University, Dz)
Prof. Bouchareb Yassine (Sultan Qaboos University, Om)
Prof. Boudaoud Khadidja (CLCC-Setif, Dz)
Prof. Bouyoucef Salahedine (Bab El Oued HUC, Dz)
Prof. Cherfa Yazid (SD-Blida University, Dz)
Prof. Djedi Noureddine (Biskra University, Dz)
Prof. Doghmane Noureddine (BM-Annaba University, Dz)
Prof. Drai Redouane (Research Centre on Industrial Technology, Dz)
Prof. Guemmmaz Mohamed (Ferhat Abbas-Setif1 University, Dz)
Prof. Guittoum Anderrahim (CRNA, Dz)
Prof. Hadid Abdenour (Oulu University, Fi)
Prof. Hachouf Fella (Constantine University, Dz)
Prof. Hamidatou Algham Lylia (Nuclear Research Centre of Birine, Dz)
Prof. Kambiz Shahnazi (PHIC, China)
Prof. Kharfi Fayçal (Ferhat Abbas-Setif1 University, Dz)

Prof. Lounis-Mokrani Zohra (CRNA, Dz)
Prof. Maalej Nabil (King Fahd University PM, KSA)
Prof. Maouche Djamel (Ferhat Abbas-Setif1 University, Dz)
Prof. Mansour Karim (Univ. Constantine 3, DZ)
Prof. Merouani Hayet Farida (Annaba University, Dz)
Prof. Meziane Abdelkrim (CERIST, Dz)
Prof. Mimi Malika (Mostaghanem University, Dz)
Prof. Mongy Tarek (Egyptian Commission of Atomic Energy, Eg)
Prof. Moussaoui Adelouahab (Ferhat Abbas-Setif1 University, Dz)
Prof. Meriç Niyazi (Ankara University, Tr)
Prof. Ounoughi Nabil (University of Jijel, Dz)
Prof. Oussalah Mourad (Oulu University, Fi)
Prof. Saint-Gregoire Jean-pierre (ASCA, Fr)
Prof. Şahiner Eren (Ankara University, Tr)
Prof. Schillinger Burkhard (TUM, De)
Prof. Seghier Mohamed (ECAE, Abu Dhabi, UAE)
Prof. Seghour Abdessalem (Nuclear Research Centre of Algiers, Dz)
Prof. Taleb-Ahmed Abdelmalik (Valencienns University, Fr)
Prof. Zaidi Habib (Geneva University Hospital, Ch)
Prof. Zidi Tahar (Atomic Energy Commission, DZ)

Preface

The second international conference and school on radiation imaging and nuclear medicine (ICSRI-2023) was held from 11 to 15 June 2023 at Ferhat Abbas-Setif1 University (UFAS1). For the second time, the scientific event has been organized in partnership with the Algerian Atomic Energy Commission (COMENA) and its different research centres. The conference was a real opportunity to bring together researchers, practitioners, and students of different backgrounds to discuss the latest advances in radiation imaging, nuclear medicine, and medical image processing.

The conference was able to cover different topics related to radiation imaging and nuclear medicine physics and technology, such as radiation detectors, imaging techniques and modalities, simulation and modelling, and image processing. Some special topics of interest on radiation therapy and medical imaging were also included. The conference featured keynote speeches from renowned experts and oral and in poster presentations from researchers and PhD students.

In addition to the conference, there was a school of three days organized just after the conference for students and early-career researchers. The school aimed to provide an opportunity for participants to learn about fundamentals and practical aspects of computed tomography, nuclear medicine, laser application in medicine, as well as to engage in hands-on training sessions and workshops on new trends in data analysis and image processing with a special focus on artificial intelligence and deep-learning. The school was focused on the following main topics:

- The role of Monte Carlo simulations in Molecular Imaging and Dosimetry,
- Advanced Anthropomorphic Computational Models,
- Medical lasers- Physics, Clinical Applications and Safety Management,
- Mammography: Physics, Image Quality, and Quality Control,
- Deep Neural Networks for Medical Data Analysis,
- X-ray and Neutron Transmission Computed Tomography.

The organizers were committed to ensuring a productive and enjoyable experience for all participants. Researchers, practitioners, and PhD students from different research institutions, with an interest in radiation imaging and nuclear medicine, attended this exciting event and presented a very interesting works.

The General chair of the organizing committee would like to thank and highlight the outstanding efforts of the local organizing committee and the international scientific Committee. We are extremely grateful to the Dean of the Faculty of Sciences of Ferhat Abbas-Sétif1 university, Prof. Layachi Louail, for his encouragement in the organization of the ICSRI-2023. Thanks are also extended to our very efficient partners: the Algerian Atomic Energy Commission (COMENA), the Nuclear Research Centre of Birine (CRNB), and the Nuclear Research Centre of Algiers (CRNA).

Prof. Fayçal KHARFI
General Chair of the ICSRI-2023 Conference
Director of the School on Radiation Imaging and Nuclear Medicine

The Editor in Chef

Prof. Fayçal Kharfi is Professor of Physics at the Department of Physics, Faculty of Sciences, Ferhat Abbas-Setif1 University. He teaches several courses on molecular imaging, computed tomography, radiation physics and application, and medical physics. He is also the actual Director of the Laboratory of Dosing, Analysis, and Characterisation with high resolution (LDAC). The focus of his actual research activities is on ionizing radiation application. His research crosscuts a range of areas in radiation dosimetry, radiation therapy, computed tomography, and nuclear medicine. His overarching goals are to understand how ionizing radiations act on matter and how to be effectively applied for therapy, imaging, archaeology, and food processing. He is associated editor of the "Technology in Cancer Research & Treatment" SAGE journal. He published many research and educational works in various international journals, books, and conference proceedings. He is a frequent reviewer, an expert in radiation application, and a member of many international associations such as the international society of neutron radiography (ISNR) and the international association of engineers (IAENG). He supervised many doctorate thesis and research projects in the fields of radiation dosimetry and application, radiation therapy, and medical imaging. He contributes to the organisation of numerous national and international conferences and workshops on medical physics and radiation application.

Second International Conference and School on Radiation Imaging and Nuclear Medicine-ICSRI-2023

11-15 June 2023, Setif, Algeria

Scientific Program of the Conference

Sunday, June 11, 2023		
08h00 08h30	**Registration**	
08h30 09h00	**Welcome and Opening Ceremony Pr. Fayçal Kharfi and Dr. Layachi Boukerdja**	
Oral Session 1 : Medical Imaging, Molecular Imaging, and Nuclear Medicine		
09h00 09h30	**Plenary Talk 1 : Pr. Habib ZAIDI** PET Instrumentation & Neuroimaging Laboratory, Geneva University Hospital, Switzerland ***The promise of artificial intelligence in multimodality medical imaging***	**Chairman : Pr. Hacene Azizi**
09h30 09h50	**I. Rekik** Department of Physics, Ferhat Abbas-Setif1 University, Setif, Algeria ***Locoregional Recurrence Prediction in Head & Neck Cancer: A Comparative Study***	
09h50 10h10	**I. Meddeb** Salah Azaïez Institute, Tunis, Tunisia ***Primary location of a neuroendocrine tumor identified by PET-CT or 18F-FD G***	
10h10 10h30	**Coffee Break**	
10h10 11h30	**Poster Session : All Topics Dr. Seif Eddine Allah Chouaba, Dr. Abderrahim Betka, and Dr. Bilal Sari**	
1	**N. Mekroud** Department of Computer Science, Ferhat Abbas-Setif1 University, Setif, Algeria ***Knowledge extraction from gene expression images: Adaptation of association rules mining for theory of evidence***	
2	**L. Boumedine** Department of Physics, Faculty of Sciences, Ferhat Abbas-Setif1 University, Setif, Algeria ***Simulation of Target Material Choice on Laser proton Dose Distribution for Biomedical Imaging***	
3	**K. Nasri** Department of Computer Science, Ferhat Abbas-Setif1 University, Setif, Algeria ***Very Deep Learning Approach for MGMT Detection***	
4	**F. Lahrache** Department of Mathematics and Computer Science, Faculty of Science and Technology, University of Ghardaia, Ghardaia, Algeria ***Medical Images Semantic Segmentation Using Deep Learning: A Survey***	
5	**N. Ait Ali Braham** Department of Physics, Faculty of Sciences, Ferhat Abbas-Setif1 University, Setif, Algeria ***Renal Time activity curves (TACs) modelling and comparison to images-based and clinical dynamic scintigraphy results***	
6	**K. Benkahila** Fighting against Cancer Medical Centre of Setif, Algeria ***Dimensions, positioning and Hounsfield unit verification of 3D printed radiotherapy bolus using X-ray CT-scanning***	

7	**Dorea Maria Khalal** Department of Physics, Faculty of Sciences, Ferhat Abbas-Setif1 University, Setif, Algeria ***Deep learning based automatic segmentation of lungs in CT images***
8	**S. Malki** Department of Physics, Faculty of Sciences, Ferhat Abbas-Setif1 University, Setif, Algeria ***Evaluation of the complexity of a Volumetric Modulated Arc Therapy (VMAT) plan***
9	**M.O. Mebarki** Department of Physics, Faculty of Sciences, Ferhat Abbas-Setif1 University, Setif, Algeria ***Automatic Detection of Anatomical Landmarks for Image Registration in Radiotherapy***
10	**M. Hebboul** Nuclear Research Centre of Birine, Algeria ***Development of a control system for neutron tomography facility***
11	**N. Osmani** Nuclear Research Centre of Birine, Algeria ***SEM and AFM study of radiation damage induced by neutron transmutation doping of Silicon***
12	**M. Sari** Department of Computer Science, Faculty of Sciences, Ferhat Abbas-Setif1 University, Setif, Algeria ***An Efficient Convolutional Neural Network Model for Detecting Colorectal Cancer From Histological Images***
13	**B. SI Tayeb** Department of Physics, Faculty of Sciences, Laboratory of Mechanics, Structures and Energy, Mouloud Mammeri University of Tizi-Ouzou, Tizi-Ouzou, Algeria ***Electrons elastic scattering by DNA and/or RNA molecules***
14	**H. Belloui** Department of Physics, Faculty of Sciences, Ferhat Abbas-Setif1 University, Setif, Algeria ***Cerebrovascular segmentation using Deep learning techniques***
15	**H. Belloui** Department of Physics, Faculty of Sciences, Ferhat Abbas-Setif1 University, Setif, Algeria ***Brain vessel segmentation using two deep learning techniques***
16	**M. Boukabcha** Department of Physics, Faculty of Exacts Sciences and Informatics, Hassiba Benbouali University of Chlef, Chlef, Algeria ***Study the effect of solar ultraviolet radiation on sunflower plants growth in Algeria***
17	**N.E.H. Boughaba** University of Science and Technology Houari Boumediene, Faculty of Physics, SNIRM Laboratory, Algiers, Algeria ***A Scintillation Dosimeter Prototype for Brachytherapy***
18	**K. Khalal-Kouache** University of Science and Technology Houari Boumediene, Faculty of Physics, SNIRM Laboratory, Algiers, Algeria ***Dosimetric benefits of adaptive radiotherapy for head and neck cancer***
19	**A.O. Meddas** Department of Physics, Faculty of Sciences, Ferhat Abbas-Setif1 University, Setif, Algeria ***Influence of the architecture's depth and data size on the model performance for breast cancer classification***

20	**M.L. Yahiaoui** Nuclear Research Centre of Birine, Djelfa, Algeria ***X-ray tomography reconstruction using TIGRE***	
21	**A. Benaidja** Mohammed Seddik Benyahia University of Jijel, Jijel, Algeria ***The impact of additional filtration on patient radiation dose in diagnostic radiology***	
22	**I. Mehidi** Department of Physics, Faculty of Sciences, Ferhat Abbas-Setif1 University, Setif, Algeria ***Retinal Vessel Segmentation: Overview, Challenges and the Future***	
23	**R. Merghem** Department of Physics, Faculty of Sciences, Ferhat Abbas-Setif1 University, Setif, Algeria ***Exploration of Medical Image Registration Methods: CNN and Transformer-based***	
24	**R.A. Boukabouya** Department of Computer Science, Ferhat Abbas-Setif1 University, Algeria ***Cross-modality learning for prostate detection***	
Videoconference Session 1 : All Topics		
10h30 10h50	**D. Gayathri** Digital Evidence Based Medicine, United Kingdom ***The use of Artificial Intelligence to optimise Pelvic Imaging for Women***	**Chairman:** **Pr. D.E. Chouaib Belkhiat**
10h50 11h10	**Y. Salimi** Geneva University Hospital, Geneva, Switzerland ***Fully Automated Multi-Organ Segmentation in CT Images via Deep Neural Networks***	
11h10 11h30	**M. Amini** Division of Nuclear Medicine and Molecular Imaging, Geneva University Hospital, Geneva, Switzerland ***Auto-PET-IQA: A Fully Automated Region-Specific PET Image Quality Assessment Tool***	
11h30 11h50	**A. Akhavanallaf** University of Michigan, Ann Arbor, MI, USA ***The predictive value of pretherapy 68Ga-DOTATATE PET and clinical biomarkers in 177Lu-PRRT tumor dosimetry***	
12h00 **13h30**	**Lunch Break**	
Oral Session 2 : Medical Images Classification and Processing		
13h30 **14h00**	**<u>Plenary Talk 2 :</u>** **Dr. Adouda ADJIRI** Department of Physics, Faculty of Sciences, Ferhat Abbas-Setif1 University, Algeria ***Understanding cancer resistance to therapy***	**Chairman:** **Pr. Habib Zaidi**
14h00 14h20	**Y.R. Haddadi** LTC Laboratory, Faculty of Technology, University of Saida , Saida Algeria ***Medical Image Denoising Based on a Novel Bio-Inspired Optimization Algorithm and Total Generalized Variation***	
14h20 14h40	**H. Chellakh** Department of Computer Science, Ferhat Abbas University of Setif 1, Algeria ***Rule Based Classifier for MRI Brain Tumor identification and classification***	

14h40 15h00	**S. Hamdi** Department of Computer Science, Ferhat Abbas Setif1 University, Setif, Algeria ***Ensemble Transfer Learning for Improved Brain Tumor Classification in MRI Images***	
15h00 15h20	**Y. Azzi** Department of Computer Science, Faculty of Sciences, Ferhat Abbas-Setif1 University, Setif, Algeria ***Class Imbalance and Evaluation Metrics for Medical Image Segmentation with Machine Learning Models***	
15h20 15h40	**Coffee Break**	
Oral Session3: Simulation in Radiation Therapy, Medical Imaging, and Dosimetry		
15h40 16h00	**N. Ounoughi** Mohammed Seddik Benyahia University of Jijel, Jijel, Algeria ***Ions beam therapy monitoring with the in-beam PET scanning: Monte Carlo simulation***	**Chairman: Pr. Abdelouahab Moussaoui**
16h00 16h20	**N. Charmat** University of Science and Technology Houari Boumediene, Faculty of Physics, SNIRM Laboratory, Algiers, Algeria ***Absorbed dose at the interface of two media under γ-rays irradiation: simulation vs experience***	
16h20 16h40	**Z.E. Bouraoui** University of Science and Technology Houari Boumediene, Faculty of Physics, SNIRM Laboratory, Algiers, Algeria ***Evaluation of morphological changes based on cone beam CT for adaptive radiotherapy***	
16h40 17h00	**M. Essmine** Algerian Institute of Nuclear Engineering, Algiers, Algeria ***Virtual reality simulation: A tool for imaging and radiation therapy training***	
Monday, June 12, 2023		
Oral Session 4 : Imaging Techniques and Modalities		
08h00 08h30	**<u>Plenary Talk 3</u>: Pr. Nabil MAALEJ** Khalifa University, United Arab Emirates ***Development of nanoparticles for X-ray and MRI imaging***	**Chairman: Pr. Yassine Boucharebb**
08h30 08h50	**N. Benmehenni** Department of Mathematics, Faculty of Sciences, University of Sétif 1, Algeria ***Watermarking Images Using Virtual Color Models***	
08h50 09h10	**O. Boukhennoufa** SUPMICROTECH, CNRS, Institute FEMTO-ST, Besançon, France ***Multistage deep learning benchmarking of OAI imaging: Contribution of ViT in medical imaging***	
09h10 09h30	**A. Lebal** Mathematics and Computer Science Department, Amar Telidji University, Laghouat, Algeria ***EEG Signal for Schizophrenia Detection Using Deep Convolutional Neural Networks and Attention Mechanism***	

09h30 09h40	**Coffee Break**	
Videoconference Session 2 : All Topics		
09h40 10h00	**O. Al-Kharusi** Department of Physics, College of Science, Sultan Qaboos University, Muscat, Oman ***In-vivo Dosimetry using Diodes and MOSFETs in Radiation Therapy***	**Chairman: Dr. Adouda Adjiri**
10h00 10h20	**E. Şahiner** Earth Sciences Application and Research Centre, Ankara University, Turkey ***Luminescence Dosimetry in Radiology and Nuclear Medicine: Advancements and Applications***	
10h20 10h30	**Break**	
Oral Session 5 : Artificial Intelligence in Medical Imaging		
10h30 11h00	**Plenary Talk 4** **Dr. Yassine BOUCHAREB** Department of Physics, College of Science, Sultan Qaboos University, Muscat, Oman ***Artificial Intelligence for Radiation Dose Optimization in Diagnostic Radiology and Molecular Imaging***	**Chairman: Pr. Nabil Maalej**
11h00 11h20	**S. Atek** Department of Physics, Faculty of Sciences, Ferhat Abbas-Setif1 University, Setif, Algeria ***Deep learning in medical image Segmentation using Multi-Modality fusion***	
11h20 11h40	**R. Bencheikh** Department of Computer Science, Faculty of Sciences, Ferhat Abbas-Setif1 University, Setif, Algeria ***Innovative Deep Neural Network Models for Multilingual Translation Applied to Dyslexia***	
11h40 12h00	**I. Mansour** Department of Computer Science, University of Ferhat Abbas Setif 1, Setif, Algeria ***Fully Attention Convolutional Deep Neural Networks for Polyp Segmentation and Classification from Histological and Colonoscopic Image***	
12h00 12h30	**Closing Ceremony**	
12h30 14h00	**Lunch**	
14h00 18h00	**Tour to the Antic Roman City of Djemila**	

Program of the School

Tuesday, 13 June	Welcome and Opening Ceremony
Morning	**Simulation and Dosimetry in Nuclear Medicine** **Pr. Habib Zaidi**
08h30-10h00	**Lecture 1** : The role of Monte Carlo simulations in molecular imaging and dosimetry
10h00-10h30	**Coffee Break**
10h30-12h00	**Lecture 2** : Advanced Anthropomorphic Computational Models
12h00-13h30	**Lunch Break**
Afternoon	**Medical lasers- Physics, Clinical Applications and Safety Management** **Dr. Yassine Bouchared**
13h30-15h00	**Lecture**: Medical Lasers - Physics and Classification of Lasers
15h00-15h30	**Coffee Break**
15h30-17h00	**Practical Session**: Medical lasers - Clinical applications & Safety Management
Wednesday, 14 June	
Morning	**Mammography Physics, Image Quality and Quality Control** **Pr. Nabil Maalej**
08h30-10h00	**Lecture** : Mammography Physics
10h00-10h30	**Coffee Break**
10h30-12h00	**Practical Session**: Image quality and quality Control in Mammography
12h00-13h30	**Lunch Break**
Afternoon	**X-ray and Neutron Imaging and Tomography** **Dr. Layachi Boukerdja, Dr. Omar Denden and Mr. Ali Abdelakder**
13h30-15h00	**Lecture** : Principles of X-ray and Neutron Imaging and Tomography
15h00-15h30	**Coffee Break**
15h30-17h00	**Practical Session** : Computed Tomography Simulation
Thursday, 15 June	
Morning	**Deep Learning in Medical Image Processing** **Pr. Abdelouahab Moussaoui**
08h00-09h30	**Lecture**: Deep Neural Networks for Medical Data Analysis
09h30-10h00	**Coffee Break**
10h00-12h00	**Practical Session** : Hands-on notebooks • CNN models for medical image classification • Transfer learning models for medical data analysis • U-Net model for medical image segmentation • Autoencoder (AE) for image generation and denoising • Vision Transformers (ViT) for image analysis
12h00-12h30	**Distribution of Attending Certificates and Closing Ceremony**
12h30-13h30	**Lunch**

List of Participants to the School

	Name	Affiliation	Speciality
1	**BOUKABCHA Maamar**	University of Chlef	Biophysics
2	**AIT CHIKH Sounya**	CLCC* of Tizi-Ouzou	Medical Physics
3	**BITAM Tariq**	University of Algiers 1	Nuclear Physics
4	**BENABDESSADOK Abdelhadi**	CLCC of Ouargla	Medical Physics
5	**SI TAYEB Belkacem**	University of Tizi-Ouzou	Fondamental Physics
6	**LAHRACHE Ferialle**	University of Ghardaia	Machine Learning
7	**OUAKOUAK Abdelkader**	University of El-Oued	Water treatment
8	**BOUKSIBA Amina**	CLCC of Bechar	Medical Physics
9	**BOUALI Insaf**	CLCC of Bechar	Medical Physics
10	**HAMZA Kheira**	CLCC of Bechar	Medical Physics
11	**CHARMAT Noura**	USTHB+, Algiers	Radiation Physics
12	**BOUGHABA Nour El Houda**	USTHB, Algiers	Radiation Physics
13	**SLAMENE Hocine**	CRNB, Djelfa	Nuclear Physics
14	**BOUROUINA Mourad**	University of Setif1	Medical Physics
15	**MALKI Souad**	University of Setif1	Medical Physics
16	**MALEK Nadjette**	University of Setif1	Medical Physics
17	**KHALAL Dorea Maria**	University of Setif1	Medical Physics
18	**GHEDIRI Noussaiba**	University of Setif1	Medical Physics
19	**MEDDAS Ahmed Omrane**	University of Setif1	Medical Physics
20	**KEBIR Hada**	University of Bordj-Bouarreridj	Radiation Physics
21	**BOUMEDINE Lydia**	University of Setif1	Medical Physics
22	**MEBARKI Oussama**	University of Setif1	Medical Physics
23	**MEZIRI Imane**	CLCC of Setif	Medical Physics
24	**BENKAHILA Karim**	CLCC of Setif	Medical Physics
25	**ALOUI Haithem**	Babors Clinic of Setif	Nuclear Medicine
26	**BENAIDJA Asma**	University of Jijel	Medical Physics

*__CLCC:__ Fighting Against Cancer Medical Centre

+__USTHB:__ University of Science and Technology Houari Boumediene

Content

Author Index

2023

Detection of the primary location of a neuroendocrine tumor by 18F-FDG PET-CT

R. Belayouni[a], I. Meddeb[a,*], M. Somai [a], O. Ben Hamida[a], I. Yeddes[a], A. Mhiri, [a]

[a] Nuclear Medicine Department, Tunis medicine University, Tunis-1006, Tunisia.

ABSTRACT: Neuroendocrine tumors (NET) are rare and heterogeneous tumors that can arise anywhere in the body. Several metabolic imaging examinations can contribute to the positive diagnosis of these tumours, the choice of which depends on several factors. The purpose of this work is to show the contribution of 18Fluor-deoxyglucose (FDG) positron emission tomography (PET) coupled to computed tomography (CT) in the detection of the primary site of a neuroendocrine tumor discovered by a single metastasis. A 75-year-old patient who presents with pain in the right hypochondrium is considered. The morphological examinations (abdominal ultrasound and hepatic MRI) requested as first intention, demonstrated the presence of a well-limited tissue mass of 6 cm long axis of segment VI of the liver, suspicious. The patient underwent liver metastasectomy. The pathological examination and the immunohistochemical complement found the appearance of a hepatic metastasis of a poorly differentiated neuroendocrine carcinoma with a tumor proliferation index (Ki67) revealed at 80%. Somatostatin receptor scintigraphy was negative. The patient was sent to us for an 18F-FDG PET scan. The examination was performed 60 minutes after IV injection of 3MBq/Kg of 18 FDG and included PET-CT acquisition from the vertex to the mid-thighs. The 18FDG PET-CT examination shows the presence of a supracentimetric pulmonary nodule under the upper lobar pleural of the intensely hypermetabolic right lung with doubt about the presence of another smaller nodule in the contralateral posterobasal segment. The examination was otherwise unremarkable. The patient had a transthoracic biopsy whose histological examination found the same histological type of hepatic localization. NETs are classified into different histoprognostic grades according to their degree of cell differentiation and their proliferation index. The nuclear medicine imaging strategy is based on these grades. 18F-FDG PET/CT is the first-line examination, requested in the presence of a grade 3 tumor or having a Ki 67 > 10%.

Keywords: Neuroendocrine tumor; Primary location; 18FDG PET-CT examination.

INTRODUCTION

Neuroendocrine tumors (NETs) are rare and heterogeneous pathologies. They can start anywhere in the body. Metabolic imaging examinations are important in the detection and diagnosis of these tumors. The choice of the examination depends on several factors.

The aim of this case report is to show the contribution of positron emission tomography (PET) coupled with 18Fluor-deoxyglucose (FDG) computed tomography (CT) in the detection of the primary site of a neuroendocrine tumor discovered by a single metastasis [1,2].

EXPERIMENTAL

A 75-year-old patient who was recently complaining of a right hypochondriac pain. Morphological examinations (abdominal ultrasound and hepatic MRI) were done. We noted the presence of a well-limited suspicious mass of 6 cm long axis of segment VI of

the liver. The patient underwent a hepatic metastasectomy. Pathological examination and immunohistochemical complement concluded to a poorly differentiated neuroendocrine carcinoma with an estimated tumor proliferation index (*Ki67*) of 80%. Somatostatin receptor scintigraphy was negative. The diagnosis of liver metastasis was confirmed. The patient was referred for 18F-FDG PET scan.

The examination was performed 60 minutes after IV injection of 3MBq/Kg of 18 FDG and included a PET-CT acquisition from the vertex to the mid-thighs.

RESULTS AND DISCUSSION

The 18FDG PET-CT scan showed a supra centimetric sub pleural upper lobar lung nodule of the right lung intensely hypermetabolic with a doubts of presence of another smaller nodule in the contralateral posterobasal segment (Fig.1). The examination was unremarkable elsewhere. The patient underwent a transthoracic biopsy, the anatomopathological examination found the same histological type of the hepatic location. Pulmonary neuroendocrine tumors arise from bronchial mucosal cells known as enterochromaffin cells which are part of the diffuse neuroendocrine system. The pathological spectrum of pNETs ranges from low-/intermediate-grade neoplasms such as bronchial carcinoids, also known as typical or atypical carcinoids, to high-grade neoplasms as large-cell neuroendocrine carcinoma and small-cell lung cancer[3]. Controversial results have been reported on the diagnostic accuracy of fluorine-18-fluorodeoxyglucose positron emission tomography in bronchial carcinoids.

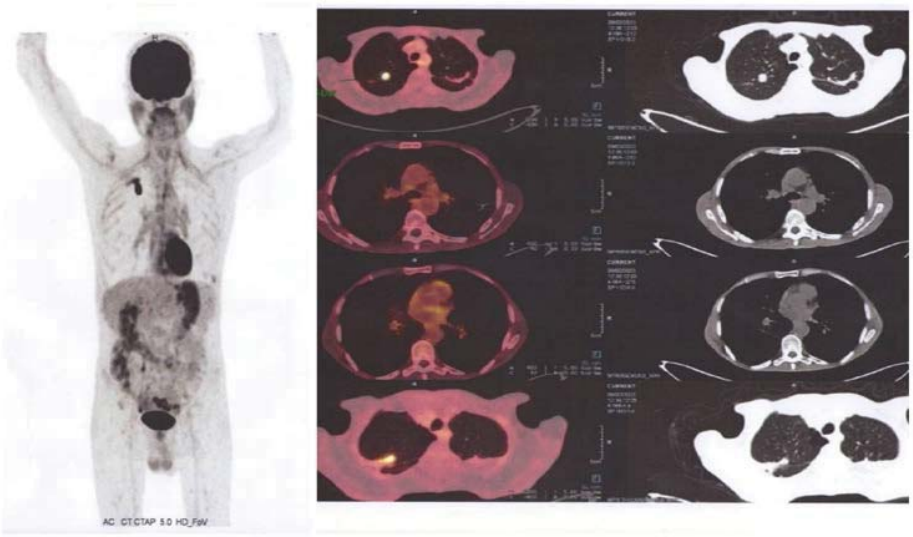

Fig.1: Upper lobar right lung nodule on the FDG PET/CT scan corresponding on CT images to a pulmonary nodule with associated post obstructive atelectasis, without evident extensive hilar or mediastinal lymph node enlargement.

CONCLUSIONS

NETs are classified into different histopronostic grades according to their degree of cellular differentiation and proliferation index. The imaging strategy in nuclear medicine is based on these grades. 18F-FDG PET/CT is the first-line examination requested for a grade 3 tumor or a tumor with a *Ki 67* > 10%.

AUTHOR INFORMATION

Corresponding Author

*Imen Meddeb Ben Slimène

Email address: imen.meddeb.bs@gmail.com

ACKNOWLEDGMENT

All Salah Azaiez Institut nuclear medicine staff (Physician Doctors and laboratory technicians)

REFERENCES

1. Principles of diagnosis and management of neuroendocrine tumours. Michael J. Raphael, MD, David L. Chan, MBBS, Calvin Law, MD, and Simron Singh, MD CMAJ. 2017 Mar 13; 189(10): E398–E404.
2. Diagnosing and Managing Carcinoid Heart Disease in Patients With Neuroendocrine Tumors: An Expert Statement. Journal of the American College of Cardiology. Volume 69, Issue 10, 14 March 2017, Pages 1288-1304.
3. PET/CT assessment of neuroendocrine tumors of the lung with special emphasis on bronchial carcinoids. Filippo Lococo et al. Tumour Biol. 2014 Sep; 35(9):8369-77.
4. Functional imaging evaluation in the detection, diagnosis, and histologic differentiation of pulmonary neuroendocrine tumors. Lococo F, et al. Thorac Surg Clin. 2014 Aug;24(3):285-92.

2023

Knowledge extraction from gene expression images: Adaptation of association rules mining for theory of evidence

N. Mekroud,[a*] A. Moussaoui,[b]

1 Department of Computer Science, Ferhat Abbas-Setif 1 University, Setif 19000, Algeria
2 Department of Computer Science, Ferhat Abbas-Setif 1 University, Setif 19000, Algeria

ABSTRACT: Imperfection is a common feature in almost all real-world data, although it usually hides crucial knowledge of major interest. Introducing theories of uncertainty to modeling gene expression areas in the embryo will help to extract hidden relationships between genes, while taking into account possible imprecisions in the boundaries of gene expression zones. Following a series of pre-processing steps on these images to improve feature extraction, the aim of our work is to propose an evidential theory based modeling of spatiotemporal data from In Situ Hybridization (ISH) sequences of images representing gene expression zones in different developmental phases of the embryo of the model species "Edinburg Mouse". We propose an adaptation of the Apriori algorithm to the evidential theory (named also Dempster-Shafer theory or belief theory) for mining association rules in the uncertain context. We have extracted two types of association rules, which will represent:

- In primal: the spatial correlations between gene expression areas in the embryo
- In dual: the relationships between genes that co-express in these ISH image sequences.

The biological interpretation of the obtained results confirmed their adequacy with the domain principles. The extracted knowledge will help biologists to better understand the interactions between genes, to discover the functional role of co-expressed groups of genes, and to model the gene expressions to detect possible anomalies.

Keywords: Knowledge extraction; Association rules; ISH images; Genetic-expression; Evidential theory.

INTRODUCTION

Bioinformatics, a topical field of research, uses computational methods to process heterogeneous and vital biological data, that is actually in wide expanding, but often imprecise and/or incomplete, and their interpretation is still a challenge[1]. Gene expression data integrate crucial knowledge about the stages of embryonic development of some model species, but (in main part) remain undiscovered and therefore unexploited by biologists.

Among the powerful forms of representation of gene expression are the ISH image sequences which indicate, in situ, zones where express each gene in the embryonic growth phases of some typical species (like "Edinburgh Mouse")[2]. These images form a spatiotemporal biological database and their study will help biologists to analyze in situ and understand the impact of gene expression in each embryonic phase, which is fundamental to detect any anomalies due to genetic causes during the preliminary developmental phases of living species (Fig.1).

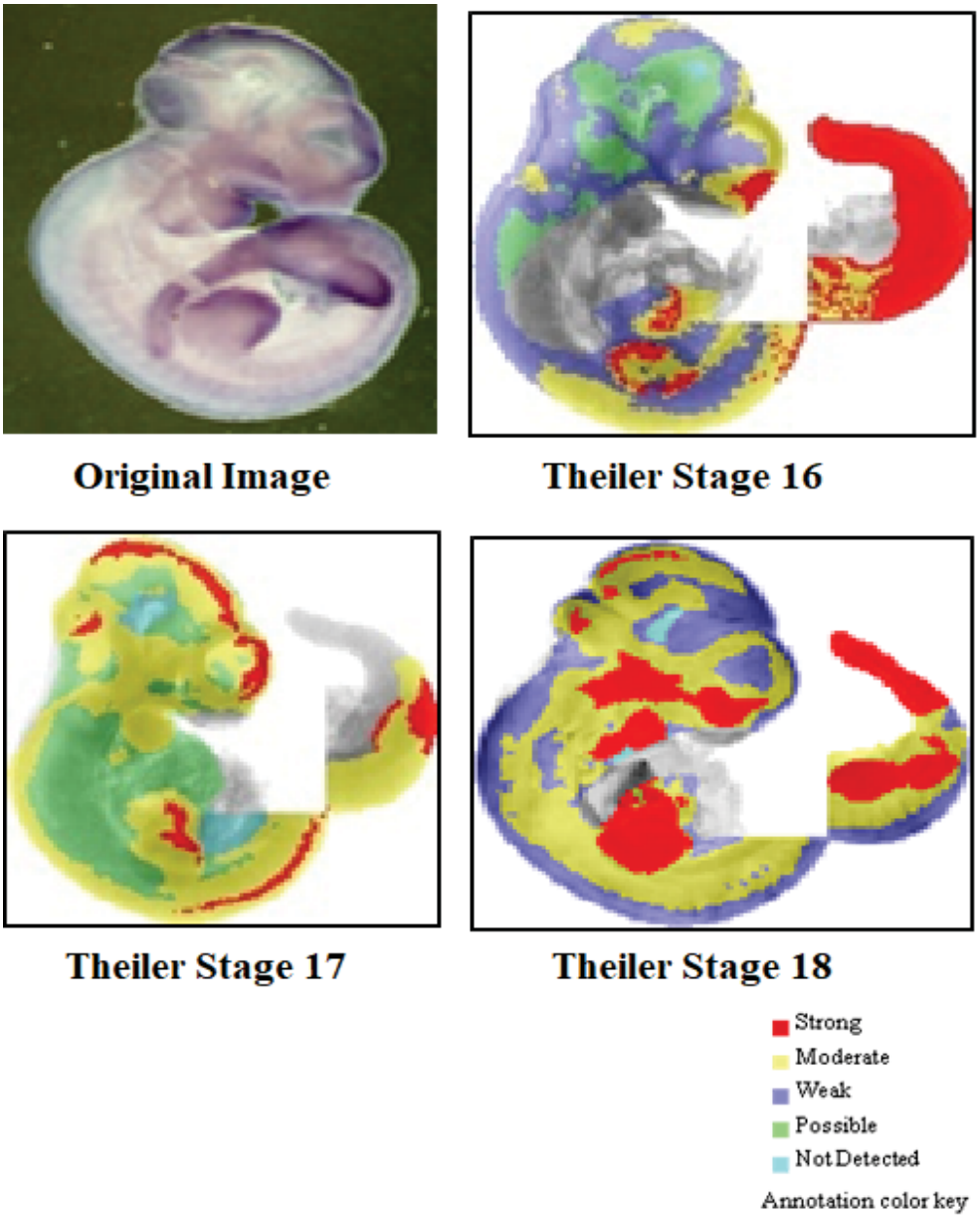

Fig. 1 : Example of genetic expression images of gene named "ATF4" mapped to the original image of a standard Edinburgh Mouse embryo (image on the left) during development phases TS16, TS17, TS18 (reference : EMAGE: 3052 in the online database: www.emouseatlas.org). The zones of genetic expression are colored according to the level of this expression[2]

For extracting hidden models and non-trivial knowledge, Association Rules (AR) are one of the most powerful algorithms in data mining, used to extract the relationships between a set of attributes initially in binary format[3]. But, in the real world, human generally dispose and deal with ambiguous knowledge about any situation, either because it has doubt about their veracity (this is ”uncertainty”) or it finds difficulties in stating them clearly (it is the ”vagueness”)[4].

Therefore, the binary representation of real-world data will generally cause a great loss of precision in their quantification and their semantics. Also, ignoring the possible imprecision in these data will influence the relevance of the results of the approaches proposed in the literature. In this work, we propose an Evidential modeling AR Mining (EARM), supporting the nuanced representation of data which is usually the closest to human reasoning and the reality of these data.

EXPERIMENTAL

The proposed approach is described in the organigram of figure 2.

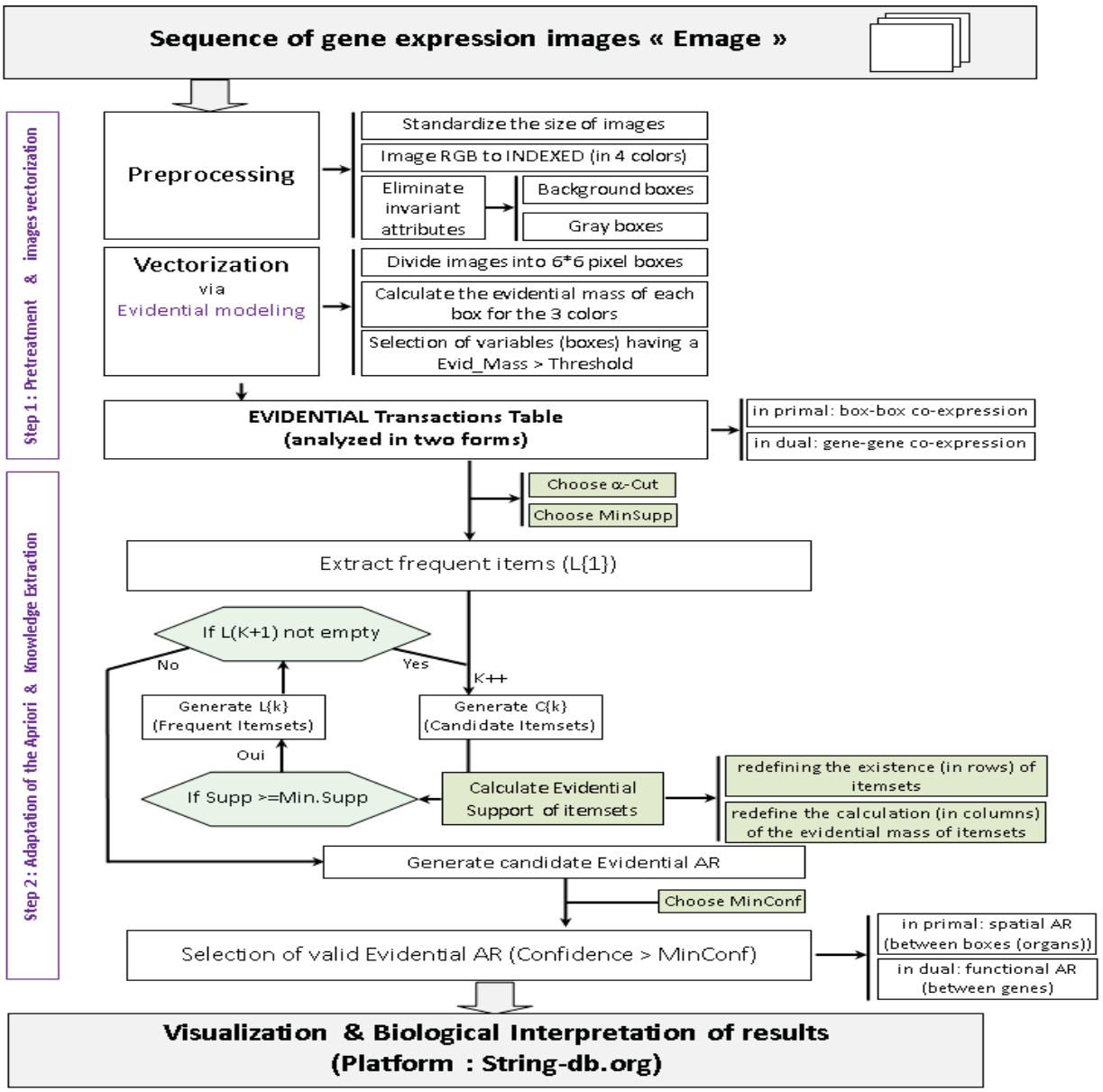

Fig. 2 : Detailed steps of the proposed approach

A sequence of preprocessing operations is carried out starting with the reduction of the dimensionality of studied images (and thus of the algorithmic complexity) while keeping the maximum of their variability, followed by their vectorization for features extraction according to the proposed modeling, this process leads to generating *evidential* transaction tables, which preserve almost all the knowledge contained in these sequences of studied ISH images. After that, we propose an adaptation of the *Apriori* algorithm to the Evidential Theory[5] (named also Dempster-Shafer Theory or Belief Theory) for mining association rules in the uncertain context by detecting:

- In primal: regions (adjacent pixels representing biological organs) that undergo synchronized genetic expression.
- In dual: sets of genes that co-express in different stages of embryonic development.

Also, the *nuanced* level of genetic expression (strong, moderate, and not detected) will be taken into consideration to extract features that represent the reality of these *not binary* biological data. All this in order to discover biological knowledge hidden in these ISH images.

RESULTS AND DISCUSSION

The figure below shows an example of AR extracted in the primal (relationship between boxes (see fig3-A) and an example of AR extracted in the dual (relationship between genes (see fig3-B).

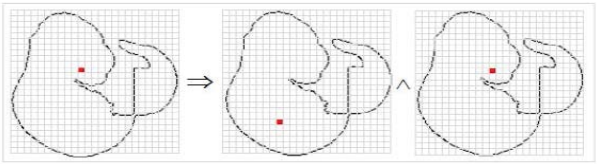

Fig. 3-A : Example of AR between boxes (AR in primal)

261_F ⇒ (484_F ∧ 262_F)

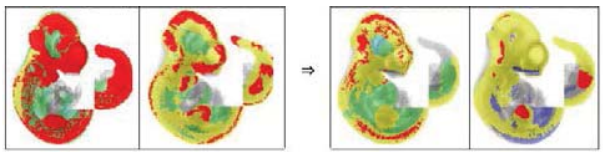

Fig. 3-B : Example of AR between genes (AR in dual)

(TS16_Zfp410 ∧ TS17_Smad4) ⇒ (TS17_Ndrg3 ∧ TS17_Rfx3)

The relations (between co-expressed genes) detected via the extracted ARs were also (for the most part) recognized (therefore approved) totally or partially by the String-db[6] platform, which proves the relevance of our results. The example below (fig. 4) shows the itemsets forming an AR extracted via the proposed approach, as well as a graph generated by String-db supporting the existence of a strong link between these genes.

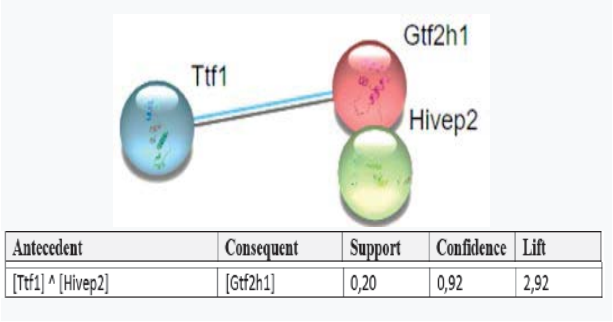

Antecedent	Consequent	Support	Confidence	Lift
[Ttf1] ^ [Hivep2]	[Gtf2h1]	0,20	0,92	2,92

Fig. 4: Example of graph generated by String-db for detected AR

CONCLUSIONS

The biological interpretation of the obtained results confirmed their adequacy with the domain principles. The extracted knowledge will help biologists to better understand the interactions between genes, and to discover the functional role of co-expressed groups of genes, also to model the gene expressions to detect possible genetic anomalies.

AUTHOR INFORMATION

Corresponding Author

*Noureddine Mekroud

Email address: Mekrroud_n@univ-setif.dz

REFERENCES

1. Keedwell, E., Narayanan, A.: Intelligent Bioinformatics: The Application of Artificial Intelligence Techniques to Bioinformatics Problems. John Wiley & Sons, 2005.
2. L.Richardson and al: EMAGE mouse embryo spatial gene expression database: (2014 update) Nucleic Acids Res. 42(1):D835-44, 2014.
3. R. Agrawal et al. Mining Association Rules between Sets of Items

in Large Databases. In Proceedings ACM SIGMOD International Conference on Management of Data, pp207, Washington DC, 1993.

4. Benfarhat, D.D.H.P.S., Denoeux, T., Dubois, D., Prade, H.: Représentations de l'incertitude en intelligence artificielle. Panorama de l'Intelligence Artificielle, Cépaduès Editions 3, 65 – 121, 2014.
5. G. Shafer : A Mathematical theory of Evidence, Princeton University Press, 1976.
6. STRING: functional protein association networks : https://string-db.org

2023

Simulation of Target Material Choice on Laser proton Dose Distribution for Biomedical Imaging

L. Boumedine,[a,*] D. Bara,[b] N. Ounoughi,[c] D. Bennaceur-Doumaz,[b] F. Kharfi[a]

[a] Dosing, Analysis, and Characterization with high resolution Laboratory (LDAC), Department of Physics, Ferhat Abbas-Setifl University, Algeria
[b] Center for the Development of Advanced Technologies, CDTA, Algiers, Algeria
[c] Radiation Physics and Applications Laboratory (LPRA), University of Jijel, Algeria

ABSTRACT: Proton imaging is a technique that uses accelerated protons in order to get morphological images. To minimise the cost/size of the instruments that produce these beams, a generation of compact accelerators have emerged called Laser-Plasma Accelerators (LPA) [1]. This study aims to compare and optimize the different dose distributions, obtained from the interaction of CPA (Chirped Pulse Amplification) laser pulses with two selected groups of metallic and polymer targets, thus shows that LPAs can integrate the proton imaging field. This work is split into two parts. First, in the framework of the Target Normal Sheath Acceleration(TNSA) regime[2], we develop a semi-analytical model within GNU Octave. A parametric study optimizing the characteristics of the accelerated proton beam is established to find a range of TNSA parameters that ensures a good proton beam, namely their number, energy and its spot size[2]. Then, we introduce the outputs resulting from the first part as initial values for the MC simulation, using the Gate software, where a comparative study of the dose distributions generated from proton beams using two target material types, metallic and polymers in the acceleration process[3] is realized. Finally, the simulation of the interaction of laser-matter and the study of the possibility to introduce them to proton radiography are proceeded. The results show an energy plateau for all the targets. The energy profiles show a prominent quasi-monoenergetic proton beams, suitable to generate high quality dose distribution, compared to the other metallic targets. It means that, they can be used to generate high mono-energetic proton beams that pass through the patient and reach a detector. These can give lower energies for the conditions given but an important number of protons. The influence of the target material choice on the dose distribution is displayed. In the framework of TNSA regime for LPA process, polymer targets represent a better choice to generate high quality dose distribution within the patient meaning high quality proton beams exploitable for proton imaging purposes. Therefore, they represent a good substitute for metallic targets, as they are rich in hydrogen atoms.

INTRODUCTION

Protons have shown incredible properties in radiation therapy due to their sharp and precise dose delivery into cancerous tissues, this ability shows better sparing of healthy tissues compared to conventional radiation therapy that uses photons instead of protons, and better dose distribution due to the Bragg peak physical property of these charged particles[4]. However, this technique requires great accuracy in terms of the range that the protons cross. To this day, we use X-Rays CT scans to get the patient's anatomy and convert electronic density of CT scans into protons stopping power therefore, calculate the protons' range. Yet, uncertainties up to 3 mm arise, affect the range of protons and jeopardize the dose distribution. These uncertainties are caused by the stopping power conversion method, the

inaccuracies in the excitation energy and electron density values assumed for the tissue and the different densities of the organs that protons encounter through their path. To alleviate the uncertainties, the implementation of imaging technics that would provide direct information on the proton path is necessary[5]. We focus on proton radiography; this technique relies on sending high energy with low intensity protons through the patient and reconstructing an image based on data displayed as the Water Equivalent Thickness (WET). Knowing that the energy loss of the transmitted protons represents the source of the image contrast resulted[6]. Many systems of proton radiography have been proposed, but we put our interest into proton radiography using Laser Plasma Accelerators (LPA). This type of accelerators has gained quite an interest in recent years in the acceleration field of heavy charged particles. A type of acceleration regime that caught our eye is Target Normal Sheath Acceleration (TNSA), it has been studied thoroughly both experimentally and theoretically[7]. It is an acceleration mechanism, which is induced by the interaction of high laser pulses up to 10^{22}W/cm^2 with a duration pulse of ~fs, with microscopic targets. There are very few published works concerning Laser Driven Radiography, for example: [8,9,10], even less on TNSA driven radiography. The attention devoted to the work cited in the [10] reference is due to the authors' use not only of LPAs but also of the TNSA regime to propose a setup for the emergence of these accelerators in the medical field of imaging by protons in radiography. The method used in this work is displayed on the section below. A theoretical model for the TNSA mechanism is suggested, where a parametric study on the target material choice for laser-matter interaction is performed, and the resulted characteristics obtained are simulated within the Gate software, to get depth-dose profiles for each material.

METHODS

To carry out this work, we propose a theoretical model implemented into the GNU Octave software, describing the interaction of ultra-high intensity laser with two types of targets: metallic and polymers using the TNSA regime. A high main laser pulse accelerates electrons created in the pre-plasma on the target's front surface. The electric field produced by the charge separation sheath on the rear surface of the microscopic target will accelerate the protons and ions perpendicular to it as some hot electrons pass through it and leave the rear surface through vacuum. Thus, the acceleration of protons depends on the production of hot electrons in the pre-plasma produced at the front surface of the target. The temperature, number, absorption factor, and angle of divergence θ_0 of the hot electrons are used to define them.

Semi-Analytical Model for TNSA X Proton Radiography

The main challenge encountered is to develop a semi-analytic model for proton radiography, in the framework of the TNSA regime, for this the basic radiography equation is used. The physical procedure for this type of radiography can be explained by taking on the angular distribution of Multi Coulomb Scattering (MCS), and a basic exponential formula for nuclear attenuation[11].

Main equations that govern our model are:

• The maximum cut-off energy is given by:

$$E_{max}=2T_{hot}\left[ln\left(\tau+\sqrt{\tau^2+1}\right)\right]^2 \quad (1)$$

Where T_{hot} represents the hot electrons temperature (Energy Boltzmann of hot electrons), $\tau = {w_{pi}t_{acc}}/{2exp(1)}$ is the normalized acceleration time with t_{acc} = 1.3 τ_L. τ_L, ω_{pi} are the laser pulse duration and the plasma frequency respectively.

• The energy spectrum is given by:

$$dN/dE = \frac{n_{e0}c_s t_{acc}}{2ET_{hot}}\, e^{-\sqrt{\frac{2E}{T_{hot}}}} \quad (2)$$

Where n_{e0} is the number of electrons at the rear surface of the target and c_s is their velocity[12].

• The basic Radiography Equation is given by:

$$T(L) = \sum_i \frac{L_i}{\lambda_i}\left(1 - e^{\frac{\theta_{cut}^2}{\theta_0^2}}\right), \quad (3)$$

where $T(L)$ describes the transmission of protons, L_i is the areal density for the i'th material, $\boldsymbol{\lambda}_i$ is the nuclear attenuation factor for the i'th material, θ_{cut} is the angle-cut imposed by the angular collimator and θ_0 is the multiple Coulomb scattering [11].

The results of this study are then simulated into Gate software, where we simulate the interaction of resulting proton beams with the required maximum cut-off energy of protons, their number and spot size of the beam, and study the effects of the LPAs on the dose distribution and the effects they have on proton radiography.

RESULTS AND DISCUSSION

First, the evolution of the maximum cut-off energy with different target types: metallic (Al and Ti) and polymers (PMMA and PET), as a function of the laser radius r_L is studied. Then, the interaction of a high-powered laser with an intensity of I=1.45 · 10^{20} W/cm^2, a laser pulse of τ_L = 800fs and a wavelength λ_L = 0.8µm with the target's thickness d = 20µm of Al, Ti, PMMA and PET is simulated. Results are shown in Fig. 1 and Fig. 2. We observe in Fig. 1, for the four targets a flat line which means a constant energy for the metallic target (up to ~160MeV) and polymers (up to ~163MeV), respectively. This flat line is more prominent and starting earlier for polymers compared to the metal Al. This is described by the quasi-mono-energetic beam given by the radius of the laser beam from the

laser radius r_L = 5µm and r_L = 3µm for metallic targets and polymers, respectively. This would be the first step into getting mono-energetic beam from LPAs and their application clinically. Thanks to the results obtained from the theoretical model, which consist on finding the adequate cut-off energy, number of protons and the spot size to get a mono-energetic and high-energy beam, the Fig. 2, represents the energy spectrum for the materials Al, Ti, PET and PMMA, respectively. Finally, the interaction of our proton beams with a water phantom is now simulated, and the dose distribution is studied. The results are shown in Fig. 3. The polymer targets allow us more depth penetration into the water phantom compared to the metallic targets: 4.3cm and 7.0cm for Al and Ti, respectively. Moreover, 7.6cm for both PET and PMMA. This means our proton beam resulting from the interaction of laser with micrometric targets of PET and PMMA allows us to enter the object, leave it and attain the detector to get an exploitable image of the objects to be imaged. This leads us to believe that polymer targets constitute a better choice in producing high quality proton beams usable in proton therapy for imaging purposes.

Compared to Wurl[10]'s work, we focus on the laser interaction part. Different types of targets are chosen, different laser parameters are explored (radius of laser beam r_L, pulse duration τ_L, wavelength λ_L) and tested to prove the laser and target choice can influence on the proton beams used, in our case proton Radiography. Higher energies are reached, thanks to the polymer targets (PET and PMMA) ~163 MeV. This result would help us image thicker objects, small animals if we reach even higher energies.

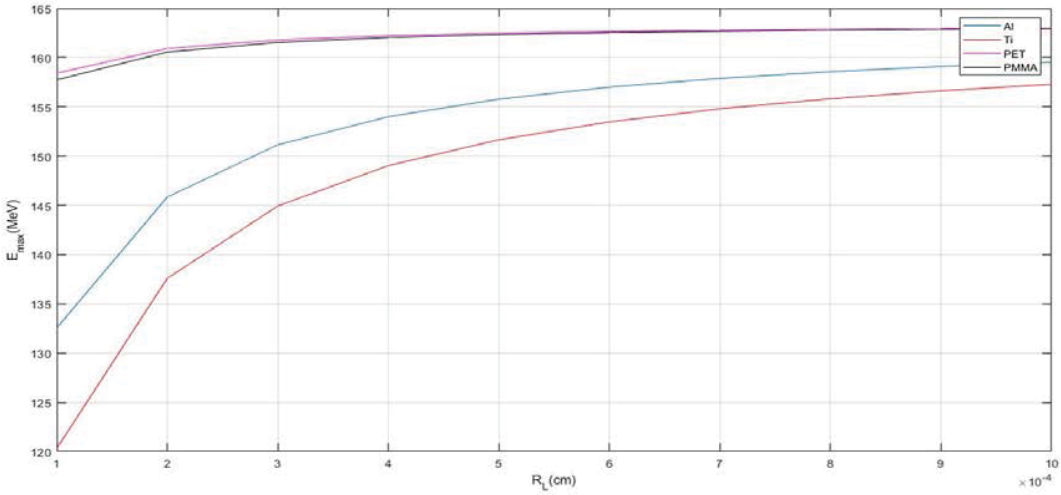

Fig. 1: Evolution of the maximum energy as a function of the laser radius r_L for metallic (Al and Ti) and polymer (PET and PMMA) targets.

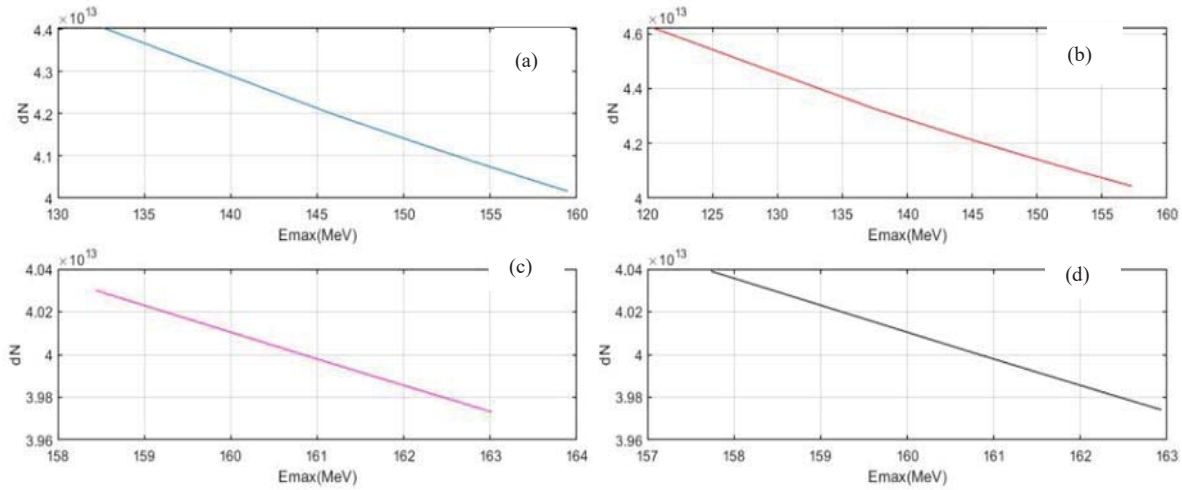

Fig. 2: Energy spectrum for Al (a), Ti (b), PET (c) and PMMA (d).

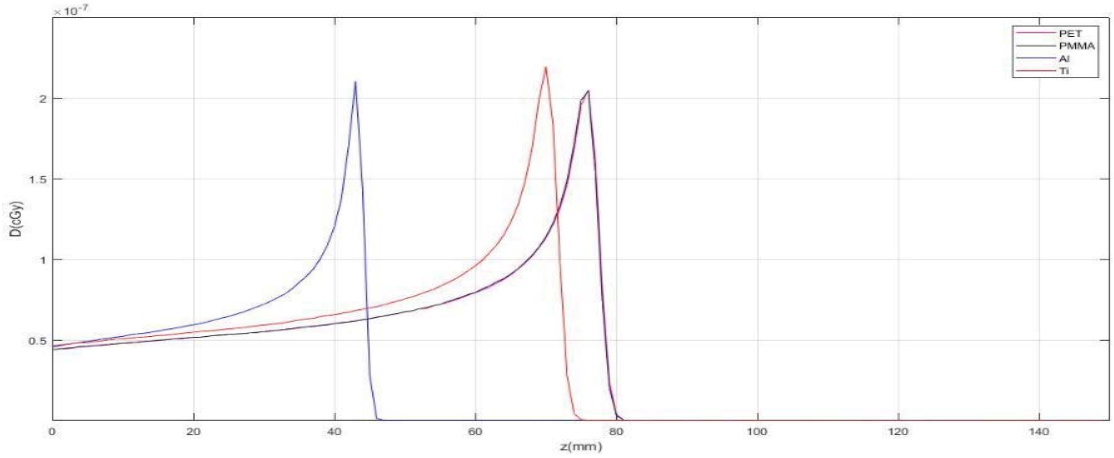

Fig. 3: Evolution of the dose as a function of depth z for laser radius r_L=0.9µm.

CONCLUSIONS

In this work, it is shown that laser driven proton beams are controllable by laser and target parameters. Energies of over 160 MeV that can penetrate objects of some centimeters are attained, and mono-energetic proton beams are found thanks to TNSA parameters. This mono-energetic state is more observed for PET and PMMA compared to the Al and Ti.

In terms of dose distribution, polymers show a better penetration into the object. Protons can cross higher depth before depositing their maximum dose into the object to be imaged for polymers against metals. These findings conclude that polymer targets are a better choice than metallic targets for producing qualitative proton beams for proton imaging.

AUTHOR INFORMATION

Corresponding Author

*L. Boumedine

Email address: boumedinelydia@gmail.com

REFERENCES

1. R. A. Snavely et al. Intense high-energy proton beams from petawatt-laser irradiation of solids. Phys. Rev. Lett. 85, 2945 (2000).
2. J. Ferri et al. Enhanced Target Normal Sheath Acceleration using colliding laser pulses. Commun Phys 2, 40 (2019).
3. E. Dahi, D. Bara, D. Bennaceur-Doumaz and B. Liani, Simulation of Proton Acceleration With Varying Laser Intensity in the Presence of Suprathermal Electrons, IEEE Transactions on Plasma Science 50, 2, 281 (2022).
4. S. Deffet. Proton radiography to reduce range uncertainty in proton therapy. Phd Thesis. University of Louvain. (2018).
5. J.T. Taylor, et al. A new silicon tracker for proton imaging and dosimetry. Nuclear Instruments & Methods in Physics Research A 0168-9002 (2016).
6. G. Poludniowski, N.M. Allinson, P.M. Evans. Proton radiography and tomography with application to proton therapy. Br J Radiol. 88-20150134 (2015).
7. D.Bara et al. Effects of pre-plasma potential on laser ion acceleration, International Journal of Nuclear and Quantum Engineering 13 6 (2019).
8. J.A. Cobble et al. High resolution laser-driven proton radiography Journal of Applied Physics 92, 1775 (2002).
9. T. Hodge. Radiographic applications and control of TNSA proton beams. Phd Thesis. Queen's university Belfast. (2020).
10. M. Würl et al. A Monte Carlo feasibility study on quantitative laser-driven proton radiography. Z Med Phys 32, 109 (2022).
11. X. Hai-Bo and Z. Na. The optimum angle-cut of collimator for the dense objects in high-energy proton radiography. Chinese Phys. *C* 40, 028201 (2016).
12. J. Fuchs et al. Laser-driven proton scaling laws and new paths towards energy increase. Nature physics 2 (2006).

2023

Medical Images Semantic Segmentation Using Deep Learning: A Survey

F. Lahrache,[a,*] A. Moussaoui,[b] N. Ferahta,[b] S. Oulad-naoui,[a,*]

[a] Department of Mathematics and Computer Science, University of Ghardaia, Ghardaia-47000, Algeria

[b] Department of Computer Science, Ferhat Abbas University of Sétif 1, Sétif -19000, Algeria

[*] Laboratoire des Mathématiques et Sciences Appliquées, University of Ghardaia, Ghardaia-47000, Algeria

ABSTRACT: Biomedical image processing and segmentation is currently an important research direction in the field of computer vision. With the rapid development of deep learning and the emergence of many neural networks architectures and other mechanisms such as vision transformers, medical image processing has become a research hotspot. This work focuses on the review of medical image segmentation and semantic segmentation based on state-of-the-art deep learning techniques.

Keywords: Semantic Segmentation; Medical Imaging; Deep Learning; Transformers; Vision Transformer (ViT).

INTRODUCTION

Image processing, analysis and understanding techniques are an integral part of many applications used in our time and a wide and important research option in the field of computer vision, especially image segmentation, which is involved in most applications, the most important of which are applications in the medical field, where the semantic segmentation of medical images is one of the most important things that are currently being addressed due to the sensitivity and importance of this field, as it is facing an unprecedented development at the present time, especially with the development of medical imaging techniques and image quality[1,2]. Currently, vision transformers are the leading research direction that is witnessing a wide publication revolution.

EXPERIMENTAL

In this section, we provide a historical overview of image segmentation and its use in medical imaging, along with some recent research.

Background

The history of image segmentation dates back to 1965, when with the widespread spread of digital images in many fields, segmenting them to obtain information from them became a necessary matter. Image segmentation is divided into semantic and instant segmentation, as shown in Fig. 1. The algorithms and techniques used in image segmentation also varied, as shown in Fig. 2.

Medical Imaging

Medical imaging is a non-invasive technology whose goal is to create visual images of the internal tissues of the human body by acquiring signals by making use of the physical principles of sound, light, electromagnetic waves, etc [3,4]. There are several medical imaging modalities that produce different types of medical images as shown in Fig. 3.

.Medical Images Segmentation

Accurate medical image segmentation is the use of computer

image processing technology to analyze and process 2D or 3D images for segmentation, extraction, 3D reconstruction, and 3D display of human organs, soft tissues and diseased bodies[5]. Medical images segmentation approaches are classified into organ specific and multi-organ categories as shown in Fig. 4.

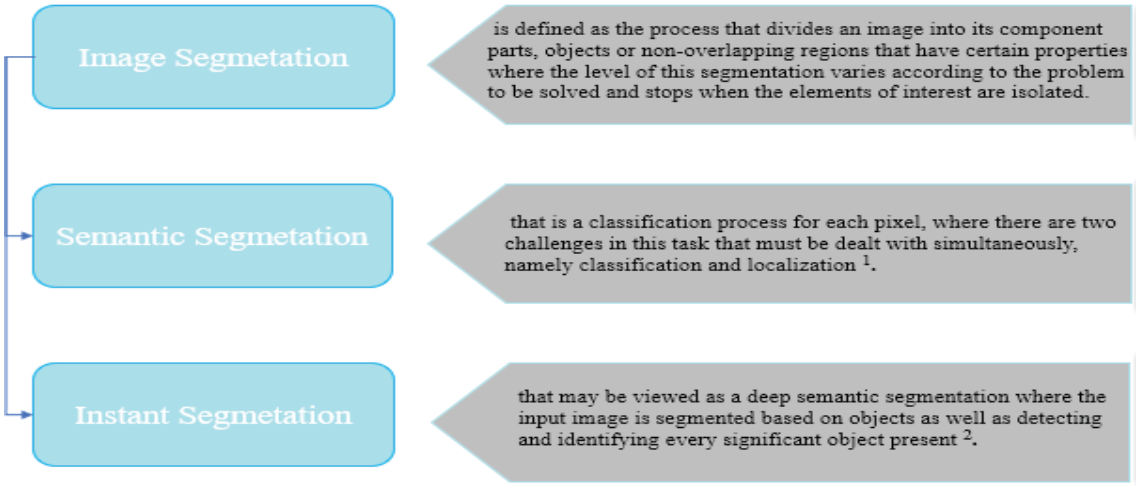

Fig. 1: Image Segmentation

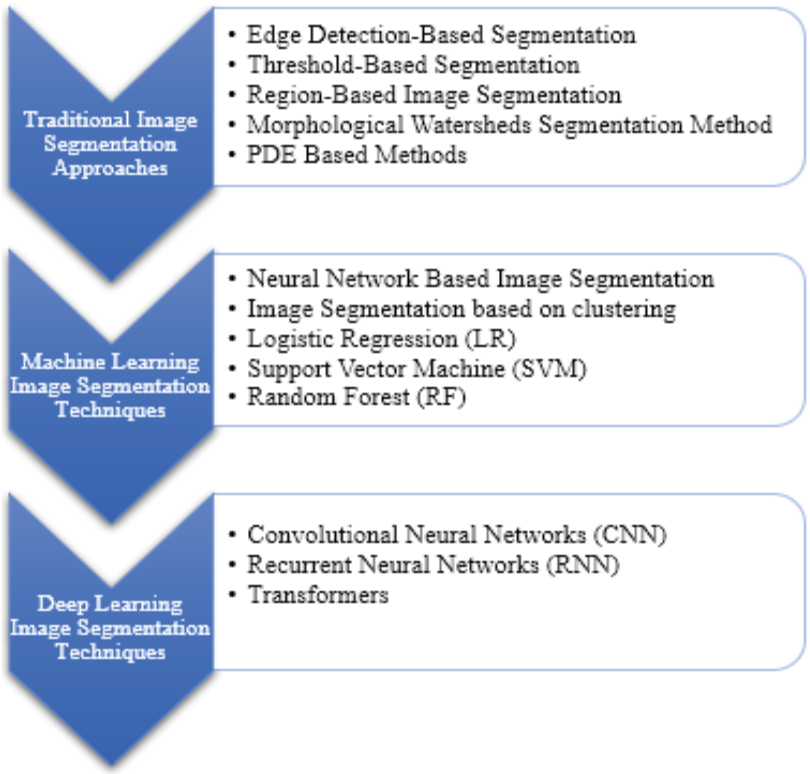

Fig. 2 : Image Segmentation Approaches

Fig. 3: Medical Imaging Modalities

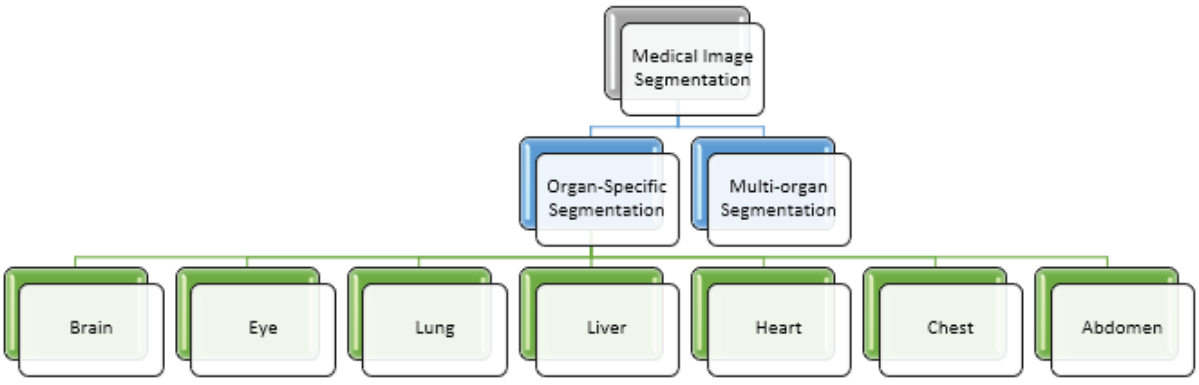

Fig. 4: Medical Imaging Segmentation

Medical Image Segmentation and Semantic Segmentation Techniques

Deep Learning Techniques: Fully convolutional network FCN was the first successfully deep learning network for image semantic segmentation that achieved outstanding results, then we find other outstanding segmentation networks such as U-Net, Mask R-CNN , RefineNet , and DeconvNet, which have a strong advantage in processing fine edges [5]. V-Net, RNNs, DeepLab and vision transformers were also used.

Convolutional Neural Networks (CNNs): for the semnatic segmentation task the basic network structure is a combination of a front-end-based CNN encoder and a back-end-based decoder [5], the famous used networks are: ResNet [6], VGGNet [7], GoogleNet [8]...ect.

Fully Convolutional Network (FCN)[9]: was proposed to overcome the limitations of CNN where the last fully connected layer of CNN was converted into a fully convolutional layer [2,8] .

U-Net [10]: is an encoder-decoder network that uses the concept of deconvolution, which was built on FCN's architecture. The encoding part includes convolutional and pooling layers while the decoding part consists of alternating upsampling that upscales the size of a feature map, and pooling layers [2,11].

V-Net[12]: is a variant of U-Net that has compression and decompression networks and contains residual connections to speed up network convergence and avoid gradient vanishing which makes it deeper and gives higher performance [2,11].

Recurrent Neural Networks (RNNs): were designed to handle sequences, but when used for semantic segmentation, they achieved very satisfactory results due to their ability to learn long-term dependencies from the sequenced data and their ability to hold memory along the sequence [11,13].

Regional Convolutional Networks (R-CNNs): traditional R-CNN creates region proposal network for bounding boxes using a selective search process, then these region proposals are warped to standard squares and forwarded to a CNN to create a feature vector map as output[2]. R-CNN variants of are: fast R-CNN, faster R-CNN, and mask R-CNN.

Deeplab Model: uses the pretrained CNN model Resnet-101/VGG-16 [8]. It has some variants that are Deeplab V1, Deeplab V2, Deeplab V3 and Deeplab V3+.

Vision Transformers (ViTs): are a variants of language transformer that rely on attention mechanism that compensated for the shortcoming of CNN networks in the lack of the ability to capture long-range dependencies such as extraction of contextual information and non-local association of objects. They were used in segmenting medical images semantically due to the fact that they scale up more easily and are more robust to corruption making them the most appropriate for complex images [3,4-,14-16].

Some famous research papers that uses those networks are mention in Table 1.

Table 1. Some Deep Learning Medical Image Segmentation Papers

References	Organ	Modalities	Network Type
Zhang et al. [17]	Brain	Multi-modality MRI	CNN
Moeskops et al. [18]	Multi-Organ	MRI, CTA	CNN
Nie et al. [19]	Brain	Multi-modality MRI	FCN
R. Roth et al. [20]	Multi-Organ	CT	FCN
Gordienko et al. [21]	Lung	X-ray	U-Net

Ye et al. [22]	Heart	CT	U-Net
Gibson et al. [23]	Multi-Organ	CT	V-Net
Z. Alom et al. [24]	Multi-Organ	Multi-modality	RCNN (Reccurent CNN)
Wang et al. [25]	Multi-Organ	CT	Mask R-CNN
Tang et al. [26]	Liver	CT	R-CNN + DeepLab
Karimi et al. [27]	Multi-Organ	Multi-modality	Pure Transformer
Wang et al. [28]	Brain	MRI	Transformer (TransBTS)
Shen et al. [29]	Kidney	CT	Transformer (COTRNet)

MRI: Magnetic Resonance Imaging; CT: Computed Tomography; CTA: Computed Tomography Angiography

RESULTS AND DISCUSSION

We can say after this study that each deep learning technique used for medical images segmentation that appears solves the problem of its predecessor, and that the pioneer is currently the vision transformers with attention mechanism.

CONCLUSIONS

Our review introduces image segmentation with its approaches and focuses on deep learning methods where we summarize several architectures and the reasons for their emergence. We concluded that the leading choices for medical image segmentation are transformers with attentional mechanisms.

AUTHOR INFORMATION

Corresponding Author

*Ferialle Lahrache

Email address: lahrache.ferialle@univ-ghardaia.dz

REFERENCES

1. C. Peng, X. Zhang, G. Yu, G. Luo, J. Sun, Large kernel matters - improve semantic segmentation by global convolutional network, CoRR abs/1703.02719 (2017). arXiv:1703.02719. URL http://arxiv.org/abs/1703.02719
2. P. Malhotra, S. Gupta, D. Koundal, A. Zaguia, W. Enbeyle, Deep neural networks for medical image segmentation, Journal of Healthcare Engineering 2022 (2022).
3. J. Li, J. Chen, Y. Tang, C. Wang, B. A. Landman, S. K. Zhou, Transforming medical imaging with transformers? a comparative review of key properties, current progresses, and future perspectives, Medical Image Analysis 85 (2023) 102762. doi:https://doi.org/10.1016/j.media.2023.102762. URL https://www.sciencedirect.com/science/article/pii/S1361841523000233
4. J. Beutel, H. L. Kundel, Y. Kim, R. L. Van Metter, S. C. Horii, Handbook of medical imaging: display and PACS, Vol. 3, Spie Press, 2000.
5. K. He, C. Gan, Z. Li, I. Rekik, Z. Yin, W. Ji, Y. Gao, Q. Wang, J. Zhang, D. Shen, Transformers in medical image analysis, Intelligent Medicine (2022). doi:https://doi.org/10.1016/j.imed.2022.07.002. URL https://www.sciencedirect.com/science/article/pii/S2667102622000717
6. X. Liu, L. Song, S. Liu, Y. Zhang, A review of deep-learning-based medical image segmentation methods, Sustainability 13 (3) (2021). doi:10.3390/ su13031224. URL https://www.mdpi.com/2071-1050/13/3/1224
7. K. He, X. Zhang, S. Ren, J. Sun, Deep residual learning for image recognition, in: 2016 IEEE Conference on Computer Vision and Pattern Recognition (CVPR), IEEE Computer Society, Los

Alamitos, CA, USA, 2016, pp. 770–778. doi:10.1109/CVPR.2016.90. URL https://doi.ieeecomputersociety.org/10.1109/CVPR.2016.90

8. K. Simonyan, A. Zisserman, Very deep convolutional networks for large-scale image recognition, Computational and Biological Learning Society, 2015, pp. 1–14.
9. C. Szegedy, W. Liu, Y. Jia, P. Sermanet, S. Reed, D. Anguelov, D. Erhan, V. Vanhoucke, A. Rabinovich, Going deeper with convolutions, in: 2015 IEEE Conference on Computer Vision and Pattern Recognition (CVPR), 2015, pp. 1–9. doi:10.1109/CVPR.2015.7298594.
10. J. Long, E. Shelhamer, T. Darrell, Fully convolutional networks for semantic segmentation, in: 2015 IEEE Conference on Computer Vision and Pattern Recognition (CVPR), 2015, pp. 3431–3440. doi:10.1109/CVPR. 2015.7298965.
11. O. Ronneberger, P. Fischer, T. Brox, U-net: Convolutional networks for biomedical image segmentation, in: N. Navab, J. Hornegger, W. M. Wells, A. F. Frangi (Eds.), Medical Image Computing and Computer-Assisted Intervention – MICCAI 2015, Springer International Publishing, Cham, 2015, pp. 234–241.
12. R. Wang, T. Lei, R. Cui, B. Zhang, H. Meng, A. K. Nandi, Medical image segmentation using deep learning: A survey, IET Image Processing 16 (5) (2022) 1243–1267. doi:10.1049/ipr2.12419. URL https://doi.org/10.1049%2Fipr2.12419
13. F. Milletari, N. Navab, S.-A. Ahmadi, V-net: Fully convolutional neural networks for volumetric medical image segmentation, in: 2016 Fourth International Conference on 3D Vision (3DV), 2016, pp. 565–571. doi: 10.1109/3DV.2016.79.
14. E. U. Henry, O. Emebob, C. A. Omonhinmin, Vision transformers in medical imaging: A review (2022). doi:10.48550/ARXIV.2211.10043. URL https://arxiv.org/abs/2211.10043
15. Parvaiz, M. A. Khalid, R. Zafar, H. Ameer, M. Ali, M. M. Fraz, Vision transformers in medical computer vision – a contemplative retrospection (2022). doi:10.48550/ARXIV.2203.15269. URL https://arxiv.org/abs/2203.15269
16. F. Lateef, Y. Ruichek, Survey on semantic segmentation using deep learning techniques, Neurocomputing 338 (2019) 321–348. doi:https://doi.org/10.1016/j.neucom.2019.02.003. URL https://www.sciencedirect.com/science/article/pii/S092523121930181X
17. W. Zhang, R. Li, H. Deng, L. Wang, W. Lin, S. Ji, D. Shen, Deep convolutional neural networks for multi-modality isointense infant brain image segmentation, NeuroImage 108 (2015) 214–224. doi:https://doi.org/10.1016/j.neuroimage.2014.12.061. URL https://www.sciencedirect.com/science/article/pii/S1053811914010660
18. P. Moeskops, J. M. Wolterink, B. H. M. van der Velden, K. G. A. Gilhuijs, T. Leiner, M. A. Viergever, I. Išgum, Deep learning for multi-task medical image segmentation in multiple modalities, in: S. Ourselin, L. Joskowicz, M. R. Sabuncu, G. Unal, W. Wells (Eds.), Medical Image Computing and Computer-Assisted Intervention – MICCAI 2016, Springer International Publishing, Cham, 2016, pp. 478–486.
19. D. Nie, L. Wang, Y. Gao, D. Shen, Fully convolutional networks for multimodality isointense infant brain image segmentation, in: 2016 IEEE 13th International Symposium on Biomedical Imaging (ISBI), 2016, pp. 1342–1345. doi:10.1109/ISBI.2016.7493515.
20. H. R. Roth, H. Oda, Y. Hayashi, M. Oda, N. Shimizu, M. Fujiwara, K. Misawa, K. Mori, Hierarchical 3d fully convolutional networks for multi-organ segmentation (2017). doi:10.48550/ARXIV.1704.06382. URL https://arxiv.org/abs/1704.06382
21. Y. Gordienko, P. Gang, J. Hui, W. Zeng, Y. Kochura, O. Alienin, O. Rokovyi, S. Stirenko, Deep learning with lung segmentation and bone shadow exclusion techniques for chest x-ray analysis of lung cancer, in: Z. Hu, S. Petoukhov, I. Dychka, M. He (Eds.), Advances in Computer Science for Engineering and Education, Springer International Publishing, Cham, 2019, pp. 638–647.
22. C. Ye, W. Wang, S. Zhang and K. Wang, "Multi-Depth Fusion Network for Whole-Heart CT Image Segmentation," in IEEE Access, vol. 7, pp. 23421-23429, 2019, doi: 10.1109/ACCESS.2019.2899635.
23. E. Gibson, F. Giganti, Y. Hu, E. Bonmati, S. Bandula, K. Gurusamy, B. Davidson, S. P. Pereira, M. J. Clarkson, D. C. Barratt, Automatic multi-organ segmentation on abdominal ct with dense v-networks, IEEE Transactions on Medical Imaging 37 (8) (2018) 1822–1834. doi:10.1109/ TMI.2018.2806309.
24. M. Z. Alom, M. Hasan, C. Yakopcic, T. M. Taha, V. K. Asari, Recurrent residual convolutional neural network based on u-net (r2u-net) for medical image segmentation (2018). doi:10.48550/ARXIV.1802.06955. URL https://arxiv.org/abs/1802.06955
25. Wang, T., Lei, Y., McDonald, M.W., Beitler, J.J., Curran, W.J., Liu, T., & Yang, X. (2021). Multi-organ segmentation on head and neck dual-energy CT using Deep Neural Networks. Medical Imaging.
26. W. Tang, D. Zou, S. Yang, J. Shi, Dsl: Automatic liver segmentation with faster r-cnn and deeplab, in: V. Kůrková, Y. Manolopoulos, B. Hammer, L. Iliadis, I. Maglogiannis (Eds.), Artificial Neural Networks and Machine Learning – ICANN 2018, Springer International Publishing, Cham, 2018, pp. 137–147.
27. D. Karimi, S. D. Vasylechko, A. Gholipour, Convolution-free medical image segmentation using transformers, in: M. de Bruijne, P. C. Cattin, S. Cotin, N. Padoy, S. Speidel, Y. Zheng, C. Essert (Eds.), Medical Image Computing and Computer Assisted Intervention – MICCAI 2021, Springer InternationalPublishing, Cham, 2021, pp. 78–88.
28. W. Wang, C. Chen, M. Ding, H. Yu, S. Zha, J. Li, Transbts: Multimodal brain tumor segmentation using transformer, in: M. de Bruijne, P. C. Cattin, S. Cotin, N. Padoy, S. Speidel, Y. Zheng, C. Essert (Eds.), Medical Image Computing and Computer Assisted Intervention – MICCAI 2021, Springer International Publishing, Cham, 2021, pp. 109–119.
29. Z. Shen, H. Yang, Z. Zhang, S. Zheng, Automated kidney tumor segmentation with convolution and transformer network, in: N. Heller, F. Isensee, D. Trofimova, R. Tejpaul, N. Papanikolopoulos, C. Weight (Eds.), Kidney and Kidney Tumor Segmentation, Springer International Publishing, Cham, 2022, pp. 1–12.

2023

Renal TAC modeling and comparison to experimental and clinical dynamic scintigraphy results

N. Ait Ali Braham,[a,*] S. Belazzoug,[a] I. Ghedbane,[c] R. Benlabga,[d] H. Aloui,[d] F. Kharfi,[a,b]

[a] Department of Physics, Faculty of Science, Ferhat Abbas-Setif1 University, Setif-19000, Algeria

[b] Laboratory Dosing Analysis and Characterization with high resolution, Ferhat Abbas-Setif1 University, Setif-19000, Algeria

[c] Centre of Scintigraphy Imaging (Dr. Ghodbane), Setif-19000, Algeria

[d] *Les Babors* Clinic, Setif-19000, Algeria

ABSTRACT: The renal time-activity (TAC) curve is a graphical representation of the distribution and elimination of a radiotracer within the kidneys over a period. It is an essential tool used in nuclear medicine and renal imaging to evaluate the function and blood flow of the kidneys. The importance of the renal time-activity curve lies in its ability to provide valuable information about renal function and to detect any anomalies or diseases affecting the kidneys. The first objective of this work is the experimental reconstruction of TACs from clinical data of dynamic scintigraphy and their comparison to those provided by scintigraphy machine in terms of main dynamic parameters. The second objective is the evaluation of some used mathematical models that fit experimental and clinical TACs based on the modelling of the physiological processes occurring within the kidneys. In this study, many renal TACs are compared, namely: TACs clinically acquired, TACs manually reconstructed based on region of interest (ROI) selection, TACs modelled with one-compartmental model using *MatLab* and *Origin*, and TACs fitted by a set of mathematical equations including mono-exponential fitting, Patlak, and bi-exponential fitting which have been taken as approximate solutions of the ordinary differential equation (ODE) describing the one -compartment model. Manual established TACs of kidneys was found ROI dependent. Bi-exponential fitting function was correctly subtracted showing no vascular phase. Established TAC with MatLab one-compartment ODE based algorithm needs more adjustment and primary information to be accurate. In this work, TAC optimal extraction and modeling conditions and approaches were compared and discussed. Some of modelled TACs were able to provide detailed information on the kinetics and can be used to estimate quantitative parameters related to the kidney function.

Keywords: TAC; Dynamic Renal Scintigraphy; Modeling; One-compartment model, Patlak model; Bi -exponential fit; Mono-expensively fit.

INTRODUCTION

Dynamic Renal Scintigraphy (DRS) assumes a robust diagnostic tool. It provides a powerful array of capabilities for functional and molecular imaging in the kidney[1]. The diagnosis is primly based on the evaluation of several dynamic parameters extracted from the time activity curve (TAC), offering real-time insights into the biodistribution and pharmacokinetics of radiotracers within the renal system.[2]

To bolster the analysis of dynamic renal scintigraphy Data, TAC modeling plays a pivotal role. It allows researchers and clinicians to extract valuable quantitative parameters related to renal physiology by mathematically representing the temporal uptake

of radiotracers. Furthermore, mathematical models shed light on the extent to which tissue radioactivity measurements align with the intended physiological function and they enhance the data's signal-to-noise characteristic by eliminating additional variability introduced by external physiological factors [3].

Nevertheless, the path from raw dynamic data to quantifiable renal parameters is laden with complexities, influenced by a numerous factors. Among these, the selection of the region of interest (ROI) method emerges as a critical step in TAC extraction. Indeed, the selection method and the shape of ROI profoundly affects the resulting TAC.

The aim of this study is, therefore, to present a comparative analysis of dynamic parameters[8] extracted from renal TACs clinically acquired, manually replotted based on two distinct methods of ROI selection , modelled with one–compartmental model [4] using *MatLab* and *Origin* , fitted by a set of mathematical equations that include mono-exponential[5,6] , patlak[7] and bi-exponential [5,6]. These functions constitute approximate solutions of the ordinary differential equation (ODE) describing the one-compartment model. An additional goal was to assess the rate elimination and absorption constants to gain insights into the kinetics of the renal system.

EXPERIMENTAL

Patient characteristics

This retrospective study included a cohort of 12 anonymous patients (15-56 years) who underwent renal cortical imaging (using 99mTc-DMSA) and dynamic renal scintigraphy using 99mTc-DTPA between 2021 and 2023 for various medical indications at the Centre of Scintigraphy Imaging, Dr. Ghodbane, of Sétif.

Patient imaging and clinical TAC generation

The imaging procedure was performed using a gamma camera, specifically the Discovery NM630 model. It involves capturing a series of 110 sequential frames, with shorter acquisition times during the first minute (one frame per second), followed by a slower rate of acquisition (1 frame per 15 seconds). This acquisition process continues for a total duration of 20 minutes in order to monitor the tracer uptake, distribution, and clearance in the kidneys.

Generating clinical TACs with *Xeleris* software involves selecting a ROI encompassing both kidneys in the image sum of 110 frames. A larger ROI is preferred to ensure comprehensive coverage for functional and drainage assessment.

ROI Selection

Primary data processing encompasses the generation of regions of interest (ROI) corresponding to the right and left kidney areas, along with the background, on the 110 frames for each patient.

Two methods for ROI selection and data extraction are applied:

Free hand method

MATLAB code was elaborated enabling the manual drawing of a region of interest (ROI) around the desired kidney on a single image (Fig.1). This drawn ROI was then saved as a mask and applied to all 110 images in the sequence. The same procedure was repeated to draw a C-shaped region of interest for the background. Subsequently, we extracted the mean grayscale values and standard deviations from each ROI, which represented the mean intensity levels within the selected areas.

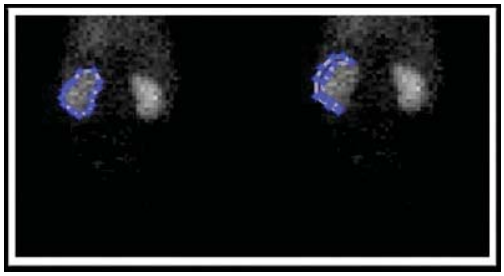

Fig. 1: The determination of the ROI for the left kidney was performed through free-hand delineation, with a C-shaped background

Regular shape method

Using Fiji software, we drew two ellipses: one to encompass the ROI of the kidney and another to enclose the background area (Fig.2). The ellipse shape was chosen for its ability to approximate the anatomical structure of the kidney and provide a standardized shape for analysis. After ROI section, the mean value and standard deviation are measured.

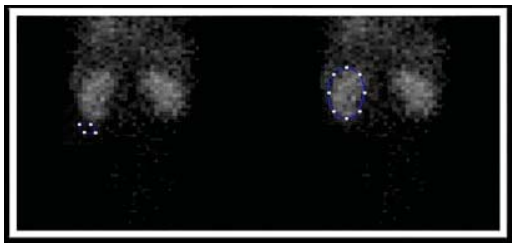

Fig. 2: The kidney ROIs are determined using Fiji software, employing an ellipse shape. It is important to note the presence of elliptical-shaped background regions positioned at the lateral edge of the kidney.

Experimental TAC generation

MatLab code was developed to export the ROI mean values and standard deviations of the kidney and the background for each method. Subsequently the net grayscale are calculated using the equation (Eq.1):

$$GS_{Net} = GS_{mean}(Kidney) - GS_{mean}(Bachgroun), \quad (1)$$

Where GS_{Net} is the net gray scale, $GS_{mean}(Kidney)$ is the mean grayscale value of kidney, and $GS_{mean}(Background)$ is the mean grayscale value of background[9].

With this net gray scale, experimental TACs are generated and following dynamic parameters are determined:

- **Time to peak (TTP ou T_{max})**: the point at which the curve reaches its maximum value,
- **The 20min/3min ratio**: the ratio between the curve's value at 20 minutes and its value at 3 minutes,
- **The 20min/peak ratio**: the ratio between the curve's value at 20 minutes and its maximum curve's value.

Renal TAC modeling: study on real case

Model selection

A one tissue compartmental model (Fig.3) is used, where the kidney is considered as a homogeneous singular body[10].

The dynamic parameters derived from the analysis of the one-compartmental model provide quantitative measurements of renal function, involving[11,12] :

k_a: The rate constant of absorption , which expresses the rate at which the radio tracer DTPA is incorporated in the kidney, is measured in s^{-1}.

k_e: The rate constant of elimination ,which expresses the rate at which the DTPA is excreted from the kidney, is measured in seconds. s^{-1}.

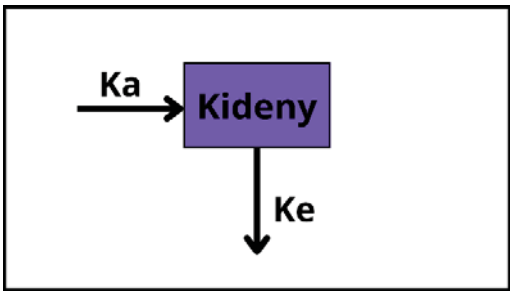

Fig. 3: Schematic representation of the single compartmental tracer kinetic model.

Mathematical fitting equations

The fitting process is performed using *MatLab* and *Origin* softwares by employing the following mathematical functions (Table.1):

Table 1: Approximation mathematical functions [5,6,7]

Method	Mathematical function	Description
Mono-exponential	$f_1 = C_0(1 - \exp(-K_a t))$	Approximation to the solution of one compartmental differential equation where C_0 is the initial concentration of radiotracer, K_a is the uptake or absorption rate, and K_e is the elimination or clearance rate),
Patlak plot	$f_2 = K_a \times t + K_e \times sqrt(t)$	Graphical approach
Bi-exponential1	$f_3 = A \times \frac{(K_e \times K_a)}{(K_a - K_e)} \times \exp(-K_a t) - \exp(-K_e t) + B$	Described in the study by Devasia et al.[5] using two rates constants K_a(uptake or absorption rate) and K_e (elimination or clearance rate). *A* is the scaling factor and *B* is the error.
Bi-exponential 2	$f_4 = A \times (1 - exp(-K_a t)) \times (\exp(-K_e t)$	*A* represents the initial concentration of radiotracer

For *MatLab*, the optimization process is facilitated using a suitable optimization function (such as "*fminsearch()"*) to minimize the sum of squared errors. *MatLab* employed the *nelder-mead simplex* as an optimization analysis.

For *Origin*, the nonlinear (NL) fit is used. To reach the optimum, users can manually adjust the parameters *y* to minimize the difference between the model and the experimental data. This iterative manual adjustments process continues until the convergence is achieved and the user is satisfied with the fit.

Origin employs the Levenberg-Marquardt algorithm.

Assessment of the modeling process

The evaluation of the modeling approach is done by the regression fit coefficient R^2 that quantifies the degree of agreement between the model prediction and observed data. It is a measure on the goodness of the fit model[13]. In the context of regression, it is a statistical measure of how well the regression line approximates the experimental data .A higher R^2 value approaching one (1) indicates a better fit.

Another quantity used to assess the accuracy of the estimated parameters in our case is the standard deviation (SD) of the rate constants drawn from the used model. Additionally dynamic parameters ($T_{max,}$ the 20min/3min ratio,..) are involved to improve the accuracy of modeled TACs when comparing it to clinical TAC.

RESULTS AND DISCUSSION

Comparative evaluation of ROI selection methods

A comparative analysis of ROI determination methods (elliptical and free hand ROIs) is conducted. The assessment considered qualitative and quantitative aspects, with a focus on comparing the outcomes to clinical results.

Qualitative analysis

The accuracy and reliability of both ROI methods (Freehand and elliptical) are assessed in capturing kidney function dynamics.

Figure 4 illustrates the comparison of left renal TACs using Freehand and elliptical ROI methods for patient 1.

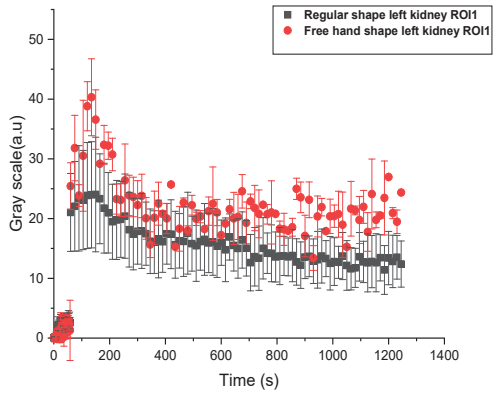

Fig. 4: Comparison of left renal TAC using Freehand and elliptical ROI Methods for patient 1

Quantitative analysis

For the purpose of this comparison, the dynamic parameters are extracted for a set of patients from the clinical TACs captured during the study. Then parallel calculations are conducted for these parameters using both manual extraction through visual assessment and a regular shape method. This allowed the evaluation of the consistency and accuracy of the results obtained through different TAC extraction approaches. The following table shows the results for patient 1.

Table 2: Comparison of the main kinetic parameters of renal functions for the two used ROI selection methods

Patient 1	Right kidney			Left kidney		
	CE	FE	RE	CE	FE	RE
T_{max} (min)	1.98	2	2.25	1.98	2.25	2.5
20mn/3mn ratio	0.49	0.51	0.59	0.54	0.61	0.83
20mn/peack ratio	053	0.49	0.45	0.58	0.6	0351

CE: Parameters were extracted from the clinical TAC displayed by Xeleris software.

FE: Parameters were extracted from experimental TAC using freehand,

RE: Parameters were extracted from experimental TAC using a regular shape.

T_max: According to the doctor, A T_max value within the normal range (<6 minutes) confirms the absence of fixation obstructions.

In summary, our findings strongly support the conclusion that the freehand segmentation method is better suited for the accurate and reliable extraction of kidney TACs in terms of qualitative adherence to the TAC shapes and quantitative consistency in determined dynamic parameters. This underscores the superiority of the freehand segmentation method for this particular application.

Renal TAC modeling

In this section, we present the results of our renal Time-Activity Curve (TAC) modeling study involving 12 patients using a one-compartmental model with four fitting functions. These findings

offer valuable insights into estimating renal function parameters and demonstrate well the alignment of TAC modeling with clinical standards by focusing on both qualitative and quantitative assessments.

Qualitative assessment of TAC modeling

An assessment of concordance between the modeled TACs and empirical experimental data was conducted for both the left and right kidneys for all patients. In this work, Patient 1 was selected as a representative case to elucidate this comparative analysis using *Origin* and *Matlab* softwares. The results are indicated on figures 5-8 for different situations and used fitting softwares and functions.

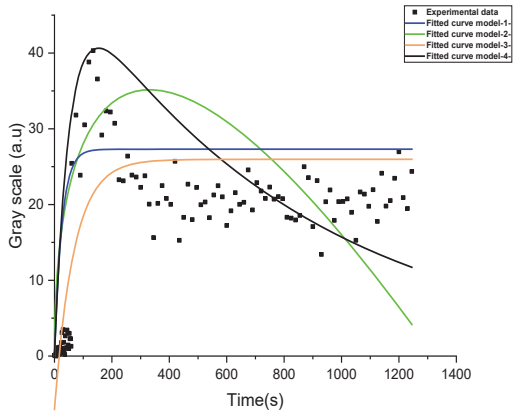

Fig.5: Comparison of modeled and experimental left kidney Time-Activity Curves for Patient 1 using *Origin*

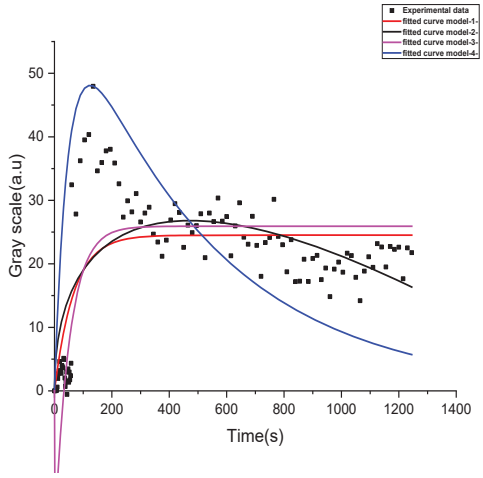

Fig.6: Comparison of modeled and experimental right kidney Time-Activity Curves for Patient 1 using *Origin*

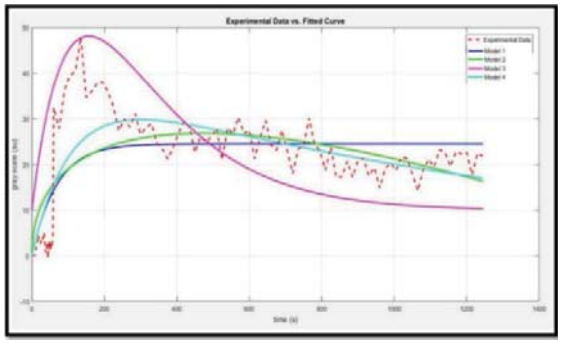

Fig.7: Comparison of modeled and experimental right kidney Time-Activity Curves for Patient 1 using Matlab.

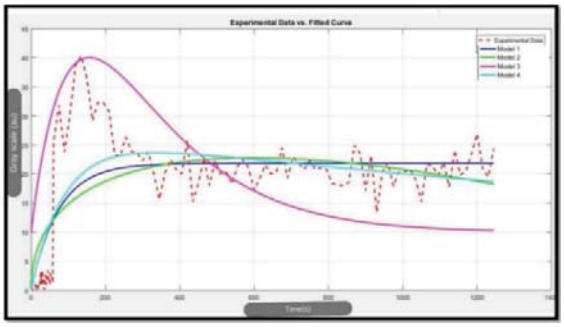

Fig.8: Comparison of modeled and experimental left kidney Time-Activity Curves for Patient 1 using Matlab

The third model (bi-exponential 1) implemented in *MATLAB* closely approximated observed time-activity curves, particularly for normal renal function. The fourth model (bi-exponential 2) using *Origin* provided an acceptable yet incomplete representation. The mono-exponential model was inadequate in capturing the phase of elimination observed in the experimental TAC, and the *Patlak* model's reliance on blood samples limited its clinical utility.

Quantitative assessment of TAC modeling

The quantitative assessment focused on two main methods:

1. ***Assessment of the elimination and absorption rate constants***

The elimination and absorption rate constants are employed to understand renal system kinetics. Functions 3 (*MATLAB*) and 4 (*Origin*) exhibited notably smaller standard deviations than Functions 1 and 2, signifying greater modeling precision. The histograms of standard deviations of rate constants are utilized to refine the analysis, offering a comprehensive view of modeling accuracy distribution (Figures 9 and 10).

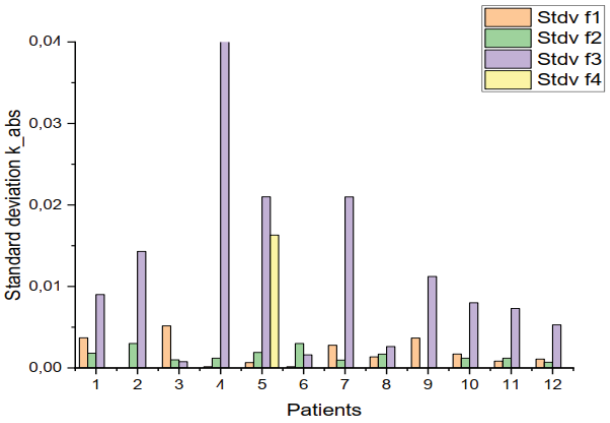

Fig.9: Histogram analysis of the Standard Deviation of rate constant K_abs for the left kidney was performed in 12 patients using *Origin* software.

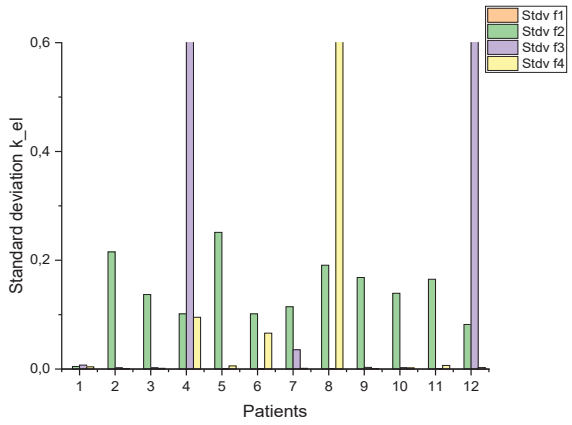

Fig.10: Histogram analysis of the Standard Deviation of the rate constant K_el for the right kidney was performed in 12 patients using *Origin* software

It's important to note that the differences in results between *Origin* and *MATLAB* can be attributed to distinct optimization algorithms. Origin employs the Levenberg-Marquardt algorithm, which combines the advantages of gradient descent and the Gauss-Newton method to optimize the fitting process while *MATLAB* utilizes the Nelder-Mead simplex algorithm, a derivative-free direct search method for optimization.

The study revealed that *MATLAB's* modeling improved with more parameters, capturing dynamics accurately. In contrast, *Origin's* limitations resulted in less precise TAC representations. This underscores the critical role of algorithm choice in optimizing modeling outcomes.

2. Evaluation of Dynamic Parameters

Parameters such as time to peak and specific ratios were extracted from clinical data to enhance the accuracy of modeled TACs derived from functions 3 and 4, which were deemed to provide an acceptable representation.

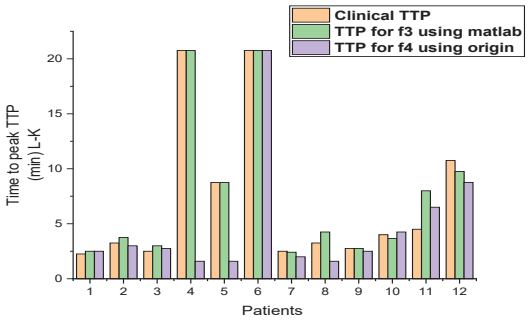

Fig.11: Histogram analysis of TTP for the left kidney for 12 patients

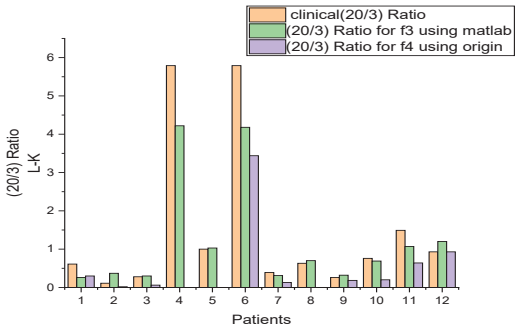

Fig.12: Histogram analysis of 20/3 ratio for the left kidney for 12 patients

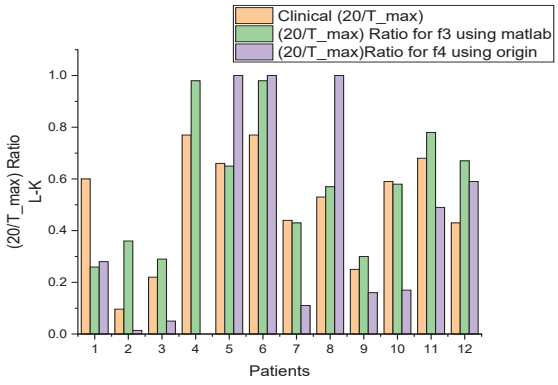

Fig.13: Histogram analysis of 20/T_{max} ratio for the left kidney for 12 patients

The findings indicate that Function $f3$ demonstrates a closer match to the clinical TACs, suggesting a more acceptable representation of the renal dynamics for both right and left in healthy subjects unlike the function $f4$. Aditionnally,in abnormal cases (patient 4, patient 6, patient 11, patient 12) the response of the model is not really satisfactory depending on dynamic parameters. Indeed, function $f3$ illustrates a higher R^2 value approaching 1, which indicates that is the better fit (Fig.14).

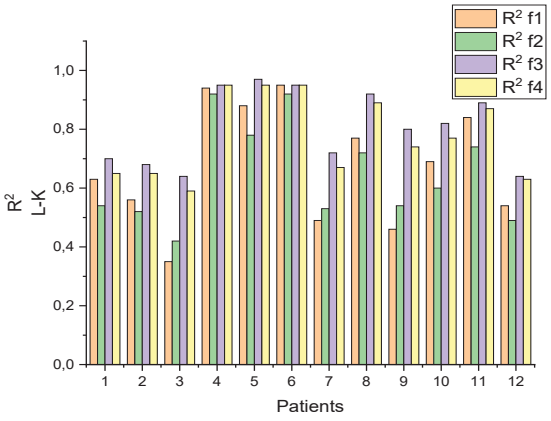

Fig.14: Histogram analysis of R^2 for the left kidney for 12 patients

CONCLUSIONS

This study focused on how selection of Regions of Interest (ROIs) for renal Time Activity Curve (TAC) reconstruction can affect the output. The freehand method for ROI selection was found to provide reasonably acceptable results when comparing reconstructed renal TACs to clinical ones. The study also employed a one-compartmental model with four fitting functions by using *MatLab* and *Origin* software to model the TACs. Bi-exponential ($f3$, $f4$) functions were identified as suitable representations of clinical renal TACs based on qualitative and quantitative assessment in terms of elimination and absorption rate constants, standard deviations , fitting regression parameter (R^2), and the extracted clinical dynamic parameters . Typically, optimal modeling necessitates extended knowledge and accurate experimental and clinical data on scanning process, blood composition, and metabolism with an intricate data processing. Deviations from the assumptions underlying these models can lead to misleading results.

AUTHOR INFORMATION

Corresponding Author

* Nadine Ait Ali Braham

Email address: aitalinadine0@gmail.com

ACKNOWLEDGMENT

The authors would like to express their gratitude to the Centre scintigraphy imaging, Dr. Ghodbane, and "*Les Babors*" Clinic for their assistance in the realization of this study.

REFERENCES

1. READER, Andrew J. et VERHAEGHE, Jeroen. 4D image reconstruction for emission tomography. *Physics in Medicine & Biology*, 2014, vol. 59, no 22, p. R371.
2. SARRUT, David, HALTY, Adrien, BADEL, Jean-Noel, *et al.* Voxel-based multimodel fitting method for modeling time activity curves in SPECT images. *Medical physics*, 2017, vol. 44, no 12, p. 6280-6288.
3. CARSON, Richard E. Tracer kinetic modeling in PET. In : *Positron emission tomography: basic sciences*. London : Springer London, 2005. p. 127-159
4. KERSTING, David, SRAIEB, Miriam, SEIFERT, Robert, *et al.* First experiences with dynamic renal [68Ga] Ga-DOTA PET/CT: a comparison to renal scintigraphy and compartmental modelling to non-invasively estimate the glomerular filtration rate. *European Journal of Nuclear Medicine and Molecular Imaging*, 2022, vol. 49, no 10, p. 3373-3386.
5. DEVASIA, Theresa P., DEWARAJA, Yuni K., FREY, Kirk A., *et al.* A novel time–activity information-sharing approach using nonlinear mixed models for patient-specific dosimetry with reduced imaging time points: Application in SPECT/CT after 177Lu-DOTATATE. *Journal of Nuclear Medicine*, 2021, vol. 62, no 8, p. 1118-1125.
6. SARRUT, David, HALTY, Adrien, BADEL, Jean-Noel, *et al.* Voxel-based multimodel fitting method for modeling time activity curves in SPECT images. *Medical physics*, 2017, vol. 44, no 12, p. 6280-6288.
7. RUTLAND, M. D. A comprehensive analysis of renal DTPA studies. I. Theory and normal values. *Nuclear medicine communications*, 1985, vol. 6, no 1, p. 11-20.
8. MITITELU, Raluca et BRATU, Ovidiu. Radionuclide Imaging. An Update on the Use of Dynamic Renal Scintigraphy. *Medicina Moderna*, 2017, vol. 24, no 4.
9. DANIEL, Gregory B., MITCHELL, Sally K., MAWBY, Dianne, *et al.* Renal nuclear medicine: a review. *Veterinary Radiology & Ultrasound*, 1999, vol. 40, no 6, p. 572-587.
10. KERSTING, David, SRAIEB, Miriam, SEIFERT, Robert, *et al.* First experiences with dynamic renal [68Ga] Ga-DOTA PET/CT:

a comparison to renal scintigraphy and compartmental modelling to non-invasively estimate the glomerular filtration rate. *European Journal of Nuclear Medicine and Molecular Imaging*, 2022, vol. 49, no 10, p. 3373-3386.

11. . FLYNN, Edward. Pharmacokinetic compartmental modeling. 2007.
12. JIANG, Kai, FERGUSON, Christopher M., ABUMOAWAD, Abdelrhman, *et al*. A modified two-compartment model for measurement of renal function using dynamic contrast-enhanced computed tomography. *PLoS One*, 2019, vol. 14, no 7, p. e0219605.
13. Coefficient of Determination (R^2) | Calculation & Interpretation: https://www.scribbr.com/ statistics/coefficient-of-determination/.
14. .D. Patil, N.D. Patil, Effect of calcium carbonate and organic
15. V. Kumar, S. Kant. P. Kumar Sharma. S. Kumar, Effect of chromium toxicity on plants: A review, *Agriways*, 2016, 4-1, 107-120.English abstract)

2023

Dimensions, positioning and Hounsfield unit verification of 3D printed radiotherapy bolus using X-ray CT-scanning

K. Benkahila,[a,c,*] F. Boulkhessaim,[a] A. Meziri,[a] F. Kharfi,[b,c]

[a]Fighting against Cancer Medical Centre of Setif, Setif-19000, Algeria

[b]Department of Physics, Faculty of Science, Ferhat Abbas-Setif1 University, Setif-19000, Algeria

[c]Laboratory Dosing Analysis and Characterization with high resolution, Ferhat Abbas-Setif1 University, Setif-19000, Algeria

.

ABSTRACT: 3D printing technology has revolutionized various industries, including healthcare and radiotherapy. In radiotherapy, a 3D printed bolus refers to a custom-made device used to modify the radiation dose distribution during treatment. 3D printed radiotherapy bolus technology must ensure customization, design flexibility, best material selection, dosimetric Accuracy, and rapid prototyping and manufacturing. The right design of such bolus enhances treatment precision, reduces side effects, and improves patient comfort during radiotherapy. The objective of this work is to use X-ray CT-scanning to ensure the conformity of some design parameters, namely: dimensions, Hounsfield unit (HU) of the used material, and right positioning of the 3D bolus. In this study, nose bolus was designed and 3D printed on the basis on real treatment data reproduced on virtual treatment case by considering "Rando" anthropomorphic phantom as physical patient. The manufactured bolus was placed on Rando to check its right positioning and final dimensions using X-ray CT-scan. The HU values were also verified for different filling rate values (5-100%) of the 3D printed material (Thermoplastic Polyurethane (TPU)). CT-scanning results demonstrate well that deviations between final dimensions of nose bolus and intended design dimensions do not exceed 5%. The bolus fit correctly the surface on which it will be placed. The HU value corresponding to 100% filling rate of the used material is 124±22 HU. CT scanning, once the bolus is printed, allows obtaining the necessary information in order to check its accuracy and functionality. The undertaken verification ensure that the bolus is accurate, will be positioned correctly and will provide the desired dose distribution and coverage.

Keywords: Radiotherapy bolus; 3D printing; CT-scanning.

INTRODUCTION

Radiotherapy is a crucial treatment modality for cancer patients, involving the precise delivery of ionizing radiation to target tumor tissues while minimizing damage to surrounding healthy tissues. To achieve this precision, various tools and techniques are employed, and one such tool is the radiotherapy bolus. Radiotherapy boluses are materials placed on the patient's skin to modify the dose distribution of radiation beams, ensuring that the maximum dose is delivered to the tumor and sparing normal tissues.

In recent years, 3D printing technology has emerged as a promising method for customizing and fabricating patient-specific radiotherapy boluses. 3D printed boluses can be tailored to fit the patient's anatomy and conform to the treatment area, which enhances treatment accuracy and patient comfort. However, ensuring the quality and efficacy of these 3D printed boluses is of paramount importance. This necessitates the need for thorough verification, particularly in terms of dimensions, positioning, and Hounsfield unit calibration using X-ray CT-scanning.

Accurate dimension verification is critical for ensuring that the 3D printed bolus aligns precisely with the patient's treatment area. The use of X-ray CT-scanning allows for high-resolution imaging, enabling clinicians to assess the bolus's thickness and contour, which should match the treatment planning requirements. Discrepancies in dimensions can lead to underdosing or overdosing of radiation, potentially compromising treatment efficacy or causing unnecessary side effects. Hence, precise measurements and comparison with treatment planning data are vital.

Proper positioning of the 3D printed bolus is essential for consistent and effective radiotherapy. Through X-ray CT-scanning, the bolus can be evaluated in situ, ensuring it accurately adheres to the patient's skin and maintains its intended position throughout the treatment course. Misalignment or movement of the bolus may result in deviations from the intended radiation dose distribution, making real-time positioning verification a crucial step in the treatment process.

Hounsfield units (HU) are a standard unit of measurement used in CT scanning to quantify the radiodensity of tissues and materials. Accurate HU calibration of the 3D printed bolus is essential to ensure proper dose calculations during treatment planning. X-ray CT-scanning is instrumental in this regard, as it allows for the assignment of appropriate HU values to the bolus material. This calibration enables the treatment planning system to accurately account for the bolus material when calculating radiation doses, improving the precision of the treatment.

The integration of 3D printing technology into radiotherapy bolus production offers a personalized and precise approach to cancer treatment. However, the use of X-ray CT-scanning for dimensions, positioning, and Hounsfield unit verification is crucial to guarantee the quality and effectiveness of these patient-specific boluses. By combining advanced technology and rigorous quality assurance measures, clinicians can optimize the benefits of 3D printed radiotherapy boluses, ensuring better outcomes for cancer patients while minimizing risks associated with radiation therapy[1-2].

In this work, nose bolus was designed and 3D printed on the basis on real treatment data reproduced on virtual treatment case by considering “Rando” anthropomorphic phantom as physical patient. The manufactured bolus was placed on Rando to check its right positioning and final dimensions using X-ray CT-scan. The HU values were also verified for different filling rate values (5-100%) of the 3D printed material (Thermoplastic Polyurethane (TPU)).

EXPERIMENTAL

In this study, nose bolus was designed and 3D printed on the basis on real treatment data reproduced on virtual treatment case by considering Rando anthropomorphic phantom as physical patient (Fig.1). The manufactured bolus was placed on Rando to check right positioning and final dimensions by X-ray CT-scanning. The HU values were also verified for different filling rate values (5-100%) of the 3D printed material (Thermoplastic Polyurethane (TPU)) (Fig.2).

The objective of this work is to ensure that the dimensions of the bolus are accurate and suitable for the patient's treatment. The dimensional verification is done by measure the dimensions of the 3D-printed bolus using software and metrics tools. The comparison between the measured dimensions with the intended design dimensions allows to verify the 3D printing geometrical accuracy. CT-scan allows to check if the fabricated bolus matches the desired specifications and fits properly the receiving surface.

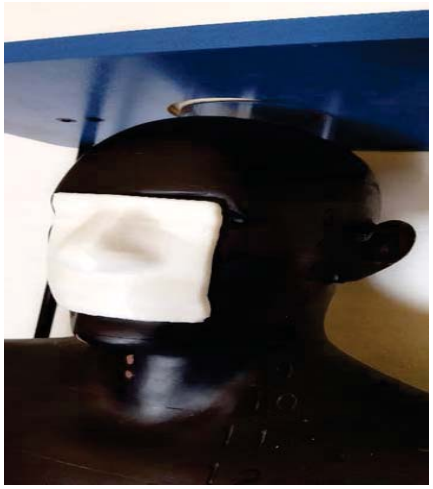

Fig.1: 3D printed noise bolus as placed on Rando phantom

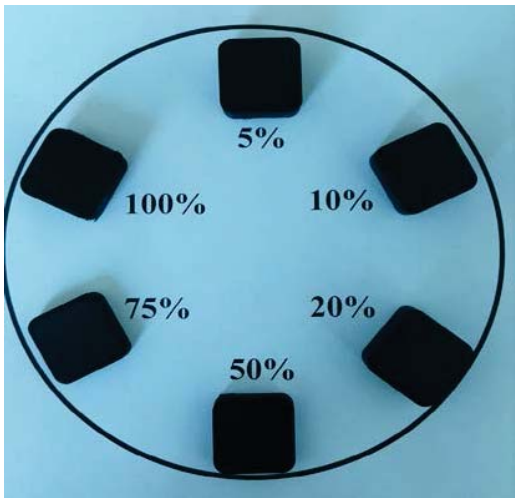

Fig.2: Different samples of 3D printing material with different filling rates

RESULTS AND DISCUSSION

CT-scanning results demonstrate well that deviations between final dimensions of nose bolus and intended design dimensions do not exceed 5% (bolus thickness and dimensions). The bolus fit correctly the surface on which it will be placed (Fig.3).

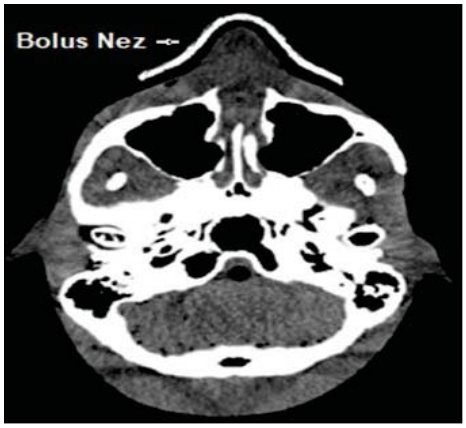

Fig.3: CT-scan of noise bolus as after positionning on Rando phantom

Fig.4 show the corresponding CT slice of the different TPU 3D printing material with different filling rates. The HU value (CT number) corresponding to 100% filling rate of the used material is 124±22 HU. HU value variation as function of filling rate is plotted in Fig.5. A linear dependence was observed for this variation. Thus, as a function of the treated case, it is possible to decrease the filling in order to get suitable HU value that is most suitable for the dose compensation.

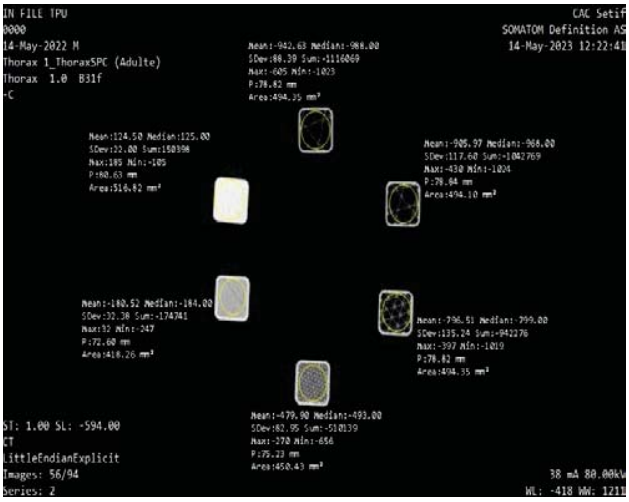

Fig.4: CT-scan slice of different TPU 3D printing samples with different filling rates

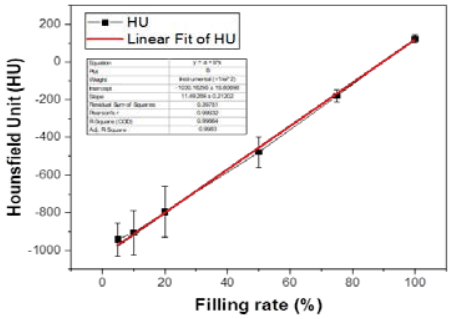

Fig.5: HU value variation as function of filling rate

CONCLUSIONS

X-ray CT Scanning, once the bolus is printed, allows obtaining the necessary information on placement adequacy and effective Hounsfield unit value that are necessary to check its accuracy and functionality. The undertaken verification ensure that the bolus is accurate, will be positioned correctly and will provide the desired dose distribution and coverage.

AUTHOR INFORMATION

Corresponding Author

*Karim Benkahila

Email address: benkahilak@gmail.com

ACKNOWLEDGMENT

This work was undertaken in the framework of the socio-economic research project on “Control and improvement of radiotherapy treatment plans using thermoluminescence dosimetry” (Contract N° 07/2019, 15/12/2019). The project is supported by the Thematic Research Agency for Sciences and Technology (ATRST) of the Directorate-General for Scientific Research and Technological Development (DGRSDT). The principal investigator of the project (Pr. F. Kharfi) and his research team are very grateful to ATRST and DGRSDT. .

REFERENCES

1. R. Tino et al., Additive manufacturing in radiation oncology: a review of clinical practice, emerging trends and research opportunities, *Int. J. Extrem. Manuf.* 2020, 2, 012003.
2. M. Lukowiak et al., Use of a 3D printer to create a bolus for patients undergoing tele-radiotherapy, *Int. J. Radiat. Res.*, 2016, 14(4), 287-295.

2023

Evaluation of the complexity of a Volumetric Modulated Arc Therapy (VMAT) plan

S. Malki,[a,b]* I. Zergoug,[c]

[a] Department of Physics, Ferhat Abbas Setif 1 University, Setif-19000,Algeria

[b] Laboratory of Dosing, Analysis and characterization in high resolution, Ferhat Abbas Setif 1 University, Setif-19000,Algeria

[c] Department of Medical Physics, Oncopole l'Espoir Clinic, Oran-31000, Algeria

ABSTRACT: Radiation therapy (RT) has evolved considerably in recent decades with the Volumetric Modulated Arc Therapy as one advanced technique. RT's main objective is to deliver a high conformal dose to the tumor while protecting organs at risk. It is a complex treatment due to the dynamics of the dose, the MLC and the gantry. The aim of this work is to evaluate the complexity of Volumetric Modulated Arc Therapy (VMAT) plans in order to predict the deliverability of those plans on the linac. We compared two complexity indexes; MIt, MD (from TPS) as means of predicting phantom-based measurement results for 21 treatments (11 H&N and 10 prostate plans) planned using TPS Monaco and clinically delivered on Elekta Infinity linac (GPR verified). MIt showed moderate to strong correlation to the local GPR with 3%3mm criterion with rs values of -0,618 (p=0,043) , -0,879 (p=0,001), -0,903 (p=0). However, MD didn't correlate with the local GPR With rs values of -0.091 (p=0.79) and 0.103 (p=0.777). ROC analysis was also performed. MIt achieved 14,29% of FPR and 75% TPR with H&N plans (AUC=0,75), 25% FPR and 100% TPR with prostate plans (AUC=0,875). MD achieved 57% of FPR and 100% TPR with H&N plans (AUC=0,428), 63% FPR and 100% TPR with prostate plans (AUC=0,5). MIt seems to be a good complexity metrics. It can be used as modulation index for VMAT plans to predict delivery..

Keywords: VMAT; Monaco; Complexity index; Modulation; ROC analysis.

INTRODUCTION

Volumetric modulated arc therapy (VMAT) is an advanced technique of radiotherapy because it is able to deliver greater dose conformity to target tissues over short delivery time and spares more normal tissues. However it is a very complex technique because the gantry, the multi leaf collimator (MLC) and the dose rate (DR) are dynamic during VMAT radiotherapy. Therefore, the patient is irradiated by rotational linear accelerator (linac) from different angles with beamlets of varying aperture shape and intensity, each rotation of linac is called an arc and one or more arcs might be used to treat patients[1,2,3,12] (Fig. 1).

Complexity indices or metrics were mainly developed with the aim of predicting the patient specific quality assurance outcome. These metrics can be used to describe the degree of dose modulation and characterize both machine parameters and plan properties, including MLC position, gantry speed and dose rate variations[2,7].

Modulated Index total (MIt): This index involves the variation in speed and acceleration of the MLC, the gantry speed and the dose rate[6]. The calculation of MIt is based on the concept of modulation index introduced by Webb[5].

Modulation Degree (MD): Monaco TPS is the only TPS providing an advanced complexity metric and among the complexity metrics, it calculates the accuracy metrics. Monaco

calculates the Modulation Degree (MD) which indicates the current total relative degree of modulation of all beams and sequences.

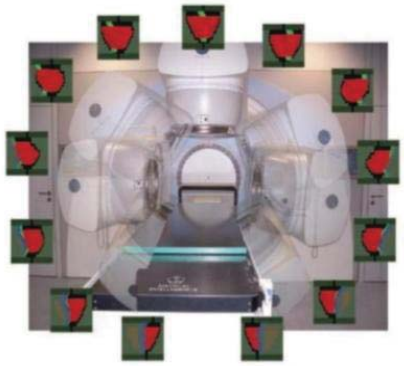

Fig. 1: VMAT delivery[15]

Overall, more complex plans should have a higher degree of modulation than simpler plan. In addition, Monaco offers segment shape optimization that smoothes and clusters segments, then optimizes beam weights and shapes in order to improve plan quality[7].

Gamma index: The gamma index method compares the planned and the measured dose distribution by using the percent dose difference (DD) and the distance to agreement (DAT)[13].

There are two types of gamma index methods:

A. The global gamma index analysis:

• Calculates the DDs relative to the maximum dose.

• Could underestimate the dose discrepancies in the low dose regions (because the DD is a percent value)[14].

B. The local gamma index analysis:

• Calculates the DDs relative to the doses at each evaluated point.

• Could exaggerate the DDs in the low dose regions (because the DD is a percent value)[14].

EXPERIMENTAL

In order to verify the deliverability of VMAT treatment plan on a Linac, a specific patient quality control was performed. We used 2 complexity metrics. Plans were calculated on Monaco TPS and then delivered on Linac and measured by MatrixX2D array detector and then measured and calculated 2D dose are evaluated using GPR method. We evaluated 2 complexity metrics whether to skip the patient quality control on a Linac. Our measurements took place at the ”Oncopole l’Espoir” clinic (Service of medical physics) .

Materials

1. Monaco TPS

Monaco is a comprehensive Treatment Planning System (TPS) for 3D, IMRT,VMAT and Stereotactic techniques (SRS/SBRT), which use the gold-standard Monte Carlo dose calculation algorithm XVMC to deliver highly accurate dose distributions with a suite of optimization tools. A collection of biological and physical dose-based planning tools and templates simplify the planning process and allow for consistent results across organizations. At the same time, multi-criteria optimization (MCO) ensures critical organs are spared to the greatest possible

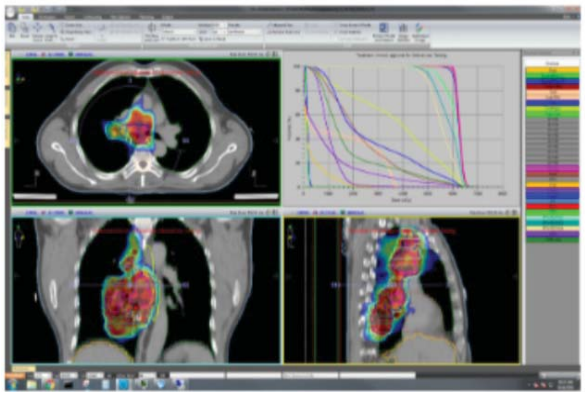

degree while maintaining target coverage (Fig 2).

Fig. 2: TPS Monaco interface (Oncopole Clinic)

2. Matrixx detector

MatriXX is a proven detector based on more than 1500 matrixx systems world-wide. The matriXX Evolution 2D ionization chamber array is developed by IBA dosimetry and it is associated with a multi-cub phantom that offers an efficient method to validate the dose according to the parameters reflecting those of

the patient during the treatment[8,10,11] (Fig3).

Fig. 3: MatriXX Evolution associated with multicub phantom (Oncopole clinic)

3. MyQA patient

The software provided by IBA is a QC solution that verifies the treatment plan by offering gamma-index verification and dose

distribution[9] (Fig 4).

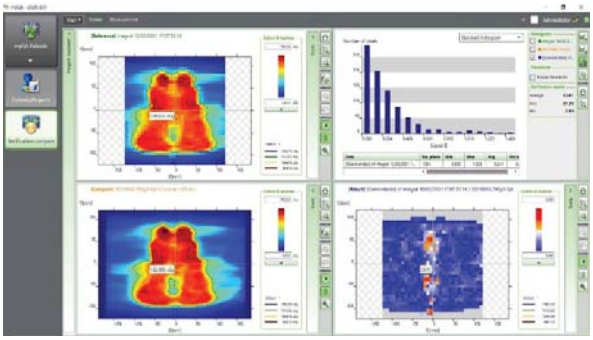

Fig. 4: MyQA patient interface (Oncopole clinic)

Methods

1. VMAT plans

Elekta infinity Linac equipped with 160 MLC was used to deliver 21 treatments (10 H&N plans and 11 prostate plans). Those treatments were randomly selected and clinically approved plans generated in Monaco (Elekta) TPS version 5.11.3, using Monte carlo Vmat algorithm XVMC. Measurements were performed using the IBA MatriXX evolution ion chamber array associated with Mutlicub phantom. My QA software was used to record measurements and compare the measured dose plans to the Monaco calculated dose plans via gamma index analysis.

2. Complexity metrics

We used MIt and MD complexity metrics in order to evaluate the degree of Complexity of VMAT treatment plans. For MIt complexity metric calculation, we put $\gamma = 1$ and $\beta = 2$ and according to the Elekta manufacturer specifications the maximum GS is 5,5◦/s and the maximum DR is 720 MU/min. The CP in VMAT plans DICOM's was defined at equiangular positions of the gantry at intervals of 2,0341 degree. We calculated the time between each CP in order to evaluate speed and acceleration of the mechanical parameters between CPs.

Time = 4.4380s is the maximum MU able to be delivered without slowing down the rotation of the gantry at a CP.

3. QA analysis

Gamma analysis was performed at 3% 3mm global, and 3% 3mm local with a tolerance of 95%. We used Python codes to calculate the complexity metric, the correlation coefficient and to plot the ROC and AUC curves. We determined the AUC for each ROC to indicate the performance of the classification using the trapezoidal numerical method.

RESULTS AND DISCUSSION

1. Gamma passing rates

Tables 1 and 2 describe the distribution of the GPR for Elekta infinity Linac using the 3% 3mm criterion (both global and local). For the global GPR all the plans would pass their QA because they have a GPR above the tolerance limit of 95%. However, in the case of the local 3% 3mm the Linac delivered 6 failing plans (2 prostate and 4 H&N) and 15 passing plans (8 prostate and 7 H&N).

Table 1. Gamma passing rates for H&N plans

Patient	γ (3%3mm) global	γ (3%3mm) local
1	97,40%	91,90%
2	99,90%	98,80%
3	100%	99,70%
4	99,20%	96,20%
5	98,30%	94,10%
6	99,90%	97,60%
7	99,80%	98,30%
8	99,80%	97,40%
9	100%	97,70%
10	99,70%	97,50%

Table 2. Gamma passing rates for Prostate plans

Patient	γ (3%3mm) global	γ (3%3mm) local
1	98,90%	97,20%
2	98,20%	94,50%
3	97,40%	90,10%
4	100%	99,10%
5	98,40%	96%
6	99%	95,80%
7	99,30%	96,70%
8	99,40%	96,50%
9	99,80%	88,60%
10	97,70%	94,80%
11	98,10%	95,10%

2. Complexity metrics

In this study, we evaluated the MIt metric that considers the variation of the Linac mechanical parameters including MLC movements, GS variations and DR variations. We also evaluated its performance in predicting Vmat delivery.

Similarly, we evaluated the MD metric that considers the dose uncertainty to predict Vmat accuracy. Tables 3 and 4 show the MIt values for GPR 3%3mm local with f = 0.2, 0.5.. Tables 5 and 6 show the MD values.

Table 3. MIt metric for H&N plans

Patient	MIt f=0,2	MIt f=0,5
1	1,535	24,359
2	2,252	25,914
3	1,911	21,567
4	1,760	33,172
5	1,513	23,294
6	1,835	30,484
7	1,670	22,233
8	1,799	22,244
9	1,987	24,993
10	1,600	23,994
11	1,990	23,144

Table 4. MIt metric for Prostate plans

Patient	MIt f=0,2	MIt f=0,5
1	1,852	28,913
2	1,469	22,867
3	1,224	19,247
4	2,009	26,654
5	1,789	25,101
6	1,634	24,355
7	1,539	23,512
8	1,699	24,580
9	1,438	22,937
10	1,827	26,909

Table 5. MD metric for H&N plans

Patient	MD
1	3,62294
2	4,02956
3	4,24858
4	3,27817
5	5,15895
6	3,02008
7	5,43684
8	4,73448
9	4,48011
10	4,48405
11	5,735

Table 6. MD metric for Prostate plans

Patient	MD
1	3,45782
2	3,83126
3	3,42598
4	3,48602
5	3,66285
6	4,29711
7	3,71987
8	3,64117
9	3,42226
10	3,17798

3. Spearman's correlation

Tables 7A, 7B and 7C summarize the corresponding values of the Spearman's rank coefficient. Overall, the MIt showed a strong correlation with gamma index (both f=0,2 and f=0,5) for the prostate plans, and for the H&N plans it showed a moderate correlation (f=0,2) and no correlation (f=0,5). The MD showed no correlation with gamma index for both H&N and prostate plan. We tested the performance of MIt and MD metrics using the Spearman's rank Correlation. The existence of correlations between Monaco TPS and Elekta Linac used in our study suggests that extreme values of MIt and MD may indicate highly complex plans and correspond to larger disagreements between the calculated and measured dose distributions.

Therefore, we found a strong correlation of MIt to the GPRs with both f=0,2 and f=0,5 in the prostate plans. In the case of the H&N plans, we found a moderate correlation between the MIt and the GPRs with f=0,2and there was no correlation with f=0,5. MD metric showed no correlation for both H&N and prostate plans. High or low values of complexity metric can suggest a large disagreement between the calculated and the measured dose distribution. In fact, the MIt is able to discriminate between plans that fail or pass and it depends on the TPS.

Table 7. Spearman's rank correlation. A: for H&N plans (MIt), B: for prostate plans (MIt) and C: for H&N and prostate plans (MD)

3/3local	MIt f=0,2	MIt f=0,5
ρ	-0,618	0,118
p	0,043	0,729

(A)

3/3local	MIt f=0,2	MIt f=0,5
ρ	-0,879	-0,903
p	0,0013	0,000

(B)

3/3local	MD(H&N)	MD(prostate)
ρ	-0.091	0.103
p	0.79	0.777

(C)

4. ROC analysis

The ROC curves are depicted in figures 5-10. For H&N plans, MIt achieved 75% TPR and 14,29% FPR with f=0,2, 75% TPR and 43% FPR with f=0,5 and MD achieved 100% TPR and 57% FPR. For the prostate Plans, MIt achieved 100% TPR with f=0,2 and f=0,5, 25% FPR with f=0,2 andF=0,5 and MD achieved 100% TPR and 63% FPR. All TPR, FPR, AUC and ROC are summarized in tables 8, 9, 10 and 11. We used the ROC curves and the AUC in order to quantify the sensitivity and the specificity of pre-treatment VMAT quality assurance technique delivery Errors. In our study, MIt yielded AUC between 0,5 and 0,875 using a local 3%3mm Criterion with 95% tolerance limit. The MIt yielded 14,29% FPR and 75% TPR (f=0,2) for H&N plans. Whereas, 25% FPR and 100% TPR for the prostate plans. Furthermore, the best threshold values that correspond to a law FPR and high TPR are 1,836 for the H&N plans and 1,7 for the prostate plans.

Table 8. ROC analysis for H&N plans (MIt)

3/3local	MIt f=0,2	MIt f=0,5
AUC	0,8125	0,875
FPR	25%	25%
TPR	100%	100%
Best threshold	1,7	24,581
G-mean	0,866	0,866

Table 9. ROC analysis for prostate plans (MIt)

3/3local	MIt f=0,2	MIt f=0,5
AUC	0,75	0,5
FPR	14,29%	43%
TPR	75%	75%
Best threshold	1,836	23,295
G-mean	0,8018	0,6547

Table 10. ROC analysis for H&N plans (MD)

3/3local	MIt f=0,2
AUC	0,428
FPR	57%
TPR	100%
Best threshold	3,623
G-mean	0,6547

Table 11. ROC analysis for Prostate plans (MD)

3/3local	MIt f=0,2
AUC	0.5
FPR	63%
TPR	100%
Best threshold	3.426
G-mean	0.6124

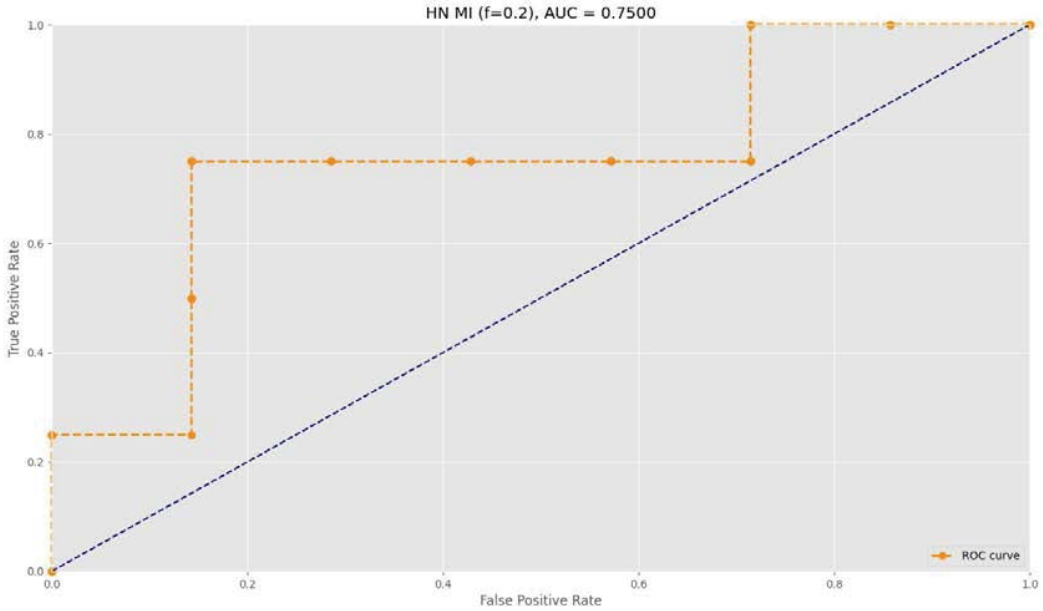

Fig. 5: ROC curve for H&N plans MIt f=0.2

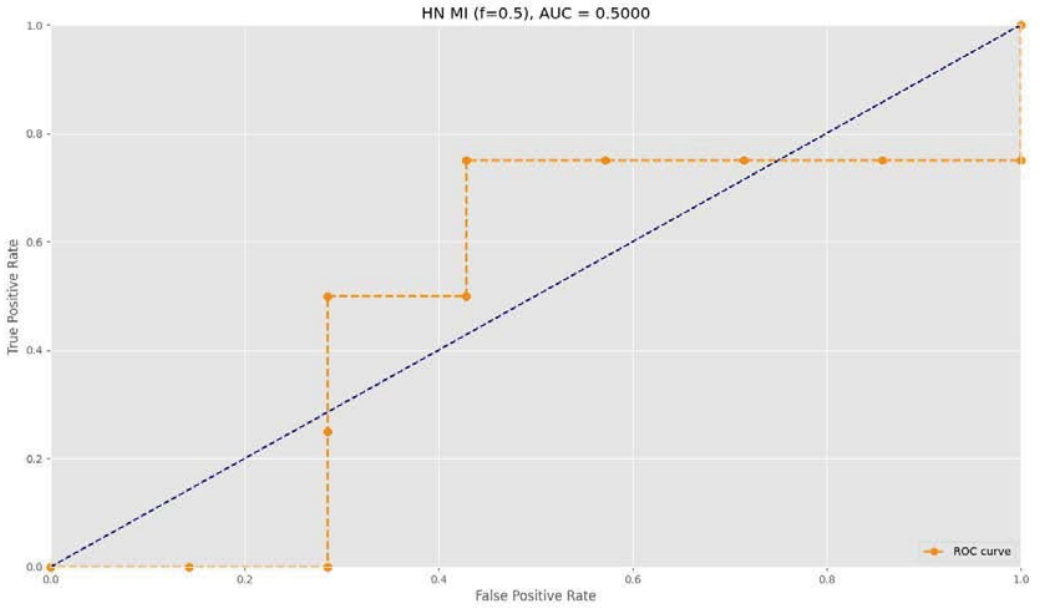

Fig. 6: ROC curve for H&N plans MIt f=0.5

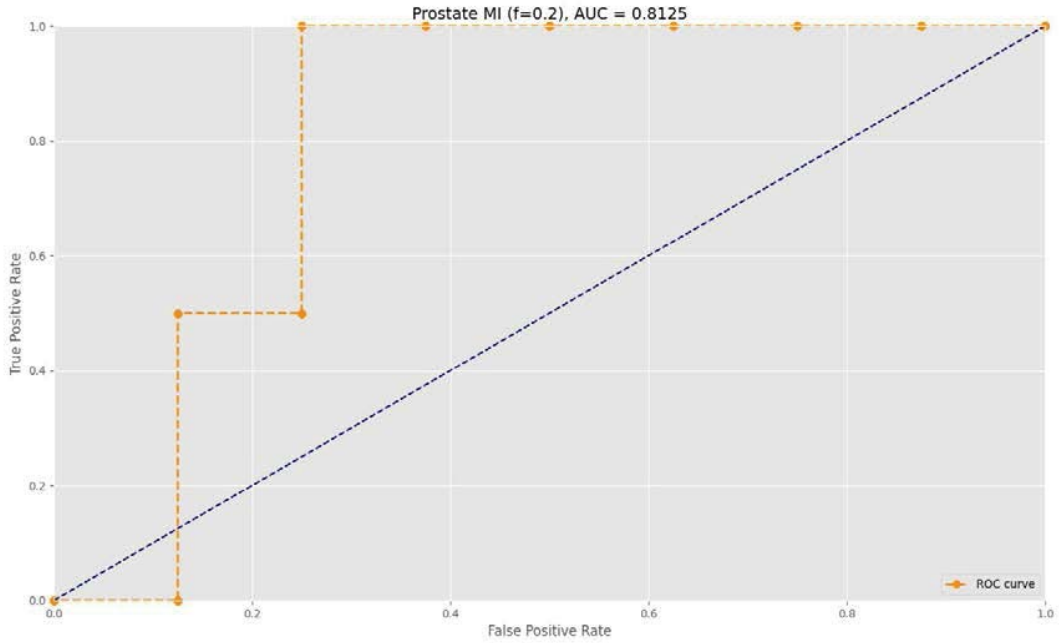

Fig. 7: ROC curve for prostate plans MIt f=0.2

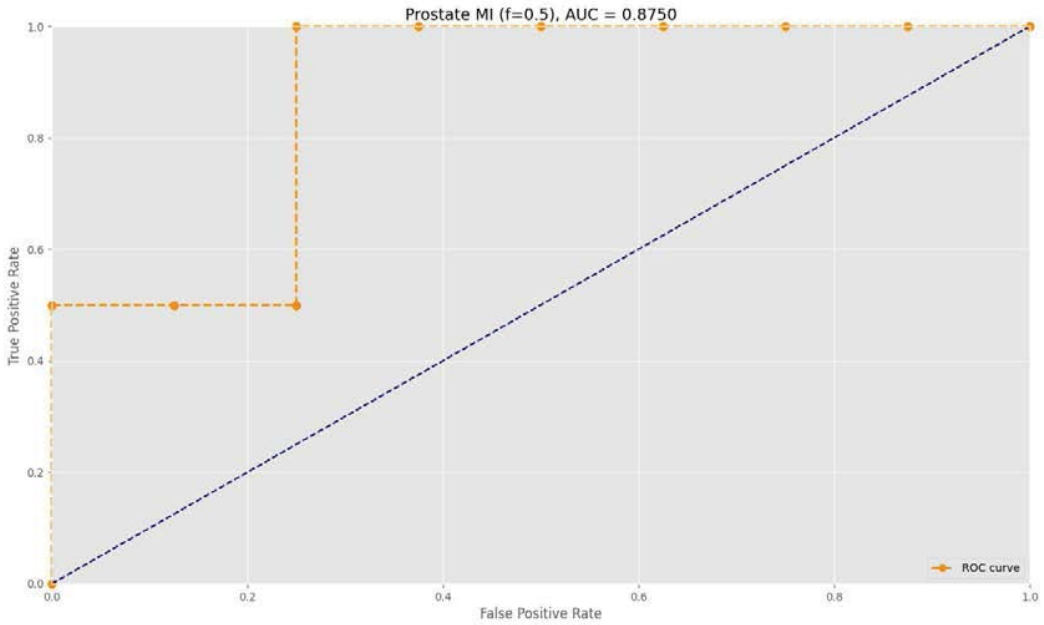

Fig. 8. ROC curve for prostate plans MIt f=0.5.

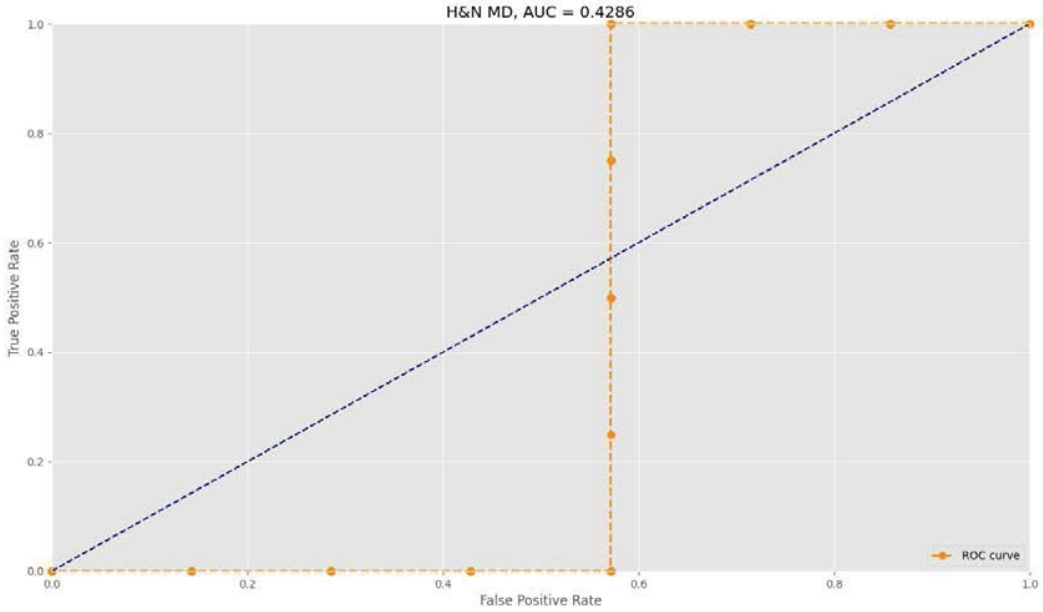

Fig. 9: ROC curve for H&N plans MD

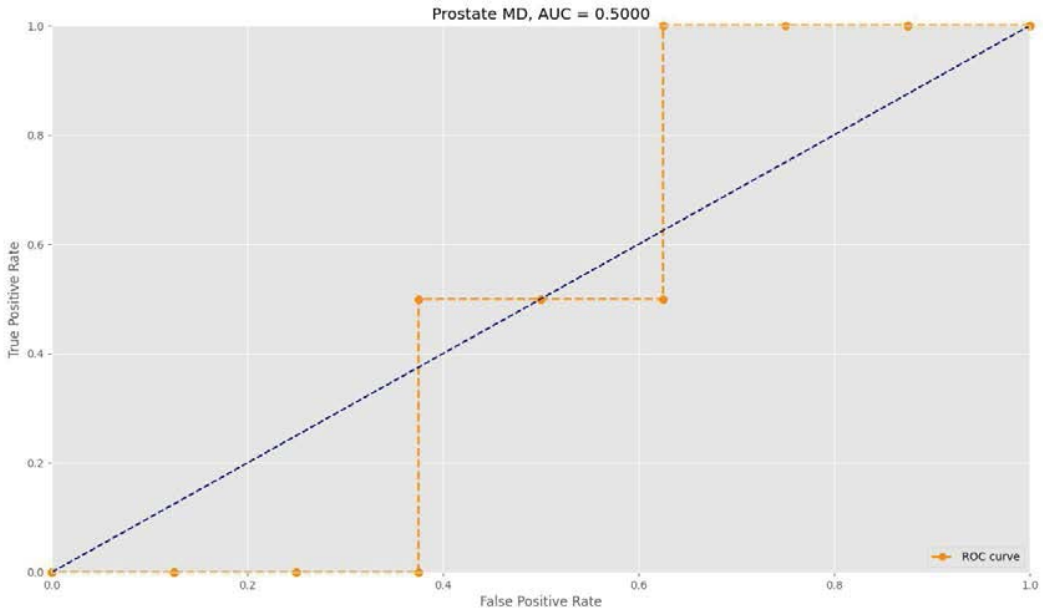

Fig. 10. ROC curve for prostate plans MD

CONCLUSIONS

In this study, we evaluated the complexity of Vmat plans using "two-complexity metrics" the MIt and the MD.

On one hand, the MIt is an index that verifies the mechanical parts of Linac's uncertainty. This index shows a strong correlation with gamma index for the prostate plans (for both f=0.2 and f=0.5) and in the case of H&N plans it correlates just for f=0.2. On the other hand, the MD is an index that verifies the dose uncertainty and the only TPS that calculates this index is the Monaco TPS. According to our results, this index does not correlate with the GPR.

MIt can be used as modulation index for VMAT plans to predict delivery. In fact, using the MIt threshold, we can predict if a plan will pass or fail.

In the future, we plan to develop new complexity indices to control both mechanical parts and dose calculation uncertainties that correlate with GPR. We also aim to implement the Artificial Intelligence AI that is a gold standard method in predication.

AUTHOR INFORMATION

Corresponding Author

*Souad Malki

Email address: malkisouadfadwa@gmail.com

REFERENCES

1. Weiliang Du, Sang Hyun Cho, Xiaodong Zhang, Karen E Hoffman, and Rajat J Kudchadker. Quantification of beam complexity in intensity-modulated Radiation therapy treatment plans. Medical physics, 41(2):021716, 2014.
14. 2020.
15. Jong Min Park, Jung-in Kim, So-Yeon Park, Do Hoon Oh, and Sang-Tae Kim. Reliability of the gamma index analysis as a verification method of Volumetric modulated arc therapy plans. Radiation oncology, 13(1):1–14,2018.
2. Michael Nguyen and Gordon H Chan. Quantified vmat plan complexity in relation to measurement-based quality assurance results. Journal of Applied Clinical Medical Physics, 21(11):132—140, 2020.
3. Efstathios Kamperis. Complexity analysis of Volumetric Modulated ArcTherapy prostate plans. PhD thesis, ARISTOTLE UNIVERSITY OF THESSALONIKI, 2020.
4. Radiation oncology vmat [online] url:https://radiationoncology.weillcornell.org/clinical-Services-and-technologies/external-beam radiation (accessed:10.04.2022).
5. S Webb. Use of a quantitative index of beam modulation to characterize doseConformality: illustration by a comparison of full beamlet imrt, few-segmentImrt (fsimrt) and conformal unmodulated radiotherapy. Physics in Medicine & Biology, 48(14):2051, 2003.
6. Jong Min Park, So-Yeon Park, Hyoungnyoun Kim, Jin Ho Kim, Joel Carlson, and Sung-Joon Ye. Modulation indices for volumetric modulated arc Therapy. Physics in Medicine & Biology, 59(23):7315, 2014.
7. Sophie Chiavassa, Igor Bessieres, Magali Edouard, Michel Mathot, and Alexandra Moignier. Complexity metrics for imrt and vmat plans: a review of current literature and applications. The British journal of radiology,92(1102):20190270, 2019.
8. Systeme matrix evolution iba [guide].
9. Solution logicielle : My qa patient [online] url:http://www.scrim.ma/radiotherapie/solution-logicielle-my-qa-patient/(Accessed:20.04.2022).
10. Matrixx-universal detector array proven accuracy and reliability [online] url:https:https://www.iba-dosimetry.com/product/matrixx-universal-Detector-array(accessed:22.04.2022).
11. Matrix evolution [online] url:https://www.iba-Dosimetry.com/product/matrixx-universal-detector-array(accessed:20.04.2022).
12. Jong Min Park, Chang Heon Choi, Hong-Gyun Wu, and Jung-in Kim. Correlation of the gamma passing rates with the differences in the dose-volumetric Parameters between the original vmat plans and actual deliveries of the vmat Plans. Plos one, 15(12):e0244690, 2020.
13. Linnea Strandell. Impact of mlc shape smoothing on vmat plan complexity and agreement between planned and delivered dose.
16. D. et all Wolff. Volumetric modulated arc therapy (vmat) vs. serial tomotherapy, step-and-shoot imrt and 3d-conformal rt for treatment of prostate cancer.Radiotherapy and Oncology, 93(2):226–233, 2009.

2023

Automatic Detection of Anatomical Landmarks for Image Registration in Radiotherapy

M.O. Mebarki,[a,b,*] A. Bahouch,[a,b] H. Azizi[a]

[a] Department of Physics, Faculty of Sciences, Ferhat Abbas Setif1 University, Setif-19000, Algeria

[b] Laboratory of Dosing, Analysis, and Characterization in high resolution (DAC-hr), Ferhat Abbas Setif1 University, Setif-19000, Algeria

ABSTRACT: Anatomical landmark correspondence in Radiation Therapy imaging provides extra guidance information for the medical imaging registration. However, manual landmark identification is intensive and time consuming. Therefore, developing a deep learning approach to automatically detect landmark correspondence in pairs of two-dimensional (2D) images of Cone-Beam CT (CBCT) and planning-CT (pCT) is extremely important. Our method consists of a U-net-based Convolutional Neural Network (CNN) that has been trained to recognize points in both image modalities and anticipate matching probabilities for landmark pairings. We trained our method using 58 scans of 2D-axial in the pelvic area. In this study, we propose an effective approach for automatic landmark detection in the field of radiotherapy using deep learning model U-Net, focusing on the precise spatial localization of these landmarks in pairs of corresponding CT and CBCT images of the pelvic area used for image registration. The first step was to train our proposed models based on U-net architecture on dataset of 58 scans of 2D-axial in the pelvic area, each scan ranges from 140 to 160 CT slices and 86 to 88 slices of CBCTs with a pre-annotated landmark coordinates realized by medical experts. The next step was to evaluate the obtained models in terms of accuracy and loss metrics. The training models showed promising results in terms of landmark predictions; in some scenarios, it surpasses the ground truth in terms of landmark distribution. With a motivation to contribute to the process of automatic landmark detection, eventually, registration methods of medical images, we employed a U-Net deep learning approach, which plays a significant role in image segmentation, for the detection and matching of landmarks in two different image pair modalities. To the best of our knowledge, this is the first approach that learns landmark locations between the CT and the CBCT images using U-net. Our proposed approach of model learning based on the U-net architecture requires a pre-annotation from experts regarding the landmark coordinates before the learning process. The appearance of landmarks in the learning process not only has given more point, but also, it precisely predicts landmarks spatial positions.

Keywords: Image registration; Landmark detection; Deep learning.

INTRODUCTION

Digital images have a profound impact on science development and many activities would not have been possible without them. It is an interdisciplinary subject that spans astrophysics to medical imaging, among other subjects. Medical imaging has been introduced as one of the most important sub-fields in scientific imaging, with Radiation Therapy (RT) imaging at the top of the pyramid.

Medical image processing applications, in general, are related to: image registration, image segmentation, image enhancement and restoration[1]. Among these procedures and analysis, we are shedding light on the process of image registration (IR) in

radiation therapy. This work discusses the techniques and applications of IR, using two distinctive RT image modalities; the planning-CT (pCT) and the in-room CT, also called cone-beam CT (CBCT). Image registration exists in almost every software system that does any sorts of image acquisition in radiotherapy, additionally, most treatment planning systems (TPS) support some form of image registration to allow the use of multimodality data to assist in target volume (TV) and organs-at-risque (OAR) delineation[2]. Treatment delivery systems perform registration between the planning-CTs and the CBCT images during the treatment to assist patient positioning or to characterize disease. Advanced applications are beginning to support daily dose assessment and enable ART to use image registration to delineate contours and accumulate dose between image data to provide updated or live estimations of the challenging anatomical changes, crucial for an accurate treatment.

In the literature, many techniques and algorithms were developed throughout the history of medical image registration, the most important ones are based on intensity, feature and iterative IRs, dating as far as 1963[3]. In 2012, Alex-Net[4] introduced state-of-the-art performance in IR by applying deep learning (DL) known today as artificial Intelligence (AI) combined with ML algorithms. DL belongs to a class of ML and consists of massive multilayer networks of artificial neurons that can automatically discover useful features, given large amounts of unlabeled or labeled data. DL was successfully applied to the most common convolutional algorithms such as iterative and intensity-based registration algorithms. Performance was outstanding[4-5] however, not enough. Further demands for higher performances and faster registration methods motivated the development of many deep learning-based algorithms and methods. During this process, many properties of DL were upgraded, such as network architectures (CNN, RL, GAN etc.), training processes (supervised, unsupervised etc.). Although there are many architectures of CNN available in literature, one important approach of neural networks is the U-Net architecture, applied in this work to train our model to detect anatomical landmarks.

Landmarks are usually understood as characteristic points of the image domain, consequently, landmark correspondences as point correspondences[6]. The process of detecting these landmarks is crucial in quantifying any medical image analysis. Manual tracing of anatomical landmarks is tedious and prone to human error[7], thereby, justifying the need to develop automated methods for anatomical landmark identification[8]. We used the U-net architecture to train our model to predict points based on a given expert-based landmark coordinates for both CBCT and CT images. Heat-map (HM) is employed to locate the predicted landmarks. The approach involves the concurrent regression of heat-maps for landmarks rather than focusing solely on absolute landmark coordinates.

EXPERIMENTAL

Dataset Description

In this work, the studies were performed on data-sets of 58 patients of different ages containing their pCT and CBCT pelvic images. These patients were treated at the Beaumont Proton Center and have been selected for a Beaumont Research Institute Institutional Review Board approved retrospective study (2014-326). Each patient received a planning CT on a 16-slice Philips Brilliance Big Bore CT scanner (Philips NA Corp, Andover, MA) covering the entire anatomic region and utilizing an immobilization system (see Figure 1). Each patient had CBCT images acquired for daily image guidance on the Proteus ONE Proton therapy machine (Ion Beam Applications S.A., Belgium). The CBCT images were 768 × 768 × 110 voxel with voxel size ranging from (0.6406 × 0.6406) to (0.5176 × 0.5176) mm^2 and 2.5 mm slice thickness for all cases. The machine iso-center is located at the center of the CBCT reconstruction image volume. The dataset was enhanced by Excel files, containing (x, y, z) landmark coordinates for each corresponding image in both pCT and CBCT modalities and for all patients.

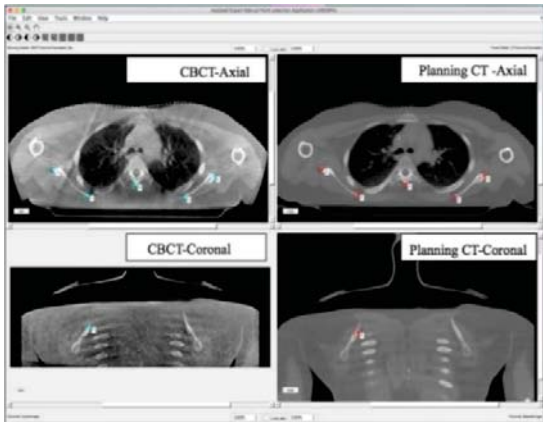

Fig. 1: Assisted expert manual point selection application interface showing sample data. The Image on the left panel (top and bottom) shows cone beam computed tomography (CBCT) of the target image and image on the right panel (top and bottom) shows the planning CT image, which is the reference image [6]

Dataset Pre-Processing

Normalization is a crucial pre-processing technique in machine learning, aimed at standardizing the scale of numeric attributes. Its purpose is to rescale real-valued attributes into a uniform range, commonly between 0 and 1. This adjustment mitigates the impact of varying feature scales during model training, leading to more effective convergence and ultimately improving model accuracy.

For the sake of our work, the objective here is to establish consistent scale for pixel values. Diverse methods exist including min-max and z-score normalizations[9]. In this work min-max normalization is used:

$$x_{normalized} = \frac{(x - x_{min})}{\left(x_{\max - x_{min}}\right)}, \quad (1)$$

where: x is the original data point. x_{min} is the minimum value of the data set. x_{max} is the maximum value of the data set. X normalized is the normalized value of x in the new range. By applying this technique, the lowest pixel value (corresponding to "Air" in this instance) is set to 0, while the highest value (HUmax, initially at 400) is scaled to 1. All other pixel values are proportionally adjusted to fall between 0 and 1, maintaining their relative relationships intact. For any given pixel value:

$$x_{normalized} = \frac{x-(-1000)}{400-(-1000)} = \frac{x+1000}{1400} \quad (2)$$

Shifting the focus to image resizing, which is a crucial pre-processing step, the context involves several constraints including hardware limitations[10]. The original pCT and CBCT images were captured with dimensions of 512x512 pixels. Given the hardware constraints, a pragmatic solution was to halve the dimensions by dividing them by a factor of 2. This maneuver resulted in images of 256x256 pixels, offering a balanced compromise between image quality and the imposed limitations. Mathematically, if Po represents the pixel value at the row io and column jo in the original image, and *Pn* represents the pixel value at row "in" and column "*jn*" in the resized image. The average values of the four pixels in the original image that correspond to the 2x2 block surrounding the pixel in the resized image operation can be expressed as:

$$P_n = \left(\frac{1}{4}\right) * \left(P_{o(2i_n,\,2j_n)} + P_{o(2i_n,\,2j_n+1)} + P_{o(2i_n+1,\,2j_n)} + P_{o(2i_n+1,2j_n+1)}\right) \quad (3)$$

Probability map (Heat map) creation

Investigating the concept introduced by Pfister et al[11], the approach involves the concurrent regression of heat-maps for landmarks rather than focusing solely on absolute landmark coordinates. In a similar manner, heat-maps are depicted as images in which Gaussian distributions are centered at the respective landmark positions. Moreover, generating heat-maps for landmark detection involves creating a visual representation of the likelihood of landmarks being present in different parts of an image, which is achieved using a Gaussian distribution. The Gaussian curve is defined by parameters such as amplitude (peak intensity), mean (centre), and standard deviations (spread) along the x and y axes. In the context of generating a Gaussian heat-map for landmark detection, the distribution is used to simulate the heat or intensity around a landmark point. The 2D Gaussian distribution is defined as:

$$gauss(x, y) = A \cdot e^{-\frac{(x-\mu_x)^2}{2\sigma_x^2} - \frac{(y-\mu_y)^2}{2\sigma_y^2}} \quad (4)$$

Where: x, y are coordinates in 2D space. A is the amplitude or peak value. μx, μy are the mean values along x and y axes. σx, σy are the standard deviations along x and y axes.

Train, Validation & Test sets

This step is important in training any DL model[12]. For training and testing purposes of our model, our data have been split into three distinct dataset (i) the training set is the set of data that is used to train and make the model learn the hidden features/patterns in the data, the training set should have a diversified set of inputs so that the model is trained in all scenarios and can predict any unseen data sample that may appear in the future; (ii) The validation set is a set of data, that is used to validate our model performance during training. This validation process gives information that helps us tune the model's hyper-parameters and configurations; (iii) The test set is a separate set of data used to test the model after completing the training. This provides an unbiased final model performance metric in terms of accuracy and precision.

In the scope of our research, we initially conducted a segregation process where 14 patients out of 58 forming our dataset, will be reserved for test set. This is done to avoid biased estimations and the necessity to accommodate certain hardware limitations and also for optimal utilization. This partitioning leaves us with a remaining set of 44 patients. Within this framework, we have formulated a scenario that encompasses a training-validation split of 80% and 20%, respectively.

Model Architecture

Our U-net architecture consists of an encoding path and a

decoding path[13]. The coding path follows the typical architecture of a convolutional network. It consists of the repeated application of two 3x3 convolutions, each followed by a 2x2 max pooling operation with stride 2 for down-sampling. Every step in the decoding path consists of an up-sampling of the feature map followed by a 2x2 convolution ("up-convolution") that halves the number of feature channels, a concatenation with the correspondingly cropped feature map from the decoding path, and two 3x3 convolutions, each followed by a ReLU. At the final layer a 1x1 convolution is used to map each 64-component feature vector to the desired number of classes. In total, the network has 23 convolutional layers. Fig.2 describes the U-net architecture (example for 32x32 pixels in the lowest resolution). Each blue box corresponds to a multi-channel feature map. The number of channels is denoted on top of the box. The x-y-size is provided at the lower left edge of the box. White boxes represent copied feature maps, the arrows denote the different operations. Fig.2 illustrates the proposed architecture, and Table 1 summarizes encoding and decoding paths.

Table 1. Proposed U-net architecture's construction and flow

	Name	Kernel size	Feature map input	Feature map output
Encoding path	2 x conv Layer	3	(256, 256, 1)	(256, 256, 16)
	Max-Pooling 2	2	(256, 256, 16)	(128, 128, 16)
	2 x conv Layer	3	(128, 128, 16)	(128, 128, 32)
	Max-Pooling 2	2	(128, 128, 32)	(64, 64, 32)
	2 x conv Layer	3	(64, 64, 32)	(64, 64, 64)
	Max-Pooling 2	2	(64, 64, 64)	(32, 32, 64)
	2 x conv Layer	3	(32, 32, 64)	(32, 32, 128)
	Max-Pooling 2	2	(32, 32, 128)	(16, 16, 128)
	2 x conv Layer	3	(16, 16, 128)	(16, 16, 256)
	Name	**Kernel size**	**Feature map input**	**Feature map output**
Decoding Path	Con2D Transpose and	2	(16, 16, 256)	(32, 32, 256)
	Max-Pooling 2	3	(32, 32, 256)	(32, 32, 128)
	Con2D Transpose and	2	(32, 32, 128)	(64, 64, 128)
	Max-Pooling 2	3	(64, 64, 128)	(64, 64, 64)
	Con2D Transpose and	2	(64, 64, 64)	(128, 128, 64)
	Max-Pooling 2	3	(128, 128, 64)	(128, 128, 32)
	Con2D Transpose and	2	(128, 128, 32)	(256, 256, 32)
	Max-Pooling 2	3	(256, 256, 32)	(256, 256, 16)
	2 x conv Layer	1	(256, 256, 16)	(256, 256, 1)

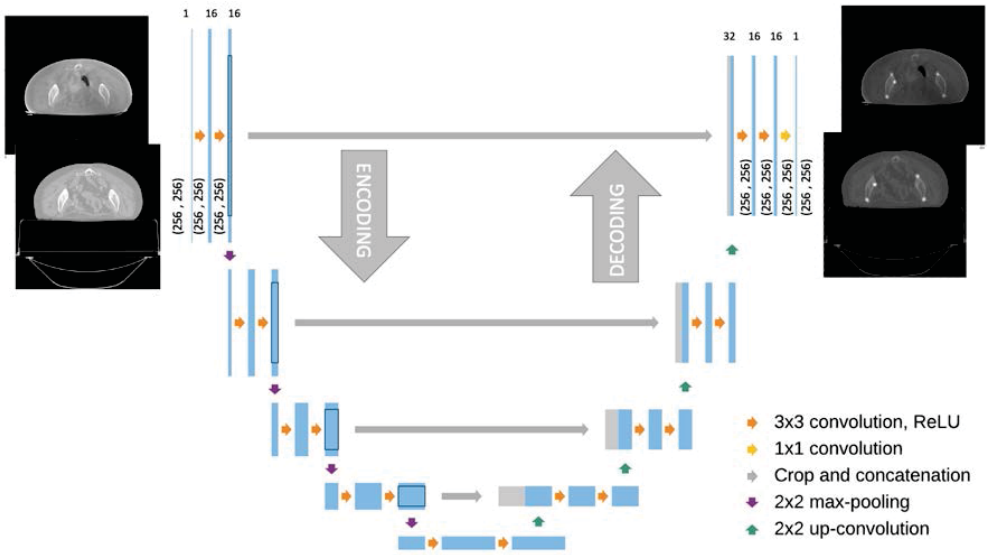

Fig. 2: Proposed U-net architecture

Performance Evaluation

The evaluation of machine learning algorithms is an essential part of any model training. Evaluation metrics explain the performance of a model and an important aspect of evaluation metrics is their capability to discriminate among model results. There are different types of evaluation metrics available, we will be focusing on the following metrics:

Accuracy:

Accuracy is the ratio of number of correct predictions to the total number of input samples. It works well only if there are equal number of samples belonging to each:

$$Accuracy(ACC) = \frac{Number\ of\ correct\ predictions}{Total\ number\ of\ predictions} \times 100\% \quad (5)$$

Where:

Number of Correct Predictions corresponds to the count of predictions made by the model that match the true values.

Total Number of Predictions corresponds to the total count of predictions made by the model.

Logarithmic Loss:

Non-Logarithmic Loss or Log Loss, works by penalizing the false classifications. It works well for multi-class classification. When working with Log Loss, the classifier must assign probability to each class for all the samples. Suppose, there are N samples belonging to M classes, then the Log Loss is calculated as below:

$$Logarithmic\ Loss = -\frac{1}{N}\sum_{i=1}^{N}\sum_{k=1}^{K} y_{ik} \cdot log\,(p_{ik}) \quad (6)$$

Where:

N is the number of samples. y_{ik} is the indicator (0 or 1) whether class k is the true class for sample i. p_{ik} is the predicted probability of class k for sample i.

Mean Squared Error:

The Mean Squared Error (MSE) or Mean Squared Deviation (MSD) of an estimator measures the average of error squares i.e., the average squared difference between the estimated values and true value. It is a risk function, corresponding to the expected value of the squared error loss. It is always non-negative and values close to zero are better.

$$Mean\ Squared\ Error(MSE) = \frac{1}{N}\sum_{i=1}^{N}(y_i - \hat{y_i})^2 \quad (7)$$

Where:

N is the number of samples. y_i is the true target value for sample i. $\hat{y_i}$ is the predicted target value for sample i.

RESULTS AND DISCUSSION

Once the development process is accurately designed and the previous conditions fulfilled, running the training code begins. For each given hyper-parameter, 100 and 150 Epochs, 64 and 80 batch-sizes (see Table 2) and by setting the call-back (early stopping) parameter for 20 repetitive MSE values, the training

results of both CBCT and pCT models are given in Figure 3 and Figure 4 respectively.

Table 2. Hyper-parameters tuning for pCT and CBCT training models

Modality	Hyper-parameters		Number of parameters
	Epoch	Batch size	
CBCT	100	64	1,940,817
	150	64	-
	100	80	-
	150	80	-
CT	100	64	1,940,817
	150	64	-
	100	80	-
	150	80	-

We first report that the landmark detection by the proposed U-net architecture has successfully learned predicting landmark correspondences of both CBCT and CT models under the inserted expert-based landmarks. From the figures above, we can state that: by fixing the EPOCH and varying the Batch-size, the more the batch-size is higher, the more landmarks are detected. However, by fixing the batch-size and varying the EPOCHs values, we clearly observe a precision in landmarks distribution positions, hence, the more EPOCHs are, the better the precision. The pCT model has shown similar results concerning landmark detection success by the U-net. Furthermore, this resemblance is not only confined to the landmark detection, it also shows similar results when tuning the hyper-parameters. We further report the change of loss function values achieved by the two models training with entire images. Training and test figures indicate almost no over-fitting or under-fitting issue for both models. We also state that, the time of the training is within 57 minutes for 100 EPOCHs and 114 minutes for 150 EPOCHs on a Google Colab GPU.

For a qualitative evaluation, we visually compared the model landmarks with the pre-defined expert-based landmarks. These landmarks will be shown and displayed on the corresponding images, we selected four random pairs of images. Figures 5 and 6 demonstrate these samples clearly. The CNN model successfully identifies landmarks in both CT and CBCT images. Notably, the model surpasses expert annotations in certain instances by correctly identifying missing landmarks.

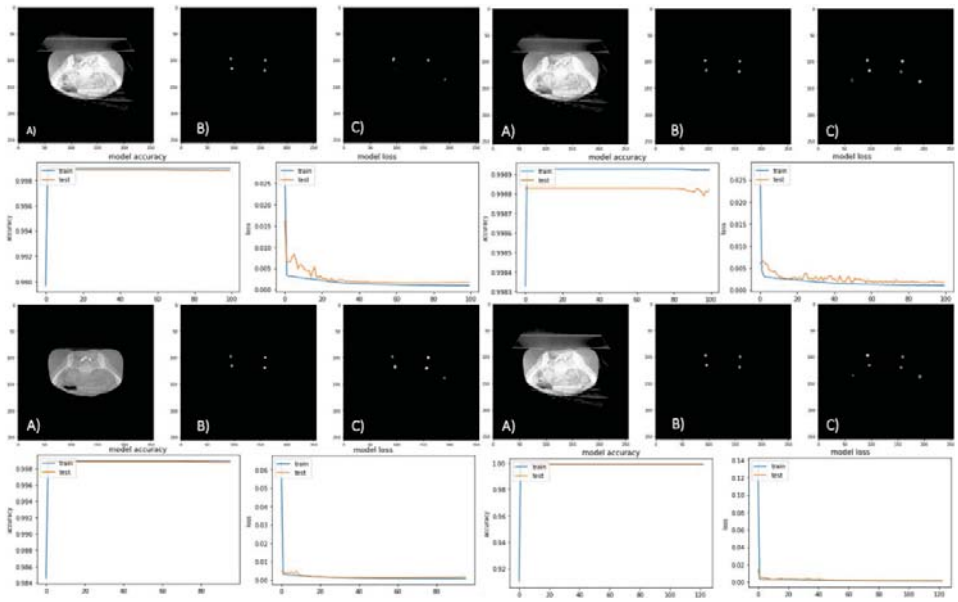

Figure 3: Results of the proposed CBCT training model of U-net architecture set on EPOCH=100 and 150& Batch-Size=64 and 80 where A) Original image B) Expert-based landmark C) Model Landmarks

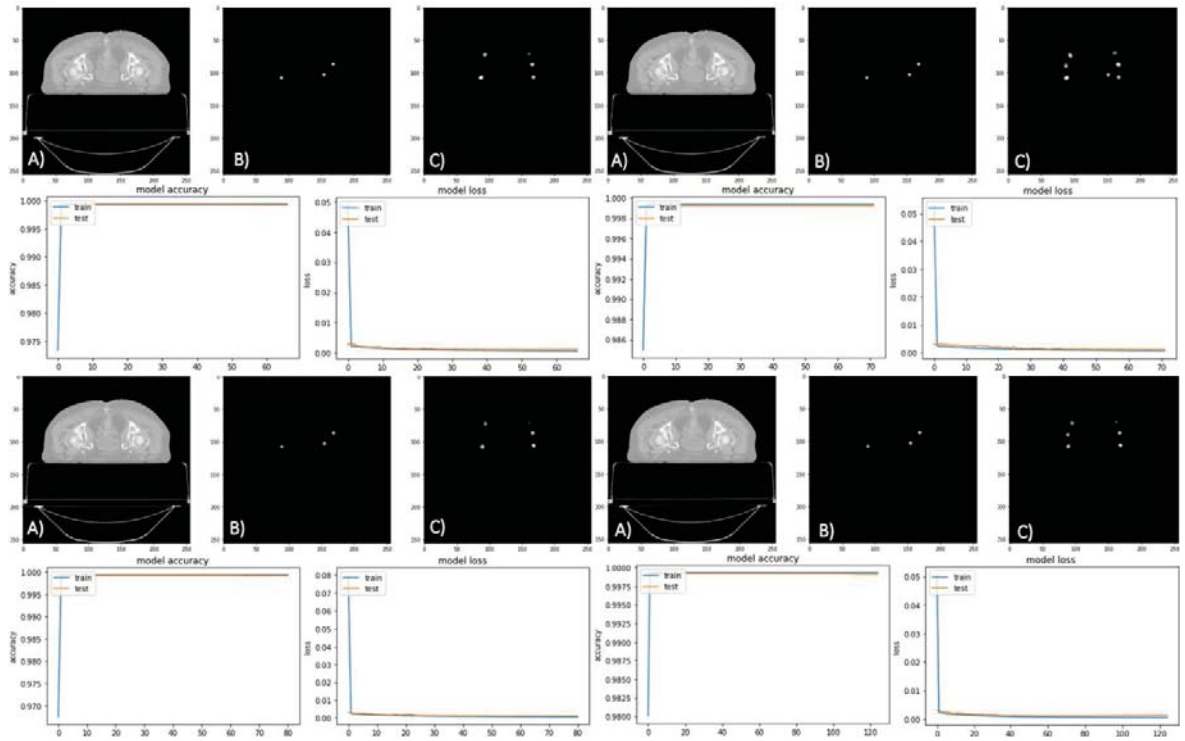

Figure 4: Results of the proposed CT training model of U-net architecture set on EPOCH=100 and 150& Batch-Size=64 and 80 where A) Original image B) Expert-based landmark C) Model Landmarks

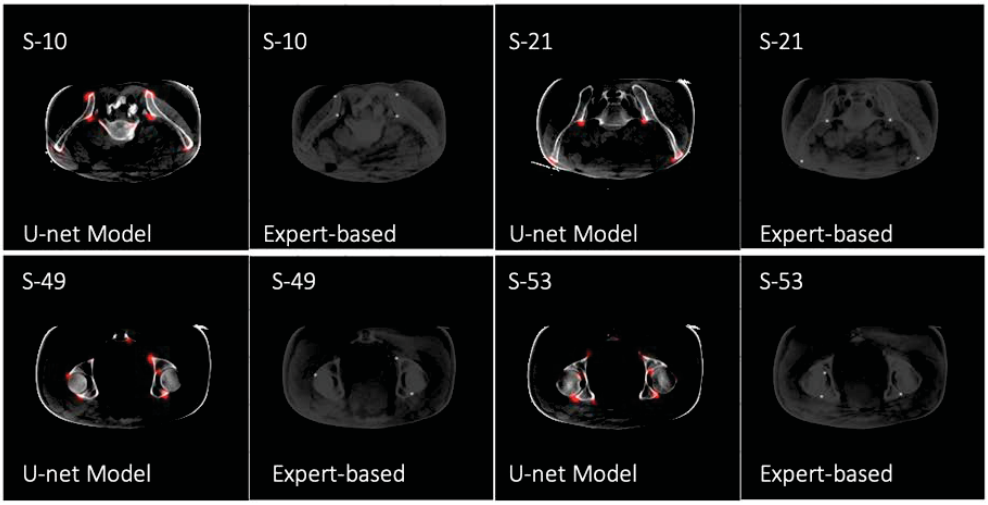

Figure 5: Illustrative representation of CBCT landmarks between pair of slices, red dotes represents the predicated landmarks and the white dotes represent the expert-based landmarks

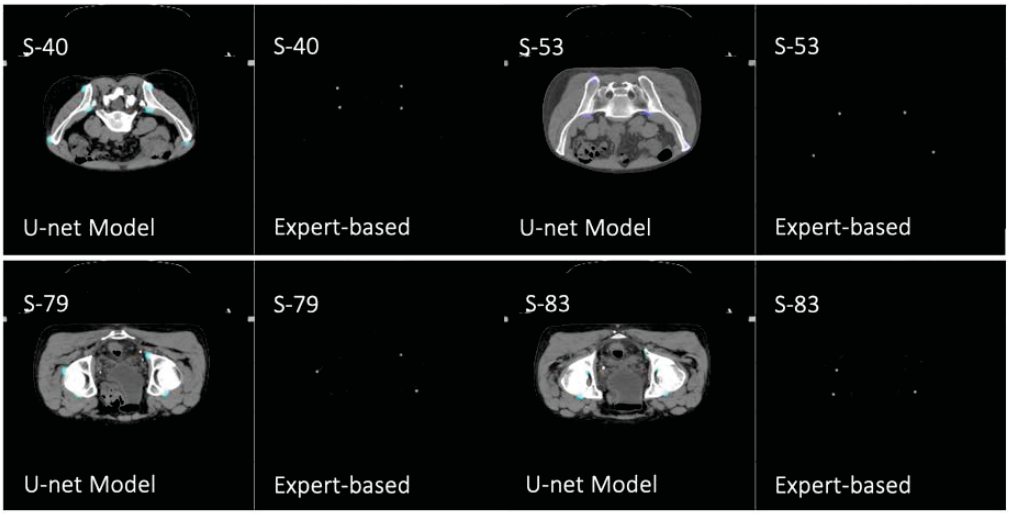

Figure 6: Illustrative representation of CT landmarks between pair of slices, blue dotes represents the predicated landmarks and the white dotes represent the expert-based landmarks

CONCLUSIONS

With a motivation to provide additional guidance information for automatic landmark detection and eventually, registration methods of medical images, we developed a deep learning approach for the detection of landmarks in two different image paired modalities. To the best of our knowledge, this is the first approach that trains landmark locations between the pCT and the CBCT images of the pelvic area using U-net. Our proposed approach of model learning based on the U-net architecture requires a pre-annotation from experts regarding the landmark coordinates before the learning process. The appearance of landmarks in the learning process has not only given more points but also precisely predicted landmarks spatial positions with high accuracy. These conditions are related to the architecture's hyper-parameters, we observed that, by establishing high tuning values, the performance is highly upgraded. Results are encouraging; however, the current method is designed for 2D images, and thus ignores the likelihood of out-of-plane correspondences in pCT and CBCT scans. As a result, extending the methodology to 3D is critical in order to speculate on the benefits of supplying extra guidance information to the new techniques on DIR systems. In addition, small number of the results showed predicted landmarks out of context, i.e. false predictions. Further, in contrast to the traditional unsupervised methods for landmark detection in medical imaging, the proposed approach requires pre- and post-processing steps and has more hyper-parameters, Finally, our approach can be viewed as a potential method to add to the radiation therapy.

AUTHOR INFORMATION

Corresponding Author

*M. Oussama Mebarki

Email address: mohamedoussama.mebarki@univ-setif.dz

ACKNOWLEDGMENT

The authors extend their gratitude to colleague Dr. Halima Saadia Kidar for her help and advices, and the medical experts at the Beaumont Proton Centre for providing their public dataset used in this study.

REFERENCES

1. Shadrack Mambo, Karim Djouani, Yskandar Hamam, Barend van Wyk, and Patrick Siarry. A review on medical image registration techniques. International Journal of Computer and Information Engineering, 12(1):48–55, 2018.

2. Kristy K Brock, Sasa Mutic, Todd R McNutt, Hua Li, and Marc L Kessler. Use of image registration and fusion algorithms and techniques in radiotherapy: Report of the aapm radiation therapy committee task group no. 132. Medical physics, 44(7):e43–e76, 2017.
3. Arthur Ardeshir Goshtasby. Theory and applications of image registration. John Wiley & Sons, 2017.
4. Grant Haskins, Uwe Kruger, and Pingkun Yan. Deep learning in medical image registration: a survey. Machine Vision and Applications, 31(1):1–18, 2020.
5. Geert Litjens, Thijs Kooi, Babak Ehteshami Bejnordi, Arnaud Arindra Adiyoso Setio, Francesco Ciompi, Mohsen Ghafoorian, Jeroen Awm Van Der Laak, Bram Van Ginneken, and Clara I Sa nchez. A survey on deep learning in medical image analysis. Medical image analysis, 42:60–88, 2017.
6. Thomas Polzin, Jan Ru haak, Ren e Werner, Jan Strehlow, Stefan Heldmann, Heinz Handels, and Jan Modersitzki. Combining automatic landmark detection and variational methods for lung ct registration. In Fifth international workshop on pulmonary image analysis, pages 85–96, 2013.
7. Van Linh Le et al. Automatic landmarking for 2D biological images: image processing with and without deep learning methods. PhD thesis, Bordeaux, 2019.
8. R Vandaele. Machine Learning for Landmark Detection in Biomedical Applications. PhD thesis, Universit e de de Li`ege, Li`ege, Belgique, 2018.
9. Patro, S. G. O. P. A. L., & Sahu, K. K. (2015). Normalization: A preprocessing stage. arXiv preprint arXiv:1503.06462.
10. Saponara, S., & Elhanashi, A. (2021, September). Impact of image resizing on deep learning detectors for training time and model performance. In International Conference on Applications in Electronics Pervading Industry, Environment and Society (pp. 10-17). Cham: Springer International Publishing.
11. Pfister, T., Charles, J., & Zisserman, A. (2015). Flowing convnets for human pose estimation in videos. In Proceedings of the IEEE international conference on computer vision (pp. 1913-1921).
12. Picard, R. R., & Berk, K. N. (1990). Data splitting. The American Statistician, 44(2), 140-147.
13. Olaf Ronneberger, Philipp Fischer, and Thomas Brox. U-net: Convolutional networks for biomedical image segmentation. In International Conference on Medical image computing and computer-assisted intervention, pages 234–241. Springer, 2015.

2023

An Efficient Convolutional Neural Network Model for Detecting Colorectal Cancer from Histological Images

M. Sari,[a] A. Moussaoui,[a] N. Frahta,[a] A. Hadid,[b]

[a] Department of Computer Science, Faculty of Sciences, Ferhat Abbas Setif1 University, Setif-19000, Algeria
[b] Sorbonne Center for Artificiel Intelligence, Sorbonne University Abu Dhabi, Abu Dhabi

.

ABSTRACT: The increasing development of machine learning (ML) and the significant progress it achieved draw attention towards coping with the medical field. Colorectal cancer (CRC) is one of the most common cancers among humans, its diagnosis is made through the visual analysis of tissue samples; artificial intelligence (AI) can automate this analysis based on histological images generated from different tissue samples. CRC is considered an abnormal growth of cells that compose a tumor; being able to differentiate normal cells from tumor cells is still a challenging problem. In this paper we aim to enhance this process by proposing a deep learning (DL) based method that is extremely accurate and reliable despite several limitations. Our method is a DL application that is based on Convolutional Neural Networks (CNN) in order to classify different classes of tissues into cancerous and non-cancerous cells based on histological images token from two different datasets. Due to the sensitivity of the problem, the performance of our work will be estimated using general accuracy, precision, recall and F-score metrics since they ensure more credibility to the classification results. Our model has been tested and evaluated under two datasets, the first one was collected from CRC-5000 datasets containing more than 10000 images (with data augmentation) of cancerous and non-cancerous tissues, our model achieved promising results with an overall accuracy of 94%, precision= 100%, recall= 100% and F1-score= 100%. The second dataset is Kather-CRC-2016, it contains more than 5000 images (without data augmentation) belonging to eight different tissue categories; our model achieved high performance for the class Tumor with precision= 96%, recall= 99% and F1-score= 98% and overcome state of the art methods.
Keywords: Deep learning; Colorectal Cancer; Histological Images; CNN; Digital Pathology.

INTRODUCTION

Colorectal cancer is considered as the fourth occurring cancer in the world[11], it is defined as an uncontrolled cell division in the colon and the rectum regions due to mutations in the cells' genes, this mass of cells form polyps, not all polyps are cancerous but over time they can develop to Colorectal Cancer. Usually the manual procedures of detecting CRC is by taking a biopsy from the existing polyps, and then study its composition using microscopes, the images resulting from this phase are called histological images, they present different types of existing cells in the studied tissue and analyzed by pathologists.

Even though CRC is the third leading cancer type to cause death[11], early detection plays a key role in saving lives and can increase the survival rate by up to nearly 90% [14]. The analysis of histological images through advanced ML techniques resulted better and more efficient diagnosis. Recent studies show that ML techniques achieved significant process in the medical field such as: radiologic diagnosis[1], disease diagnosis through gross and microscopic images[2] tumor detection, classification, especially for breast[3], brain[4], lung[5], gastric[6], ovarian, and prostate[7,8] cancers.

In addition, there have been various attempts to apply Artificial Intelligence (AI) techniques in the pathologic image analysis of CRC.

A traditional classification system consists of three phases, namely image pre-processing, feature extraction and classification; an automated system would let the machine learns the optimal features by its own instead of involving human beings. The most successful ML models are the ones based on Deep Learning (DL) especially Convolutional Neural Networks (CNN), they can automatically extract features from raw input images and this represents the main reason and success factor that makes it more efficient and reliable.

CNN are a type of Neural Networks where we alternatively use two types of layers: convolutional and pooling layers, and the end a fully connected layer that connects to the output layer. The main difference between CNN and regular neural networks is that CNN uses multiple hidden layers instead of just one.

In this paper we present a DL method based on CNN in order to classify histological images token from two datasets into cancerous and non cancerous tissue cells, the evaluation is done using different metrics in order to ensure the efficiency of the model; our method shows promising results compared to state of the art methods [12, 13].

The rest of the paper is organized as next: section 2 talks about the experimental method, section 3 shows the obtained results and their discussions then a conclusion is given at the end.

EXPERIMENTAL

In this paper, we proposed a model based on CNN due to its efficiency in the problem of image classification. Our model consists of the use of three convolutional layer blocks followed by max pooling layer each, then a fully connected layer and at the end an output layer that contains the number of output classes. The general architecture of our model is shown in Figure 1.

Our model is tested under two different datasets, the first one is collected from the CRC-5000 dataset; the original database[9] contains 25000 images of lung and colon cancer disease; we collected 10000 images divided equally into two classes: cancerous colon cells and non cancerous colon cells each class contains 5000 images of size 768*768 and in jpeg format.

The second dataset is collected from the Kather-CRC-2016 database[10]; it contains 5000 images divided into eight different tissue classes: empty, adipose, mucosa, debris, lympho, complex, stroma and tumor.

Our model was trained for 30 epochs; batch size was set to 64 for the first dataset and 32 for the second; we used data augmentation techniques for both datasets. Dropout and Batch normalization layers were added to improve the performance of the model.

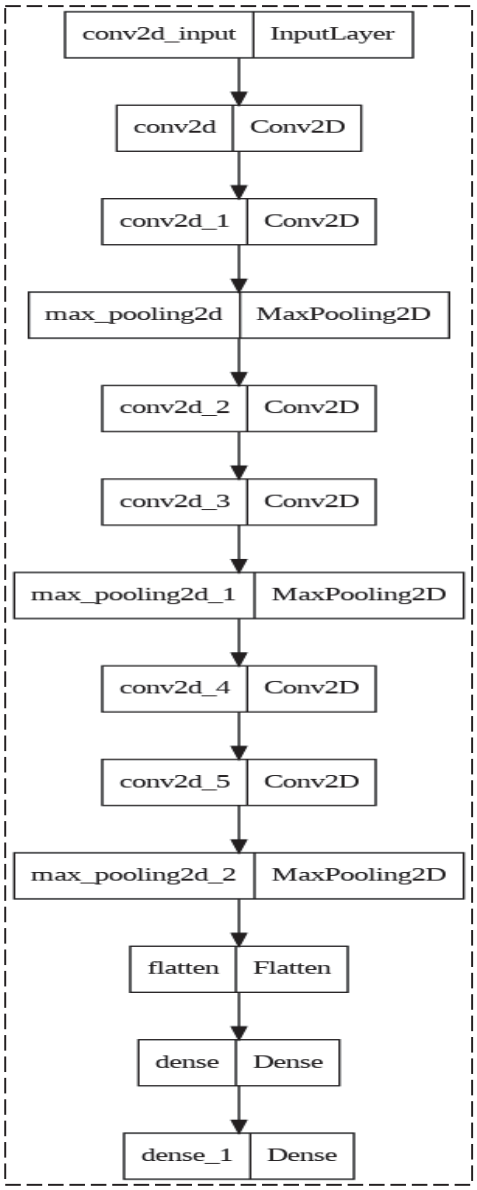

Fig. 1: The General Architecture of the Model

RESULTS AND DISCUSSION

In this work, we conducted a study based on CNN architecture; it was tested under two datasets and evaluated using different metrics in order to prove its efficiency and reliability. In addition to model general Accuracy which is the main metric for almost each study we also used Precision, Recall and F1-Score.

Precision measures the correctness of positive predictions, while recall measures the completeness of positive predictions, Precision can be seen as a measure of quality, and recall as a measure of quantity. Precision measures the proportion of correctly predicted positive instances. Accuracy assesses the

overall correctness of predictions. Recall evaluates the proportion of actual positive instances correctly identified by the model.

The F1-Score combines the Precision and Recall metrics, the higher the F1-Score is the more reliable the model is.

For the first dataset (CRC-5000) our model achieved an overall accuracy of 94% with precision= 100%, recall= 100% and F1-score= 100%. Classification report for this dataset is shown in Table 1. You can find the accuracy curve in figure 2.

Tissue Classes	Precision	Recall	F1-Score
Cancerous	100%	100%	100%
Non Cancerous	100%	100%	100%

Table 1. Classification report for the CRC-5000 Database

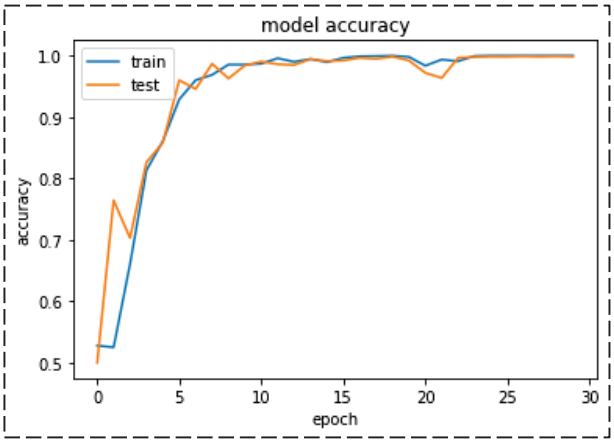

Fig. 2: Model Accuracy Curve for the CRC-5000 Database

For the second dataset (Kather-CRC-2016) our model achieved high performance for the class Tumour with precision= 96%, recall= 99% and F1-score= 98%. The classification report for this dataset is shown in Table 2.

Table 2. Classification Report for the Kather-CRC-2016 Database

Tissue Classes	Precision	Recall	F1-Score
Empty	0.80	0.89	0.84
Adipose	0.61	0.77	0.68
Mucosa	0.82	0.60	0.69
Debris	0.90	0.87	0.89
Lympho	0.70	0.62	0.66
Complex	0.81	0.78	0.80
Stroma	0.90	0.95	0.93
Tumor	0.96	0.99	0.98

Table 3 presents a comparison between state-of-art methods and our proposed method. Results shown clearly the performances of our proposed method.

Table 3. Comparison of State of the Art Methods and the Proposed Model

Technique	Data base	Accuracy	Precision	Recall	F1-Score
Reference 12	CRC - 5000	89.9%	99.9%	99.9%	98.85%
Reference 13	CRC - 5000	88.26%	-	-	-
Proposed Model	CRC - 5000	94%	100%	100%	100%

CONCLUSIONS

In this paper we presented a novel architecture based on CNN in order to classify histological images into cancerous and non-cancerous cells, we tested our model under two different datasets and evaluated it using different metrics; our model achieved significant results and proved that machine learning can be a leading technique for medical classification problems.

AUTHOR INFORMATION

Corresponding Author

*Meriem Sari

Email address: meriem.sari@univ-setif.dz

REFERENCES

1. Hosny, A.; Parmar, C.; Quackenbush, J.; Schwartz, L.H.; Aerts, H.J.W.L. Artificial intelligence in radiology. Nat. Rev. Cancer 2018, 18, 500–510.

2. Nam, S.; Chong, Y.; Jung, C.K.; Kwak, T.-Y.; Lee, J.Y.; Park, J.; Rho, M.J.; Go, H. Introduction to digital pathology and computer-aided pathology. J. Pathol. Transl. Med. 2020, 54, 125–134.

3. Ehteshami Bejnordi, B.; Veta, M.; Johannes van Diest, P.; van Ginneken, B.; Karssemeijer, N.; Litjens, G.; van der Laak, J.A.W.M.; Consortium, a.t.C. Diagnostic Assessment of Deep Learning Algorithms for Detection of Lymph Node Metastases inWomenWith Breast Cancer. JAMA 2017, 318, 2199–2210.

4. Ertosun, M.G.; Rubin, D.L. Automated Grading of Gliomas using Deep Learning in Digital Pathology Images: A modular approach with ensemble of convolutional neural networks. AMIA Annu. Symp. Proc. AMIA Symp. 2015, 2015, 1899–1908.

5. Teramoto, A.; Tsukamoto, T.; Kiriyama, Y.; Fujita, H. Automated Classification of Lung Cancer Types from Cytological Images Using Deep Convolutional Neural Networks. Biomed Res. Int. 2017, 2017, 4067832.

6. Meier, A.; Nekolla, K.; Earle, S.; Hewitt, L.; Aoyama, T.; Yoshikawa, T.; Schmidt, G.; Huss, R.; Grabsch, H.I. 77PEnd-to-end learning to predict survival in patients with gastric cancer using convolutional neural networks. Ann. Oncol. 2018, 29.

7. Litjens, G.; Sánchez, C.I.; Timofeeva, N.; Hermsen, M.; Nagtegaal, I.; Kovacs, I.; Hulsbergen-van de Kaa, C.; Bult, P.; van Ginneken, B.; van der Laak, J. Deep learning as a tool for increased accuracy and e_ciency of histopathological diagnosis. Sci. Rep. 2016, 6, 26286.

8. Chang, H.Y.; Jung, C.K.; Woo, J.I.; Lee, S.; Cho, J.; Kim, S.W.; Kwak, T.-Y. Artificial Intelligence in Pathology. 1. J. Pathol. Transl. Med. 2019, 53, 1–12.

9. Andrew A Borkowski, Marilyn M Bui, L Brannon Thomas, Catherine P Wilson, Lauren A DeLand, and Stephen M Mastorides. Lung and colon cancer histopathological image dataset (lc25000).

10. Kather JN, Weis CA, Bianconi F, Melchers SM, Schad LR, Gaiser T, Marx A, Zollner F: Multi-class texture analysis in colorectal cancer histology (2016), Scientific Reports (in press).

11. World Health Organization, https://www.who.int/colorectal-cancer.

12. Mehmood, S., Ghazal, T.M., Khan, M.A., Zubair, M., Naseem, M.T., Faiz, T., Ahmad, M.: Malignancy detection in lung and colon histopathology images using transfer learning with class selective image processing. IEEE Access 10, 25657–25668 (2022).

13. Wahid, R.R., Nisa, C., Amaliyah, R.P., Puspaningrum, E.Y.: Lung and colon cancer detection with convolutional neural networks on histopathological images. In: AIP Conference Proceedings. vol. 2654. AIP Publishing (2023).

14. American Cancer Society https://www.cancer.org/cancer .

2023

Electrons elastic scattering by DNA and/or RNA molecules

B. Si Tayeb,[a,b,*] S. Mokrani,[a,b] H. Aouchiche,[a,b] C. Champion,[c,d]

[a] Department of Physics, Faculty of Sciences, Mouloud Mammeri University, BP 17, 1500 Tizi-Ouzou, Algeria
[b] Laboratory of Mechanics, Structures and Energy (LMSE), BP 17, 1500 Tizi-Ouzou, Algeria
[c] Department of Physics, Faculty of Sciences, University of Bordeaux, France
[d] Intense Lasers and Applications Center (Celia), Domaine Du Haut-Carré, 33405, Talence, France

.

ABSTRACT: Nowadays, several authors have investigated electron interaction with molecules constituting the deoxyribonucleic acid (DNA). It is known that all cellular molecules and constituents can be affected by radiation. The aim of these different studies was to understand the various processes leading to the radiation damages of a living cell. Knowing that today, it is clearly recognized that the carrier of genetic information (DNA) is the sensitive entity of an irradiated organism. The damage suffered by this molecule influences the functioning cellular such that in the normal functioning of the living cell. Particularly after exposure, some radiation-induced DNA damage can lead to mutations of the cells. In some cases, they persist and can promote the emergence of cancers after few years. It therefore appears necessary to fully understand the biological mechanisms leading to cell death. Thus, we propose to calculate numerically, at low and high energies, the differential and integral cross sections of the electrons scattered elastically by biomolecular targets that constitute the deoxyribonucleic acid and ribonucleic acid. Our choice is, particularly, focused on the tetrahydrofuran (THF, C_4H_8O) molecule, since it is similar to the sugar of DNA and RNA. The calculation method developed is based on the model of independent atoms, taking into account the various interaction potentials at short- and long-range between the biomolecular and the incident radiation as well as the multiple scattering effects. The doubly differential cross sections have been calculated as a function of the scattering angles for many incident energies, while the integral cross sections are calculated for the energies ranging from 20eV to 100keV. The effects of the various interaction potentials are analyzed. In addition, the obtained results are discussed and compared to the experimental data available in the literature and very good agreements are found.

Keywords: Electrons elastic scattering; differential and integral cross-sections; THF; DNA; Independent atom model.

INTRODUCTION

The radiation-matter interaction is involved in a wide variety of research fields such as plasma physics[1], astrophysics[2], or even radiobiology[3]. Indeed, when the radiation penetrates the matter, it modifies certain properties of the irradiated matter. In the specific case of biological matter, this alteration, when not corrected, can lead to the appearance of chromosomal aberrations that can lead to mutations, cancers or cell death. Paradoxically, the aim of irradiation is to destroy cancer cells while preserving as much as possible healthy tissue and surrounding organs: this is the case with radiotherapy. Thus, in order to understand in detail the action of ionizing radiation on the biological medium, both at the macroscopic and molecular level, it is therefore important to be able to follow the path of the incident particle in biological matter in order to better predict and control its effects.

THEORETICAL MODEL

In the independent atom model IAM, the interactions between the fast incident electron and the target molecule can be represented in the optical potential formalism by the sum of a short-range potential $V_s(r)$ and a long-range potential $V_L(r)$. The first, presenting a Colombian type interaction for each nucleus, composed of two contributions: electronic $V_i(r)$ and ionic $V_{ion}(r)$.

$$V_s(r) = \sum_i^N (V_i(r) + V_{ion}(r)) \quad (1)$$

where N is the number of atoms composing the molecule.

The term $V_L(r)$, presenting the long-range potential, is composed of two important contributions. Therefore,

$$V_L(r) = V_{ex}(r) + V_{cp}(r) \quad (2)$$

Where $V_{ex}(r)$ and $V_{cp}(r)$ are respectively the exchange potential and the correlation-polarization potential.

The differential cross section (DCS), defined as $d\sigma/d\Omega$, is expressed in our case by the sum of the different contributions due to the different acting potentials between the incident charged particle and the molecular target, its expression is given by

$$\frac{d\sigma}{d\Omega} = I_S + I_L + I_{LS} + I_{SS} + I_{SD}^{(1)} + I_{SD}^{(2)} + I_{DD}^{(0)} \quad (3)$$

$$I_S = \sum_{i=1}^N |f_i|^2 \quad \text{and} \quad I_L = |f_l|^2 \quad (4)$$

Where $|f_i|$ and $|f_l|$ are respectively the short and long-range scattering amplitudes of i^{Th} atom of the molecule.

The interference between the two potentials $V_s(r)$ and $V_L(r)$ gives:

$$I_{LS} = 2\,|f_l| \sum_{i=1}^N |f_i| \cos(\eta_l - \eta_i) \frac{\sin(KR_i)}{KR_i} \quad (5)$$

$I_{SS} = \sum_{i\neq j}^N f_i^* f_j \frac{\sin(KR_{ij})}{KR_{ij}}$ is the interatomic interaction term. The last terms $I_{SD}^{(1)}$, $I_{SD}^{(2)}$ and $I_{DD}^{(0)}$ describe multiple scattering and define respectively the interference between the single and double scattering at first and second order as well as pure double scattering. They are given by[4]:

$$I_{SD}^{(1)} = \frac{i}{k} \sum_{i\neq j}^N (f_i + f_j)^* \sum_{l_1 l_2 l_3} (2l_1+1)(2l_2+1) \times (2l_3+1) P_{l_2}(\cos\theta) \begin{pmatrix} l_1 & l_2 & l_3 \\ 0 & 0 & 0 \end{pmatrix}^2 \times j_{l_3}^2(kR_{ij}) A_{l_1}(k,j) A_{l_2}(k,i) \quad (6)$$

$$I_{SD}^{(2)} = \frac{4\pi i}{k} \sum_{K\neq(i\neq j)}^N f_K^* \sum_{\substack{l_1 l_2 l_3 \\ l_4 l_5 m_3}} i^{l_3 - l_4 + l_5} (-1)^{m_3} \times (2l_1+1)(2l_2+1)^{1/2}(2l_3+1) \times (2l_4+1)(2l_5+1)^{1/2} j_{l_3}^2(kR_{ij}) \times j_{l_4}(kR_{ij}) j_{l_5}(2kR_{ij}\sin(\theta/2)) \times \begin{pmatrix} l_1 & l_2 & l_3 \\ 0 & 0 & 0 \end{pmatrix} \begin{pmatrix} l_1 & l_2 & l_3 \\ 0 & -m_3 & m_3 \end{pmatrix} \times \begin{pmatrix} l_4 & l_5 & l_3 \\ 0 & 0 & 0 \end{pmatrix} \begin{pmatrix} l_4 & l_5 & l_3 \\ 0 & -m_3 & m_3 \end{pmatrix} \times Y_{l_2}^{-m_3}(\theta,0) Y_{l_5}^{-m_3}\left(\tfrac{1}{2}(\pi-\theta),0\right) \times p_{l_5}(cos\varphi_{ijK}) A_{l_1}(k,j) A_{l_2}(k,i) \quad (7)$$

$$I_{DD}^{(0)} = \frac{\pi}{k^2} \sum_{i\neq j}^N \sum_{l_3,m_3} (2l_3+1) j_{l_3}^3(kR_{ij}) \times \Big| \sum_{l_1 l_2} (2l_1+1)(2l_2+1)^{1/2} \times \begin{pmatrix} l_1 & l_2 & l_3 \\ 0 & 0 & 0 \end{pmatrix} \begin{pmatrix} l_1 & l_2 & l_3 \\ 0 & -m_3 & m_3 \end{pmatrix} \times Y_{l_2}^{-m_3}(\theta,0) A_{l_1}(k,j) A_{l_2}(k,i) \Big|^2 \quad (8)$$

The integral cross section (ICS) is obtained by integrating the differential cross sections (DCSs) over the entire solid angle $d\Omega$:

$$\sigma(E) = \int \frac{d\sigma}{d\Omega}\, d\Omega = 2\pi \int_0^\pi \frac{d\sigma}{d\Omega} sin\,\theta\, d\theta \quad (9)$$

RESULTS AND DISCUSSION

Results of the actual study are presented in figures 1 and 2. We observe at $50eV$ that our DCS results including all physical phenomena (solid magenta line) are in satisfactory agreement with the experimental data reported with uncertainties of $\sim 25\%$ by Milosavljevic et al. [6] (solid black squares), by Homem et al. [8] (solid purple triangles) and by Colyer et al. [9] (blue stars) even considering that a little minimum is nevertheless reported around $\theta \approx 38°$. Note that the current modified IAM version clearly improves the original IAM model [5], dashed black line) that only used the static-polarization potential - in particular for scattering angles $\theta \leq 18°$ and $85° \leq \theta \leq 120°$. At 80 eV, our DCS show a good

agreement despite a little deviation around $\theta \approx 75°$ with the measurements reported by Milosavljevic et al.[6] (solid black squares) and by Baek et al. [7] (solid green circles). For higher impact energies, our DCS are in excellent agreement with all the experimental data.

Concerning the integral cross section, we observe that it decreases monotonically as a function of projectile energy and exhibits good agreement with experimental measurements of THF. Considering the generally good agreement here obtained, we validate our corrected-IAM.

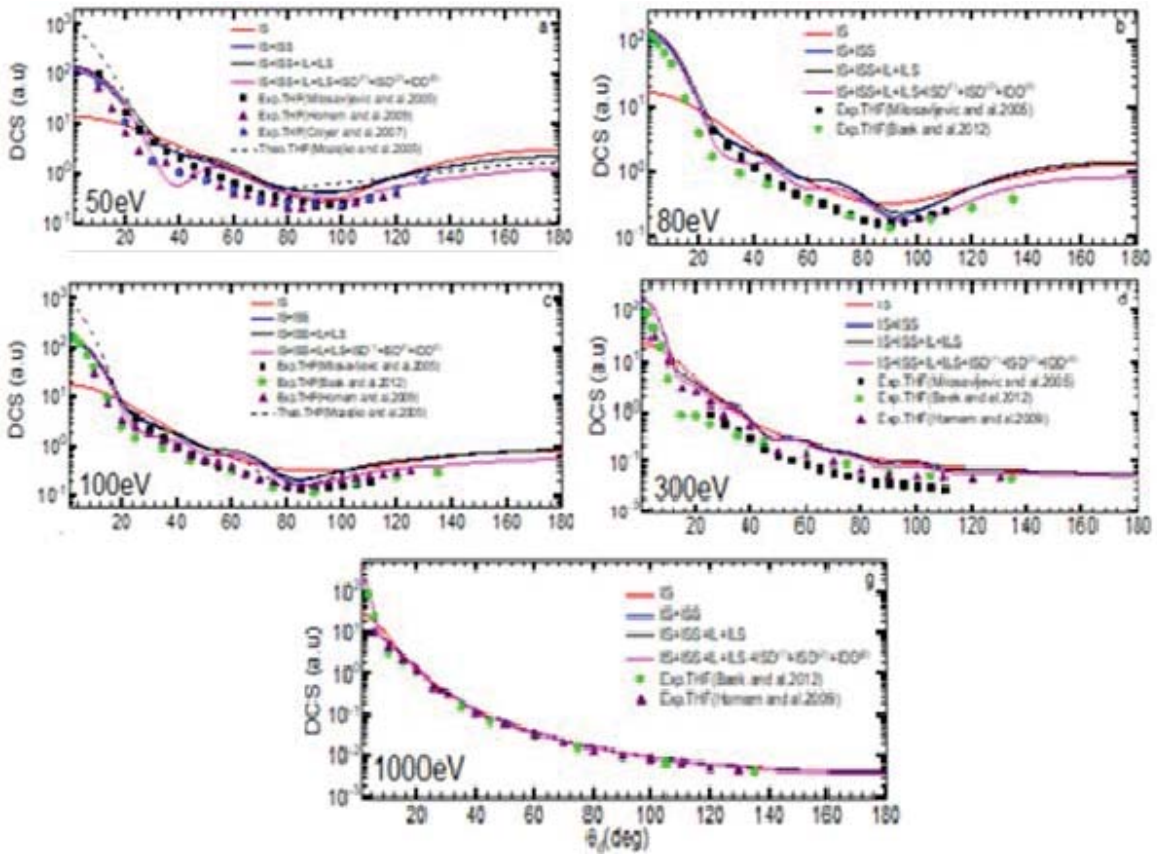

Fig.1: Variation of different contributions reported in eq.3 to the differential cross sections (DCS) of THF (C_4H_8O) molecule as a function of scattering angles for incident energies of: 50eV, 80eV, 100eV, 300eV and 1000eV. Available theoretical (dashed black line[5]) and experimental (solid black squares[6], solid green circles[7], solid purple triangles8 and blue stars[9]) data taken from the literature are also reported for comparison.

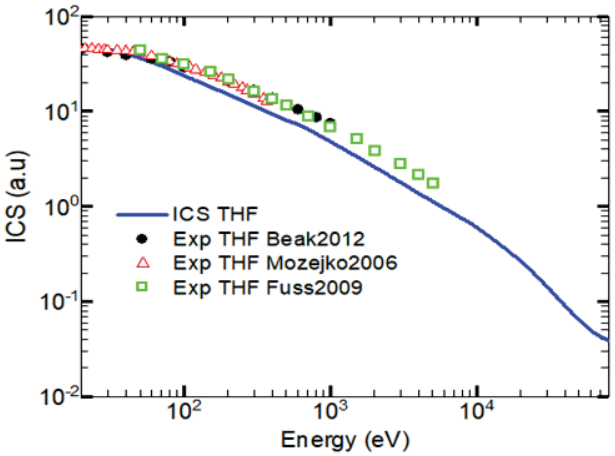

Fig.2: Variation of the elastic integral cross section (ICS) for electron scattering by THF molecule as a function of the incident energy (solid bleu line). Available experimental (solid black circles[7], open red triangles[10] and open green squares[11]) data taken from the literature are reported for comparison.

CONCLUSIONS

- We have developed a theoretical model based on the partial wave method for the calculation of the elastic differential cross sections for electrons scattering by the molecular target: THF, which is similar to the deoxyribose sugar.
- The contribution of the static term is found as significant over the whole range of scattering angles for all incident energy values.
- The contribution of the interatomic term is found negligible in the range of high scattering angles for high impact energies. While it is important for scattering angles below 10° over the entire incident energy range.
- The effects of exchange and correlation-polarization potentials are negligible for incident energies greater than 100eV over the entire scattering angular range.
- The multiple scattering effects are more significant at low incident energies.
- The integral cross section decreases monotonically as a function of projectile energy and exhibits good agreement with experimental measurements of THF.

AUTHOR INFORMATION

Corresponding Author

* Belkacem Si Tayeb

Email address: bsitayeb53@gmail.com

REFERENCES

1. Hans Bethe Annalen der Physik, 397(3): 325-400, 1930.
2. U Fano Annual Review of Nuclear Science, 13(1):1-66, 1963.
3. Colleen DesRosiers, V Moskvin, Alex F Bielajew, and L Papiez. 150-250 mev electron beams in radiation therapy. Physics in Medicine & Biology, 45(7):1781, 2000.
4. S. Hayashi, K. Kuchitsu, J. Phys. Soc. Jpn. 41 (1976) 1724 – 1732.
5. P. Mozejko, L. Sanche, Radiat, Phys. Chem. 73 (2005) 77-84.
6. A.R. Milosavljevic, A. Giuliani, D. Sevic, M.J. Hubin-Franskin, B.P. Marinkovic, Eur. Phys. J. D 35 (2005) 411 – 416..
7. W.Y. Baek, M. Bug, H. Rabus, E. Gargioni, B. Grosswendt, Phys. Rev. A 86 (2012), 032702.
8. M.G.P. Homem, R.T. Sugohara, I.P. Sanches, M.T. Lee, I. Iga1, Phys. Rev. A 80 (2009),032705.
9. C.J. Colyer, V. Vizcaino, J.P. Sullivan, M.J. Brunger, S.J. Buckman, New J. Phys. 9 (2007),41
10. P. Mozejko, E.P. Denga, A. Domaracka, C. Szmytkowski, Phys. Rev. 74 (2006), 012708.
11. M. Fuss, A. Munoz, J.C. Oller, F. Blanco, D. Almeida, P. Limao-Vieira, T.P.D. Do, M.J. Brunger, G. García, Phys. Rev. 80 (2009), 052709.

2023

Study of the effect of ultraviolet sunlight on sunflower plants grown in Algeria

M. Boukabcha,[a,b,c,*] K. El-Miloudi[c]

[a] Department of Physics, Faculty of Science and Informatics, Hassiba Ben Bouali University of Chlef, Chlef-2000, Algeria

[a] Institute of Sea Science and Techniques of Tenes, Chlef-2000, Algeria

[b] Laboratory of Theoretical and material physics, Hassiba Ben Bouali University of Chlef,-2000, Chlef, Algeria

ABSTRACT: Natural radiation from the sun, especially ultraviolet radiation, plays an important and essential role in the growth and development of many plants on the surface of the globe. This study aims to know the effect of ultraviolet sunlight on the growth of sunflower plants grown in greenhouses. Sunflower plants are exposed to ultraviolet sunlight during the day for approximately ten hours, according to experiments conducted during the spring semester at the Hassiba BENBOUALI University of Chlef in Algeria, for a period of more than three months, starting from planting their seeds. We tracked the behavior of these plants throughout their growth stages in natural conditions inside greenhouses. We did not notice any effects of the sun's ultraviolet radiation on the structure or weight of the living matter that makes up the studied sunflower plants, or on the natural compounds that absorb ultraviolet sunlight, according to our observations with the naked eye and comparison with previous studies of the same species. While ultraviolet sunlight inhibits the process of photosynthesis throughout the plant growth period, which we describe in this study. Our study indicates that the current level of solar UV radiation influences the performance of sunflower plants even though the dry plant biomass may not be affected.

Keywords: Ultraviolet sunlight; Sunflower plant, Photosynthesis, Greenhouses.

INTRODUCTION

This study aims to determine the effect of solar ultraviolet radiation on the growth of sunflower plants inside greenhouses[1]. Solar radiation is based on UV-B and UV-A in the range of 280-400 nm[1-2]. The effect on plants of this minor percentage of solar energy is potentially harmful because these short wavelengths are capable of causing deleterious damage to plant cells[2-3]. Plants are vulnerable to increased solar ultraviolet radiation because many cellular components such as nucleic acids, proteins, lipids, and quinines can directly absorb solar ultraviolet radiation[3]. The effect of increased solar ultraviolet radiation on the growth and physiology of many plants, including cultivated or forest tree species, both in greenhouses and in the open field, has become one of the research topics the most critical of recent decades[4]. Studies of the effect of natural solar ultraviolet radiation on five tropical species have shown that tropical vegetation responds to the actual level of natural solar radiation[5]. A reduction in biomass accumulation due to exposure to solar ultraviolet radiation has been observed in several tree and crop species[6]. Increased exposure to solar ultraviolet radiation reduced the photosynthetic rate of many species and, in general, the reduction was more pronounced under growth chamber or greenhouse conditions than under field conditions[7]. Reduction in the rate of photosynthesis can result from damage to various molecular mechanisms of the photosynthetic machinery[8-9]. There is evidence that solar ultraviolet absorbing pigments have adaptive value in plants growing in regions of high solar ultraviolet radiation[9-10]. The defense mechanism of increasing solar

ultraviolet absorbing compounds partially neutralizes the harmful effects of solar ultraviolet radiation[10]. Solar ultraviolet radiation induces photo protection by increasing the production of compounds that strongly absorb solar ultraviolet radiation in leaf epidermal tissues[11]. Tropical plants receive much higher levels of ambient solar ultraviolet radiation than those growing in temperate regions[12]. The gradual reduction of solar ultraviolet radiation indicates the impact of sunflower plants on the level of biological activities and processes related to biophysics[13-14]. The primary objective of this study was to determine whether sunflower plants are sensitive to solar ultraviolet radiation by measuring its effects on growth and solar ultraviolet absorbing compounds[14-15].

EXPERIMENTAL

Sunflower seeds (*Helianthus annuus L.*) were planted in 50 pots filled with a special mixture of high-quality soil, vermiculite and peat. The plants were thinned to one per pot and were grown in a greenhouse at Hassiba BenboualI University under natural photoperiod between February and June 2016. The daily maximum and minimum temperatures were close to 24 and 20°C, respectively. The incoming solar ultraviolet radiation was provided from its main source during the daily period and for a period of approximately ten hours as an average time throughout the growth period of the studied sunflower plant. All measurements were performed on at least 5–7 individual plants per treatment. Treatments were compared using independent samples Student's t test at the 5% level (Microsoft Excel/PC 9.0 for Windows).

RESULTS AND DISCUSSION

Our descriptive study showed that solar ultraviolet radiation did not affect the biomass of sunflower plants grown in the greenhouse, regardless of the sampling period. Tissues that lack compounds that absorb more solar UVB may nevertheless have other protective mechanisms, such as epidermal wax and/or trachoma. Future studies should investigate the effects of solar UV radiation on alternative protection mechanisms of sunflower plants. Reduced growth is caused by leaf expansion, which is a result of the effects of solar ultraviolet radiation on the rate and duration of cell division and elongation of sunflower plants. While our study showed that the prominent effect of the sun's ultraviolet rays on the sunflower plant is the process of photosynthesis, which helped this plant to grow normally under normal conditions. The process of photosynthesis is considered the basic foundation for the growth of sunflowers and other plants. Biophysics and biochemistry study this phenomenon, each in its own field. For this purpose, we wanted to address in this study the benefit of the effect of ultraviolet solar rays on plants, especially sunflowers[15-16]. Sunflowers turn their faces to follow the path of the sun as it crosses the sky. But how does this happen, according to plant biologists? They use a new mechanism different from what was previously thought, according to many recent studies. Most plants exhibit phototropism, the ability to grow toward a light source. Botanists have hypothesized that the ability of sunflowers to follow the path of the sun depends on the ability of sunflowers to swing their heads. It has long been suggested that east–west oscillations in sunflower plants (Figures 1 and 2) lead to improved photosynthetic activity of upper leaves. In this study, the direct photon flux density coming from the sun source through the greenhouse and onto the surface of the upper leaves is not clear. To estimate the amount of photon exposure resulting from the sun's ultraviolet rays and the exchange of carbon dioxide resulting from photosynthesis in sunflower leaves, there are several methods according to many previous studies. Finally, our meta-study shows that the light-dependent CO2 uptake rate in the upper leaves of solar trackers can be improved. However, many open questions regarding the physiology and adaptive importance of heliotropism in the development of sunflower plants (Figure 1) remain unanswered. (1) How is night rerouting organized? (2) Do light-dependent movements of shoots and leave exhibit independent responses or coordinated processes? (3) Is heliotropism in sunflowers a blue light-mediated process, or are other photoreceptors involved? (4) What plant hormones are causally involved in growth redistribution leading to organ bending? (5) What are the sites of light perception? (6) Are solar movements of the stem and upper leaves true irreversible growth processes or, at least in part, swelling-driven nastastic bending responses? These and other questions must be answered before we can fully understand one of the most common physiological processes in the plant kingdom. In a comprehensive analysis of phototropism in angiosperms, Iino (2001) concluded that, with reference to work on sunflower, shade avoidance is the key process behind heliotropic movements. Our observations and measurements on stem and leaf phototropism in sunflower plants (Figures 1 and 2) do not add new insights on this topic. Nevertheless, we conclude that a photomorphogenic, photochromic-regulated shade-avoidance response is a major biological function of the heliotropic growth movements in sunflower plants, and not optimization of photosynthesis per [se] [16-17].

Fig.1: One of the stages of the sunflower plant

Fig. 2: Sunflower plant flower

CONCLUSIONS

In this study, enhanced solar ultraviolet radiation did not cause any damage to sunflower plants on the second sampling. This could be a consequence of leaf shading as plants developed during the period of rapid growth, leading to decreased levels and duration of exposure of lower leaves to solar ultraviolet radiation. Compared to the upper leaves[17]. These facts could contradict the harmful effects of increased solar ultraviolet radiation on plants[17-18]. Future studies should aim to investigate the effects of increased solar ultraviolet radiation at an early stage of sunflower development and should include the study of alternative defense mechanisms, such as epicuticular waxes, trachoma and antioxidants[18].

AUTHOR INFORMATION

Corresponding Author

*Maamar Boukabcha

Email address: m.boukabcha@univ-chlef.dz

ACKNOWLEDGMENT

The Authors thanks the General Directorate of Scientific Research and Technological Development in Algeria, the biology students of Hassiba Benbouali University of Chlef, Algeria, and all those who contributed directly or indirectly to the completion of this study.

REFERENCES

1. ALLEN, D.J. et al. Analysis of limitations to CO2 assimilation on exposure of leaves of two Brassica napus cultivars to UV-B. Plant Cell Environment, v.20, p.633-640, 1997.
2. ARNON, D.I. Copper enzymes in isolated chloroplasts. Polyphenol oxidases in Beta vulgaris. Plant Physiology, v.24, p.1-15, 1949.
3. Agrawal SB (1992). Effects of supplemental UV-B radiation on photosynthetic pigment, protein and glutathione contents in green algae. Environ. Exp. Bot., 32(2): 137-143.
4. Allen DJ, Nogues S, Baker NR (1998). Ozone depletion and increased UV-B radiation: is there a real threat to photosynthesis? J. Exp. Bot., 49: 1775–1788.
5. Al-Oudat M, Baydoun SA, Mohammad A (1998). Effects of enhanced UV-B on growth and yield of two Syrian crops wheat (Triticum durum) and broad beans (Vicia faba) under field conditions. Environ. Exp. Bot., 40: 11–16.
6. Barabas KN, Szegletes Z, Pestenacz A, Fulop K, Erdei L (1998). Effects of excess UV-B irradiation on the antioxidant defense mechanisms in wheat (Triticum aestivum L.) seedlings. J. Plant Physiol., 153: 146-153.
7. Barsig M, Malz R (2000). Fine structure, carbohydrates and photosynthetic pigments of sugar maize level under UV-B radiation. Environ. Exp. Bot., 43: 121–130.
8. Beggs CJ, Schenider-Ziebert U, Wellmann E (1986). UV-B and adaptive mechanisms in plants. In: Stratospheric Ozone Reduction, Solar Ultra-violet Radiation and PlantLife. (Edited by R. C. Worrest and M. M. Caldwell), Springer Verlag,Berlin. pp. 235-250.
9. Bjorn LO (1996). Effect of ozone depletion and increased UV-B on terrestrial ecosystems. Int. J. Environ. Stud., 51: 217-243.
10. Björn LO, Callaghan TV, Johnsen I (1997). The effects of UV-B radiation on European heathland species. Plant Ecol., 128: 252–264.
11. Bolhar-Nordenkampf HR, Quist G (1993). Chlorophyll fluorescence as a
12. tool in photosynthesis research. In Photosynthesis and Production

in a Changing Environment, pp. 193-207.

13. Bornman JF (1989). Target sites of UV-B radiation in photosynthesis of higher plants. J. Photochem. Photobiol., 4: 45-158.
14. Bouchereau A, Duhaze C, Martin-Tanguy J, Guegan JP, Larher F (1999). Improved analytical methods for determination of nitrogenous stress metabolites occurring in Limonium species. J. Chromatogr. A, 836: 209-221.
15. Braun J, Tevini M (1993). Regulation of UV-protective pigment synthesis in theepidermal layer of Rye seedlings (Secale cereale L.). Photochem.Photobiol., 57: 318-323.
16. Britt AB (1999). Molecular genetics of DNA repair in higher plants. Trends Plant Sci., 4: 20-25.H. Nasri. H. Shirzad, J HerbMed Pharmacol. 2013, 2-2, 21-22.
17. A. M.O. Ajasa, M.O. Bello.. A.O. Ibrahim. I.A. Ogunwande, N.O. Olawore, Heavy trace metals and macronutrients status in herbal plants of Nigeria. *Food Chem*, 2004, 85, 67–71.
18. K. Subramanian. D. Sankaramourthy. M. Gunasekaran, Toxicity studies related to medicinal plants, In: Natural products and drug discovery an integrated approach, 2018, *Elsevier Ltd*, 491-505

2023

Influence of the architecture's depth and data size on the model's performance for breast cancer classification

A.O. Meddas,[a] D. Jabri,[a] D.E.C. Belkhiat,[a]

[a] Laboratory of Dosing, Analysis and Characterization with High Resolution DAC HR, Ferhat Abbas University, Setif, Algeria

.

ABSTRACT: Deep leaning models have shown great promise in cancer detection and classification. They possess numerous advantages over previous methods; however, training well-rounded models is very difficult due to several obstacles, namely the data size and architecture depth. Although the technology and hardware have seen major developments in the last decade, the task still requires lots of data and deep network architectures. Convolutional Neural Networks (CNNs) are the most basic of feed forward deep learning architectures, their simple design and straightforward approach compared to more complex architectures makes them ideal for the conducted study as the influence of network depth and data augmentation is much more pronounced when working with CNNs. Our objective is to investigate the impact of the architecture's depth and data size on the model's performance for breast cancer classification. We compared between three models trained on the BreaKHis dataset, the first 2 models (model 1 and model 2) had more depth with 5 convolution layers to the model 3's 3 convolution layers, model 1 was trained using data augmentation and model 2 without data augmentation. Model 3 had the better accuracy between the three models, however, model 1 and model 2 had a better performance in terms of precision, recall and F1 score, with model 1 (using data augmentation) having the best results in these metrics than the other 2.

Keywords: Deep Learning; Breast Cancer; Cancer Classification; Convolutional Neural Networks

INTRODUCTION

Breast cancer early diagnosis through screening programs is the key to helping cancer patients overcome their disease[1]. However, the sheer number of participants requiring their medical images to be evaluated by a medical expert rendered the task nearly impossible to perform seamlessly. This necessitated the development of Computer Assisted Diagnosis (CAD) systems, using a machine learning approach at first and eventually substituting the latter for deep learning, to assist specialists and doctors[1].

CAD systems are used for medical image analysis tasks, mainly segmentation and, the focus of this study, classification[2]. With the latter task focusing on detecting lesions within the breast images and classifying them as either malignant (cancer) or benign (non-cancer)[2]. Spawning from the same base architecture, models are designed with some minor modifications to tweak the performance to better suit the task and the means available. Alongside these modifications, there's also data augmentation methods to help with the training of a model, leading to an overall better performance[2]. Therefore, just how much can these two factors (architecture depth and data augmentation) influence a model's overall performance for breast cancer classification?

EXPERIMENTAL

Convolutional Neural Networks (CNNs) play a crucial role in numerous deep learning applications, particularly in the field of computer vision[2]. Their ability to extract features makes them

highly adaptable and versatile. Today, there are various CNN-based architectures with different underlying philosophies, and when implemented properly, many of these modern architectures outperform a standard CNN. However, due to the design of these architectures, which allows for the addition of convolution layers without sacrificing efficiency, the impact of network depth is not as significant as it is with a standard CNN.

This is the reason why for this study we only consider and compare the results from standard CNN-based models.

Dataset

The BreaKHis dataset[5] (Table 1) is a collection of histopathological breast tissue images acquired through Surgical Open Biopsy (SOB) from a total of 82 patients. The dataset contains 7909 images divided into 2 classes (Benign and Malignant), and each class is divided into 4 subclasses each. The dataset provides the images at different magnification level (x40, x100, x200 and x400) which results in an overall well diversified dataset for breast cancer classification training.

Table 1. BreaKHis Dataset Summary[1]

Magnification	Benign	Malignant	Total
40x	625	1,370	1,995
100x	644	1,437	2,081
200x	623	1,390	2,013
400x	588	1,232	1,820
Total	**2,480**	**5,429**	**7,909**
# Patients	**25**	**58**	**82**

Compared Models

To thoroughly examine the effect of architecture depth, we have conducted a comparison between standard CNNs where three models were evaluated. The first (model 1) and second (model 2) models (shown in figure 1) are based on a CNN architecture consisting of 5 convolutional layers, 3 pooling layers, and 2 fully connected layers for classification [3]. Model 1 was trained with data augmentation, while model 2 was trained without data augmentation[3]. The third model (model 3, shown in figure 2) employs a CNN architecture with 3 convolutional layers, 3 pooling layers, and 3 fully connected layers[4]. Similarly, model 3 was trained without data augmentation[4]. More information on the three models is available on Tables 2 and 3.

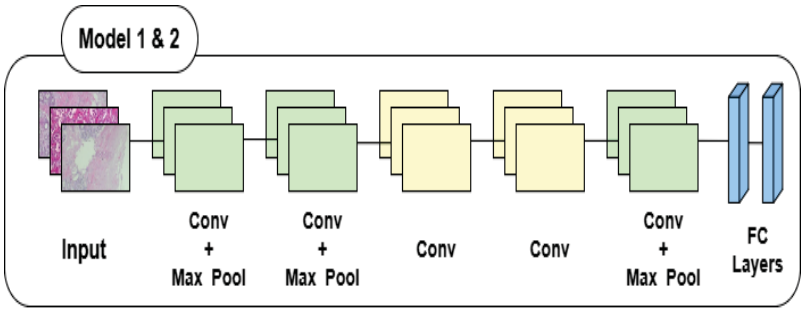

Fig. 1: Models 1 & 2 Design

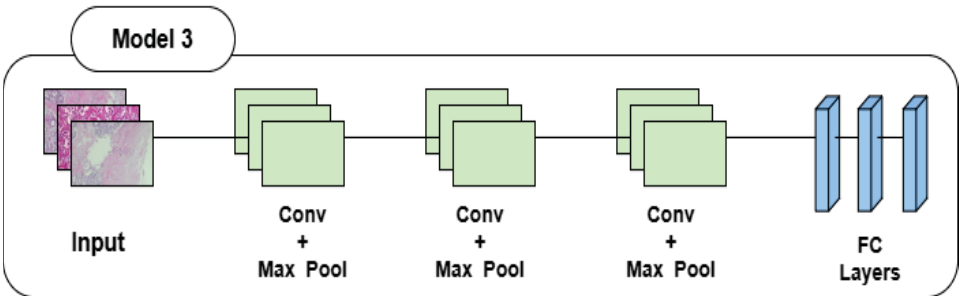

Fig. 2: Model 3 Design

Table 2. Models 1 & 2 Specifications

Model	Author	Layers					
Model 1 & Model 2	Bardou et al.	Type	Conv + Max Pool	Conv + Max Pool	Conv	Conv	Conv + Max Pool	FC
		Channels	64	96	128	256	256	2000, 2
		Filter Size	3x3	3x3	3x3	3x3	3x3	
		Pooling Size	3x3	3x3			3x3	
		Pooling Stride	2x2	2x2			2x2	

Table 3. Model 3 Specifications

Model	Author	Layers				
Model 3	Dabeer et al.	Type	Conv + Max Pool	Conv + Max Pool	Conv + Max Pool	FC
		Channels	32	64	128	64, 64, 2
		Filter Size	5x5	5x5	5x5	
		Pooling Size	3x3	3x3	3x3	
		Pooling Stride	1x1	1x1	1x1	

Table 4. Comparison Results of the Three Models

N°	Model	Performance			
		Accuracy	Recall	Precision	F1 Score
1	Model 1	96.53%	97.58%	97.38%	97.47%
2	Model 2	94%	/	/	/
3	Model 3	99.86%	93%	93%	93%

RESULTS AND DISCUSSION

The results of each model's performance is shown in Table 4. The performance of the different models was assessed based on some quantitative metrics. Model 1 (with data augmentation) achieved a better accuracy (96.53%) than model 2 (94.26%) (without data augmentation)[3]. However, model 3, based on a different architecture and trained without data augmentation, provided the best accuracy (99.86%)[4]. Furthermore, model 1 showed overall better results in terms of F1 score (97.47% opposed to 93%), Precision (97.38% opposed to 93%) and Recall (97.58% opposed to 93%) when compared with model[3-4]. Note that, accuracy alone isn't sufficient as an evaluation metric, nor is it dependable due to the occurrence of overfitting in smaller data sets.

While model 3 makes use of larger convolution filter sizes (meaning it has a larger receptive field), model 1 still outperformed it in terms of recall and precision, which reflects the importance of architecture depth. Model 1 sacrificed the larger receptive fields for more hierarchical feature extraction, which provided higher level feature maps.

As for data augmentation, model 1 employed a series of geometrical transformations such as rotations (90, 180 and 270) and horizontal flipping, which not only provided more data for the model to train on, but it helped significantly in improving the model's ability to generalize its outcome over the data and avoid overfitting.

CONCLUSIONS

In this work, we compared between similar CNN architectures that were trained on the BreaKHis dataset with the main focus being the influence of data augmentation and architecture depth. We proceeded by highlighting the differences in training approach between three models and establish a relation between the outcomes of the models and influence depth as well as data

augmentation. As a result, model 3 performed best in terms of accuracy (99.86%), but model 1 outperformed model 3 in terms of precision (97.38%) and most importantly recall (97.58%) and it also outperformed model 2 in terms of accuracy (96.53% to 94.26%) which doesn't employ data augmentation. Therefore, the deeper the network is, the better is the overall performance of the network. Even when spatial context was better captured with higher receptive fields, more depth provided better results. We can also conclude that data augmentation is a net positive during a network's training process granted that the training data is augmented to reasonable sizes.

AUTHOR INFORMATION

Corresponding Author

*Ahmed Omrane Meddas

Email address: omrane.meddas39@gmail.com

REFERENCES

1. World Health Organization [WHO], 2022.
2. Khan, S., Rahmani, H., Shah, S. A. A., & Bennamoun, M. (2018). *A Guide to Convolutional Neural Networks for Computer Vision*. (Synthesis Lectureson Computer Vision; Vol. 8, No. 1). Morgan & Claypool Publishers. https://doi.org/10.2200/S00822ED1V01Y201712COV015.
3. Bardou, D., Zhang, K., & Ahmad, S. M. (2018). Classification of breast cancer based on histology images using convolutional neural networks. Ieee Access, 6, 24680-24693.
4. Dabeer, S., Khan, M. M., & Islam, S. (2019). Cancer diagnosis in histopathological image: CNN based approach. Informatics in Medicine Unlocked, 16, 100231.
5. F. A. Spanhol, L. S. Oliveira, C. Petitjean, and L. Heutte, "Breast cancer histopathological image classification using convolutional neural networks," in 2016 international joint conference on neural networks (IJCNN). IEEE, 2016, pp. 2560–2567.

2023

X-ray Tomography Reconstruction Using TIGRE

M.L. Yahiaoui,[a,*] O. Dendene,[a] A. Bourenane,[a] L. Boukerdja,[a] F. Kharfi,[b]

[a] Nuclear Research Centre of Birine, Djelfa-17200, Algeria

[b] Department of Physics, Ferhat Abbas-Setif1 University, Setif-19000, Algeria

ABSTRACT: This study investigates the performance of four different reconstruction algorithms - FDK (Feldkamp-Davis-Kress), CGLS (Conjugate Gradient Least Squares), LSMR (Least Squares Minimum Residual), and MLEM (Maximum Likelihood Expectation Maximization) in the context of 3D X-ray imaging. Using the TIGRE (Tomographic Iterative GPU-based Reconstruction) toolkit, these algorithms were applied to the SophiaBeads dataset, a resource specifically developed for testing and comparing reconstruction methods in X-ray computed tomography. Our findings indicate that despite the FDK algorithm is simple and fast, the LSMR algorithm provides height detail sharpness, good measurement and low noise. While CGLS and MLEM provide more or less good object detail separations, proving to be more effective in handling noise and artifacts. Future studies might delve into optimizing algorithm parameters to improve the quality of reconstruction.

Keywords: X-ray Computed Tomography, TIGRE Toolkit, Reconstruction algorithms, SophiaBeads dataset.

INTRODUCTION

Three-dimensional (3D) X-ray imaging has known a revolutionary development in several fields, ranging from medicine and biology to engineering and archaeology. It offers unprecedented three-dimensional visualization of the internal structures of objects and organisms, enabling non-destructive inspection. The recent integration of 3D X-ray imaging systems in industrial and research facilities has increased the need for efficient and accurate reconstruction algorithms to convert the acquired data into meaningful images.

Reconstruction algorithms play an essential role in the 3D X-ray imaging process as they transform the projection data collected by the imaging system into a 3D representation of the scanned object. A wrong choice of the reconstruction algorithm can significantly affect the quality of the reconstructed image and, therefore, the accuracy of the subsequent analysis.

This paper focuses on a comparative study of four reconstruction algorithms - FDK (Feldkamp-Davis-Kress)[1], CGLS (Conjugate Gradient Least Squares)[2], LSMR (Least Squares Minimum Residual)[3], and MLEM (Maximum Likelihood Expectation Maximization)[4]. These algorithms were applied to the SophiaBeads dataset using the TIGRE (Tomographic Iterative GPU-based Reconstruction) toolkit[5].

The aim of this study is to assess the performance of these reconstruction algorithms in terms of 2D reconstructed image quality.

METHODS

The study made use of the SophiaBeads dataset and the TIGRE toolkit to apply and compare the FDK, CGLS, LSMR, and MLEM reconstruction algorithms.

SophiaBeads Datasets

The SophiaBeads dataset[6-8], developed specifically for testing and comparing X-ray computed tomography reconstruction methods, served as our data source. The dataset is a scan of a plastic tube filled with uniform Soda-Lime glass beads (SiO2-Na2O), offering

a complex yet regular internal structure that is ideal for evaluating reconstruction algorithms. The sample was scanned by 512 projections under consistent conditions across datasets. Figure 1 shows one projection image from the SophiaBeads dataset.

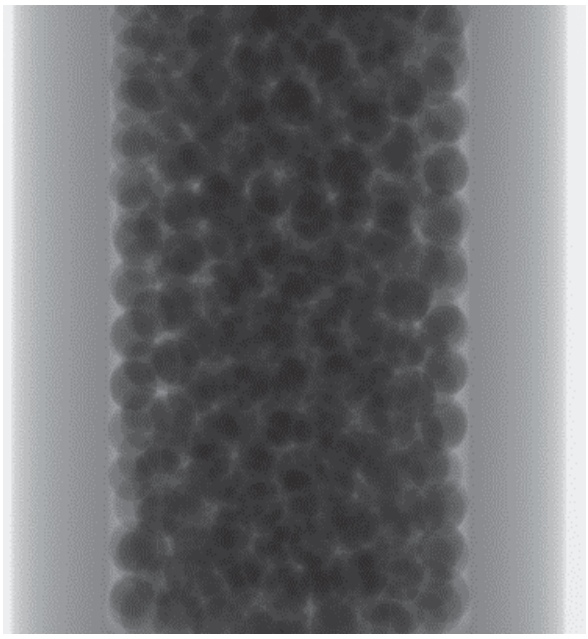

Fig. 1: Projection image from the SophiaBeads dataset

TIGRE Toolkit

We utilized the TIGRE (Tomographic Iterative GPU-based Reconstruction)[9] toolkit for our image reconstruction analyses. TIGRE is an open-source toolbox dedicated to computer-aided tomography, designed to be both flexible and efficient. It enables users to easily test new reconstruction methods while leveraging the power of modern GPUs. TIGRE offers a variety of reconstruction algorithms, from analytical methods like FDK to iterative methods like CGLS, LSMR, and MLEM. These algorithms can be easily applied to the data, with numerous options for adjusting the reconstruction parameters and visualizing the results.

Algorithms of Reconstruction

For this study, we chose to compare four distinct reconstruction algorithms: FDK (Feldkamp-Davis-Kress), CGLS (Conjugate Gradient Least Squares), LSMR (Least Squares Minimum Residual), and MLEM (Maximum Likelihood Expectation Maximization). Each of these algorithms offers a unique approach to image reconstruction from computer-aided tomography data. The FDK algorithm is an analytical reconstruction method designed for cone tomography. In contrast, CGLS, LSMR, and MLEM are iterative reconstruction algorithms. This means they do not directly compute the solution but rather refine an initial estimate step-by-step until a satisfactory result or convergence is achieved.

Specifically, these iterative algorithms, namely CGLS, LSMR, and MLEM, continuously refine the image estimate to reduce the disparity between the measured projection data and the projection data simulated from the current image estimate. The aim is to ensure that the reconstructed image, when projected, would closely match the actual measured data.

Of these iterative methods, MLEM stands out as it incorporates a statistical model of the data acquisition process. While CGLS and LSMR primarily focus on minimizing the algebraic difference between measured and estimated data, MLEM considers the inherent randomness and noise in the data. It uses a probabilistic approach, optimizing the likelihood that the simulated data from the current image estimate would give rise to the observed measurements, given the statistical nature of the acquisition process.

Our data preparation and analysis were conducted on a high-performance HP Z8 workstation, which allowed efficient and accurate analysis through modern high-performance computing technologies.

RESULTS AND DISCUSSION

Our analysis of the four reconstruction algorithms - FDK, CGLS, LSMR, and MLEM - produced a variety of notable results, allowing for a thorough evaluation of each method's performance.

The reconstructed images from each algorithm provided a direct visualization of their capabilities to reconstruct the internal structure of the sample from the projection data. Figure 2 shows the reconstructed images obtained from each algorithm. On visual inspection, it appears that while the FDK algorithm provides a clear overview of the structure with good resolution, the CGLS, LSMR, and MLEM algorithms also seem to offer less noisy results.

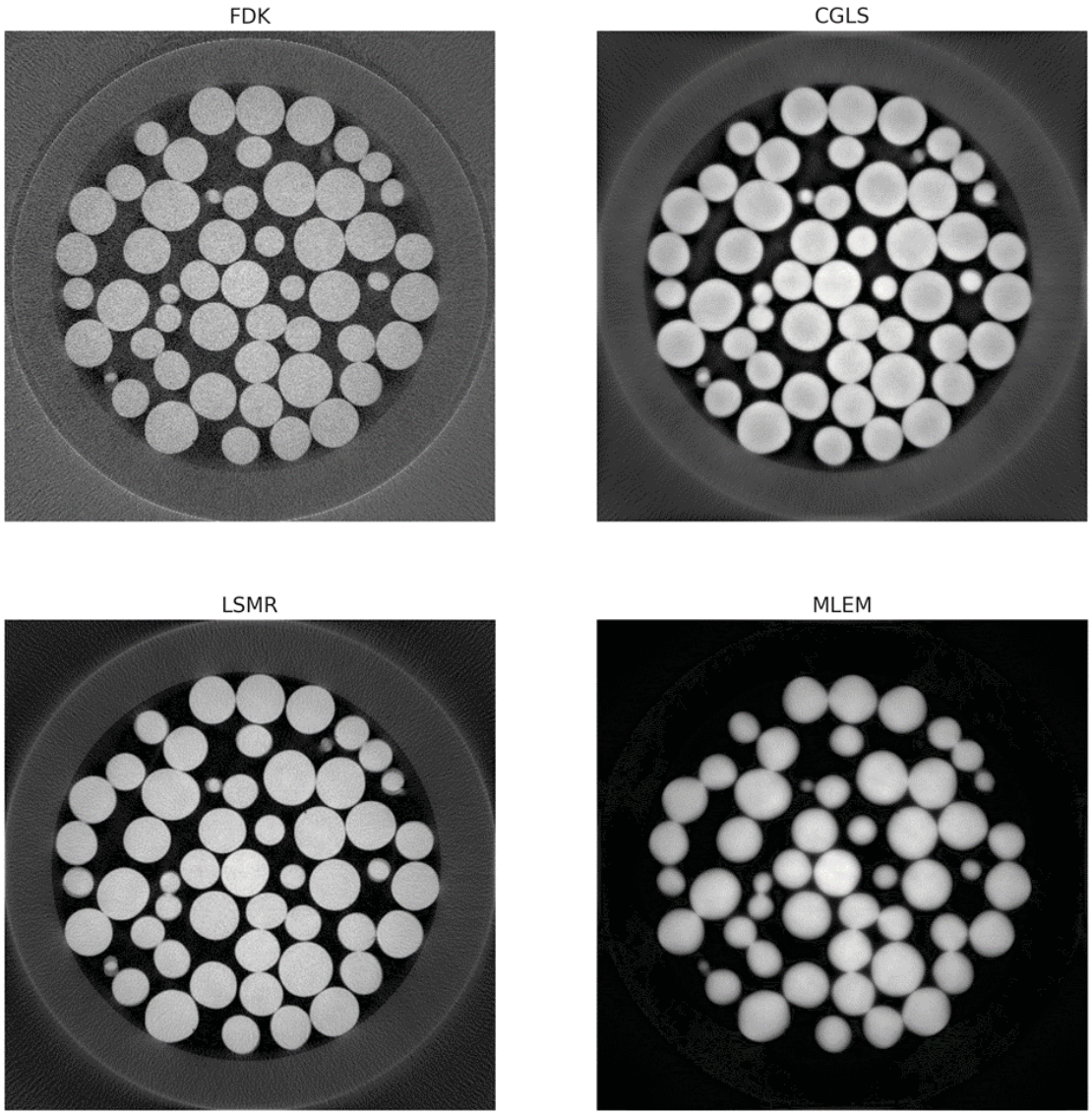

Fig. 2: Reconstructed images obtained by studied algorithms

Diving deeper into the quantitative attributes, Figure 3 showcases line profile graphs, which offer insights into the spatial resolution across the reconstructed images. The sharper transitions exhibited by the CGLS, LSMR, and FDK algorithms underscore their proficiency in capturing fine details, rendering them superior in terms of spatial resolution compared to the MLEM algorithm. The latter, however, stands out in its ability to suppress noise, an attribute that can be paramount for certain applications.

Further elucidation is provided by the pixel intensity histograms in Figure 4. These histograms shed light on the contrast dynamics of the reconstructed images. Notably, the CGLS and LSMR algorithms demonstrate a more pronounced separation between the glass beads and the plastic tube intensities, suggesting their adeptness at delineating different materials. In contrast, the FDK and LSMR histograms reveal an overlap in the pixel intensities of the plastic and the void, which could pose challenges during segmentation tasks. The MLEM algorithm, despite its underwhelming performance in representing the glass beads, presents a redeeming quality by distinctly portraying the plastic, showing slight separation from the void.

Figure 5 zooms in on a 100x100 pixels window at the center of each reconstructed image, offering a closer look at the detail sharpness. The reconstruction algorithms FDK and LSMR appear to produce sharper images than CGLS and MLEM

algorithms, further supporting the quantitative evaluations showed in Figure 3.

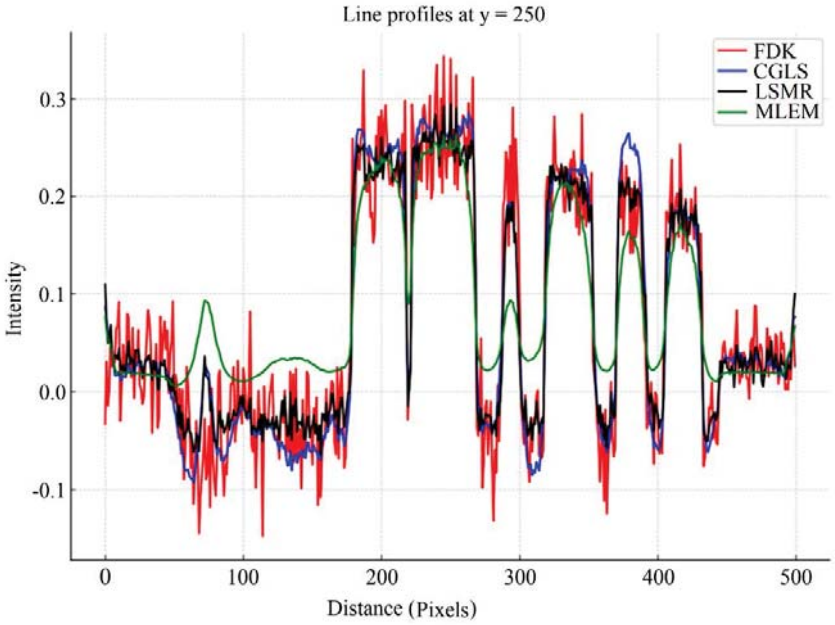

Fig. 3: Line profiles for each reconstruction algorithm

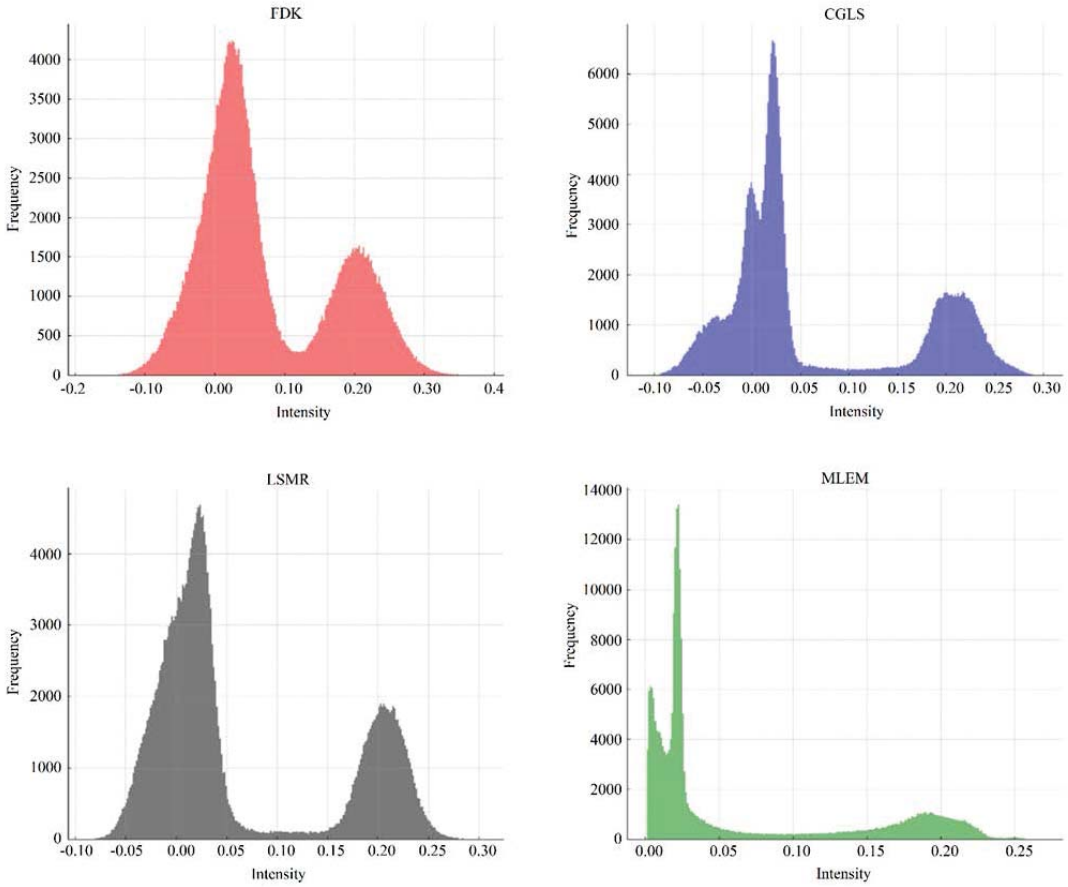

Fig. 4: Pixel intensity histograms for each reconstruction algorithm

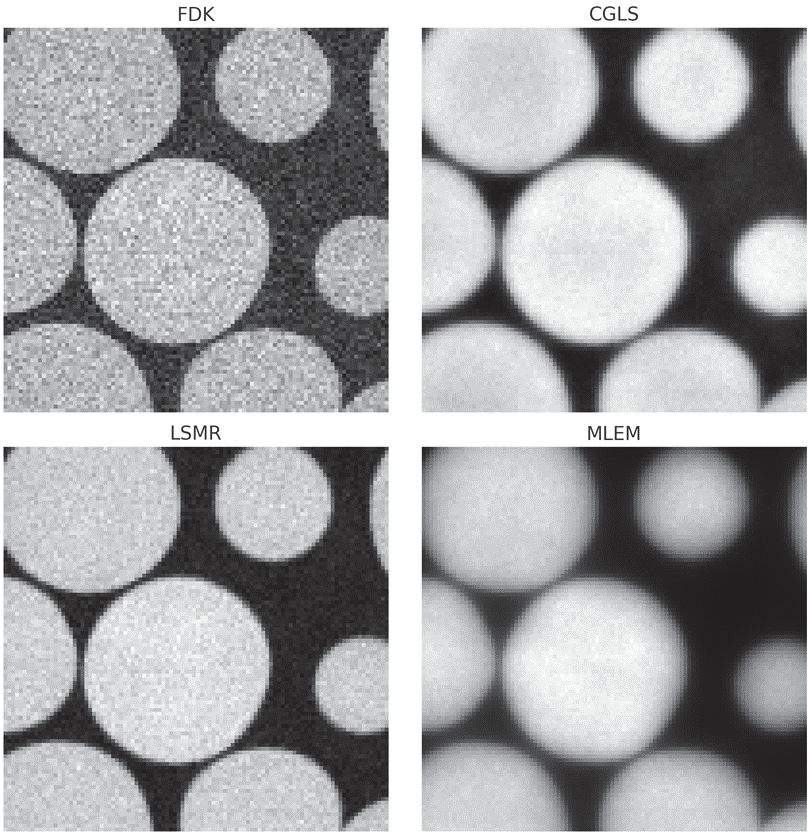

Fig. 5: Zoom (100 pixels x 100 pixels window in the center of each image) on the images reconstructed by studied algorithms

Furthermore, our study incorporated a statistical analysis of pixel intensities in the reconstructed images, as presented in Table 1. The analysis of pixel intensities is paramount as it mirrors the physical properties, such as attenuation coefficients, which are essential for interpreting images in tomography. Even though the average pixel intensity values for the different algorithms are relatively close, these slight variations can have substantial implications on the image quality, especially when assessed in conjunction with the standard deviation. For instance, the FDK displays the highest mean value and the largest standard deviation, indicating a more significant variability in pixel intensities. This could translate to a superior delineation of object details compared to other algorithms. However, LSMR and MLEM, with their marginally reduced standard deviations, might offer enhanced performance in terms of noise reduction, even though the difference between FDK and CGLS is subtle.

Table 1. Descriptive statistics of pixel intensities for each reconstruction algorithm

Statistic	FDK	CGLS	LSMR	MLEM
Count	250000	250000	250000	250000
Mean	0.072218	0.063639	0.064980	0.065388
Standard Deviation	0.096188	0.096144	0.093083	0.074485
Minimum	-0.181705	-0.108001	-0.087765	0.000892
25%	0.004615	-0.000298	-0.001081	0.015317
50%	0.039362	0.022439	0.023612	0.023018
75%	0.164413	0.178406	0.179257	0.128712
Maximum	0.384844	0.298797	0.304676	0.268748

For the studied object, the results of our study suggest that while the FDK algorithm is simpler, LSMR might give higher quality of measure, offering a better balance between detail sharpness, and noise handling. However, the choice of the reconstruction algorithm should be based on the type of object to be explored and the specific requirements of the application, considering both the quality of the reconstructed image and the computational efficiency.

CONCLUSIONS

The present study, aimed to provide a comparative analysis of four reconstruction algorithms - FDK, CGLS, LSMR, and MLEM in the context of 3D X-ray imaging. Our findings highlighted distinct strengths and weaknesses of each algorithm, offering valuable insights into their applicability in different settings.

While the FDK algorithm's simplicity, superior detail sharpness and speed are attractive, our results suggest that LSMR algorithm offer height detail sharpness and good attenuation coefficient measurement, proving more effective in handling noise and artifacts. Depending on the internal composition of the object to be studied, LSMR and MLEM algorithms could offer a good segmentation and separation of the different details of the object. These observations were supported by both visual inspection and quantitative analysis of the reconstructed images.

The results of this study underscore the importance of ongoing research in the field of 3D X-ray imaging, particularly in the area of algorithm development and optimization. Future research could explore the optimization of algorithm parameters and the testing of these algorithms with multiple datasets, potentially enhancing the quality of reconstruction and pushing the boundaries of what can be achieved with 3D X-ray imaging.

AUTHOR INFORMATION

Corresponding Author

*Mohamed Laid Yahiaoui

Email address: laidastro@hotmail.fr

REFERENCES

1. Xue, L., Suzuki, H., Ohtake, Y., Fujimoto, H., Abe, M., Sato, O., & Takatsuji, T. Numerical analysis of the feldkamp–davis–kress effect on industrial X-ray computed tomography for dimensional metrology.2015, *Journal of Computing and Information Science in Engineering*, 15(2), 021008.
2. May, K. H., Keil, A., Von Freymann, G., & Friederich, F. The conjugate gradient least square algorithm in terahertz tomography. 2021, *IEEE Access*, 9, 142168-142178.
3. Chillarón Pérez, M., Vidal, V. E., Verdú, G. J., & Quintana-Ortí, G. Few-View CT Image Reconstruction via Least-Squares Methods: Assessment and Optimization. 2023, *Nuclear Science and Engineering*, 1-14.
4. Prakash, J., Agarwal, U., & Yalavarthy, P. K. Multi GPU parallelization of maximum likelihood expectation maximization method for digital rock tomography data. 2021, *Scientific Reports*, 11(1), 18536.
5. Biguri, A., Dosanjh, M., Hancock, S., & Soleimani, M. TIGRE: a MATLAB-GPU toolbox for CBCT image reconstruction. 2016, *Biomedical Physics & Engineering Express*, 2(5), 055010.
6. Coban, S. B. SophiaBeads datasets project documentation and tutorials. 2015, *MIMS Eprints*.
7. Coban, S. B., Withers, P. J., Lionheart, W. R. B., & McDonald, S. A. When do the iterative reconstruction methods become worth the effort. 2015.
8. Coban, S. B. SophiaBeads dataset project codes. https://zenodo.org/record/16474#.Y-DIutLMJH4
9. Biguri, A. Iterative GPU-based Reconstruction Toolbox. European Organization for Nuclear Research, TIGRE: Tomographic Iterative GPU-based Reconstruction Toolbox, https://github.com/CERN/TIGRE

2023

The impact of additional filtration on patient radiation dose in diagnostic radiology

A. Benaidja [a,*], N. Ounoughi [a], F. Kharfi, [b]

[a]Laboratory Of Radiation Physics And Applications, Faculty of Exact and Computer Sciences, University of Jijel, Jijel-18000, Algeria.

[b]Dosing, Analysis, and Characterization with high resolution Laboratory (LDAC), Department of Physics, University of Ferhat Abbas-Setif1, Algeria

ABSTRACT: In diagnostic radiology, the radiation exposure of a patient is performed by keeping the dose received by the patient as low as reasonably achievable (ALARA). Additional X-ray beam filtration is a solution that may contributes to enhance the beam quality and to reduce patient dose. The added filtering material type and its thickness play an important role to achieve optimally this goal. In this work many type of X-ray filtration are simulated by Monte Carlo method. Obtained results demonstrate well that it is possible to reduce dose received by patients and staff in diagnostic radiology by using thin filtration made from Tantalum, Tungsten, or Gold. It was, particularly, found that Tantalum filters could significantly reduce the dose due to scattered radiation and improve image quality without compromising diagnostic accuracy. Moreover, Tantalum filters do not constitute any significant risks to patients and their use is cost-effective.

Keywords: Diagnostic radiology, Additional filter, Radiation dose, Monte Carlo simulation.

INTRODUCTION

Diagnostic radiology plays a pivotal role in modern healthcare, providing invaluable information for the diagnosis and treatment of various medical conditions. It employs ionizing radiation, such as X-rays, to produce detailed images of the human body. While diagnostic radiology has revolutionized medical practice, concerns about patient radiation dose have always been at the forefront of discussions surrounding its safety. In recent years, the focus has shifted towards the impact of additional filtration on patient radiation dose in diagnostic radiology.

Radiation exposure is an inherent part of diagnostic radiology, and it is essential for obtaining high-quality images. However, excessive radiation exposure can lead to adverse effects, including an increased risk of cancer and tissue damage. To mitigate these risks, healthcare providers have been exploring various strategies to optimize radiation dose while maintaining diagnostic image quality. One such strategy is the use of additional filtration in the X-ray beam.

Additional filtration involves the insertion of filters, such as aluminum or copper, into the X-ray tube. These filters absorb low-energy photons, resulting in a higher mean energy of the X-ray beam. The primary objective is to enhance the diagnostic quality of the images and, concurrently, reduce the radiation dose delivered to the patient.

This topic is of significant interest because it presents a delicate balance between diagnostic accuracy and patient safety. On one hand, improved image quality can lead to more accurate diagnoses, potentially reducing the need for additional procedures and their associated risks. On the other hand, optimizing radiation dose by incorporating additional filtration can lower the long-term radiation risk to the patient, contributing to safer medical practices.

This introduction sets the stage for a comprehensive discussion on the impact of additional filtration on patient radiation dose in

diagnostic radiology. We will explore the principles of additional filtration, its potential benefits, challenges, and the ongoing efforts to strike the right balance between diagnostic accuracy and patient safety in the field of radiology. Understanding the implications of additional filtration is crucial in ensuring that diagnostic radiology continues to provide the maximum benefits to patients while minimizing their exposure to ionizing radiation. .

The elimination of the X photons of low energy from the spectrum by the additional filtration is an essential element, both for the radiation protection of patients and for the quality of the image. The objective of this work is to study the effectiveness of additional X-ray beam filtering by different materials on the reduction of the absorbed dose.

EXPERIMENTAL

The aim of this study was to investigate the effect of some materials, like tantalum, tungsten, or gold, used in thin additional filtration on the x-ray spectrum by means of Monte Carlo simulation.

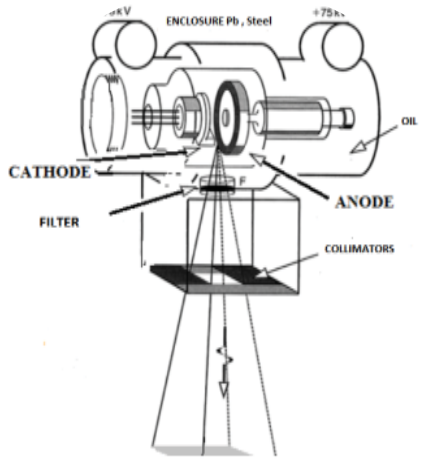

Fig.1: X-ray tube

The additional tantalum filter has been shown to improve image quality in various radiographic explorations, including chest, abdominal, and pelvic radiography. By reducing scatter radiation, the filter enhances the differentiation between different tissues, allowing for clearer and more detailed images. This is particularly useful in exams where the contrast between tissues is critical, such as in the detection of lung nodules or abdominal masses.

The X-ray tube with tungsten anode and additional filter was modeled by Monte Carlo simulation (code PENELOPE). The typically utilized additional filtration is based on aluminum. The simulation can predict the X-ray spectrum after passing filters of different materials W, Au, Ta and radiation dose in a cranium phantom.

RESULTS AND DISCUSSION

Additional filtration is used to increase the average energy of the polychromatic X-beam, and to eliminate low energy photons unable to reach the film, but of sufficient energy to reach and unnecessarily irradiate the patient. The all-purpose filter is made of aluminum, which is a great filter for low-energy photons before they reach the patient. According to results of Figure 2, 2 mm of Al absorbs all photons with energies below 20 keV. A thickness of more than 3 mm does not bring any advantage, because there is absorption of photons of greater energy, which requires an unconsidered increase in the exposure time.

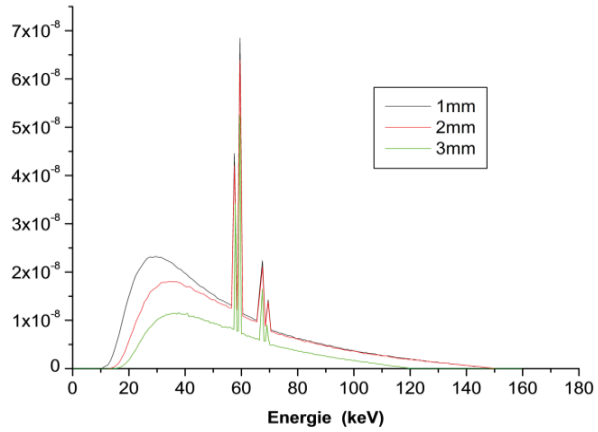

Fig.2: The effects of the thickness filtration (aluminum) on the X ray spectrum

The NCRP (National Council on Radiation Protection and Measurements) has established the following recommendations regarding total filtration (inherent + additional): *below 50keV: 0.5mm Al, between 50 and 70 keV: 1.5mm Al and Above 70 keV: 2.5mm Al.* Potential disadvantages for using aluminum as additional filters: Although aluminum is a light and economical material, it can be relatively fragile and easily damaged. Additionally, aluminum can chemically react with certain types of liquids or gases, which can reduce its effectiveness as a filter. Using filters made of different materials *such as aluminum, tungsten, gold or tantalum* in radiology has been a subject of much interest in recent years due to their ability to improve image quality while reducing radiation exposure. The spectrum

of x-rays after different filters is well illustrated in the figure below.

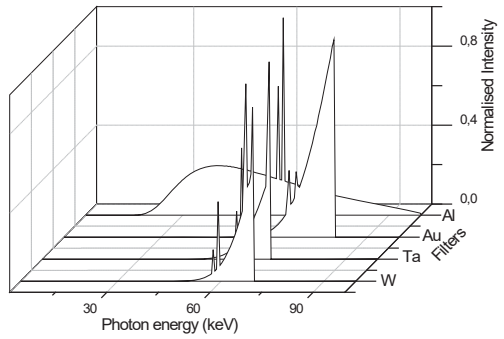

Fig.3: X-ray spectrum after Aluminum, gold, tungsten and tantalum filtration

We notice, when replacing the Al filter with a Au, W or Ta filter, a large part of X photon with a lower energy base of 50keV are eliminated, these photons do not participate in the formation of the radiographic image because these photons are absorbed in the human body, but they participate in dose deposition, so the Ta filter minimizes the deposited dose received by the patient during radiology. We also note that the Ta filter eliminated X photons for an energy greater than *70keV*, which scatter before waiting for the X-ray film. These photons are detrimental to the formation of images (image blur) and contribute to a dose deposit in the patient as well as in the operator. The elimination of these photons improves the radiographic image and minimizes the dose received by the patient and the operator. The geometry used for the simulation of the radiation dose in a cranial phantom is illustrated in the figure 4.

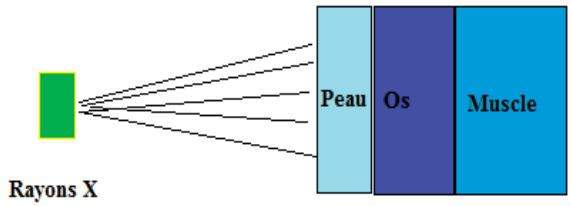

Fig.4: The geometry used for the simulation of the radiation dose in a cranial phantom

It is important to note that the change of filter material plays an important role on the distribution of the dose in depth and therefore on the dose delivered to the patient.

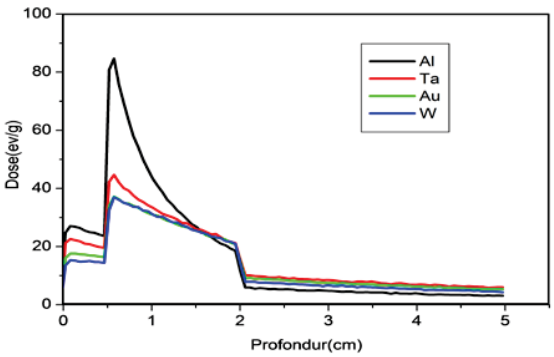

Fig.5: The dose in depth in a cranial phantom

Despite the good results obtained by Al, Au and W, the Ta is the best choice in reality for the following reasons: The Tungsten is a very dense and tough material but it can be very expensive and difficult to work with. Additionally, it can be susceptible to corrosion and other types of damage which can shorten its life and its effectiveness as a filter. Gold is a precious metal with high density, its use as an additional filter may be l expensive. As well as the gold has high reflectivity, this can cause X-rays to reflect, resulting in loss of image quality and increased radiation dose to the patient. While Tantalum is a hard material that is highly resistant to corrosion and mechanical damage, making it an excellent choice for filters.

CONCLUSIONS

Thus study shows clearly that It is possible to reduce doses to patients and staff in diagnostic radiology by using thin filtration made of Tantalum, Tungsten, or Gold. Several studies have investigated the effectiveness and safety of the additional Tantalum filter in radiology. The results suggest that the use of Tantalum filters can significantly reduce the dose received by the patient due to the scattered radiation without affecting the image quality or compromising the diagnostic accuracy. Moreover, Tantalum filters do not induce any significant risk to patients and their use is cost-effective.

AUTHOR INFORMATION

Corresponding Author

*Asma Benaidja

Email address: asma.benaidja@univ-jijel.dz

REFERENCES

1. Eunhye Kim, Kenzo Muroi, Takahisa Koike and Jungmin Kim. Dose Reduction and Image Quality Optimization of Pediatric Chest Radiography Using a Tungsten Filter, 2022. Bioengineering 2022, 9, 583.

2. Hiroki Kawashima, Katsuhiro Ichikawa , Daisuke Nagasou , Masayuki Hattori. X-ray dose reduction using additional copper filtration for abdominal digital radiography: Evaluation using signal difference-to-noise ratio, 2017. j.ejmp.2017.01.015

3. Ji Sung Jang, Hyung Jin Yang, Hyun Jung Koo, Sung Ho Kim, Chan Rok Park, Suk Hwan Yoon, So Youn Shin, Kyung-Hyun Do, Image quality assessment with dose reduction using high kVp and additional filtration for abdominal digital radiography, 2018. Physica Medica 50 (2018) 46–51

4. Taku Kuramoto , Shinya Takarabe , Kenshi Shiotsuki , Yusuke Shibayama , Hiroshi Hamasaki , Hiroshi Akamine , Kazutoshi Okamura , Toru Chikui , Toyoyuki Kato , Kazunori Yoshiura. X-ray dose reduction using additional copper filtration for dental cone beam CT, 2021. Physica Medica 81 (2021) 302–307

5. Ernest U. Ekpo, Alishja C. Hoban, Mark F. McEntee. Optimisation of direct digital chest radiography using Cu filtration, 2014. Radiography 20 (2014) 346e350

6. M. A. Staniszewska, T. Biegan´ski, A. Midel and D. Baran´ska. Filters for dose reduction in conventional x ray examinations of children radiation protection dosimetry, 2000. vol. 90, nos 1–2, pp. 127–133 (2000)

7. Marie-Louise Butler, BSca, and Prof. Patrick C. Brennan, PhDa. Nonselective Filters Offer Important Dose-Reducing Potential in Radiological Examination of the Paediatric Pelvis, 2009. Journal of Medical Imaging and Radiation Sciences 40 (2009) 15-23.

2023

Retinal Vessel Segmentation: Overview, Challenges and the Future

I. Mehidi,[a,b]* D. Jabri,[b] D.E.C. Belkhiat, [a,b]

[a] Department of Physics, Faculty of Sciences, Ferhat Abbas University, 19000, Setif, Algeria.

[b] Laboratory of Dosing, Analysis and Characterization with High Resolution DAC HR, Ferhat Abbas University, Setif, Algeria.

ABSTRACT: Retinal vessel segmentation is vital in medical image analysis, providing crucial insights for diagnosing and managing eye diseases like diabetic retinopathy, hypertension-related issues, and age-related macular degeneration. These conditions can cause irreversible vision impairment if not promptly detected. However, segmenting retinal vessels from fundus images is challenging due to factors like image noise, varying vessel characteristics, and the presence of anatomical structures. This paper offers a comprehensive overview of current segmentation methods, analyzing strengths and weaknesses. It emphasizes persistent challenges, such as image quality issues, driven by factors like resolution and lighting conditions. With a growing demand for real-time solutions, the pursuit of effective segmentation remains critical, especially in clinical settings. While deep learning shows promise, addressing remaining obstacles requires ongoing research. Despite progress, the quest for improved retinal vessel segmentation methods remains dynamic and essential in medical imaging and ophthalmology.

INTRODUCTION

The human eye is a remarkable organ, capable of capturing intricate details of the world around us. Among its many components, the retina plays a pivotal role in translating light into meaningful visual information. Within this delicate layer of tissue lies a complex network of blood vessels that nourish the retina and are integral to its functioning. The analysis of these retinal vessels has emerged as a critical field in medical imaging, with profound implications for the diagnosis and management of various ocular and systemic diseases.

Retinal vessel segmentation, a process aimed at delineating these intricate blood vessels from retinal images, has garnered significant attention in the realms of ophthalmology, medical imaging, and artificial intelligence. It is a fundamental step in the analysis of retinal images and plays a vital role in the early detection and monitoring of conditions such as diabetic retinopathy, hypertension, and cardiovascular disease. By automating the segmentation of retinal vessels, clinicians can make more accurate diagnoses, track disease progression, and tailor treatment plans to individual patients' needs[1-5].

This article provides a comprehensive exploration of retinal vessel segmentation, delving into its historical evolution, the fundamentals of the process, the transition from traditional techniques to cutting-edge machine learning and deep learning methods, and the associated challenges and opportunities. Moreover, it discusses the recent advances that have propelled this field to new heights and contemplates the exciting future that awaits, where retinal vessel segmentation stands poised to revolutionize medical diagnostics and patient care.

FUNDAMENTALS OF RETINAL VESSEL SEGMENTATION

To understand the complexities and nuances of retinal vessel segmentation, it is essential to grasp the following key fundamentals:

1. Anatomy of the Human Retina

The eye, a highly intricate organ essential for our visual perception, consists of numerous crucial components, including the cornea, iris, lens, retina, optic nerve, sclera, and retinal vessels, as depicted in Figure 1. The cornea serves as the transparent outer layer responsible for directing incoming light. Meanwhile, the iris, the eye's colorful portion, regulates the pupil's size, thereby controlling the amount of light entering the eye. Positioned behind the iris, the lens, a flexible and transparent structure, aids in focusing light onto the retina. Located at the eye's posterior, the retina is a delicate layer of tissue housing photoreceptor cells, which detect light and relay visual information to the brain via the optic nerve. To safeguard the eye's inner components, the sclera functions as a resilient, white outer layer. The eye's circulatory system, comprised of blood vessels, performs a pivotal role in upholding the eye's well-being and optimal operation. These vessels are responsible for delivering essential oxygen and nutrients to the eye's diverse structures. Additionally, the retinal vessels contribute to the elimination of waste products and the regulation of intraocular fluid pressure, a critical aspect in preserving the eye's correct form and shielding its delicate components from harm[6-7].

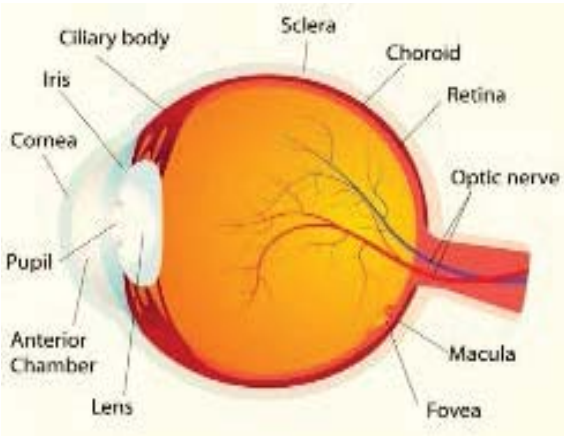

Fig. 1 Anatomy of the eye[8].

2. Role of Retinal Blood Vessels

The retinal blood vessels are responsible for supplying oxygen and nutrients to the retinal tissue. They form a dense network that spans across the entire retina, branching into arterioles and venules. This vascular system is highly organized and plays a critical role in maintaining the health and functionality of the retina[9].

3. Image Acquisition

To perform retinal vessel segmentation, high-quality retinal images must be acquired. This typically involves techniques such as fundus photography, optical coherence tomography (OCT), or fundus fluorescein angiography (FFA). Each imaging modality has its own advantages and limitations, and the choice depends on the specific clinical context and diagnostic objectives[10].

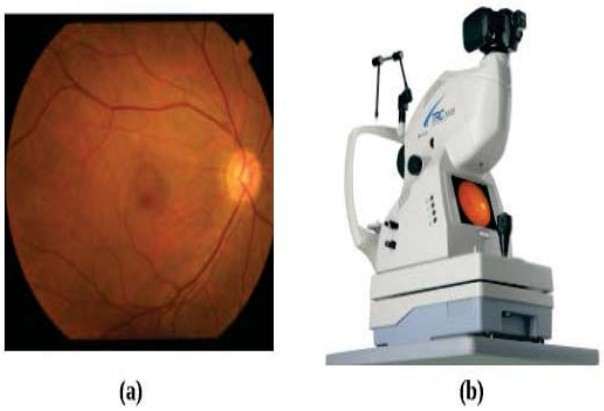

Fig. 2: a) Sample fundus image. and (b) fundus camera[11]

4. Retinal Vessel Segmentation

Retinal vessel segmentation is a crucial step in the analysis of retinal images, as it involves the identification and delineation of blood vessels within the retina (see fig.3). This process serves as a foundational element for various medical applications, enabling the early detection and monitoring of ocular and systemic diseases. Retinal vessel segmentation has come a long way, evolving from manual methods to advanced automated techniques. Early efforts involved manual tracing of vessels in retinal images, a painstaking and time-consuming process. With the advent of digital imaging, computer-aided methods emerged, laying the foundation for modern segmentation techniques.

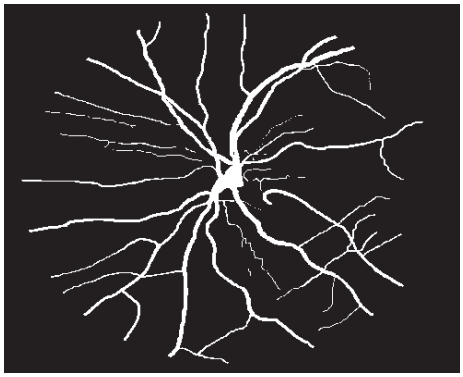

Fig. 3: Retinal vessel segmentation[12]

5. Challenges in Retinal Vessel Segmentation

Several factors contribute to the complexity of retinal vessel segmentation (see fig.4). These include variations in vessel appearance, noise and artifacts in retinal images, low contrast in some areas of the retina, and the presence of pathologies that can alter vessel morphology. Overcoming these challenges is essential for accurate segmentation and clinical utility. Understanding these fundamentals is essential for anyone entering the field of retinal vessel segmentation[13-14].

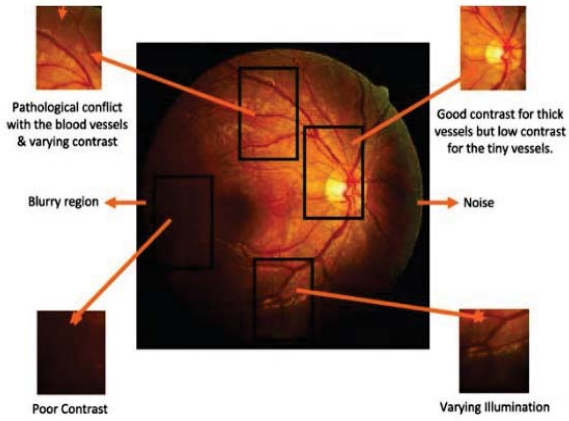

Fig. 4: Complexities of retinal fundus imaging[13]

In the subsequent sections of this article, we will explore the evolution of segmentation techniques, the advent of machine learning and deep learning approaches, and the ongoing challenges and future prospects of this critical field in medical imaging.

RETINAL VESSEL SEGMENTATION METHODS

An essential aspect of analyzing retinal images involves the precise identification of key attributes within blood vessels. The accuracy of this identification heavily relies on the effectiveness of blood vessel segmentation. The categorization of retinal vessel segmentation methods into systematic groups, based on their underlying methodologies, has been an ongoing endeavor in the field. Initially, these methods were categorized as contour-based or region-based. However, as research has advanced, novel techniques have emerged, giving rise to various subcategories.

In recent years, researchers have adopted hybrid approaches that blend multiple algorithms, blurring the traditional boundaries between these methods. For a comprehensive understanding of this field, it is beneficial to consult surveys published in the literature[1-2].

It is crucial to acknowledge that the categorization of retinal blood vessel segmentation methods in this review does not intend to establish a rigid classification system.

Many contemporary methods often incorporate techniques proposed by earlier researchers to address specific challenges, such as image smoothing, feature extraction, and pattern recognition. Some methods even employ hybrid approaches. In this research, the classification of vessel segmentation methods is based on a distinction between supervised and unsupervised methods[15-16].

1. Unsupervised methods

Unsupervised learning techniques harness the inherent patterns within retinal images to determine whether a specific pixel belongs to the vascular structure, operating independently of ground truth information. The primary objective of unsupervised learning approaches is to autonomously acquire and extract these intrinsic patterns from the data, eliminating the requirement for explicit human annotation or labeling. These extracted patterns subsequently facilitate the segmentation of retinal images into regions of interest, such as blood vessels, and enable the identification of potential retinal abnormalities or diseases.

The unsupervised methods reviewed for retinal vessel segmentation are primarily divided into six categories, as

depicted in fig.5: matched filtering, mathematical morphology approach, multi-scale approach, model-based approach, vessel tracing approach, and other general approaches. In comparison to supervised methods, unsupervised approaches offer the advantages of increased processing speed and reduced computational complexity. Therefore, our focus will be on exploring these unsupervised methods [17-20].

2. Supervised methods

Supervised methods rely on pre-existing labeling information to determine whether a pixel belongs to a blood vessel or not. These algorithms learn a set of rules for vessel extraction based on a training dataset consisting of reference images that have been manually segmented by professionals, typically ophthalmologists. This set of labeled data is commonly referred to as the "ground truth". However, acquiring a reliable ground truth can be challenging in real-world applications, as noted in prior research.

Supervised techniques employ a collection of samples from the ground truth to train a classifier capable of distinguishing between vessel and non-vessel pixels, creating what is known as the training set. These techniques have evolved into machine learning and deep learning algorithms, such as Random Forest, Support Vector Machine (SVM), K Nearest Neighbors (KNN), and Artificial Neural Networks (ANN), which are extensively used in the medical field[21-22].

Deep-learning networks, when trained on labeled data, demonstrate an extraordinary capacity to deal with unstructured data, a feature that endows them with the ability to process an exceptionally vast and diverse range of input data when contrasted with traditional machine learning methodologies. This inherent adaptability positions deep learning models at the forefront of many fields, offering the promise of superior performance across various applications. However, it is crucial to acknowledge that achieving such high-performance levels in deep learning models often comes with certain prerequisites and challenges.

One of the primary requirements is the availability of a substantial training database, meticulously annotated to facilitate the model's learning process. This requirement becomes particularly pronounced in complex tasks such as retinal vessel segmentation, where the model must accurately delineate intricate structures within medical images. Consequently, the acquisition and curation of a sufficiently large and well-annotated dataset can pose a formidable obstacle in the pursuit of excellence in deep learning-based retinal vessel segmentation[23-24]. Addressing these challenges effectively is pivotal to harnessing the full potential of deep learning in medical image analysis and other data-driven domains[24].

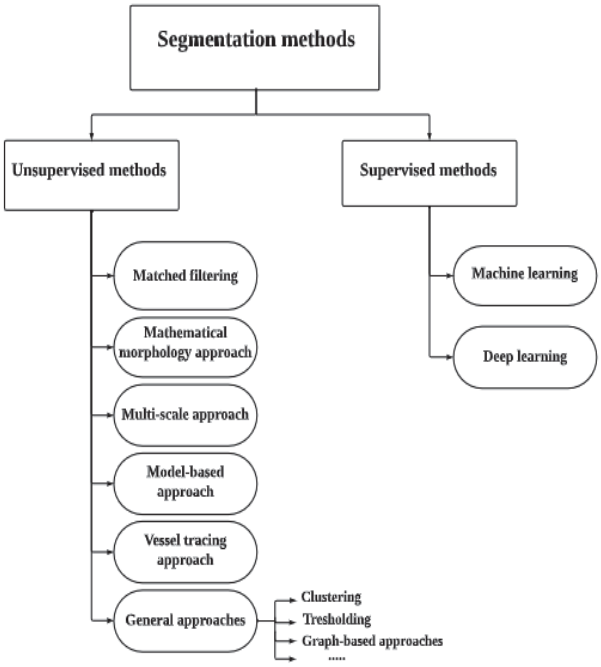

Fig. 5: Classification of retinal vessel segmentation methods

THE FUTURE OF RETINAL VESSEL SEGMENTATION

The future of retinal vessel segmentation promises a transformative trajectory marked by a convergence of cutting-edge technologies and clinical applications. Deep learning methodologies, powered by increasingly sophisticated neural network architectures and augmented by expansive, diverse datasets, will underpin significant strides in accuracy and robustness. Real-time, point-of-care solutions will enable early disease detection and telemedicine applications, democratizing access to eye health assessments.

The integration of multimodal imaging data will provide a holistic view of retinal structures, while personalized medicine approaches will cater to individual patient profiles, optimizing diagnostics and treatments. Collaboration between computer scientists and healthcare professionals will remain pivotal, ensuring clinically relevant and ethically sound AI solutions. Additionally, the field will grapple with regulatory and ethical considerations, establishing standards for AI-assisted diagnostics while safeguarding patient privacy. As retinal vessel segmentation advances, it holds the promise of revolutionizing retinal disease management, ultimately improving patient outcomes and reshaping the landscape of ophthalmic healthcare[25-26].

CONCLUSIONS

In conclusion, retinal vessel segmentation methods hold a critical position in the field of medical image analysis and ophthalmology. These techniques are indispensable for the extraction and isolation of blood vessels within retinal images, thereby aiding in the diagnosis and monitoring of various eye diseases such as diabetic retinopathy and glaucoma. Over the years, the field has experienced significant advancements, particularly with the integration of cutting-edge technologies like deep learning. Nevertheless, challenges persist, including the necessity for large, well-annotated datasets and the demand for robust models capable of handling diverse image characteristics.

As technology continues its relentless march forward, retinal vessel segmentation methods are poised to assume an increasingly crucial role in early disease detection, treatment planning, and enhancing the overall quality of eye care. Continuous research and innovation in this domain are essential to further improve the accuracy and accessibility of these methods in clinical practice. Ultimately, these efforts will benefit patients and healthcare providers alike.

AUTHOR INFORMATION

Corresponding Author:

* Imane Mehidi

Email address: imane.mehidi@univ-setif.dz

REFERENCES

1. M. R. K. Mookiah, S. Hogg, T. J. MacGillivray, V. Prathiba, R. Pradeepa, V. Mohan, R. M. Anjana, A. S. Doney, C. N. Palmer, and E. Trucco, "A review of machine learning methods for retinal blood vessel segmentation and artery/vein classification," Medical Image Analysis, vol. 68, p. 101905, 2021.
2. A. A. Abdulsahib, M. A. Mahmoud, M. A. Mohammed, H. H. Rasheed, S. A. Mostafa, and M. S. Maashi, "Comprehensive review of retinal blood vessel segmentation and classification techniques: intelligent solutions for green computing in medical images, current challenges, open issues, and knowledge gaps in fundus medical images," Network Modeling Analysis in Health Informatics and Bioinformatics, vol. 10, no. 1, pp. 1–32, 2021.
3. M. Niemeijer, J. Staal, B. van Ginneken, M. Loog, and M. D. Abramoff, "Comparative study of retinal vessel segmentation methods on a new publicly available database," in Medical imaging 2004: image processing, vol. 5370, pp. 648–656, International Society for Optics and Photonics, 2004.
4. C. L. Srinidhi, P. Aparna, and J. Rajan, "Recent advancements in retinal vessel segmentation," Journal of medical systems, vol. 41, no. 4, p. 70, 2017.
5. Almotiri, K. Elleithy, and A. Elleithy, "Retinal vesse segmentation techniques and algorithms: a survey," Applied Sciences, vol. 8, no. 2, p. 155, 2018.
6. M. R. K. Mookiah, U. R. Acharya, C. K. Chua, C. M. Lim, E. Ng, and A. Laude, "Computer-aided diagnosis of diabetic retinopathy: A review," Computers in biology and medicine, vol. 43, no. 12, pp. 2136–2155, 2013.
7. S. Melmed, K. S. Polonsky, P. R. Larsen, and H. M. Kronenberg, Williams text book of endocrinology E-Book. Elsevier Health Sciences, 2015.
8. https://www.news-medical.net/health/How-Does-the-Eye-Work.aspx.
9. M. Rosenfield and N. Logan, Optometry: Science, Techniques and Clinical Management E-Book. Elsevier Health Sciences, 2009.
10. L. A. Yannuzzi, M. D. Ober, J. S. Slakter, R. F. Spaide, Y. L. Fisher, R. W. Flower, and R. Rosen, "Ophthalmic fundus imaging: today and beyond," American journal of ophthalmology, vol. 137, no. 3, pp. 511–524, 2004.
11. "Trc-NW8/8f." https://topconhealthcare.com/products/trc-nw8f/
12. M. M. Fraz, P. Remagnino, A. Hoppe, B. Uyyanonvara, A. R. Rudnicka, C. G. Owen, and S. A. Barman, "Blood vessel segmentation methodologies in retinal images–a survey," Computer methods and programs in biomedicine, vol. 108, no. 1, pp. 407–433, 2012.
13. O. O. Sule, "A survey of deep learning for retinal blood vessel segmentation methods: Taxonomy, trends, challenges and future directions," IEEE Access, vol. 10, pp. 38202–38236, 2022.
14. W. Tasman, E. Jaeger, and L. W. Duane's Ophthalmology, "Helmut greim 3.11. 1 structure and function," Toxicology and Risk Assessment: A Comprehensive Introduction, p. 343, 2008.
15. G. A. Williams, I. U. Scott, J. A. Haller, A. M. Maguire, D. Marcus, and H. R.McDonald, "Single-field fundus photography for diabetic retinopathy screening: a report by the american academy of ophthalmology," Ophthalmology, vol. 111, no. 5, pp. 1055–1062, 2004.
16. W. Liu, Y. Jiang, J. Zhang, and Z. Ma, "Rfarn: Retinal vessel segmentation based on reverse fusion attention residual network," Plos one, vol. 16, no. 12,p. e0257256, 2021.
17. K. B. Khan, A. A. Khaliq, A. Jalil, M. A. Iftikhar, N. Ullah, M. W.

Aziz, K. Ullah, and M. Shahid, "A review of retinal blood vessels extraction techniques: challenges, taxonomy, and future trends," Pattern Analysis and Applications, vol. 22, pp. 767–802, 2019.

18. I. Qureshi, J. Ma, and Q. Abbas, "Recent development on detection methods for the diagnosis of diabetic retinopathy," Symmetry, vol. 11, no. 6, 2019.
19. A. T. Ahamed, A. Jothish, G. Johnson, and S. B. Krishna, "Automated system for retinal vessel segmentation," in 2018 Second International Conference on Inventive Communication and Computational Technologies (ICICCT), (Coimbatore,India), pp. 717–722, IEEE, April 2018.
20. S. Dash, S. Verma, M. Khan, M. Wozniak, J. Shafi, M. F. Ijaz, et al., "A hybrid method to enhance thick and thin vessels for blood vessel segmentation," Diagnostics, vol. 11, no. 11, p. 2017, 2021.
21. .M. M. Fraz, P. Remagnino, A. Hoppe, B. Uyyanonvara, A. R. Rudnicka, C. G. Owen, and S. A. Barman, "An ensemble classification-based approach applied to retinal blood vessel segmentation," IEEE Transactions on Biomedical Engineer-ing, vol. 59, pp. 2538–2548, Sep. 2012.
22. A. Budai, R. Bock, A. Maier, J. Hornegger, and G. Michelson, "Robust Vessel Segmentation in Fundus Images," International Journal of Biomedical Imaging, 2013.
23. J. H. Holland, "Genetic algorithms and adaptation," Adaptive control of illdefined systems, pp. 317–333, 1984.
24. J. Schmidhuber, "Deep learning in neural networks: An overview," Neural net-works, vol. 61, pp. 85–117, 2015.
25. K. Balasubramanian and N. Ananthamoorthy, "Robust retinal blood vessel segmentation using convolutional neural networ and support vector machine," Journal of Ambient Intelligence and Humanized Computing, vol. 12, no. 3, pp. 3559–3569, 2021.
26. V. Saravanan, R. Samuel, S. Krishnamoorthy, and A. Manickam, "Deep learning assisted convolutional auto-encoders framework for glaucoma detection and anterior visual pathway recognition from retinal fundus images," Journal of Ambient Intelligence and Humanized Computing, pp. 1–11, 2022.

2023

A Novel Bio-Inspired Optimization Algorithm for Medical Image Denoising Using Total Generalized Variation

Y.R. Haddadi,[a] B. Mansouri,[a]

[a] LTC Laboratory, Faculty of Technology, Department of Electronics, University of Saida, Saida, Algeria

ABSTRACT: In the present work, we propose a novel approach for medical image denoising process based on Gaussian Quantum Behaved Particle Swarm Optimization algorithm and Total generalized variation of second order, in parallel with regularization estimation. We demonstrate the effect of regularization estimation alternatives on the denoising behavior and we evaluate the regularization operation by applying our proposed method TGV-GQPSO. The experimental outcomes show an efficient performance of the medical image denoising operation by applying our proposed approach, achieving a denoising performance ratio of 98.66%, in comparison with other experimental state-of-the-art image denoising methods for variable noise value during the filtering process. This work represents a novel medical image denoising method using the intelligent optimization theory for regularization estimation. This latter commands the behavior of the noise during the medical image filtering process and enhance the performance of the denoising operation in terms of image quality. The application of our proposed approach would be of great importance in real medical images since that the denoising process is essential in the subsequent analysis of medical image.

Keywords: Total generalized variation of second-order; Image filtering; Quantum particle swarm optimization with gaussian mutation; regularization estimation, Optimization issue.

INTRODUCTION

Image denoising is one of the fundamental challenges in the image-processing field, where the primary aim is to estimate the original image by suppressing noise from a noise-contaminated version of the image [1-3]. As an ill-posed inverse problem, image denoising is defined below:

$$H = G + \delta \quad (1)$$

Where G is the original image and H is deemed the measured one, δ is the element of the equation that represents the noise-related information. Using regularization methods is essential to deal with the ill-posed issue [4-6]. The most known formulation of inverse problem regularization is demonstrated based on the following form:

$$\min_u F(u)+R(u) \quad (2)$$

$F(u)$ is the fidelity term, which defines the difference between the estimated as well as the measured data, $R(u)$ is the regularization term. It is represented in the regularization approach as $\lambda R(u)$ where λ is the regularization parameter of the equation.

Total generalized variation TGV is considered a modern concept of mathematical regularization [7-10]. It has several advantages over the classical total variation.

B.komander et al [11] investigated variational denoising using total variation penalties and gradient estimate of the image; they aimed to give a new interpretation of the TGV. *Florian et al* [12]

applied TGV for MRI images denoising and reconstruction. Thereafter, they compared TGV with TV performance. Their results demonstrate the advantages of TGV over classical TV. K.Bredies et al [13] studied the application of TGV in inverse problems with blurred and noisy data to confirm the solution's stability, In this context, those authors have discussed the choice of regularization parameter and its influence in terms of balancing the regularization term and the data fidelity term.

TGV method was applied in other image processing operations including medical image reconstruction, *Shanzhou Niu et all* [14] investigated the quality of CT reconstruction via TGV by introducing an optimization process.

Regarding optimization approach and bio-inspired algorithms, these methods are highly recommended also in image segmentation operations [15-18]. This framework has an effective performance in improving segmentation results.

Based on the aforementioned, we conclude that the regularization parameter estimation is critical during several image processing operations including the denoising process. In this paper, we investigate the impact of regularization parameter choice on the total generalized variation of second-order denoising based on Gaussian Quantum Behaved Particle Swarm Optimization approach [19]. We present our intelligent algorithm TGVG_QPSO to estimate the highly significant stable value of the regularization parameter for the best performance image denoising operation.

The application of the aforementioned approach would be of great importance, particularly in real medical images. This is because the denoising process is essential in the subsequent analysis of the image and leads to an efficient diagnosis of pathologies experimented with by specialists.

The remaining of this paper is organized as follows. In Section2, the Total Generalized Variation TGV method is introduced with the presentation of the Gaussian Quantum Behaved Particle Swarm Optimization algorithm GQPSO. In section3, our proposed method is presented. Experimental results are described in section4. Finally, the conclusion is represented as section5.

BACKGROUND

Total Generalized Variation

As previously stated the classical total variation TV, can be defined as follows:

$$TV(u) = \int_{\Omega} |\nabla u| \ dx \tag{3}$$

On the other hand, the total generalized variation of second-order TGV_{α}^{2} is expressed as a minimization problem following the equation below:

$$TGV_{\alpha}^{2}(u) = \ \frac{1}{2\pi}\int_{\Omega}|\nabla u|dx + \alpha_0 \ \int_{\Omega}|\varepsilon(v)|dx \tag{4}$$

Classical TV merely takes into account the first derivative contrary to TGV_{α}^{2} that gives the balance between the first and the second derivatives. TGV_{α}^{2} has many advantageous proprieties in comparison with classical TV [20-23]. With its application in medical images denoising [24-26]. Including; a well-developed mathematical theory, the convergence of TGV_{α}^{2} values as well as the invariance of the method. All these elements allow TGV_{α}^{2} to exceed the classical approach of the total variation.

Gaussian Quantum Particle Swarm Optimization

Leandro dos Santos Coelho [11] proposed the gaussian quantum particle swarm optimization GQPSO approach as a combination of quantum particle swarm optimization and gaussian distribution. The classical particle swarm optimization is an intelligent algorithm that is based on computational simulation of organisms' movements such as, flocks and birds. The state of the particle in PSO is defined by position and velocity [27]. The extension of quantum behavior presented in [28-30] allows PSO to work in different ways because the particle is depicted by a wave function. The new approach of QPSO combined with gaussian mutation shows efficient performance for reaching significant solutions if we compare it with both QPSO and PSO algorithms [31-33].

When we combine the concept of QPSO with operator mutation using Gaussian probability distribution, the particles move according to the following iterative equation:

$$x_i(t+1) = P + \ \beta \ .|Mbest_i - x_i(t)| \ .\ln\left(\frac{1}{G}\right) \quad ifk \geq 0.5$$

$$x_i(t+1) = P - \beta \ .|Mbest_i - x_i(t)| \ .\ln\left(\frac{1}{G}\right), \ ifk < 0.5,$$

(5)

where β is the contraction-expansion coefficient. G and K values are related to the probability distribution function range. The Mbest is a global point (mainstream thought or mean best) of the population. It represents the mean of the Pbest (Individual Best Solution) positions of all particles. It is defined as:

$$Mbest = \frac{1}{N}\sum_{d=1}^{N} P_{g,d}\,(t) \tag{6}$$

The best particle in the swarm is represented with g. The convergence concept is defined as:

$$P = \frac{c_1 P_{i,d} + c_2 P_{g,d}}{c_1 + c_2} \tag{7}$$

where c_1 and c_2 are the acceleration coefficients.

PROPOSED MODEL

In Our proposed approach, we proceed in two steps:

Firstly, we study the influence of regularization parameter choice on image denoising using TGV_α^2. The quality of image denoising can be evaluated by utilizing peak signal to noise ratio (PSNR), mean squared error (MSE), mean absolute error (MAE), and Structure Similarity Index Map (SSIM). In this research, we use PNSR and SSIM as criteria to compare the overall results. The computational simulation of TGV_α^2 contains two regularization parameters λ_1,λ_2 as defined in (8). In this respect, the choice of the values: λ_1 and λ_2, the amount quantified the difference between them, the relationship between the noise with the regularization parameter variations, and the estimation of λ_1 and λ_2 relevant best values for each noise variation are discussed.

$$TGV_\alpha^2(u) = \lambda_2 |p_2(c) - p_1(c)| + \lambda_1 |p_1'(c) - p_2'(c)| \tag{8}$$

Secondly, we apply our TGVG_QPSO method (Table 1) to solve our optimization problem, which is defined as the choice for the regularization parameter to get the best image denoising quality. Our objective function chosen will be the one that relates λ_1, λ_2, and noise value δ, all combined.

Table1. TGVG_QPSO Algorithm

1	Fixe GQPSO parameters d, n
2	Choosing lb,ub (lower and upper bound) values (related to δ value)
3	Fixe number of iterations, and constants c1,c2,w1,w1
4	Generate initial population
5	Evaluate the objective function (Eq. 9 (1 or 2) for $\boldsymbol{\lambda_1}$ or $\boldsymbol{\lambda_2}$)
6	Initialize Pbest and Gbest
7	GQPOS main loop
8	Iter = 1
9	While iter<iermax
10	Update position (solution to Mbest Eq. 6)
11	Check Bounds
12	Update Pbest
13	Update Gbest
14	Plotting the convergence results (fitness value
15	/iteration)
16	End
17	/// STEP2 TGV
18	Fixe TGV values (n, ($\boldsymbol{\lambda_1}$ and $\boldsymbol{\lambda_2}$ as the fitness
19	value))
20	Input : Original image Add Gaussian noise to the image δ $\boldsymbol{TGV_\alpha^2}$ denoising function
21	Output : Denoised Image

RESULTS AND DISCUSSION

The Impact of the Regularization Parameter Choice on the Denoising Process

Our experimental approach is mainly composed of two sections. In the first section, the impact of the regularization parameter choice on the denoising process and its relation with the noise variation has been pinpointed. Fig. 1 Illustrates the variation of peak signal to noise ratio with increasing regularization parameters and noise values. As clearly shown, there is one best solution of regularization parameter for best denoising quality in case of noise variation. And since our computational simulation of TGV_α^2 contains two regularization parameters λ_1, λ_2, the

solution is deemed a combination of two values together.

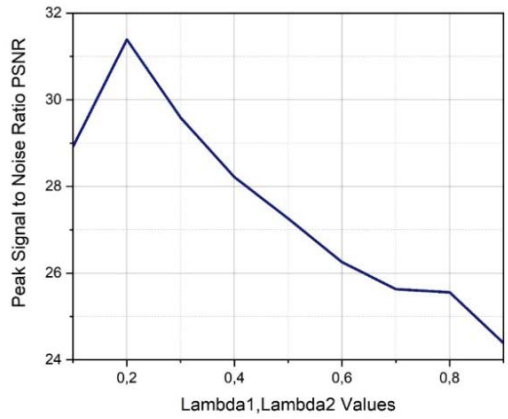

Fig. 1: Peak signal to noise ratio variation with increasing λ_1, λ_2 noise value [10%-50%].

The quantified amount difference between these two values: λ_1, λ_2 has a significant impact on TGV_α^2 and the denoising behavior. In this regard, Fig. 2 represents Peak signal to noise ratio variation with $\lambda_1$and λ_2 different gap values with noise fixed, it confirms that increasing the difference between the values: λ_1, λ_2 leads to a completely different denoising process. Furthermore, denoising behavior can be affected as well by the fixation of one of the following values λ_1 , λ_2 as demonstrated in both graphs shown in Fig. 3.

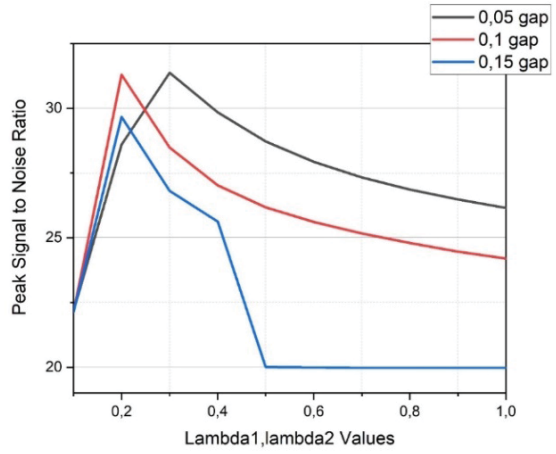

Fig. 2: Peak signal to noise ratio variation with$\lambda_1$and λ_2 different gap values, noise fixed

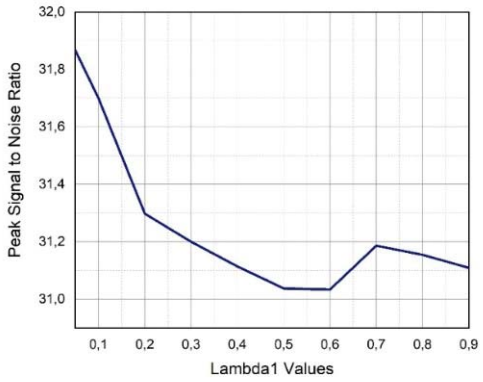

(a)

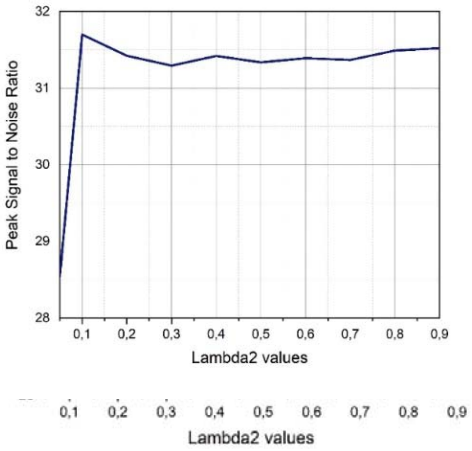

(b)

Fig. 3: Peak signal to noise ratio variation with $\lambda_1$and $\lambda_2$different values, (a): fixed λ_1 values, (b): fixed λ_2 values

As matter of fact, there is a relation as well between the qualities of the denoising operation with the noise variation. Fig. 4 illustrates the variation of PSNR with the regularization parameter that increased for a specific value of the noise. Consequently, the second section of this experimental approach aims to estimate the best solution for the regularization parameter using TGV_GQPSO.

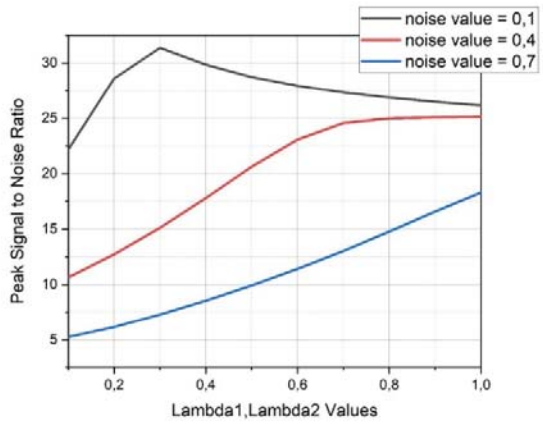

Fig. 4 Peak signal to noise ratio variation with $\lambda_1$and λ_2 and three different noise values

Regularization Estimation

Our objective function that defines the optimization problem is the fit relationship function between the regularization parameter:λ_1, $\lambda_2$and noise δ since it is considered the solution of the best performance of the denoising process. The objective function described below has been fitted after performing several tests.

$\boldsymbol{\lambda_1}$ = 370,6 + 0,2408.sin (0,5401. π . $\boldsymbol{\lambda_2}$.$\boldsymbol{\delta}$) – 370,4. exp(-(0,0401.$\boldsymbol{\delta}$)²)

$\boldsymbol{\lambda_2}$ = 0,2266 + 1,493.sin (0,1797. π .$\boldsymbol{\lambda_1}$.$\boldsymbol{\delta}$) -0,000271.exp(-(- 0,1628.$\boldsymbol{\delta}$)²) (9)

We utilize (9) to calculate the best combination of regularization parameters using our proposed method TGVG_QPSO. MRI and CT images used are taken from Radiopaedia [34]; the frames are extracted and saved in TIFF format. The Gaussian noise levels are [10%-90%]. The Regularization parameters values interval is between [0-1], our approach was performed using the following parameters values: number of iterations n = 100/500, dimension d = 2, Acceleration coefficients c1 = c2 = 1, inertia weights w1= w2=1.

The main challenge of this study involved the determination of the objective function that represents the the fit relationship function between the two regularization parameters and the noise value, if the fit relationship is inappropriate. The denoising performance will be less efficient.

As shown in Table 2, the estimation of λ_1 λ_2 for each particular noise value based on our proposed approach leads to a better denoising performance represented with PSNR and SS IM values, instead of choosing one random value of the regularization parameter. Fig. 5 demonstrates the impact of the estimation on image quality using our TGV_GQPSO method in comparison with $\mathrm{TGV}_{\alpha}^{2}$.

Table 2. PSNR and SSIM values of brain MRI image denoising with TGV and our proposed method TGV_GQPSO, noise value [0.1-0.9]

TGV	**δ**	0.1	0.2	0.3	0.4	0.5	0.6	0.7	0.8	0.9
	λ_1	0.1	0.1	0.1	0.1	0.1	0.1	0.1	0.1	0.1
	λ_2	0.15	0.15	0.15	0.15	0.15	0.15	0.15	0.15	0.15
	PSNR	31.3747	23.3549	16.7162	12.7358	9.8991	7.8365	6.1108	4.7449	3.5922
	SSIM	0.8733	0.3536	0.1435	0.0817	0.0511	0.0349	0.0252	0.0185	0.014
TGV_GQPSO	**λ_1**	0.21	0.24	0.29	0.35	0.44	0.55	0.66	0.79	0.91
	λ_2	0.23	0.26	0.30	0.36	0.43	0.52	0.63	0.75	0.88
	PSNR	31.8902	28.1065	26.3551	24.3851	23.0344	21.9445	21.3598	20.8016	20.5170
	SSIM	0.8942	0.8094	0.6499	0.5271	0.4332	0.4041	0.3685	0.3741	0.3468

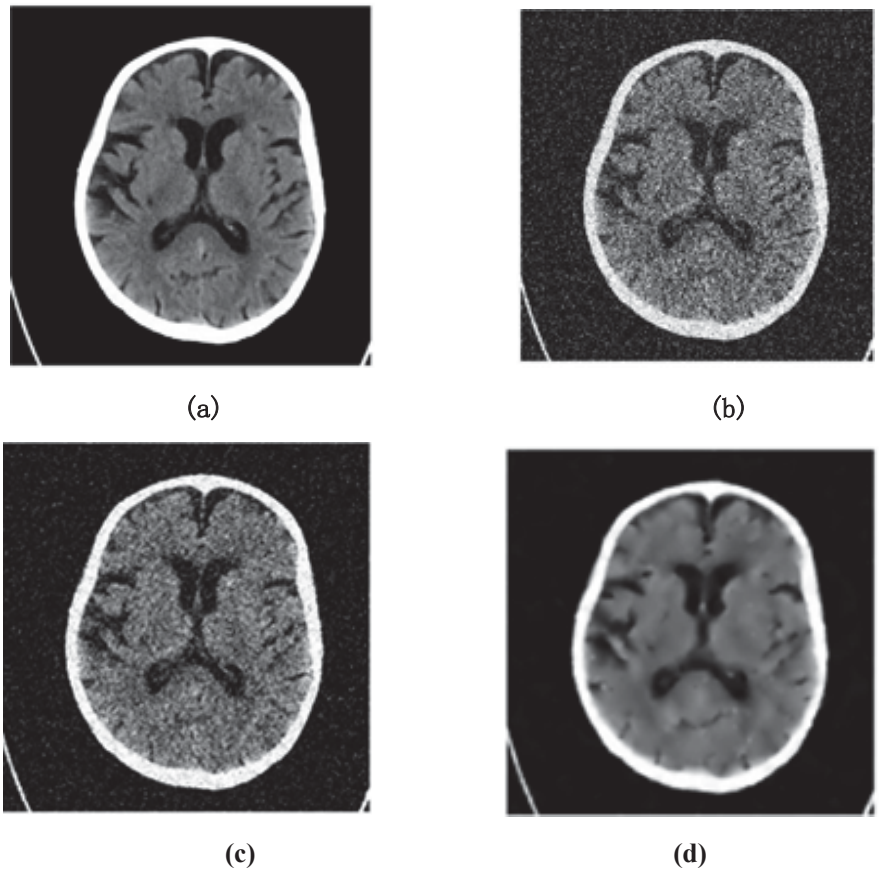

Fig. 5: Denoising of CT Brain image using TGV and our proposed TGV_GQPSO method. (a): Original Image, (b): Noised image δ=0.3, (c): Denoised image using TGV; (d): Denoised image using our proposed TGV_GQPSO approach

Based on applying TGV_GQPSO, we can provide the best solution for the regularization parameter choice and superior denoising performance through the optimization of the objective function (9). Fig. 6 proves the effectiveness of our TGV_GQPSO method in comparison with other state-of-the-art experimental denoising algorithms including Bilateral Filter, Total Variation TV, and ordinary Total Generalized Variation of second order TGV_{α}^{2}. The denoising quality of our approach surpasses the aforementioned ones, including using TGV_{α}^{2} with particle swarm optimization PSO and Artificial Bee Colony ABC Algorithms for regularization parameter estimation as shown in Table 3 with the higher values of PSNR, SSIM and Denoising Performance Ratio (DPR).

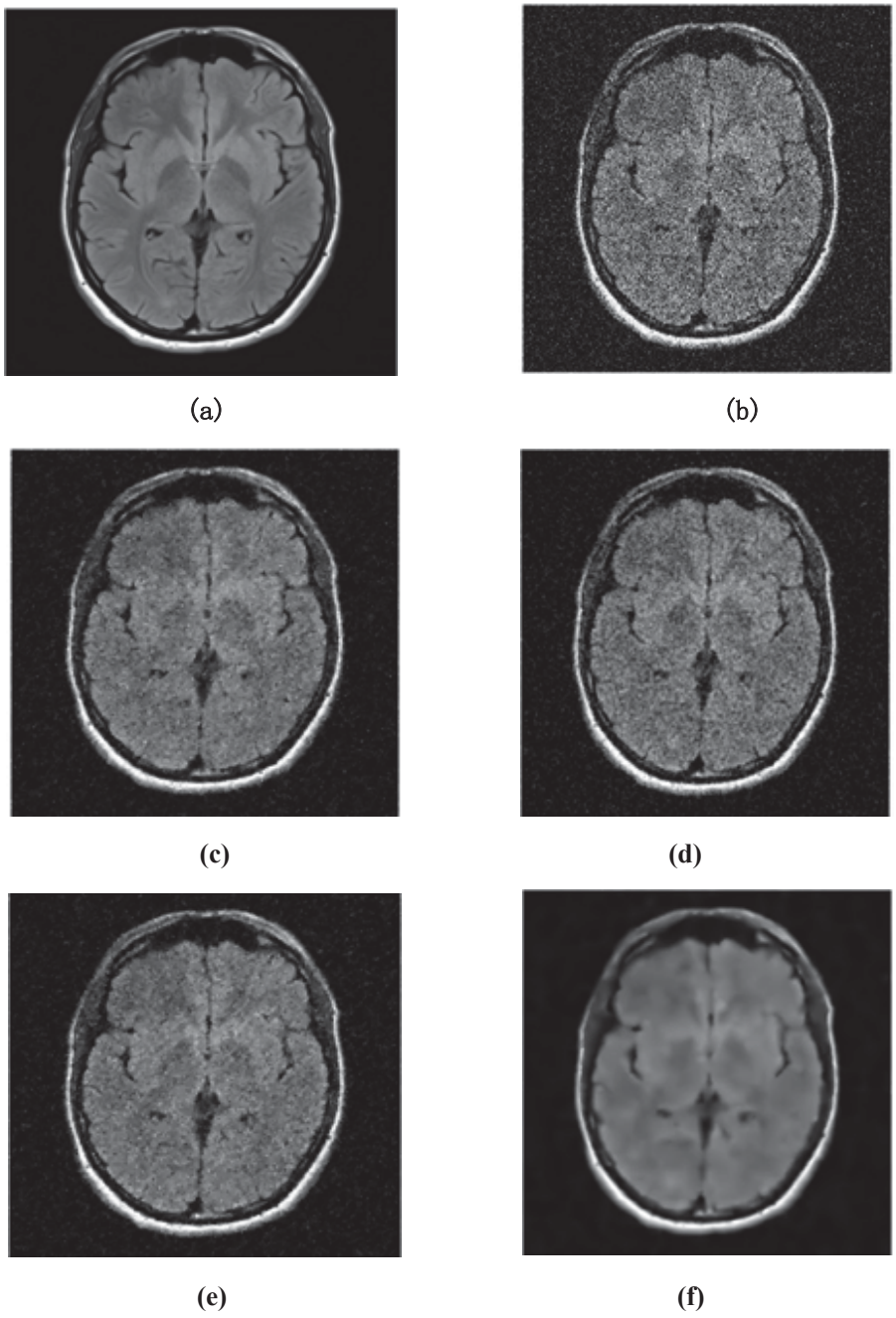

Fig. 6: Denoising of MRI Brain image using our proposed algorithm and other different experimental denoising methods (a): Original Image, (b): Noised image δ=0.2, (c):Denoised image using TV , (d): Denoised image using Bilateral Filter, (e) : Denoised image using TGV, (f) : Denoised image using our TGVGQPSO method.

Table 3. PSNR, SSIM and DPR values of MRI Brain image denoising using our proposed algorithm and other experimental methods, noise value δ=0.2

Denoising Algorithm	PSNR	SSIM	DPR
Bilateral Filter	23.3868	0.33116	52.86%
TV	23.4260	0.35171	48.32%
$\mathbf{TGV}_{\alpha}^{2}$	24.4414	0.36366	51.98%
$\mathbf{TGV}_{\alpha}^{2}$-PSO	25.2314	0.68254	93.85%
$\mathbf{TGV}_{\alpha}^{2}$-ABC	25.4532	0.69425	95.64%
TGV_GQPSO	27.9460	0.80907	98.66%

Our TGV_GQPSO method gives the most accurate estimation of regularization Parameter choice despite any probable noise value. The expression of the denoising operation as an optimization problem provides effective results in the denoising process and image enhancement. The main advantage of our proposed approach is that it considers the noise information and employs the appropriate regularization parameters values for the best denoising performance. Future studies could examine several medical image-processing applications based on the same principle to improve the filtering and noise specifications for different medical imaging data.

CONCLUSION

We investigate in the present paper the impact of regularization parameter estimation on the performance of medical image denoising using our TGVG_QPSO approach based on a total generalized variation of second-order and Gaussian quantum behaved particle swarm optimization. Our intelligent algorithm is applied for estimating the best solution of regularization parameter choice with noise variation. The experimental results confirms the obvious effect on the medical images denoising process with the application of our proposed approach in comparison with other experimental state-of-the-art image denoising methods. This optimization-denoising process is efficient in improving medical image enhancement approaches including image restoration, reconstruction, and deconvolution.

AUTHOR INFORMATION

Corresponding Author

*Yasser Radouane Haddadi

Email address: Radouane.haddadi@univ-saida.dz

REFERENCES

1. Fan, Linwei, et al. "Brief review of image denoising techniques." Visual Computing for Industry, Biomedicine, and Art 2.1:1-12 (2019)
2. Goyal, Bhawna, et al. "Image denoising review: From classical to state-of-the-art approaches." Information fusion 55 : 220-244 (2020)
3. Sagheer, S. V. M., & George, S. N. A review on medical image denoising algorithms. Biomedical signal processing and control, 61, 102036 (2020).
4. Gu, S., & Timofte, R. A brief review of image denoising algorithms and beyond. Inpainting and Denoising Challenges, 1-21 (2019)
5. Thanh, Dang NH. "Medical images denoising method based on total variation regularization and anscombe transform." 2019 19th International Symposium on Communications and Information Technologies (ISCIT). IEEE (2019)
6. Renaut, Rosemary A., Iveta Hnětynková, and Jodi Mead. "Regularization parameter estimation for large-scale Tikhonov regularization using a priori information." Computational statistics & data analysis 54.12 : 3430-3445 (2010)
7. Ma, T. H., Huang, T. Z., & Zhao, X. L. Spatially dependent regularization parameter selection for total generalized variation-based image denoising. Computational and Applied Mathematics, 37(1), 277-296. (2018)
8. Bredies, Kristian, Karl Kunisch, and Thomas Pock. "Total generalized variation." SIAM Journal on Imaging Sciences 3.3 492-526 (2010)
9. Bredies, Kristian, and Martin Holler. "Regularization of linear inverse problems with total generalized variation." Journal of inverse and ill-posed problems 22.6 871-913 (2014)
10. Valkonen, Tuomo, Kristian Bredies, and Florian Knoll. "Total generalised variation in diffusion tensor imaging." (2012)
11. Komander, Birgit, Dirk A. Lorenz, and Lena Vestweber. "Denoising of image gradients and total generalized variation denoising." Journal of Mathematical Imaging and Vision 61.1 : 21-39 (2019)
12. Knoll, Florian, et al. "Second order total generalized variation (TGV) for MRI." Magnetic resonance in medicine 65.2 : 480-491 (2011)
13. Bredies, Kristian, and Tuomo Valkonen. "Inverse problems with second-order total generalized variation constraints." arXiv preprint arXiv:2005.09725 (2020)
14. Niu, Shanzhou, et al. "Sparse-view x-ray CT reconstruction via total generalized variation regularization." Physics in Medicine & Biology 59.12 : 2997 (2014)
15. Semchedine, Moussa, and Abdelouahab Moussaoui. "An efficient particle swarm optimization for MRI fuzzy segmentation." (2018)
16. Mirghasemi, Saeed, Ramesh Rayudu, and Mengjie Zhang. "A new modification of fuzzy c-means via particle swarm optimization for

noisy image segmentation." Australasian Conference on Artificial Life and Computational Intelligence. Springer, Cham (2016)

17. Tan, Teck Yan, et al. "Evolving ensemble models for image segmentation using enhanced particle swarm optimization." IEEE access 7 : 34004-34019 (2019)
18. Farshi, Taymaz Rahkar, John H. Drake, and Ender Özcan. "A multimodal particle swarm optimization-based approach for image segmentation." Expert Systems with Applications 149 : 113233 (2020)
19. Dos Santos Coelho, Leandro. "Gaussian quantum-behaved particle swarm optimization approaches for constrained engineering design problems." Expert Systems with Applications 37.2 : 1676-1683 (2010)
20. Zhang, Lan, and Lei Xu. "A new method for choosing the regularization parameter of rof total variation image denoising." 2016 8th International Conference on Intelligent Human-Machine Systems and Cybernetics (IHMSC). Vol. 1. IEEE (2016)
21. Thanh, Dang NH, and VB Surya Prasath. "Total variation L1 fidelity salt-and-pepper denoising with adaptive regularization parameter." 2018 5th NAFOSTED Conference on Information and Computer Science (NICS). IEEE (2018)
22. He, C., Hu, C., Zhang, W., & Shi, B. A fast adaptive parameter estimation for total variation image restoration. IEEE Transactions on Image Processing, 23(12), 4954-4967: (2014)
23. Prasath, VB Surya, et al. "Image restoration with total variation and iterative regularization parameter estimation." Proceedings of the Eighth International Symposium on Information and Communication Technology (2017)
24. Kumar, Manoj, and Manoj Diwakar. "A new exponentially directional weighted function based CT image denoising using total variation." Journal of King Saud University-Computer and Information Sciences 31.1 113-124 (2019)
25. Shi, F., Cheng, J., Wang, L., Yap, P. T., & Shen, D. LRTV: MR image super-resolution with low-rank and total variation regularizations. IEEE transactions on medical imaging, 34(12), 2459-2466 (2015)
26. Li, Bei, and DaShun Que. "Medical images denoising based on total variation algorithm." Procedia Environmental Sciences 8 227-234 (2011)
27. Wang, RuiYing. "Research on image processing based on improved particle swarm optimization." 2018 10th International Conference on Measuring Technology and Mechatronics Automation (ICMTMA). IEEE (2018)
28. Zhai, Daoyuan, Minshen Hao, and Jerry M. Mendel. "A non-singleton interval type-2 fuzzy logic system for universal image noise removal using quantum-behaved particle swarm optimization." 2011 IEEE International Conference on Fuzzy Systems (FUZZ-IEEE 2011). IEEE (2011)
29. Elsayed, Eman Karam, Dina Refaet Salem, and Mohammed Aly. "A fast quantum particle swarm optimization algorithm for image denoising problem." International Journal of Intelligent Engineering and Systems 13.1 : 98-112 (2020)
30. Di Zhoua, Jun Suna, Choi-Hong Laib, Wenbo Xu and Xiaoguang Lee, ‘’ An improved quantum-behaved particle swarm optimization and its application to medical image registration”, International Journal of Computer Mathematics, Vol. 88, No. 6, April 2011, 1208–1223 (2011)
31. Han, M., Fan, J., & Wang, J. A dynamic feedforward neural network based on Gaussian particle swarm optimization and its application for predictive control. IEEE Transactions on Neural Networks, 22(9), 1457-1468 (2011)
32. Sun, Jun, et al. "Quantum-behaved particle swarm optimization with Gaussian distributed local attractor point." Applied Mathematics and Computation 218.7 : 3763-3775 (2011)
33. Sun, Y., & Gao, Y. A multi-objective particle swarm optimization algorithm based on gaussian mutation and an improved learning strategy. Mathematics, 7(2), 148 (2019)
34. R.Organization,"Radiopaedia,"2021.[Online].Available:https://radiopaedia.org/encyclopaedia/cases/all?modality=MRI/CT. [Accessed 01 10 2021]

2023

Rule Based Classifier for MRI Brain Tumor Identification and Classification

H. Chellakh [a,c,*], A. Moussaoui[a], A. Attia,[b,c]

[a] Department of Computer Science, Ferhat Abbas University of Setif 1, Algeria

[b] Department of Computer Science, Mohamed El Bachir El Ibrahimi University of Bordj Bou Arreridj, Algeria

[c] LMSE Laboratory: University Mohamed El Bachir El Ibrahimi of BordjBouArreridj, Algeria

ABSTRACT: MRI brain tumor identification and classification is costly and time-consuming owing to the difficulty and complication of tumors. The process is highly influenced by the experience and knowledge of radiologists and neurologists. For this reason, automating this process becomes indispensable to overcome the drawbacks. In this work, we propose a new model, called DRB-BSIF (i.e., Deep Rule Based Classifier using Binarized Statistical Image Features), to enhance classification performances and reduce the complexity implicated in the diagnostic decision. Specifically, the tumor region is augmented by image dilation and used as the Region of Interest (ROI) instead of the initial tumor region. Then, features are extracted using BSIF image descriptor. Furthermore, we have constructed a Bank-BSIF, which is founded by the best parameters of BSIF filters. In the classification step, a deep-rule based classifier (DRB) has been used. The main of the BRD classifier is a self-organized set of IF and THEN fuzzy rules guided by the prototypes. These fuzzy rules are generated by DRB classifier and represented its 'engine'. We studied classification of different kinds of brain tumors (e.g., Meningioma, Glioma, and Pituitary tumor). The proposed model is evaluated on publicly available brain CE-MRI images via different measures such as performance accuracy, sensitivity and specificity. Experimental results demonstrated that the DRB-BSIF is effective and can be used in computer aided brain tumor classification.

Keywords: MRI brain tumor; region of interest; feature extraction; BSIF descriptor; DRB classifier.

INTRODUCTION

Nowadays, automatic tissue type classification of magnetic resonance imaging (MRI) is very necessary in computer-aided diagnosis. Early and accurate identification and detection of brain tumor are keys for implementing successful therapy and treatment planning. MRI is the most popular technique for identification and detection of brain tumors [1]. The most important advantage of MR imaging is that it is non-invasive technique. However, brain tumor classification is a tedious task because of the diversity and emergency of tumors, which relies on the experience and knowledge of radiologists. Moreover, supervised classification methods are inefficient and non-reproducible for large amounts of data. Therefore, computer-aided diagnosis tools are highly desirable to address these problems[2]. There exist several studies for MRI brain tumor classification using machine learning techniques. For instance, use of Fuzzy Clustering Means (FCM) [3], brain diagnosis based on fuzzy system [4], Support Vector Machine (SVM) [5], Artificial Neural Network (ANN) [6] and Expectation-Maximization (EM) algorithm technique [7]. These techniques have been employed for segmentation and extraction of relevant information from the medical imaging modalities [1]. In particular, Zhang et al. [5] have proposed a method based on

Principle Component Analysis (PCA) and SVM techniques for MRI brain tumor classification. The method first extracted features from images by using wavelet transform then reduced the dimensions of the extracted features by applying PCA technique. The reduced features were used as an input to a kernel of SVM to classify MRIs as normal or abnormal. This technique achieved an accuracy of 99.38%. While, Cheng et al. [8] have introduced a new method for classification of MRI images into different kinds of tumors. To increase the accuracy of the proposed method, the tumor region was augmented by image dilation and used as the ROI instead of the initial tumor region. This technique attained the accuracies of 82.31%, for intensity histogram, 84.75% for Gray-Level Co-occurrence Matrix (GLCM), and 88.19% for Bag-of-Words (BoW) model.

In the other work, Shree et al. [1] have given attention to elimination of noise, which can occur, after segmentation by using morphological filtering technique. GLCM features and discrete wavelet transformation (DWT) were employed to enhance the performance of proposed method in [1]. Whereas, the probabilistic neural network (PNN) was used to classify MRI brain tumor images. Joshi et al. [9] presented a scheme based on the analysis of statistical structure of both normal and abnormal tissues for MRI brain tumor segmentation. Features were extracted by co-occurrence matrix, and then reduced to the only relevant component. An ANN and fuzzy c-means have been used for classification. Bahadure et al. [10] proposed Berkeley Wavelet Transformation (BWT) with SVM classifier. The technique in [8] achieved 96.51%, 94.2% and 97.72% accuracy, specificity, and sensitivity, respectively.

Recently, deep learning has gained a lot of interest due to the advance in computational both hardware and software resources [11][12]. Several works have shown deep learning based methods outperforming previous state-of-the-art classical techniques in various domains, e.g., handwritten digits recognition [13], object recognition [14], image classification [15] and visual recognition [16]. Many works also focused on using deep learning models for MRI brain tumor, segmentation, classification and identification, e.g., Pereira et al. [30] proposed an automatic segmentation method based on Convolutional Neural Networks (CNN). While, Naser et al. [31] used CNNwith U-net for segmentation. Ismael et al. [31] developed residual network-based approach for classifying brain tumor types from MRI images. Also, Angelov and Gu in [17] presented a Deep Rule Based (DRB) classifier. The DRB classifier achieved impressive results on different benchmark datasets outperforming some of the previous methods.

In this paper, we propose a new approach for classification of MRI imaging into different kinds of brain tumors. Multiclass classification is at times a tedious and challenging problem in comparison with binary classification (e.g., in pathological and non-pathological) [8]. The presented framework first extracts ROI from MRI brain images, which contains the main disease information. Then, BSIF descriptor is used to extract features from each ROI. This descriptor is very robust and gives best results in comparison with the state-of-the-art descriptors. Furthermore, to enhance the performance of the proposed system, the best BSIF features that attain higher performances are combined to construct a bank of BSIF filters. Later, the DRB classifier is applied to classify the given ROI of MRI brain tumor into different pathological types.

The rest of the paper is structured as follows. Section 2 presents the flowchart of the proposed approach, including the extraction of ROI method, feature descriptor and DRB classifier used in the proposed system. Validation process, data set and experimental results are discussed in Section 3. Conclusion and future work are presented Section 4.

ARCHITECTURE OF PROPOSED DRB-BSIF CLASSIFIER

The flowchart of DRB-BSIF classifier is presented in Figure 1. The framework contains four steps:

- Step 1: It consists of the segmentation and extraction of the ROI in the medical image, which is very important to improve the classification performance.
- Step 2: The features are extracted from the ROI using BSIF descriptor, which is detailed in section 2.2.
- Step 3: The DRB classifier is applied to classify the given ROI of MRI brain tumor into different pathological types, which is presented in details in section 2.3.
- Step 4: The final step consists of the decision maker, which decides the class label that tested image belongs to.

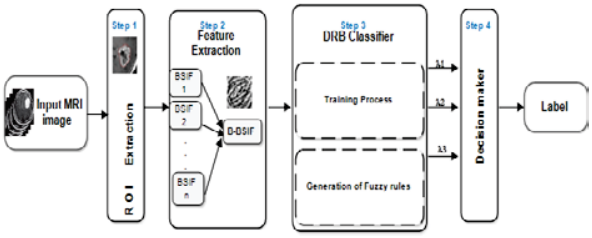

Fig. 1: DRB-BSIF Classifier Architecture

Extraction of the Region of Interest (ROI)

For medical images, the region of interest is the lesion area for doctors, which contains the main disease information. In this work, the procedure employed for the extraction of the ROI is same as used in [8]. The ROI extraction technique is as follows: first, the tumor region is augmented by image dilation and used as the ROI rather than the initial tumor region, because tumor-neighboring tissues can provide significant indications for the identification of tumor types. Second, the augmented tumor region is fragmented to progressively fine ring-form sub regions. Finally, we can apply a local feature descriptor to extract the features from the extracted ROI.

Feature Extraction

Good feature descriptor is important to produce satisfactory classification results [18]. Several local image descriptors are proposed in the literature, e.g., WLD (Weber Local Descriptor) [19] [20], PHOG (Pyramid of Histogram of Oriented Gradients) [21], LBP (Local Binary Pattern) [22], LPQ (Local Phase Quantization) [23] and BSIF (Binarized Statistical Image Features) [24]. Motivated by the success of BSIF technique in natural images classification and iris recognition [24] [25] [26], we intend to explore this technique in this work of MRI brain tumor classification.

Exploring Binarized Statistical Image Features (BSIF)

In this work, we have explored BSIF [24], which is a local image descriptor founded on LBP and LPQ techniques. In contrast to these methods, BSIF does not use predefined set of filters but learns the filters from natural images. These learned filters are used to describe each pixel of the ROI as a binary string, which corresponds to binarized responses of learned convolution filters. Further, the histogram of the pixels binary string values produces BSIF features describing efficiently texture proprieties of the image sub regions. A group of filters of patch size $l \times l$ are learned using input images and independent component analysis (ICA) [24][27]. Patch size l is given as: $l = (2 * n + 1)$,

Where $n \in \{1, 2...8\}$. The set of pre-learnt filters from natural images is used to extract the texture features from images. Suppose that an image is presented as $I(x, y)$ and the filter is represented by $h_i(u, v)$, where i represents the basis of filter, the linear response of filter s_i can be given as [24]:

$$s_i = \sum_{x,y} I(u,v) h_i(u,v) \quad (1)$$

Where x and y stand for the dimension of image and filter, respectively. Hence, the response is binarized based on the attained response value. In this case, if the linear filter response is more than the threshold, a value of 1 is assigned, otherwise 0. This process is defined as:

$$b_i = \begin{cases} 1 & if\ s_i > 0 \\ 0 & otherwise \end{cases} \quad (2)$$

The obtained responses at different basis are used to construct the new gray code for the pixel value. Since the descriptors are constructed using the filters learnt through set of natural images, the response of the filters achieved is maximally independent in terms of statistical significance [24]. Descriptor being derived from the statistics of the image, the constructed feature set of image is termed as Binarized Statistical Image Features [27][24]. Finally, the BSIF features are obtained as a histogram of pixel's binary codes, which can efficiently describe the texture components of the MRI image. There are two essential factors into BSIF descriptor explicitly: the filter size and the length of the filter. Single filters with a fixed length may not be capable of generalizing well the brain tumor patterns with varying intensities, scale and orientations. Therefore, we propose to utilize high performing multiple filters with different scales in order to capture eminent features, thus the named bank of BSIF (B-BSIF), which are further detailed in the experimental section. **Figure 2** shows an example of an MRI image and the results of BSIF filters processing. **Figure 2a** presents the input ROI MRI image. **Figure 2b** illustrates the learned BSIF filter with a size 17 × 17 and of length 11 bits. While, **Figure 2c** depicts the results of the individual convolution of the ROI MRI image with respective BSIF filters. **Figure 2d** presents the final BSIF encoded feature/image.

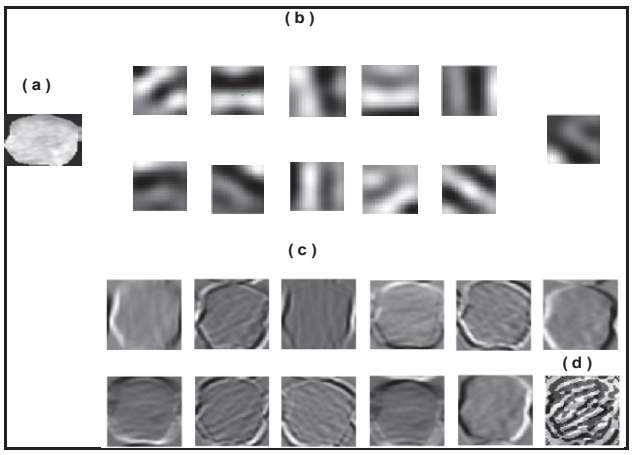

Fig. 2: (a) Example of the MRI ROI image, (b) BSIF filter (17 x 17) length 11, (c) features by BSIF filter, (d) final result of BSIF

Classification

There are various techniques proposed for classification of data. Motivated by the high classification accuracy achieved by the DRB classifier in [17], we explore it for the classification of MRI brain tumors. To the best of our knowledge, this is the first work to utilize this technique for MRI brain tumor classification.

Deep Rule-Based Classifier for MRI Brain Tumor Classification

The advantage of deep rule-based classifier approach is that it combines two powerful and successful techniques that have proven their efficiently and highly accurate results in various image-processing problems [28][29]. However, these two techniques have a number of shortcomings and deficiencies that the DRB system benefits from. The first technique is the Deep Convolutional Neural Networks (DCNNs) that can achieve very high classification accuracy. However, the most important problem is that they require a huge amount of training data and a full retraining for images for new classes. They produce good results only when the images show similar properties with the training images, but they are not able to deal with uncertainties [28]. Furthermore, their parameters are usually unclear and not easily interpretable [30]. In contrary to the DCNNs, the second technique, traditional Fuzzy Rule Based (FRB) system, is an efficient approach to deal with uncertainties by offering a transparent and understandable structure. Nonetheless, they could not achieve high level performance as DCNNs due to their small internal structure [30][29][31]. Therefore, the DRB classifier combines the advantages of FRB system applied to image classification problem with the deep learning, which offers the concept of multi-layer Fuzzy structure.

In this work, we have explored the FRB layer, which represents the "engine" of the DRB classifier and is based on the autonomously self-developing fuzzy rule-based models of the AnYa type [29]. AnYa represents a set of IF…THEN… fuzzy rules that are non-parametric and do not require the membership function to be pre-defined. Instead, they emerge from the data pattern automatically following the concept of Empirical Data Analytics. This layer contains two main processes (i.e., training process and generation of fuzzy rules). The process contains three stages (i.e., initialization, preparation and update of the system). Large dataset is used to train the DRB system. Once the training process is completed, every subsystem generates one fuzzy rule corresponding to its own class based on the identified prototypes. The fuzzy rules generated by our proposed system BRB-BSIF are represented in Table 9.

Different Steps of the FRB Layer

Step 1: Initialization

The system is initialized by the image of the C^{th} class by applying the vector normalization to the global vector *Ic1*, denoted by: $x_{c,l} = [x_{c,1}, x_{c,2,\ldots\ldots\ldots x_{c,d}}]$, where *d* is the dimensionality.

$$x_{c,l} \Big/ \|x_{c,l}\| \tag{3}$$

The different parameters of the system are initialized as follows:

$$k_{\leftarrow}1;\ \mu_{c\leftarrow}\bar{x}_{cl}\ ; N_{c\leftarrow}1; P_{c,Nc\leftarrow}I_{c,1;}\ P_{c,Nc\leftarrow}\bar{x}_{cl}\ ;\ S_{c,Nc\leftarrow}1; r_{c,Nc\leftarrow}r_0, \tag{4}$$

where *K* represents the current instance; μ_c is le global mean of the observed images of the cth class, $P_{c,Nc}$ is the mean of feature vectors of images related with the first data cloud with the prototype $P_{c,Nc}$, $S_{c,Nc}$ is the number images related with the date cloud, and $r_{c,Nc}$ represents the radius of the area of the data cloud initialized by r_0, which is a small value to stabilize the new created data cloud.

Step 2: Preparation

For each image arrived Kth, $k \leftarrow k+1$ that represent the current time instance

For the Cth class, the vector normalization is applied to its corresponding feature vector and the global mean μc is updated by equation (5):

$$\mu_c \leftarrow \frac{k-1}{k}\ \mu_c + \bar{x}_{c,k} \tag{5}$$

The data densities of all the identified prototypes are calculated as equation (6):

$$D(\mathbf{P}_{c,i}) = \frac{1}{1+\ \|P_{c,i}-\ \mu_c\ \|^2/\sigma_c^2} \tag{6}$$

where $\sigma_c^2 = 1 - \|\mu_c\|^2$ due to the vector normalization operation.

Step 3: Updating System

In this stage, two conditions are checked:

The first one is checked to see whether the newly image Ick becomes new prototype and initialize a new data cloud by using Equation 8:

Condition1:

$$IF\ \left(D\ (\ I_{c,k}\right) >^{max}_{j=1,2,\ldots\ldots Nc}\ (D(P_{c,i})))$$

$$OR(D(I_{c,k}) <^{min}_{j=1,2,\ldots\ldots Nc}\ (D(P_{c,i})))$$

$$THEN\ I_{c,k}\ \text{is a new prototype} \tag{7}$$

$$N_{c\ \leftarrow} + N_c\ + 1;\ \mathbf{P}_{c,Nc\leftarrow}I_{c,k}; P_{c,N_c\leftarrow}\bar{x}_{c,k}; S_{c,Nc\leftarrow}1;\ r_{c,Nc\leftarrow}\ r_0 \tag{8}$$

- Otherwise, the process finds the nearest prototype to $I_{c,k}$ denoted as $P_{c,n}$
- In this case, the second condition is checked:

Condition 2:

$$IF\ (\ \|\bar{x}_{c,k} -\ P_{c,n}\|) < r_{c,Nc})$$

$THEN\ (I_{c,k}\ is\ assigned\ to\ P_{c,n})$ (9)

If it is met, the new image is affected to the data cloud formed around the prototype $P_{c,n}$ - and the system updates the meta parameters of this data cloud as equation 10

$$S_{c,n} \leftarrow S_{c,n} + 1;\ P_{c,n} \leftarrow \frac{S_{c,n}-1}{S_{c,n}}\ P_{c,n} + \frac{1}{S_{c,n}} + \overline{x}_{c,k}; r^2_{c,n} \leftarrow \frac{1}{2} r^2_{c,n} + \frac{1}{2}\sigma^2_{c,n} \quad (10)$$

- Otherwise, the system initializes a new data cloud by $I_{c,k}$, which is considered as its new prototype $(N_c \leftarrow N_c + 1)$

Step 4: Fuzzy rules generation

After all the training data has been processed, the system will generate one Fuzzy rule based (Rulec) on each identified prototype.

$$IF\ \left(I\ \sim P_{c,1}\right)\ OR \ldots OR\left(I\ \sim P_{c,Nc}\right)\ THEN\ (classe\ c) \quad (11)$$

Decision Maker

In our work, 3 classes are considered, i.e., Meningioma, Glioma and Pituitary. For each image I in test, each one of the C fuzzy rules generate a score of confidence $\lambda_c(I)$ based on the feature vector of I denoted by x:

$$\underset{j=1,2,\ldots,N_c}{\arg max}\left(exp\left(-\|x - P_{cj}\|^2\right)\right) \quad (12)$$

Finally, we can get three scores of confidences $\lambda_1(I), \lambda_2(I), \lambda_3(I)$ for each image, which represent the input to the last step 'Decision Maker'. The system decides the label of the current tested image as follows:

$$\underset{c=1,2,3}{\arg\max}(\lambda_c(I)) \quad (13)$$

EXPERIMENT

In this section, we present an experimental evaluation of the proposed DRB-BSIF classifier based on Bank BSIF descriptor.

1. Database

The proposed model is evaluated on the publicly available brain T1-weighed CE-MRI dataset. This database was collected by Cheng et al [8] from Nanfang Hospital, Guangzhou, China, and General Hospital, Tianjing Medical University, China, from 2005 to 2010. Where, 3064 slices were collected from 233 patients, having 708 slices infected by Meningiomas, 1426 slices infected by Gliomas, and 930 slices infected by Pituitary tumors. The images contained an original size of 512 x512 in pixels. Three examples are illustrated in Figure 3.

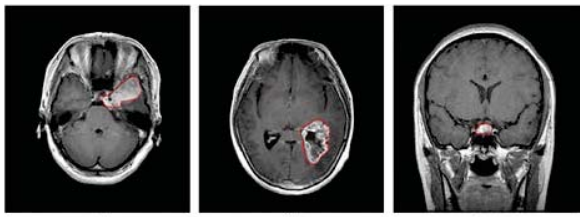

Fig.3: Illustrations of three typical brain tumors provided in the dataset [8]: (a) meningioma; (b) glioma; and (c) pituitary tumor. Red lines indicate the tumor border.

Performance Evaluation Measurements

To evaluate the performance of the classifier, three different metrics were computed, i.e., accuracy, specificity and sensitivity. The performance analysis is presented in Table 1 and Table 2. In Table 1 and Table 2, TP refers to the true positive, which is the total number of abnormal regions correctly classified. TN stands for the true negatives, which is the total number of normal regions correctly classified. FP is the number of false positive, and it is used to indicate wrongly detected or classified abnormal cases. FN is the number of false negatives; it is used to indicate wrongly classified or detected normal cases. The accuracy is the ratio of total correctly classified regions (TP+TN) and the total number of all examined regions [10].

Table 1. Confusion matrix in terms of TP, TN, FP, and FN

Expected outcome	Ground truth Positive	Negative	Row total
Positive	TP	FP	TP + FP
Negative	FN	TN	FN + TN
Column Total	TP + FN	FP + TN	TP + FP + FN + TN

Table 2. Metrics used for validation

Metrics	Formula
Accuracy	$\frac{TP + TN}{TP + TN + FP + FN}$
Sensitivity	$\frac{TP}{TP + FN}$
Specificity	$\frac{TN}{TN + FP}$

RESULTS AND DISCUSSION

Here, we report three different experiments: Experiment 1 – Construction of bank of BSIF filters, and Comparison between BSIF and B-BSIF, Experiment 2: Impact of feature descriptor used with the DRB-Classifier, and Experiment 3:

Evaluation of DRB-BBSIF model for MRI brain tumor classification.

Experiment 1 – Construction of Bank of BSIF Filters

The goal of this experiment is to boost the accuracy of our system by constructing a bank of filters BSIF. In order to select the best BSIF parameters and respective filters, several sub-experiments were performed and the results are reported in Table 3. We have explored different filters with different parameters (i.e., filter size (k) and filter length (n)). The parameters that achieve high performance have been selected and used to build the bank of BSIF (BBSIF).

These parameters are presented in Table 4, which are at this stage been fixed and used as estimated parameters for subsequent experiments. The model of the B-BSIF descriptor is illustrated in Figure 4, which represents an example using B-BSIF. As can be noticed, the bank is composed of different BSIF descriptor sizes, i.e., 17 × 17, 15 × 15, 13 × 13, 11 × 11 with the length of 11 bits. This bank of filters is introduced as an input to the DRB classifier.

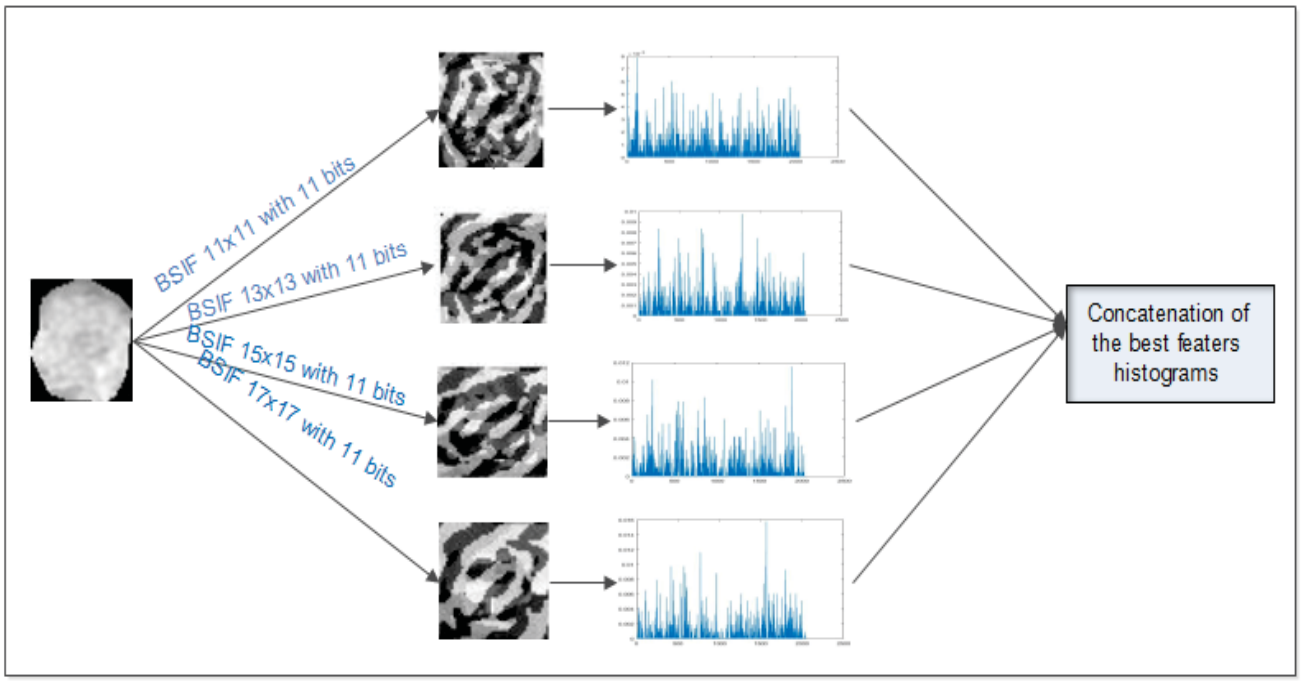

Fig. 4: The model of the B-BSIF descriptor: (a) input ROI of MRI, (b) results of applying the different BSIF descriptor (BSIF code images), and (c) the histograms of the BSIF code images

Table 3. All parameters of BSIF applied on the MRI brain tumor

Parameters		Accuracy (%)	Sensitivity (%)	Specificity (%)
k	n			
17 × 17	12	81.79	85.88	80.56
17 × 17	11	84.30	86.44	83.66
17 × 17	10	83.39	85.88	82.64
15 × 15	12	82.08	84.89	81.24
15 × 15	11	83.71	85.59	83.15
15 × 15	10	83.26	88.42	81.71
13 × 13	12	81.89	84.04	81.24
13 × 13	11	82.70	86.86	81.45
13 × 13	10	82.25	86.86	80.86
11 × 11	12	80.97	83.05	80.35
11 × 11	11	82.60	85.03	81.88
11 × 11	10	83.62	85.03	83.19

Table 4. Best BSIF filters

Parameters	
k	***n***
17 × 17	11
15 × 15	11
13 × 13	11
11 × 11	11

After the construction of the bank of BSIF filters, we attempt a comparison between the B-BSIF and BSIF descriptors. In Table 5, it can be seen that the B-BSIF gives better results, the accuracy ranging from 84.30% to 84.73%, sensitivity from 86.44% to 87.57%, and specificity from 83.66% to 83.87%.

Table 5. Comparison between BSIF descriptor and Bank BSIF

Feature descriptor	Accuracy (%)	Sensitivity (%)	Specificity (%)
BSIF	84.30	86.44	83.66
BBSIF	84.73	87.57	83.87

Experiment 2: Impact of Feature Extractor Methods used with the DRB-Classifier

In this experiment, we discuss the impact of using different feature descriptor methods with the DRB classifier.

Table 6 presents the results using different feature descriptors, including LBP, LPQ, WLD and PHOG with DRB classifier. It can be observed from table 6 that the B-BSIF descriptor used in the proposed method accomplished the best results with the DRB classifier in term of accuracy, sensitivity and specificity compared with the popular and widely used descriptors. The different feature extraction methods tested in the current work are similar because all of them represent an image as a histogram of local features. The reason for this difference in their results is that they use different local features.

Table 6. Performance of feature descriptor methods with the DRB classifier

Method	DRB With LBP	DRB with LPQ	DRB with WLD	DRB with PHOG	DRB with BSIF	DRB with B-BSIF
Accuracy (%)	73.99	77.15	75.78	79.31	84.30	84.73
Sensitivity (%)	57.77	74.72	64.97	74.29	86.44	87.57
Specificity (%)	78.86	77.89	79.03	80.81	83.66	83.87

Experiment 3: Evaluation of the DRB-BBSIF Model for MRI Brain Tumor Classification

The aim of this experiment is to study the performance of the proposed system. Table 7 shows the accuracy of the proposed system for each class. We also compared the proposed system DRB BSIF with k nearest neighbors (kNN) classifier as shown in Table 8. As shown in Table 8, the DRB-BSIF gives best performance.

Table 7. Performance of feature descriptor methods with the DRB classifier

	Meningioma	Glioma	Pituitary
Meningioma	620/708	33/708	55/708
Glioma	95/1426	1265/1426	66/1426
Pituitary	115/930	104/930	711/930
Accuracy	87.57	88.71	76.45

Table 8. Comparison of the DRB-BSIF with KNN

Method	DRB-BSIF	1NN	3NN	7NN	15NN	45NN
Accuracy (%)	84.73	80.01	81.69	83.14	83.37	83.09

Table 9. Fuzzy rules generated through the training process

Fuzzy Rules
(IF MRI~ ) OR (MRI ~ ) OR (MRI~ ) OR (MRI~ ) THEN (Meningioma)
(IF MRI ~ ) OR (MRI ~ ) OR (MRI~ ) OR (MRI~ ) THEN (Glioma)
(IF MRI ~ ) OR (MRI ~ ) OR (MRI~ ) OR (MRI ~ ) THEN (Pituitary)

CONCLUSION AND FUTURE WORK

This paper presents a new approach for MRI brain tumor classification. The main goal is to classify three types of brain tumors (i.e., Meningioma, Glioma, and Pituitary). To this objective, four main steps are involved. The first step is extraction of region of interest. The second step is the extraction of features from each ROI traits using BSIF descriptor. Moreover, we have explored different filters with different parameters (i.e., filter size (k) and filter length (n)). The parameters that achieve high performance have been selected and used to build the B-BSIF features. These features have boosted the accuracy of our system. In the third step, a deep-rule based classifier (DRB) is used for classification. DRB classifier is prototype-based natural process, which learns from data patterns and generates a fuzzy rule for each class in the same way as human. Finally, the system decides the winning class. A large dataset of T1-weighted CE-MRI brain tumors was used to test and demonstrate the effectiveness of the proposed method. Also, we have demonstrated in the current study that good visual feature is crucial to produce satisfactory classification results. As a future work, we will extend the proposed method to identify and classify other types of brain tumors. In addition, we will explore and devise different feature extraction methods based on deep learning models.

AUTHOR INFORMATION

Corresponding Author

*Hafida Chellakh

Email address: hafidachellakh@gmail.com

REFERENCES

[1] N. V. Shree and T. N. R. Kumar, "Identification and classification of brain tumor MRI images with feature extraction using DWT and probabilistic neural network," *Brain informatics*, vol. 5, no. 1, pp. 23–30, 2018.

[2] A. Attia, A. Moussaoui, and Y. Chahir, "Epileptic seizures identification with autoregressive model and firefly optimization based classification," *Evol. Syst.*, pp. 1–10, 2019.

[3] M. A. Balafar, "Fuzzy C-mean based brain MRI segmentation algorithms," *Artif. Intell. Rev.*, vol. 41, no. 3, pp. 441–449, 2014.

[4] A. Attia, A. Moussaoui, and Y. Chahir, "An EEG-fMRI Fusion Analysis Based on Symmetric Techniques Using Dempster Shafer Theory," *J. Med. Imaging Heal. Informatics*, vol. 7, no. 7, pp. 1493–1501, 2017.

[5] Y-D. Zhang and L. Wu, "An MR brain images classifier via principal component analysis and kernel support vector machine," *Prog. Electromagn. Res.*, vol. 130, pp. 369–388, 2012.

[6] R. Nalbalwar, U. Majhi, R. Patil, and S. Gonge, "Detection of Brain Tumor by using ANN," *Image (IN).*, vol. 2, no. 3, p. 7, 2014.

[7] K. Van Leemput, "Brain mri segmentation using an expectation-maximization algorithm," *Tutor. MICCAI 2003*, 2003.

[8] J. Cheng *et al.*, "Enhanced performance of brain tumor classification via tumor region augmentation and partition," *PLoS One*, vol. 10, no. 10, p. e0140381, 2015.

[9] J. Joshi and A. C. Phadke, "Feature extraction and texture classification in MRI," *Energy*, vol. 1, p. 0, 2010.

[10] N. B. Bahadure, A. K. Ray, and H. P. Thethi, "Image analysis for MRI based brain tumor detection and feature extraction using biologically inspired BWT and SVM," *Int. J. Biomed. Imaging*, vol. 2017, 2017.

[11] I. Goodfellow, Y. Bengio, and A. Courville, *Deep learning*. MIT press, 2016.

[12] Y. LeCun, Y. Bengio, and G. Hinton, "Deep learning," *Nature*, vol. 521, no. 7553, p. 436, 2015.

[13] D. C. Ciresan, U. Meier, L. M. Gambardella, and J. Schmidhuber, "Convolutional neural network committees for handwritten character classification," in *2011 International Conference on Document Analysis and Recognition*, 2011, pp. 1135–1139.

[14] K. Jarrett, K. Kavukcuoglu, Y. LeCun, and others, "What is the best multi-stage architecture for object recognition?," in *2009 IEEE 12th international conference on computer vision*, 2009, pp.

2146–2153.
[15] S. Gao, L. Duan, and I. W. Tsang, "DEFEATnet—A deep conventional image representation for image classification," *IEEE Trans. Circuits Syst. Video Technol.*, vol. 26, no. 3, pp. 494–505, 2015.
[16] K. Kavukcuoglu, P. Sermanet, Y.-L. Boureau, K. Gregor, M. Mathieu, and Y. L. Cun, "Learning convolutional feature hierarchies for visual recognition," in *Advances in neural information processing systems*, 2010, pp. 1090–1098.
[17] P. P. Angelov and X. Gu, "Deep rule-based classifier with human-level performance and characteristics," *Inf. Sci. (Ny).*, vol. 463, pp. 196–213, 2018.
[18] D. Selvaraj and R. Dhanasekaran, "A review on tissue segmentation and feature extraction of MRI brain images," Int. J. Comput. Sci. Eng. Technol., vol. 4, no. 10, pp. 1313–1332, 2013. [19] S. Li, D. Gong, and Y. Yuan, "Face recognition using Weber local descriptors," *Neurocomputing*, vol. 122, pp. 272–283, 2013. [20] S. Liu, Y. Zhang, and K. Liu, "Facial expression recognition under partial occlusion based on Weber Local Descriptor histogram and decision fusion," in *Proceedings of the 33rd Chinese Control Conference*, 2014, pp. 4664–4668.
[21] A. Bosch, A. Zisserman, and X. Munoz, "Representing shape with a spatial pyramid kernel," in *Proceedings of the 6th ACM international conference on Image and video retrieval*, 2007, pp. 401–408.
[22] T. Ojala, M. Pietikäinen, and T. Mäenpää, "Multiresolution gray-scale and rotation invariant texture classification with local binary patterns," *IEEE Trans. Pattern Anal. Mach. Intell.*, no. 7, pp. 971–987, 2002.
[23] A. Dhall, A. Asthana, R. Goecke, and T. Gedeon, "Emotion recognition using PHOG and LPQ features," in *Face and Gesture 2011*, 2011, pp. 878–883.
[24] J. Kannala and E. Rahtu, "Bsif: Binarized statistical image features," in *Proceedings of the 21st International Conference on Pattern Recognition (ICPR2012)*, 2012, pp. 1363–1366.
[25] K. B. Raja, R. Raghavendra, and C. Busch, "Binarized statistical features for improved iris and periocular recognition in visible spectrum," in *2nd International Workshop on Biometrics and Forensics*, 2014, pp. 1–6.
[26] A. Attia, M. Chaa, Z. Akhtar, and Y. Chahir, "Finger kunckcle patterns based person recognition via bank of multi-scale binarized statistical texture features," *Evol. Syst.*, pp. 1–11, 2018.
[27] A. Hyvärinen, J. Hurri, and P. O. Hoyer, *Natural image statistics: A probabilistic approach to early computational vision.*, vol. 39. Springer Science & Business Media, 2009.
[28] P. Angelov, *Autonomous learning systems: from data streams to knowledge in real-time*. John Wiley & Sons, 2012.
[29] P. Angelov and R. Yager, "A new type of simplified fuzzy rule-based system," *Int. J. Gen. Syst.*, vol. 41, no. 2, pp. 163–185, 2012.
[30] P. Angelov and X. Gu, "Autonomous learning multi-model classifier of 0-order (ALMMo-0)," in *2017 Evolving and Adaptive Intelligent Systems (EAIS)*, 2017, pp. 1–7.
[31] P. P. Angelov and X. Zhou, "Evolving fuzzy-rule-based classifiers from data streams," *IEEE Trans. Fuzzy Syst.*, vol. 16, no. 6, pp. 1462–1475, 2008.

2023

Ensemble Transfer Learning for Improved Brain Tumor Classification in MRI Images

S. Hamdi,[a,*] A. Moussaoui,[a] M. Berrimi,[a] A. Laouarem,[a] M. Chabane,[a]

[a] Department of computer Science, University of Ferhat Abbes Setif 1, 19000, Algeria

ABSTRACT: Brain tumors are a common type of cancer that affects the central nervous system, and their accurate diagnosis is crucial. Deep learning models have shown remarkable success in medical imaging applications, including brain tumor classification from MRI images. Transfer learning, using pre-trained models as a starting point, is an effective technique for developing DL models for medical imaging. The study aims to validate the effectiveness of ensembling different pre-trained models to classify four categories of brain tumors; Glioma Tumor, Meningioma Tumor, Pituitary Tumor, or No Tumor. Also, the study aims to compare the performance of the proposed approach with individual pre-trained models. The method utilizes transfer learning with an ensemble approach for brain tumor classification from MRI images. The three pre-trained models used are ResNet50, EfficientNet, and MobileNet, with weights assigned to the ImageNet dataset. The pre-trained models are combined using a simple averaging ensemble method. We used 15% of the dataset for testing and the rest for training and validation. The performance of the ensemble method is compared with each of the individual pre-trained models using various evaluation metrics. The proposed approach achieved the highest accuracy (97.14%) and outperformed the individual pre-trained models in terms of most of evaluation metrics. Overall, the results show that the proposed method is effective for brain tumor classification from MRI images. In conclusion, our proposed approach based on the ensemble of ResNet50, EfficientNet, and MobileNet achieved superior classification performance compared to each individual model for the task of brain tumor classification. Our results validate that employing an ensemble of different pre-trained classifiers can be a valuable tool for improving the performance of medical image analysis, where accurate diagnosis is critical for patient treatment.

Keywords: Brain Tumours; Medical imaging; Magnetic Resonance Imaging (MRI); Transfer Learning; Convolutional Neural Networks.

INTRODUCTION

Brain tumors are one of the most common types of cancers that affect the central nervous system. According to the American Brain Tumor Association, about 80,000 new cases diagnosed each year. Brain tumors can be classified into several types based on their origin, location, and histological characteristics. The most common types of brain tumors include Gliomas, Meningiomas, and Pituitary tumors. Magnetic Resonance Imaging (MRI) is a non-invasive medical imaging technique that provides high-resolution images of the brain. It is the preferred imaging modality for the diagnosis and monitoring of brain tumors. MRI images of brain tumors are complex, with variations in shape, size, and texture. Manual interpretation of MRI images is a time-consuming and error-prone task, requiring specialized training and expertise. Deep learning (DL) models have shown remarkable success in various medical imaging applications, including the detection and classification of brain tumors from MRI images. These models can automatically learn the relevant features from the images and classify them into different categories, providing accurate and efficient diagnosis. Transfer learning, which involves using pre-trained models as a starting point and fine-tuning them for a specific task, has become a popular technique for developing DL models for medical imaging. Several studies have reported the effectiveness of pre-trained DL models for brain tumor classification from MRI images. For instance, a study by R. Hao et al.[1], compared two versions of AlexNet, the first was trained from scratch and the second was the original pre-trained. The superiority of the pre-trained version was demonstrated by showing an Area Under Curve score of 79.91%. Another study conducted by C. Srinivas et al.[2], three pre-trained models have been evaluated VGG16, ResNet50 and InceptionV3. It has been denoted that VGG16 achieved 96% of overall accuracy. M. Arbane et al.[4] proposed to

use ResNet, Xception, and MobilNetV2, and the latter achieved 98.24% of accuracy. Another recent work by M. M. Islam et al.[5] achieved the highest performance using MobileNet by injecting one fully connected layer to classify four types of brain tumors, reaching 99.60% of accuracy. The motivation behind this study is to develop an accurate and efficient DL model for the classification of brain tumors from MRI images info four categories: Gliomas, Meningiomas, Pituitary and the absence of tumors, by using an ensemble model that combines the output of ResNet50, EfficientNet, and MobileNet. This study will also compare and validate the effectiveness of our ensembling method against each of the used trained models; ResNet50, EfficientNet and MobileNet. The objective of this study is to propose a new ensemble learning approach that combines three pre-trained Convolutional Neural Network (CNN) models for the classification of brain tumors from MRI images. Specifically, we aim to classify the images into four categories: Glioma Tumor, Meningioma Tumor, Pituitary Tumor, or No Tumor. We will compare the performance of our ensemble model with the individual pre-trained models (ResNet50, EfficientNet, and MobileNet) to determine the effectiveness of our proposed approach. Our proposed approach aims to achieve a higher classification accuracy than the individual pre-trained models, and, more precisely, demonstrates the performance boosting using ensemble techniques, which would improve the diagnosis and treatment of brain tumors.

EXPERIMENTAL

The proposed method utilizes transfer learning with an ensemble approach for brain tumor classification from MRI images. Figure 1 illustrates the general structure of our approach. We used the weights assigned to the ImageNet dataset for all three pre-trained models, ResNet50, EfficientNet, and MobileNet. A GlobalAveragePooling2D layer, which is a common choice for transfer learning, as it allows reducing computational cost of the pre-trained models, while also providing regularization benefits, followed by a Dropout layer with a rate of 0.5 to prevent overfitting, and then, an output layer with 4 units (corresponding to the number of classes) and Softmax activation function. The input of our model is an image of size 150x150 pixels and 3 color channels. The outputs of the three pre-trained models are then combined by a simple averaging ensemble method, taking their average as the output. We employed a total of 3264 images, with 15% used for the unseen testing set and the remaining 85% divided into training (85%) and validation (15%) sets. We used a publicly available dataset, available in Kaggle platform[3].

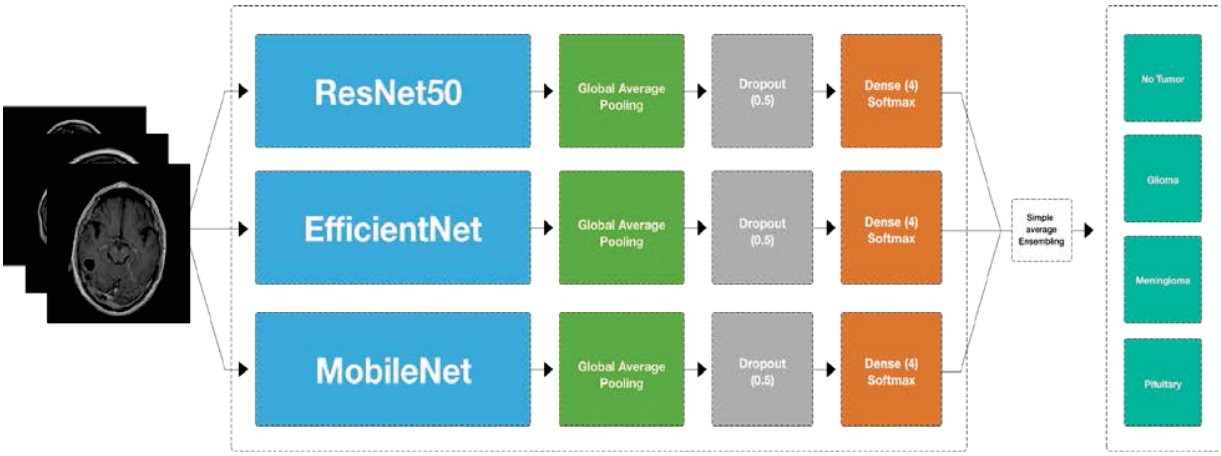

Fig. 1: Systematic overview of the proposed system

Table 1 shows the distribution of each of the four classes while Figure 2 exemplified one image sample of each class. To demonstrate the effectiveness of our proposed approach, we compare the performance of our averaging ensemble method with each of the three pre-trained models. We evaluate our model using various metrics such as Accuracy, Precision, Sensitivity, AUC, and Specificity. We used categorical cross-entropy as a loss function and Adam optimizer. Our ensemble model has been trained for 50 epochs. The model's validation has been done using 5-Fold Cross-Validation using the same hyper-parameters.

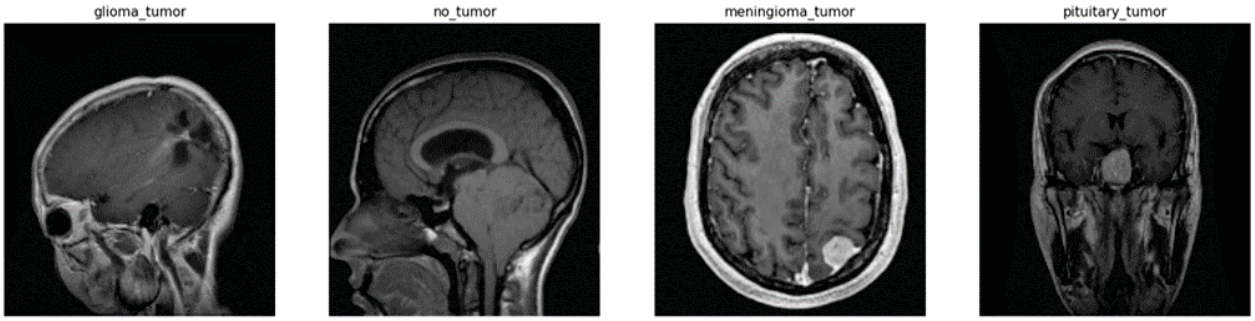

Fig. 2: A sample of each of the four classes

Table 1. The number of samples count of the employed dataset

	No Tumor	Glioma	Meningioma	Pituitary
Image count	500	926	937	901

RESULTS AND DISCUSSION

After training our model in about 18 minutes, the aforementioned evaluation metrics (Accuracy, Precision, Sensitivity, AUC, and Specificity) were computed. Table 2 summarized all obtained testing results for ResNet50, EfficientNet, MobileNet, and Ensemble-based method. Our proposed approach based on the ensemble of ResNet50, EfficientNet, and MobileNet achieved an accuracy of 97.14%, which is slightly higher than the accuracy of each individual model. The ensemble approach also achieved higher precision, sensitivity, and specificity values than each individual model, indicating better performance across different evaluation metrics. However, the results have shown a slightly better performance of EfficientNet in terms of AUC metric. These results demonstrate the effectiveness of ensemble learning in improving the classification performance of pre-trained models on brain tumor images. It is important to note that the improvement in performance achieved by our ensemble method is relatively small compared to the performance of individual pre-trained models. This was attributed to the fact that ResNet50, EfficientNet, and MobileNet are already powerful models with high accuracy rates for image classification tasks (as shown in Table 3). However, even small improvements in performance can be significant in medical image analysis, where accurate diagnosis is crucial for patient treatment. We note as well for the cross-validation results, a small values of standard deviation for all metrics, and this is attributed to the model's stability and performance consistency. Our results are also consistent with previous studies that have shown the effectiveness of pre-trained models in various image classification tasks. We introduced a simple averaging ensemble method to reduce possible overfitting, improve generalization, and increase the models' robustness in handling different data variations.

Table 2. Summary of testing results for each of the pre-trained models, as well as the proposed approach.

	Accuracy	Precision	Sensitivity	AUC	Specificity
ResNet50	96.53%	96.31%	96.65%	99.80%	96.65%
EfficientNet	96.93%	97.04%	97.19%	99.84%	97.19%
MobileNet	96.93%	97.01%	96.97%	99.48%	96.97%
Proposed Approach	**97.14%**	**97.30%**	**97.42%**	99.73%	**97.42%**

Table 3. 5-Fold Cross-validation average results of the proposed approach (Average ± Standard Deviation).

	Accuracy	Precision	Sensitivity	AUC	Specificity
Proposed Approach	98.6% ± 0.07%	96.94% ± 0.095%	97.36% ± 0.11%	99.55% ± 0.03%	97.36% ± 0.11%

CONCLUSIONS

In conclusion, our proposed approach based on the ensemble of ResNet50, EfficientNet, and MobileNet achieved superior classification performance compared to each individual model for the task of brain tumor classification. Our results validate that employing an ensemble of different pre-trained classifiers can be a valuable tool for improving the performance of medical image analysis, where accurate diagnosis is critical for patient treatment. As perspective, we aim to consider a larger dataset with model fine-tuning and then weighting each of the pre-trained models to benefit from strengths of each of them in the ensemble approach.

AUTHOR INFORMATION

Corresponding Author

Skander Hamdi

Email address: skander.hamdi@univ-setif.dz

REFERENCES

1. R. Hao, K. Namdar, L. Liu, F. Khalvati, A Transfer Learning–Based Active Learning Framework for Brain Tumor Classification, Front. Artif. Intell. 4 (2021). https://doi.org/10.3389/frai.2021.635766.
2. C. Srinivas, N.P. K. S., M. Zakariah, Y.A. Alothaibi, K. Shaukat, B. Partibane, H. Awal, Deep Transfer Learning Approaches in Performance Analysis of Brain Tumor Classification Using MRI Images, J. Healthc. Eng. 2022 (2022) 3264367. https://doi.org/10.1155/2022/3264367.
3. S. Bhuvaji, A. Kadam, P. Bhumkar, S. Dedge, and S. Kanchan. (2020). Brain Tumor Classification (MRI) [Data set]. Kaggle. https://doi.org/10.34740/KAGGLE/DSV/1183165
4. M. Arbane, R. Benlamri, Y. Brik and M. Djerioui, "Transfer Learning for Automatic Brain Tumor Classification Using MRI Images," 2020 2nd International Workshop on Human-Centric Smart Environments for Health and Well-being (IHSH), Boumerdes, Algeria, 2021, pp. 210-214, doi: 10.1109/IHSH51661.2021.9378739.
5. M.M. Islam, P. Barua, M. Rahman, T. Ahammed, L. Akter, J. Uddin, Transfer learning architectures with fine-tuning for brain tumor classification using magnetic resonance imaging, Healthc. Anal. 4 (2023) 100270. https://doi.org/https://doi.org/10.1016/j.health.2023.100270.

2023

Class Imbalance and Evaluation Metrics for Medical Image Segmentation with Machine Learning Models

Y. Azzi,[a]* A. Moussaoui,[a] M.T. Kechadi,[b]

[a] Department of Computer Science, Faculty of Sciences, Ferhat Abbas Setif1 University, Sétif-19000, Algeria

[b] University College Dublin, Ireland

.

ABSTRACT: Automatic image segmentation is a crucial aspect of image analysis that has seen significant advancements and challenges with the emergence of machine learning algorithms. The effectiveness of a machine-learning model depends on its ability to produce results that closely resemble the ground truth image, and this is measured using various metrics. However, not all metrics are equally suitable for evaluating image segmentation especially with the presence of the class imbalance problem, which refers to the imbalance distribution of the classes with one or more classes having significantly fewer pixels than others where the segmentation focuses on infrequent classes and this can affect the accuracy and reliability of the evaluation metrics. This study aims to determine the most critical metrics suitable for image segmentation, with a focus on medical images, using some supervised machine-learning model for brain tumour segmentation and shows the negative impact of the class imbalance problem on the evaluation metrics. In this study, we propose a deep learning, support vector machine and random forest models to segment brain gliomas from multi-modal MRI images to whole tumor, tumor core and enhancing tumor classes.. The metrics used are Accuracy, Dice-Score, Sensitivity and specificity. This method achieved a Dice score that varies between 0.35 and 0.95 with sensitivity between 0.70 and 0.95 and specificity from 0.82 to 0.99 on all training, test datasets and all classes including whole tumour, tumour core and enhancing tumour. Despite this, the accuracy metric achieved 0.96 to 0.99 overall, which raises concerns about its reliability in this context. In conclusion, this study highlights the importance of choosing the most appropriate evaluation metrics when assessing the performance of machine learning models for image segmentation, especially in the medical field. Our experiments show that while the accuracy metric achieved highs scores, it may not be the most reliable metric to use in this context due to the presence of the class imbalance. The other metrics such as Dice-Score, Sensitivity and Specificity may provide a more nuanced and robust evaluation of model performance.

Keywords: Class imbalance; Metrics; Image Segmentation; Machine Learning.

INTRODUCTION

In computer vision, image analysis is the ability of computers to extract useful hidden patterns in the image scene for deeper context understanding. Image segmentation stands as a pivotal technique within the realm of image analysis it represents the process of dividing an image into a set of regions to identify and locate the objects that are in the scene. It is used in different domains like content-based image retrieval, medical imaging, robotics, real-time self-driving cars, video surveillance and automatic traffic control.[1-2]. Over the years, Automatic medical image segmentation has been a very competitive research[3] field since the beginning of image processing technologies. Numerous approaches have been proposed, studied, and used. One can distinguish two categories of techniques: classical and

machine learning-based the classical techniques are those based on low-level pixel processing. They use the pixel values to detect contours like Canny, Laplacian detectors, or determine regions like the thresholding method, region growing algorithm Machine-learning techniques represent a quantum leap in general artificial intelligence. They are free of rigid prior programmed rules. The core concept is to learn hidden patterns (features) from data and construct predictive models that can segment unseen data. The learning process can be either supervised or unsupervised. They are recently the most frequently implemented for automatic medical image segmentation. Unsupervised-learning algorithms are designed for unlabeled datasets. Clustering is a well-known technique in this category; it aims to group pixels or voxels into a set of unknown classes using similarity criteria like Euclidian distance. They are considered as optimization problems where the objective function is to maximize intra-class similarity and inter-class dis-similarity. K-means and fuzzy c-means are popular algorithms in this context. Moreover, prior human expert knowledge is necessary to interpret the results correctly. Supervised techniques use labelled segmented data as training data to build the models. In other words, the model takes the input data and the desired output during the training phase to produce results close to the desired outputs. There is a panoply of methods, such as K-nearest neighbors (KNN), Support Vector Machines (SVM)[4-5-6-7]Random Forest (RF)[8] and deep neural network (DNN)[9].

However, this process in such a sensitive field is fraught with several challenges[10], which encompass variations in image quality and acquisition due to diverse imaging technologies, anatomical differences among individuals, complexities presented by structures with ambiguous boundaries, the computational demands required to process large datasets efficiently and class imbalance issues that affect minority class segmentation.

The class imbalance is regarded as a reputed challenge that faces image segmentation with machine learning techniques[11], It refers to a situation in which the distribution of the label classes is significantly imbalanced, this means that one class often the majority class is represented by a remarkably higher number of instances and predominate other classes which can impact the model learning process, leading to a highly biased model toward the majority class and a neglect of the minority class due to the difficulty to effectively capturing its feature.

The class imbalance in medical images refers to the unequal distribution of pixels or voxels belonging to different classes or structures within the images where the minority class typically is the region of interest such as tumors and lesions which is the aim region of the segmentation process and the remaining areas such as normal healthy tissues and background as the majority class. This imbalance can markedly affect the learning process, potentially resulting a model that predominantly segments normal and background pixels only (Fig 1).

Due to this issue, selecting metrics for evaluating machine learning model performance becomes challenging, because it highly influences metrics that heavily weigh the majority class or consider true negatives in evaluations, potentially yielding misleading results.

To handle this problem several solutions have been proposed such as data augmentation, oversampling, under-sampling, patch based segmentation and the appropriate choice of evaluation metrics to detect the correct performance of the model; numerous works have focused on this last point to expose the most suitable evaluation metrics for image segmentation tasks [12-13-14].

This study aims to exhibit the impact of the class imbalance problem on machine learning evaluation metrics in medical image segmentation in which we propose to perform a brain tumor segmentation using different machine learning models as deep learning, support vector machines and random forest.

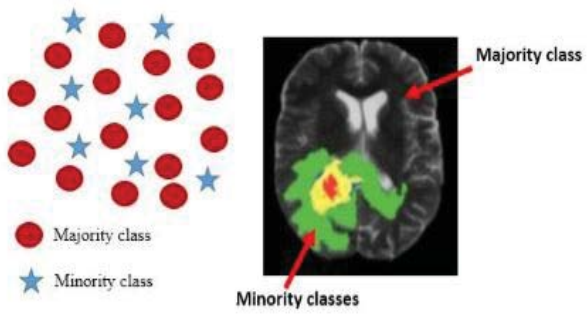

Fig.1: Class imbalance

EXPERIMENTAL

Methods

In this work, we propose to segment a kind of the most life-threatening primary brain tumors called gliomas from multi-modal MRI images (T1CE, T1, T2, Flair) using a deep learning(DL) architecture, a support vector machine(SVM) and random forest(RF) models.

Our DL architecture is inspired from the well-known deep learning architecture used for biomedical image segmentation U-net[15], where we proposed a customized u-net used in multi-pathway mode to deal with MRI modalities. Each image modality goes through a processing U-net pathway and before generating the final prediction map the final pathways results are merged or concatenated. The customized U-net is designed symmetrically as follows: the contraction path: also called the encoder path, consists of three levels each level is made of two consecutive (3*3)

convolution layers of 16 learning filters doubled for each level, each followed by an Activation Layer with RELU function parameters, then the result (R) of these layers go through a (2*2) pooling layer followed by batch normalization layer and Dropout layer to prevent over-fitting. The expanding path: also called the decoder path, consists of three levels too each level is made of a transposed convolution layer, then a concatenation layer known also as skip connection between the two symmetric path where the result (R) is concatenated with the transposed convolution result to get more information, then a dropout layer and two consecutive (3*3) convolution layers each followed by an Activation Layer with RELU function parameters are applied. The paths are related between them by two consecutive (3*3) convolution layers each followed by an Activation Layer with RELU function parameters called a bridge. The final outputs of the expanding paths from each modality are concatenated and then the resulting map goes through a (1*1) convolution layer with a sigmoid activation function to generate the final prediction map Fig 2.

Fig. 2: The parallel pathway architecture

For both SVM and RF we suggest using predefined scikit-learn python models with a customized feature selection step. Feature extraction is a primordial step in this context, from the fact that each pixel has characteristics used for the discrimination between the tumour and the healthy pixels. For both SVM and RF a feature selection step was performed naively, the first main feature was the image pixel intensities in addition to a texture feature computed using Gabor filter and some edge features computed by Sobel, Roberts, Canny, Scharr, prewit Gaussian and median kernels.

DATASETS

The Data sets used in this work are the brain tumor segmentation training 2020, 2018 release (BRATS2020) which contains a set of MRI images of 369,288 patients respectively diagnosed with high-grade gliomas (Glioblastoma) and low-grade gliomas. Each patient has four MRI modalities images: native pre-contrast (T1), post-contrast T1-weighted (T1c), T2-weighted (T2), and T2 Fluid Attenuated Inversion Recovery (FLAIR). In addition to the manual segmentation file where all pixels were segmented into four classes with four rates (0, 1, 2, 4) summarized in Table 1, All Brats multi-modal scans are pre-processed: co-registered to the same anatomical template, interpolated to the same resolution (1 mm3^) and skull stripped . Table 1 expose the data information.[16-17-18]

Table 1. BRATS 2018/2020 releases training sets information

BraTS_2018		BraTS_2020
Gliomas grade	HGG & LGG	
# of patients	285	369
Modalities	T1, T1CE, T2, FLAIR	
Dimension	(240,240,155)	
Format	Nifty (Nii.gz)	
Ground truth	Available in seg.nii.gz file	
Labels	0 =background and healthy tissue 1= Necrotic /non-enhancing (NCR/NET). 2= Peritumoral edema (ED) 4 =Enhancing tumour (ET)	

Implementation

To simplify the work and avoid the multi-class segmentation problem the BRATS challenge organization propose to use new

classes instead those in Table 1 and perform binary segmentation for each class separately then merge the final results. The new labels are as follows:

- Whole Tumor: group labels(1,2,4) into 1
- Tumor Core: group labels (1,4) into 1 and the remaining classes to 0
- Enhancing Tumor: turn label 4 into 1 and the remaining classes to 0

Our Deep Learning model was implemented using Python3 with the Keras library. The experiments were run on the UB2-HPC

(University of BATNA 2-Algeria-) GPU node which contains 4 Nvidia GPUs configured with CUDA 10.0 and CuDNN 5.6.7. The Brats 2020 training dataset was split randomly into Train set 80% and Valid set 10% and Test set 10% with 42 random states. The model is trained over the Train set and to prevent over-fitting the Valid set is used, finally, the built final model is tested over the Test set.

For each class a DL model is trained over 2D MRI images in the axial view each cropped from (240,240,155) to (160,160,128) with the following indices [40:200,40,200,12:140] the slices are

organized as follows:

- Each slice in Each modality must be from the same patient and the same index to respect the parallel pathways inputs
- The slices in the same modality are charged as follows: each index slice is charged from all patient's files to guarantee the perfect data shuffle.

The final Network parameters are in Table 2.

Table 2. **Deep Learning Architecture Parameters**

Parameters	Values
Views	Axial
Initial filters N°	16
Batch size	16
Dropout rate	0.4
Optimizer	Adam (default)
Epochs	100
Loss function	Dice Loss
Model checkpoint	Active
Early stopping	Active (patience epochs=20)

In the case of SVM and RF, we suggested using BRATS 2018 training data of 285 patients splited to 80% as a training data and 20% as a Test set and due to limited available resources and high memory consumption from SVM and RF; we customized both of datasets as follows:

- Each modality and ground truth were cropped from (240,240,155) to (128,128,30) with the following indices [56:184,56:184,sl-15:sl+15] where sl is the index of the slice in the ground truth which contains the maximum non zero pixels(or the large tumor region)
- The models were trained over the axial view only

RF and SVM were implemented in python using numpy, opencv and sklearn libraries, the configuration parameters for each model are:

- SVM: the Stochastic Gradient Descent (SGD) classifier was used with Radial Basis Function (RBF) kernel approximation RBFSampler and maximum number of iterations set to 10000,n_job set to -1 for parallel CPU cores execution and class weight set to Balanced to address the class imbalance problem.
- RF: The Random Forest Classifier was used with a number of estimators set to 10,n_job=-1 -1,class_weight set to Balanced and max_samples set to 0.2 and Gini impurity criteria.

Evaluation Metrics

Evaluation metrics are quantitive measures used to assess the performance and the effectiveness of machine learning models. They are frequently computed based on the confusion matrix (Fig 3).

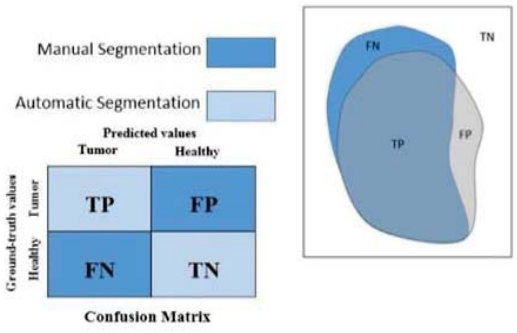

Fig.3: Confusion Matrix

The evaluation metrics[19-20] used in this work are: Dice Score, Accuracy, Sensitivity and specificity. These metrics, except accuracy, are widely used in the context of image segmentation and highly recommended to address the class imbalance problem because of their focus on the infrequent classes; however, traditional metrics like accuracy are still used and can be misleading in imbalanced datasets. A model might achieve high accuracy by simply predicting the majority class or the healthy tissue and background pixel and this, which is proved through these experiments

Dice Score: one of the primmest pixel level metrics, used to evaluate the quality of image segmentation, it measures the overlap between the prediction map and the ground truth, it cares only for true positive pixels.

$$Dice = \frac{2|A \cap B|}{|A|+|B|} = \frac{2TP}{2TP+FP+FN} \quad (1)$$

Accuracy: measures the proportion of true negative and true positive pixels that are correctly predicted compared to the ground truth.

$$Acc = \frac{TP+TN}{TP+FP+FN+TN} \quad (2)$$

Sensitivity: measures the proportion of true positives pixel that correctly predicted comparing to the ground truth

$$Sensitivity = \frac{TP}{TP+FN} \quad (3)$$

Specificity: measures the proportion of true negative pixel that correctly predicted compared to the ground truth.

$$Specificity = \frac{TN}{TN+FP} \quad (4)$$

Where A and B refers to the prediction mask and the ground truth respectively.TP, FP, FN, TN are the number of: True positive pixels , False positive pixels, False Negative pixels and True Negative pixels respectively.

RESULTS AND DISCUSSION

Table 3 and Table 4 exhibit the summary results of the models on the training and test set respectively.

A large panoply of metrics is used for the performance evaluation of the Machine Learning models. Still, there are some constraints because they are not all suited for all tasks where each task may require specific metrics; for example, in this work, which tackles the image segmentation problem, we proposed using Dice score, Accuracy, sensitivity, and specificity. From the exhibited results in Table 1, we can see the accuracy is always 99%; however, the Dice varies between 35% to 90%. The Dice score considered as a similarity measure which measures the overlap between the predicted map and the ground truth, it depends on the true positive pixels only which are the objective of the segmentation or the wanted area of interest, that represents the tumour area in our case but the accuracy is the percentage of pixels in the image that are classified correctly, it depends on the true positive and true negative pixels, in this study the true negative pixels represent the healthy tissue and the background, which is the large class in term of pixels that dominate the image that is why accuracy is near to 100% and this is due to the class imbalance, the gap is highly noted in the SVM and Random forest model, where there is a significant difference between the accuracy and the Dice coefficient and this raises concerns about its reliability and precision which justify that is not adaptable for such problem because high accuracy does not imply high model segmentation ability. As we mentioned previously that dice score focuses on true positives only which is the infrequent class and penalize false positive which makes it more sensitive and suitable metrics for this kind of tasks and a good solution for the class imbalance problem. [8]. For the sensitivity and the specificity, as we previously mentioned, sensitivity refers to the proportion of true positives that are correctly segmented compared to the ground truth, which is, in our task, the rate of indeed predicted tumorous pixels. Inversely, specificity refers to the proportion of true negatives that mean the proportion of pixels that are predicted healthy and background exactly like the ground-truth, both metrics works with one class separately so they are not affected by the class imbalance. They are adaptable for this task. They evaluate the model's capability in detecting tumorous pixels and healthy ones, respectively.

The limitation of this study is attributed to the use of a limited number of evaluation metrics. As future directions for this work, it is recommended to consider alternative solutions, including the exploration of a broader range of evaluation metrics, as well as the implementation of techniques such as under sampling and patch-based segmentation to effectively address this challenge.

Table 3. The training Results of the brain tumour segmentation

Models		**DL**			**SVM**			**RF**	
Classes	WT	TC	ET	WT	TC	ET	WT	TC	ET
DICE	0.95	0.90	0.87	0.65	0.47	0.37	0.75	0.55	0.37
ACC	**0.99**	**0.99**	**0.99**	**0.98**	**0.97**	**0.99**	**0.98**	**0.98**	**0.97**
SEN	0.95	0.89	0.86	0.71	0.78	0.79	0.75	0.78	0.81
SPEC	0.96	0.98	0.99	0.82	0.84	0.90	0.85	0.88	0.90

Table 4. The test results of the brain tumour segmentation

Models		**DL**			**SVM**			**RF**	
Classes	WT	TC	ET	WT	TC	ET	WT	TC	ET
DICE	0.91	0.88	0.85	0.66	0.46	0.35	0.74	0.50	0.34
ACC	**0.99**	**0.99**	**0.99**	**0.98**	**0.97**	**0.99**	**0.98**	**0.98**	**0.97**
SEN	0.90	0.85	0.83	0.70	0.78	0.82	0.73	0.72	0.81
SPEC	0.98	0.99	0.99	0.82	0.84	0.91	0.85	0.87	0.90

CONCLUSIONS

In this research, we examined the common issue of class imbalance in medical image segmentation. Our study focused on illustrating the adverse effects of this imbalance on various evaluation metrics within the context of machine learning models. Furthermore, we underscored the significance of carefully selecting suitable evaluation metrics when gauging the performance of machine learning models in image segmentation. This involves taking into account the influence of class imbalance to ensure the accuracy and dependability of results in image segmentation tasks.

AUTHOR INFORMATION

Corresponding Author

*Yamina Azzi

Email address Yamina.azzi@univ-setif.dz

REFERENCES

1. Zhifei Lai and Huifang Deng. Medical image classification based on deep features extracted by deep model and statistic feature fusion with multilayer perceptron. Computational Intelligence and Neuroscience, 2018, 2018.
2. Ruixin Yang and Yingyan Yu. Artificial Convolutional Neural Network in Object Detection and Semantic Segmentation for Medical Imaging Analysis. Frontiers in Oncology, 11(March):1–9, 2021.
3. Sharma, N., & Aggarwal, L. M. (2010). Automated medical image segmentation techniques. *Journal of Medical Physics / Association of Medical Physicists of India*, *35*(1), 3-14. https://doi.org/10.4103/0971-6203.58777
4. Zhang, T.C., Yang, J., Zhang, J.P., 2016. SVM Methods in Image Segmentation , 62–65.
5. Rajan, J.K., Shahil, D.F.D., Elakkiya, M.T., Prasad, R., 2017. Image Seg-
mentation Using SVM Pixel Classification 3, 45–51
6. Wasule, V., Poonam, S., 2017. Classification of Brain MRI Using SVM and
KNN Classifier , 218–223
7. Ayachi, R., Ben Amor, N., 2009. Brain tumor segmentation using support vector machines, in: Lecture Notes in Computer Science (including subseries Lecture Notes in Artificial Intelligence and Lecture Notes in Bioin-formatics), pp. 736–747. doi:10.1007/978-3-642-02906-6_63
8. Kapás, Z., Lefkovits, L., Szilágyi, L., 2016. Automatic Detection and Segmentation of Brain Tumor Using Random Forest Approach, in: Torra, V.,Narukawa, Y., Navarro-Arribas,G.,Yañez,C.(Eds.),http://link.springer.com/10.1007/978-3-319-45656-0_25,doi:10.1007/978-3-319-45656-0_25
9. Kumar, A., Bi, L., Kim, J., Feng, D.D., 2020. Machine learning in medical imaging,167 196 doi:10.1016/B978-0-12-816034-3.00005-5
10. Hesamian, M.H., Jia, W., He, X. *et al.* Deep Learning Techniques for Medical Image Segmentation: Achievements and Challenges. *J Digit Imaging* **32**, 582–596 (2019). https://doi.org/10.1007/s10278-019-00227-x

11. Johnson, J.M., Khoshgoftaar, T.M. Survey on deep learning with class imbalance. *J Big Data* **6**, 27 (2019). https://doi.org/10.1186/s40537-019-0192-5
12. Xiaoling Xia *et al* 2019 *J. Phys.: Conf. Ser.* **1213** 022003
13. Basak, H., Ghosal, S., Sarkar, R. (2022). Addressing Class Imbalance in Semi-supervised Image Segmentation: A Study on Cardiac MRI. In: Wang, L., Dou, Q., Fletcher, P.T., Speidel, S., Li, S. (eds) Medical Image Computing and Computer Assisted Intervention – MICCAI 2022. MICCAI 2022. Lecture Notes in Computer Science, vol 13438. Springer, Cham. https://doi.org/10.1007/978-3-031-16452-1_22
14. Small, Hattie Thompson and Brown. "Handling Unbalanced Data in Deep Image Segmentation." (2017).
15. Olaf Ronneberger, Philipp Fischer, and Thomas Brox. U-Net: Convolutional Networks for Biomedical Image Segmentation. IEEE Access,9:16591–16603, may 2015.
16. Spyridon Bakas, Hamed Akbari, Aristeidis Sotiras, Michel Bilello,Martin Rozycki, Justin S. Kirby, and Et al. Advancing The Cancer Genome Atlas glioma MRI collections with expert segmentation labels and radiomic features. Scientific Data, 4(1):170117, dec 2017.
17. Spyridon Bakas, Mauricio Reyes, Andras Jakab, Stefan Bauer, Markus Rempfler, Alessandro Crimi, and Et al. Identifying the Best Machine Learning Algorithms for Brain Tumor Segmentation, Progression Assessment, and Overall Survival Prediction in the BRATS Challenge. nov2018.
18. Bjoern H Menze, Andras Jakab, Stefan Bauer, Jayashree Kalpathy-Cramer, Keyvan Farahani, Justin Kirby, and Et al. The Multimodal Brain Tumor Image Segmentation Benchmark (BRATS). IEEE Transactions on Medical Imaging, 34(10):1993–2024, oct 2015.
19. Abdel Aziz Taha and Allan Hanbury. Metrics for evaluating 3D medical image segmentation: Analysis, selection, and tool. BMC Medical Imaging, 15(1):29, dec 2015.
20. Dominik M uller, I naki Soto-Rey, and Frank Kramer. Towards a guideline for evaluation metrics in medical image segmentation. BMC Research Notes, 15(1):1–7, 2022.

2023

Ions beam therapy monitoring with the in-beam PET scanning: Monte Carlo simulation

N. Ounoughi,[a,*] L. Boumedine,[b] D. Bara,[c] F. Kharfi,[b]

[a] Radiation Physics and Applications Laboratory, University of Jijel, Algeria

[b] Dosing, Analysis, and Characterization with high resolution Laboratory (LDAC), Department of Physics of Ferhat Abbas-Setif1 University, Algeria

[c] Center for the Development of Advanced Technologies, CDTA, Cité 20 août 1956 Baba Hassen, Algiers, Algeria

.

ABSTRACT: To fully benefit from the precise dose delivered during hadrontherapy treatment, in-vivo dose monitoring methods are required. The activation caused by the beam in tissues can be detected by Positron Emission Tomography (PET) scanners and hence dose monitoring. Oxygen ion beams are programmed to be introduced into clinical practice due to their potential for treating hypoxic tumors. The PET scanner performance has already been tested in-vivo during proton and carbon treatment sessions. In this work, we will focus on the performance of the PET scanner as a monitoring system during 0xygen (^{16}O) ion treatments. Monte Carlo simulation with Particle and Heavy Ion Transport Code System (PHITS) code was performed to predict the possible positron emitters that can be created in soft tissue during ^{16}O irradiation. The ^{11}C, ^{15}O, ^{10}C and ^{13}N are also among the most important positron emitters created isotopes. Because of its short half-life, and production intensity, ^{15}O is the best-adapted positron emitter for PET imaging that may guarantee a short scanning time. Very short-lived positron emitters such as ^{12}N ($T_{1/2}$ = 11ms) can be adapted for milliseconds scanning.

Keywords: Ion therapy; Radiation dose; PET scanning; Monte Carlo simulation.

INTRODUCTION

Ion beam therapy is an advanced type of external beam radiotherapy that takes advantage of the useful interaction features of heavy fast ions in matter, particularly their short range and maximum dose deposition in depth known as the Bragg peak[1]. In compared to the frequently used photon therapy, ion beams can provide steeper dose gradients which allow conformal tumor coverage while sparing surrounding normal tissues. Additionally, heavier ions such as carbon offer added biological advantages because they exhibit a specific rise in ionization density as they approach the end of their penetration range. This leads to a distinctive boost in relative biological effectiveness (RBE), which can amplify the destruction of cancerous cells within the tumor while preserving the integrity of adjacent healthy tissue, all while maintaining the same physical dose deposition in the tumor[2]. However, full exploitation of these physical and biological advantages in clinical applications, it is essential to have a comprehensive understanding of the precise location where the ion beam stops within the patient's body. Hence, in vivo delivered dose monitoring systems are required. Positron-emission tomography (PET) can be utilized to monitor ion beam therapy involving both lightweight (protons, helium..) and heavier ions (carbon, oxygen..) by reconstructing the distributions of positron-emitting substances through simultaneous detection of gamma rays generated during annihilation events occurring in opposite directions [3].

During the irradiation with ions beams, a mixture of positron

emitting isotopes with different half-lives is produced .The spatial distribution of activity does not correlate with the administered dose, as dose deposition and the generation of beta activity result from distinct physical processes. Consequently, the expected distribution of positron emitters must be computed using a Monte Carlo (MC) simulation based on the treatment plan[4]. MC simulations play a crucial role in evaluating the quality of treatment.

Simulation using Monte Carlo method and PHITS code was performed to predict the possible positron emitters that can be created in soft tissue during ^{16}O irradiation.

Because of its short half-life, and production intensity, ^{15}O is the best-adapted positron emitter for PET imaging that may guarantee a short scanning time.

METHODS AND MATERIALS

PHITS (Particle and Heavy Ion Transport Code System) is a multipurpose 3D Monte Carlo code that simulates the transport and interaction of most particle species over wide energy ranges (10−5 eV– 1 TeV) using theoretical models and nuclear data files. PHITS has proven to be very useful in a wide range of research fields, most notably medical physics[5]. PHITS is benchmarked for Bragg curves and deposit energy of ^{1}H, ^{4}He, ^{12}C and ^{16}O beams ions beam[6] and has been validated for a variety of experiment cases including particle production in heavy ion reactions[7].

In this study, a phantom representing a soft tissue target of 40x40x40 cm^3 dimension is irradiated by a mono-energetic ^{16}O ions beam. This Soft phantom has a density of 1g.cm^{-3} and it is composed from: 76.2% O, 11,1% C, 10.1% H, and 2.6% N. The ^{16}O ions beam energy is chosen at 260 MeV/u, corresponding to a range of around 10 cm. The most important positron emitters isotopes created in soft tissue during ^{16}O irradiation are computed. The maps of spatial distribution of ^{16}O dose and ^{15}O fluence are showed.

RESULTS AND DISCUSSION

1. Positron emitters' production

During the irradiation of the phantom with ^{16}O ions beams, the most abundant positron emitting isotopes, with different half-lives, are ^{11}C (T ½ = 1222.8 s), ^{15}O (T 1/2 = 121.8 s), ^{13}N (T1/2 = 597.6 s) and ^{10}C (T 1/2 = 19.3 s). Figure1 shows the fluence of the main positron emitters during the interaction of ^{16}O ions of energy 260 MeV/u in the soft tissue phantom as predicted with PHITS. Statistical uncertainties are below 1%. The fluency of the ^{15}O positron emitter radioisotope is higher than the other radioisotopes; usually it is the dominant radionuclide. ^{15}O can be the best-adapted positron emitter for PET imaging that may guarantee a short scanning.

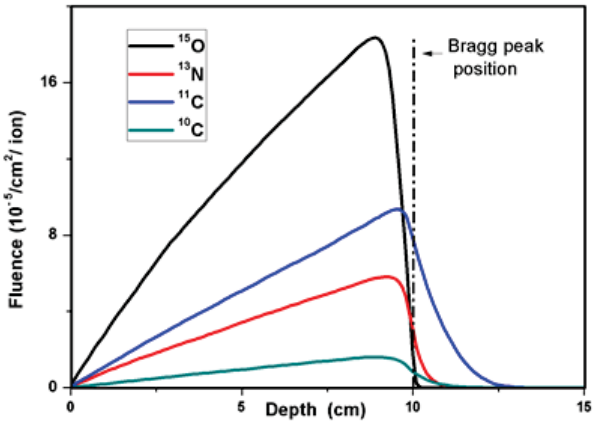

Fig. 1: Fluence of the main positron emitters during the interaction of ^{16}O ions of energy 260 MeV/u in a soft tissue phantom

2. Spatial map of ^{16}O dose and ^{15}O fluence

In this section, we conducted calculations to determine the 2D spatial distribution of energy deposition by ^{16}O ions interacting with a soft tissue phantom at 260 MeV/u. The beam exhibits a cylindrical shape, characterized by a diameter of 2 cm. Furthermore, we computed the spatial distribution of the fluence of ^{15}O secondary ions. Figure 2 displays the outcomes of these simulations.

Mapping the production of ^{15}O during ^{16}O ion therapy, alongside in-beam PET imaging, can provide valuable insights into the spatial distribution of deposited energy within the patient's body. In addition, the flux of ^{15}O ions produced also exhibits a significant decrease just before reaching the Bragg peak. This phenomenon offers an improved correlation between the depth distributions of activity and dose, which enhances the effectiveness of range monitoring.

Ideally, in-beam data should be analyzed in real-time to enable the cessation of treatment if substantial deviations from the treatment plan are detected. Very short-lived positron emitters such as ^{12}N ($T_{1/2}$ = 11ms) can be adapted for milliseconds scanning. Advancements in rapid electronic systems and ultrafast scintillating crystals lead to reduced signal acquisition time and enhanced image quality.

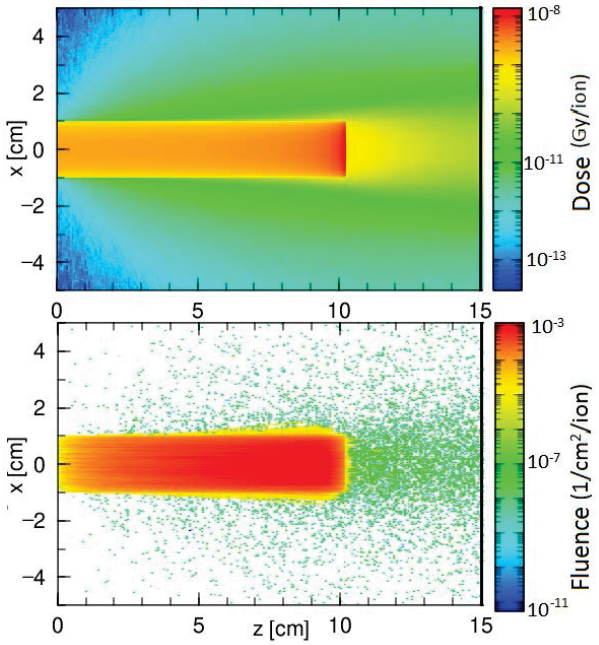

Fig. 2: 2D spatial distribution of ^{16}O dose and ^{15}O fluence

CONCLUSIONS

The study presented in this work served as a foundational proof-of-concept investigation with the goal of assessing the viability of utilizing ^{15}O production as a target for in-beam monitoring applications involving positron emission tomography (PET). The primary aim was to enhance the precision of verifying ^{16}O treatment plans and verifying the range of the treatment. To achieve this objective, we conducted Monte Carlo simulations, specifically utilizing the PHITS code, to predict the potential generation of positron-emitting substances within soft tissue when exposed to ^{16}O irradiation. Among the various options considered, ^{15}O emerged as the optimal positron emitter for PET imaging due to its remarkably short half-life and high production rate, which enables rapid and efficient scanning procedures.

AUTHOR INFORMATION

Corresponding Author

*Nabil Ounoughi

Email address: n_ounoughi@univ-jijel.dz

REFERENCES

1. O. Jäkel, Br J Radiol 2020, 93, 20190428.
2. H. Paganetti, Phys Med Biol 2012, 57, R99.
3. F. Ponisch, K. Parodi, BG. Hasch, W. Enghardt. Phys Med Biol 2004, 49, 5217-32.
4. K. Parodi, T. Yamaya, P. Moskal, Z. Med. Phys. 2023, 33, 22–34.
5. T. Sato, Y. Iwamoto, S. Hashimoto, T. Ogawa, T. Furuta, S. Abe, T. Kai, P.E. Tsai, N. Matsuda, H. Iwase, H. Shigyo, L. Sihver, K.Niita, J. Nucl. Sci. Technol. 2018, 55-6, 684-690.
6. Y. Iwamoto, T. Sato, S. Hashimoto, T. Ogawa, T. Furuta, S. Abe, T. Kai, N. Matsuda, R. Hosoyamada, K. Niita, Journal of Nuclear Science and Technology, 2017, 54-5, 617-635.
7. N. Ounoughi, Y. Dribi, A. Boukhellout, F. Kharfi, Polish Journal of Medical Physics and Engineering, 2022, 28-3, 160-168.

2023

Watermarking Images Using Virtual Color Models

N. Benmehenni,[a] A. Benhocine,[a] N. Mouhoub,[b]

[a] Faculty of Sciences, LMFN, Ferhat Abbes University of Sétif 1, Sétif-19000, Algeria
[b] Faculty of Mathematics and Computer, M'sila University, M'sila-28000, Algeria

ABSTRACT: The RGB color model allows displaying millions of different colors in digital screens like those of monitors, televisions, smart phones, cameras, etc. It is based on combination of three colors (red, green, blue) making easy expression of colors with vectors. The YUV model is another color space defined by three components, the luminance Y (grayscale part of the signal) and the chrominance, U and V. This paper deals with watermarking color and grayscale images, especially medical images. Watermarking a medical image is imbedding invisible patient data in the area of interest, to prevent loss or falsification of them after transferring the image. The extraction of the mark will allow retrieving these data without changing important parts of the host image, to avoid distortion of the medical diagnosis. For this, we have used matrix transformations of order three. The first algorithm transform the RGB color cube into an infinite family of parallelepipeds and the second transforms YUV model into an infinite family of same type model. In each case, a benchmark is applied for testing robustness.
Keywords: Color model; YUV model; Grayscale image; Transformation domain; Watermarking.

INTRODUCTION

With the rapid development of internet and digital technology, the digital media can be perfectly copied without the owner's permission, easily modified and instantly distributed over internet. Protecting the copyright of the digital media is therefore an important topic. As a result, techniques of watermarking are currently used for the copyright protection and have nowadays received considerable attention.

Watermarking a digital image, or another medium like audio or video, consists of embedding an image or a message, called watermark, in an image, called cover image or host image. Some applications need a visible watermark like a logo, while others need an invisible watermark. The watermark should be robust, i.e. it must be difficult to remove and despite attacks, it still can be extracted and identified. Moreover, it must not affect the quality of the cover image and must be unambiguous when extracting it.

An important bulk of research work has been published in this area. Watermarking techniques are now usually classified into spatial domain methods and transform domain methods. Spatial domain methods[1-5] are less complex but not robust against tampering and attacks [6-9]. The watermark is embedded into the host image by directly changing the colors of some pixels in the host image. The Least Significant Bit (LSB) methods are currently used because of their simplicity. The transform domain methods[10-16] are more robust but are time consuming. A mathematical transform is applied to the host image, the watermark is then embedded into the transform coefficients and finally the inverse transform is applied to get the watermarked image. The watermark is placed in the most perceptually significant components of the transform domain. To insert an invisible and robust watermark into the host image, the human visual system (HVS) model should be exploited to perceptually determine significant regions of the host image[17-21]. For example, the blue component of an RGB image is well suited for watermarking and so is the Y component in YIQ and YUV models. The most frequently used methods are the Discrete

Cosine Transform (DCT), the Discrete Fourier Transform (DFT) and the Discrete Wavelet Transform (DWT), and recently the Singular Value Decomposition (SVD)[22-29]. SVD is used as a different transform and many papers combine SVD with DCT or DWT.

This paper is organized as follows. Section I defines a general watermarking scheme to be used in subsequent sections. In Section II, we define the matrix transformation of the RGB color cube into an infinite family of RGB color parallelepipeds, representing a scaling followed by a translation. In Section III, we define an infinite family of matrices that are analogous to YUV.

The embedding and extracting algorithms are subject to many tests in results and discussion section.

We get the watermarked image iw by applying in each case linear interpolation to i and w, that is iw = (1-t) w + t i where t controls the embedding strength.

EXPERIMENTAL

The general watermarking scheme

Fig. 1 shows an embedding scheme where $\boldsymbol{T_i}$, $\boldsymbol{T_w}$ and $\boldsymbol{T_{iw}}$ are invertible matrices with order 3 or 4 (homogeneous coordinates), depending upon the algorithms explained in the following sections. For each pixel $(r,g,b)^t$ in $\boldsymbol{i}$, we get the pixel $(R,G,B)^t = \boldsymbol{T}_i \times (r,g,b)^t$ if $\boldsymbol{T_i}$ is of order 3 and $(R,G,B,t)^t = \boldsymbol{T}_i \times (r,g,b,1)^t$ if $\boldsymbol{T_i}$ is of order 4. The same holds for $\boldsymbol{T_w}$ and $\boldsymbol{T_{iw}}$. By applying linear interpolation with parameter *t*, we get $\boldsymbol{i_{Tw}} = (1-t)\boldsymbol{w}_T + t\boldsymbol{i}_T$. Finally, the watermarked image is given by:

$$\boldsymbol{i_w} = T_{iw}{}^{-1}\boldsymbol{i}_{Tw} = T_{iw}{}^{-1}\left((1-t)\boldsymbol{w}_T + t\boldsymbol{i}_T\right)$$

$$= T_{iw}{}^{-1}((1-t)T_{\boldsymbol{w}}\boldsymbol{w} + tT_{\boldsymbol{i}}\boldsymbol{i}) \quad \text{, so}$$

$$\boldsymbol{i_w} = \boldsymbol{(1-t)T_{iw}T_w w + tT_{iw}{}^{-1}T_i i)} \qquad (1)$$

The extraction process is depicted Fig. 2. $\boldsymbol{i_{wa}}$ is $\boldsymbol{i_w}$ after an attack, $\boldsymbol{w_{Ti}}$ is $\boldsymbol{w_T}$ "watermarked" with $\boldsymbol{i_{wT}}$ using linear interpolation with same parameter *t*, and $\boldsymbol{w_{aT}}$ is $\boldsymbol{w_{Ti}}$ after "extraction" of $\boldsymbol{i_{waT}}$ that is given by: $\boldsymbol{w}_{T_i} = (1-t)i_{w_T} + t\ \boldsymbol{w}_T$ and $\boldsymbol{w_{aT}} = \frac{\boldsymbol{1}}{\boldsymbol{t}}\ \boldsymbol{w}_{T_i} + \boldsymbol{t}\ \boldsymbol{w_T} - \frac{\boldsymbol{1-t}}{\boldsymbol{t}}\ \boldsymbol{i}_{w_{aT}}$. We get the modified watermark $\boldsymbol{w_a} = T_{\boldsymbol{w}}^{-1}\ \boldsymbol{w}_{aT}$. Then, we deduced easily the following:

$$\boldsymbol{w_a} = \boldsymbol{w} + \tfrac{(1-t)}{t}\ T_{\boldsymbol{w}}^{-1}\boldsymbol{T_{iw}}\varepsilon, \quad \text{where } \varepsilon = \boldsymbol{i}_{w_a} - \boldsymbol{i_w}, \text{ so}$$

$$\boldsymbol{w_a} = \boldsymbol{w} + \tfrac{(1-t)}{t}\ (T_{\boldsymbol{iw}}^{-1}\boldsymbol{T_w})^{-1}\varepsilon \qquad (2)$$

In the following sections, we study two transformations: the first one is a matrix of order 4 representing a scaling followed by a translation and the second one is analogous to YUV.

In figures 1 and 2, the transformations $\boldsymbol{T_i}$, $\boldsymbol{T_w}$ and $\boldsymbol{T_{iw}}$ must be different otherwise $\boldsymbol{i_w} = (1-t)T_{\boldsymbol{iw}}^{-1}T_{\boldsymbol{w}}\boldsymbol{w} + t\ T_{\boldsymbol{iw}}^{-1}T_{\boldsymbol{i}}\boldsymbol{i}$ and $\boldsymbol{w_a} = \boldsymbol{w} + \frac{\boldsymbol{1-t}}{\boldsymbol{t}}\ (\ T_{\boldsymbol{iw}}^{-1}\ T_{\boldsymbol{w}})^{-1}\ \boldsymbol{\varepsilon}$ become respectively $\boldsymbol{i_w} = \boldsymbol{(1-t)w} + \ \boldsymbol{ti}$ and $\boldsymbol{w_a} = \boldsymbol{w} + \frac{\boldsymbol{1-t}}{\boldsymbol{t}}\ \boldsymbol{\varepsilon}$, then T is not needed. For this reason, we must build three different matrices for each method (RGB and YUV).

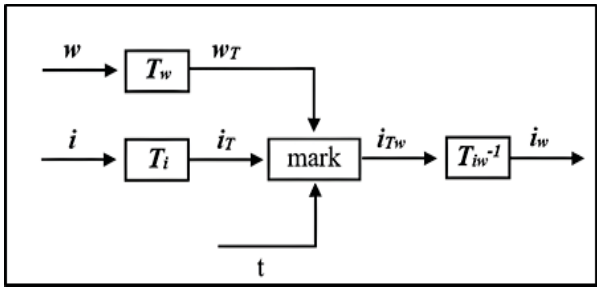

Fig. 1: Embedding the watermark

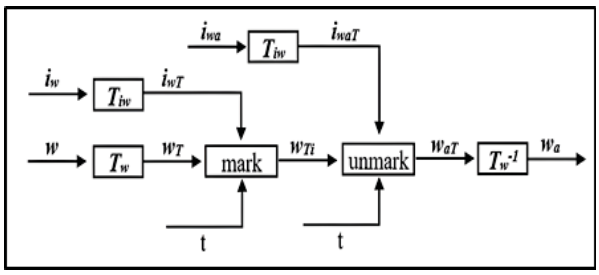

Fig. 2: Extracting the watermark

Transformation of the RGB color cube into a parallelepiped

We get the transformation of the RGB-color cube $\boldsymbol{C} = [0,255] \times [0,255] \times [0,255]$ into the parallelepiped $\boldsymbol{P} = [R_1,R_2] \times [G_1,G_2] \times [B_1,B_2]$, with $R_1 > R_2$, $G_1 > G_2$, $B_1 > B_2$ by using linear interpolation, that is $\frac{r}{255} = \frac{R-R_1}{R_2-R_1}$, $\frac{g}{255} = \frac{G-G_1}{G_2-G_1}$, and $\frac{b}{255} = \frac{B-B_1}{B_2-B_1}$ Let $\rho = \frac{R_2-R_1}{255}$, $\gamma = \frac{G_2-G_1}{255}$ and $\beta = \frac{B_2-B_1}{255}$. Then $(R,G,B,1)^t = T \times (r,g,b,1)^t$, where:

$$T = \begin{bmatrix} \rho & 0 & 0 & R_1 \\ 0 & \gamma & 0 & G_1 \\ 0 & 0 & \beta & B_1 \\ 0 & 0 & 0 & 1 \end{bmatrix}.$$

Without loss of generality, suppose that $\boldsymbol{R} = (\boldsymbol{r},\boldsymbol{R},\boldsymbol{R_1},\boldsymbol{R_2},\boldsymbol{\rho})$ represents any one of (r,R,R_1,R_2,ρ), (g,G,G_1,G_2,γ) or (b,B,B_1,B_2,β).

Let $\boldsymbol{i}$ be the host image, $\boldsymbol{w}$ the watermark and $\boldsymbol{i_w}$ the watermarked image. The transformations of these images will be represented by the sets $\boldsymbol{R_i}, \boldsymbol{R_w}, \boldsymbol{R_{iw}}$, respectively. If we consider the quadrangle

$R_{i1}, R_{i2}, R_{w2}, R_{w1}$, we get by bilinear interpolation $R_{iw_1} = (1-t)R_{w_1} + t\ R_{i_1}, R_{iw} = (1-t)R_w + t\ R_i$, $R_{iw_2} = (1-t)R_{w_1} + t\ R_{i_2}$ and $\rho_{iw} = (1-t)\rho_w + t\rho_i = \frac{R_{iw2} - R_{iw1}}{255}$ so that $T_{iw} = (1-t)T_w + t\ T_i$.

Transformation of an image from rgb color space to another yuv color space

Any color which was represented in rgb-color cube is now represented in another color space, like YUV, YIQ, etc,… We suppose here that any triplet $(r,g,b)^t$ is transformed into $(R,G,B)^t = T \times (r,g,b)^t$ where T is a 3×3-matrix which is calculated later. Any 3×3-matrix can be obtained, provided that the final results are images (like the watermarked image $\boldsymbol{i_w}$ or the extracted watermark $\boldsymbol{w_a}$) that have pixel values (that is values in $[0,255]$).

A. Preliminaries

Let T be the set of the 3×3 – matrices $\boldsymbol{T}(a,b,p,q)$ such that

$$\boldsymbol{T}(a,b,p,q) = \begin{bmatrix} a & b & 1-a-b \\ -pa & -pb & p(a+b) \\ q(1-a) & -qb & -q(1-a-b) \end{bmatrix}, b,p,q \neq 0.$$

The determinant of $\boldsymbol{T}$ is bpq, so, since $b,p,q \neq 0$, $\boldsymbol{T}$ is invertible and its inverse is given by:

$$\boldsymbol{T^{-1}} = \begin{bmatrix} 1 & 0 & 1/q \\ 1 & -(1-a-b)/(pb) & -a/(qb) \\ 1 & 1/p & 0 \end{bmatrix}$$

Suppose now $\boldsymbol{L}(a,b,p,q), \boldsymbol{M}(c,d,r,s) \in T$. We get an invertible matrix given by:

$$\boldsymbol{L^{-1}M} = \begin{bmatrix} x_1 & y_1 & 1-x_1-y_1 \\ c+cx_2-(1-c)y_2 & d+dx_2+dy_2 & 1-c-d-(c+d)x_2+(1-c-d)y_2 \\ x_3 & y_3 & 1-x_3-y_3 \end{bmatrix},$$

where:

$$x_1 = \frac{(1-c)s}{q} + c\ , y_1 = -d\frac{s}{q} + d,$$

$$x_2 = \left(\frac{1}{b} - \frac{a}{b} - 1\right)\frac{r}{p}\ , y_2 = \left(\frac{a}{b}\right)\left(\frac{s}{q}\right),$$

$$x_3 = -\frac{cr}{p} + c = -\frac{dr}{p} + d.$$

Let $c \in]0,1[$ and $d \in]0,1-c[$, then:

$$\frac{d}{1-c}, \frac{c}{c+d}, \frac{d}{c+d} \in]0,1[$$

$$0 < \frac{1-c-d}{c+d} < \frac{1-c-d}{d} < \frac{1-c}{d}$$

$$0 < \frac{c}{1-c} < \frac{c}{d} < \frac{1-d}{d} \qquad (3)$$

We have $\frac{s}{q} = \frac{x_1-c}{1-c}$ and $y_1 = \frac{-d(x_1-1)}{1-c}$. Note that:

$y_1 \neq d \iff x_1 \neq c \Leftrightarrow s \neq 0$. Analogously, $\frac{r}{p} = \frac{(x_3-c)}{-c}$ and $y_3 = \frac{d}{c}x_3$ and $y_3 \neq d \iff x_3 \neq c \Leftrightarrow r \neq 0$.

The initial set of equations for $\boldsymbol{L^{-1}M}$ is then:

$$c \in]0,1[\ ,\ d \in]0,1-c[$$

$$y_1 = -\frac{d(x_1-1)}{1-c}\ ,\ y_3 = \left(\frac{d}{c}\right)x_3$$

$$\frac{s}{q} = \frac{x_1-c}{1-c}\ ,\ \frac{r}{p} = \frac{x_3-c}{-c}\ ,\ \frac{a}{b} = \frac{y_2(1-c)}{x_1-c}$$

$$\frac{1}{b} = \frac{x_2(-c)}{x_3-c} + \frac{y_2(1-c)}{x_1-c} + 1 \qquad (4)$$

A matrix is said to be strictly positive if all its elements are strictly positive.

B. Choosing the parameters in L(a,b,p,q) and M(c,d,r,s) ∈ T so that $\boldsymbol{L^{-1}M}$ is strictly positive.

For the first line, we must have $x_1 > 0, y_1 > 0,\ 1-x_1-y_1 > 0$, and $y_1 = -\frac{d(x_1-1)}{1-c}$.

The same is deduced for the third line: we must have $x_3 > 0$, $y_3 > 0,\ 1-x_3-y_3 > 0$ and $y_3 = \left(\frac{d}{c}\right)x_3$.

For the second line and according to the choice of c and d and the inequalities (3), the inequalities $c + cx_2 - (1-c)y_2 > 0, d + dx_2 + dy_2 > 0$, and $1-c-d-(c+d)x_2 + (1-c-d)y_2 > 0$ are represented by the interior of a triangle. Using bilinear interpolation, any point N_2 in this area has coordinate:

$$N_2 = (x_2, y_2)^t = (1 - u_2)\ A + u_2((1 - v_2)B + v_2\ C), \quad u_2, v_2 \in]0,1[$$

The set (4) of equations for $\boldsymbol{L^{-1}M}$ strictly positive become:

$$c \in]0,1[$$

$$d \in]0,1-c[$$

$$y1 = -\frac{d(x_1-1)}{1-c}, x_1 \in]0,1[, x_1 \neq c$$

$$(x_2, x_2)t = (1-u_2)A + u_2((1-v_2)B + v_2C), u_2, v_2 \in]0,1[$$

$$y_3 = (\frac{d}{c})x_3, x_3 \in]0, \frac{c}{c+d}[$$

$$\frac{s}{q} = \frac{x_3 - c}{1-c}$$

$$\frac{r}{p} = \frac{x_3 - c}{-c}$$

$$\frac{a}{b} = \frac{y_2(1-c)}{x_1 - c}$$

$$\frac{1}{b} = x_2 \frac{-c}{(x_3-c)} + \frac{y_2(1-c)}{x_2-c} + 1 \qquad (5)$$

We say that a matrix M is a *nearly identity matrix* if [non-diagonal elements of M]≈ 0 and [diagonal elements of M] ≈1.

C. Transforming an image i using a strictly positive and nearly identity matrix $L^{-1}M$

Let $\boldsymbol{I} = \boldsymbol{L^{-1}M}\ \boldsymbol{i}$. If (r,g,b')^t is a pixel color in **i** and (R,G,B)^t the corresponding pixel color in **I** (we say b' instead of b which is an element of L), then

$$R = x_1\ r + y_1\ g + (1-x_1-y_1)b',$$

$$G = (c + cx_2 - (1-c)y_2)r + (d + dx_2 + dy_2)g + ((1-c-d) - (c+d)x_2 + (1-c-d)y_2)b',$$

$$B = x_3\ r + y_3\ g + (1-x_3-y_3)b'.$$

Our aim is to choose the parameters so that **i** and **I** are "visually similar", that is R≈r, G≈g, B≈b'. $\boldsymbol{L^{-1}M}$ is then a nearly identity matrix of order 3 which implies easily $x_1 \approx 1, x_3 \approx 0, d + dx_3 + dy2 \approx 1$, then $u_2 \approx 0$ and v_2 arbitrary.

D. Choosing L(a,b,p,q), M(c,d,r,s), M'(c',d',r',s') ∈ T so that $L^{-1}M$ and $L^{-1}M'$ are simultaneously strictly positive and nearly identity matrices .

Since we have many parameters, one can take c = c'∈]0,1[,and d = d'∈]0,1− c[. We deduce:

- **Equations for $L^{-1}M$**:

$$x_1 \in]0,1[, x_1 \neq c, x_1 \approx 1, y1 = -\frac{d(x_1-1)}{1-c}$$

$$(x_2, y_2)t = (1-u_2)A + u_2((1-v_2)B + v_2C), u_2, v_2 \in]0,1[, u_2 \approx 0$$

$$x_3 \in]0, \frac{c}{c+d}[, x_3 \approx 0, y_3 = (\frac{d}{c})\ x_3$$

$$q = \frac{s(1-c)}{x_1-c}, \quad p = -\frac{rc}{x_3-c}, \quad \frac{a}{b} = \frac{y_2(1-c)}{x_1-c}$$

$$\frac{1}{b} = -x_2 \frac{c}{x_3-c} + \frac{y_2(1-c)}{x_1-c} + 1 \qquad (6)$$

- **Equations for $L^{-1}M'$**:

$$x_1' \in]0,1[, x_1' \neq c, x_1' \approx 1, y1' = -\frac{d(x_1'-1)}{1-c}$$

$$(x_2', y_2')t = (1-u_2')A + u_2'((1-v_2')B + v_2'C), u_2', v_2' \in]0,1[, u_2' \approx 0$$

$$x_3' \in]0, \frac{c}{c+d}[, x_3' \approx 0, y_3' = \frac{d}{c}\ x_3'$$

$$q = s' \frac{1-c}{x_1' - c}$$

$$\frac{a}{b} = y_2' \frac{1-c}{x_1' - c}$$

$$\frac{1}{b} = -x_2' \frac{c}{x_3'-c} + y_2' \frac{1-c}{x_1'-c} + 1 \qquad (7)$$

- **Derived equations:**

$$s' = \frac{s(x_1'-c)}{x_1-c}, \quad r' = r \frac{x_3'-c}{x_3-c}$$

$$y_2' = y_2 \frac{x_1'-c}{(x_1-c)}, \quad x_2' = \frac{x_2(x_3'-c)}{x_3-c} \qquad (8)$$

The point $N_2'(x'_2, y_2')$must be inside the triangle ABC and close

to A (we have chosen $c = c'$ and $d = d'$. Put $h = \frac{x_1'-c}{x_1-c}$and $k = \frac{x_3'-c}{x_3-c}$then $s' = hs$, $r' = kr$, $y_2' = hy_2$, and $x_2' = ky_2$.

Now choose h and k to ensure that N_2' is inside ABC and close to A. Let $(x_2', y_2')t = (1-u_2')A' + u_2'((1-v_2')B' + v_2'C', u_2', v_2' \in]0,1[$, where $A' = (\frac{h(1-c-d)}{d}, \frac{kc}{d})^t, B' = (-h,0)^t$and $' = (0,-k)^t$.

Choose h $\in]\frac{d}{c+d}, 1[$, then B' is in ABC. To have A' in ABC, let's use linear interpolation to get k in terms of h, that is: $\frac{kc}{d} = (1-u)y_{21} + uy_{22}$ where $y_{21} = \frac{h(c+d)-d}{d}$, $y_{22} = \frac{hc(1-c-d)+cd}{d(1-c)}$ and $u \in]0,1[$. Note that $k \in]0,1[$ then C' is in ABC.

Since $x_1' = h(x_1-c)+c, and\ x_3' = k(x_3-c)+c$, we get no contradiction with $x_1' \in]0,1[$, $x_1' \neq c$, and $3' \in]0, c/(c+d)[$.

Choose $h, k \approx 1$then $x_1' \approx 1$, and $x_3' \approx 0$.

Finally, the equations for $\boldsymbol{L^{-1}M}$ and $\boldsymbol{L^{-1}M'}$ simultaneously strictly positive and nearly identity matrices are:

$c \in]0,1[, d \in]0,1-c[$,

$$x_1 \in]0,1[, x_1 \neq c, x_1 \approx 1, y_1 = -\frac{d(x_1-1)}{1-c}$$

$$(x_2, y_2)^t = (1-u_2)A + u_2((1- v2)B + v_2C), u_2, v_2 \in]0,1[, u_2 \approx 0$$

$$x_3 \in]0, \frac{c}{c+d}[,\ x_3 \approx 0, y_3 = (\frac{d}{c})x_3$$

$$h \in]\frac{d}{c+d}, 1[, h \approx 1$$

$$y_{21} = \frac{h(c+d)-d}{d}$$

$$y_{22} = \frac{hc(1-c-d)+cd}{d(1-c)}$$

$$k = (\frac{d}{c})((1-u)y_{21} + uy_{22}), u \in]0,1[$$

$$x1' = h(x1-c) + c, y_1' = -\frac{d(x_1'-1)}{1-c}$$

$$x_3' = k(x_3-c) + c, y_3' = (\frac{d}{c})\ x_3'$$

$$x_2' = hx_2$$

$$y_2' = ky_2 \qquad (9)$$

E. Embedding/Extracting the watermark, Algorithm 2Em/2Ex

Let $\boldsymbol{T_{iw} = L}$, $\boldsymbol{T_i = M}, \boldsymbol{T_w = M'}$.

We get respectively from (1) and (2):

$$\boldsymbol{i_w} = (1-t)\boldsymbol{T_{iw}}^{-1}\boldsymbol{T_w}\ \boldsymbol{w} + t\ \boldsymbol{T_{iw}}^{-1}\boldsymbol{T_i}\ \boldsymbol{i} \quad and$$

$$\boldsymbol{wa} = \boldsymbol{w} + \frac{1-t}{t}\ (\boldsymbol{T_{iw}}^{-1}\boldsymbol{T_w})^{-1}\ \boldsymbol{\varepsilon}\ .$$

RESULTS AND DISCUSSION

In what follows, we apply embedding *Algorithm 1Em* and *Algorithm 2Em* to watermark host image *i* with watermark *w*, then we attack watermarked image i_w using various attacks and finally, we extract the attacked watermark w_a by applying extraction *Algorithm 1Ex* and *Algorithm 2Ex*. Suppose ***i*** and ***w*** are the images in Fig. 3.

Fig. 3: Host image *i* and watermark *w(Resp)*

A. Testing Algorithm 1Em

Table 1 shows ***w*** embedded into ***i*** using *Algorithm 1Em* and some watermarked images $\boldsymbol{i_w}$ for $R_{i1} = G_{i1} = B_{i1} = R_{w1} = G_{w1} = B_{w1} = 0$ and various values of t, $\rho_i$and ρ_w.

A great number of cases occurs but we apply the algorithm only in the case $\rho_i = \gamma_i = \beta_i$ and $\rho_w = \gamma_w = \beta_w$

B. Testing Algorithm 1Ex

We have attacked all the watermarked images shown Table 1, obtaining images iwa. We then have proceeded to extracting the attacked watermark wa from *iwa*. As expected, the best-extracted watermarks are obtained when ρi≈ρw and $t \approx 1$ (Table 2). In

particular, see extractions in case of JPEG, noise and Gaussian blur attacks.

C. Testing Algorithm 2Em

We have considered image i and watermark w in Fig. 3 and we have arbitrarily chosen $= 0.99,\ c = 0.5,\ d = (1-c)/4,\ u = 0.9,\ u_2 = v_2 = 0.1, h = d/(c+d) + (1 - d/(c+d))/10$. All the images in Table **3** are watermarked and as expected, the watermarked image with $x_1 = 0.9$ and $x_3 = [c/(c + d)]/2000$ is the nearest from image *i*.

D. Testing Algorithm 2Ex

We have attacked the watermarked images using same benchmark. With the values of the parameters chosen in embedding algorithm, we obtained results given in Table 4, below. We see that the extracted watermarks are very close to the original watermark proving robustness of the algorithm.

Table 1. Embedding a watermark using Algorithm 1Em

	$\rho i = 5000, \rho_w = 500$	$\rho_i = 5000, \rho_w = 4020$	$\rho_i = 500, \rho_w = 5000$
$t = 0.2$			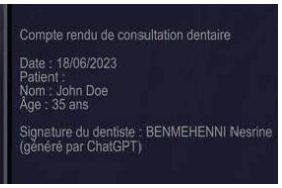
$t = 0.5$	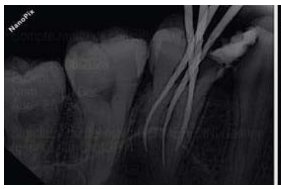	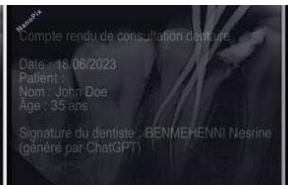	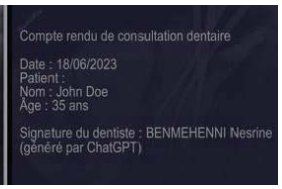
$t = 0.9$	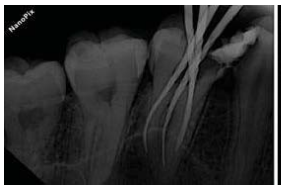	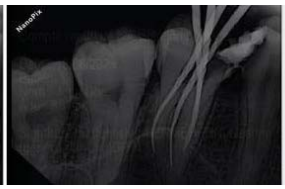	

Table 2. Extracting a watermark using *Algorithm 1Ex* ($t = 0.9,\ \rho\ i = 5000, \rho_w = 500$)

i_{wa}	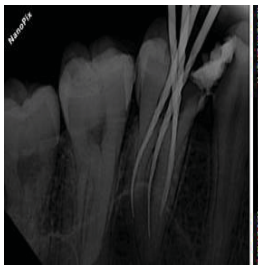	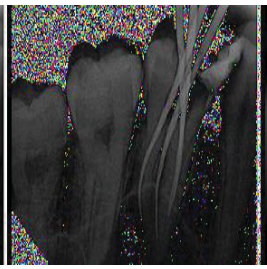	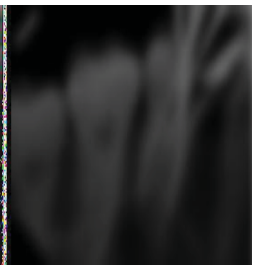
w_a		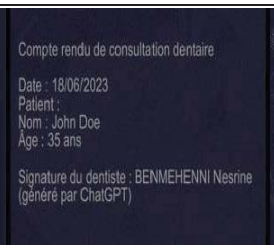	
	JPEG_50	**Noise_(0,5)**	**Gaussian blur radius=5**

Table 3. Embedding a watermark using *Algorithm 2Em with t = 0.99*

X1 / X3	0.1	0.5	0.9
$\frac{c}{c+d} * \frac{1}{2000}$	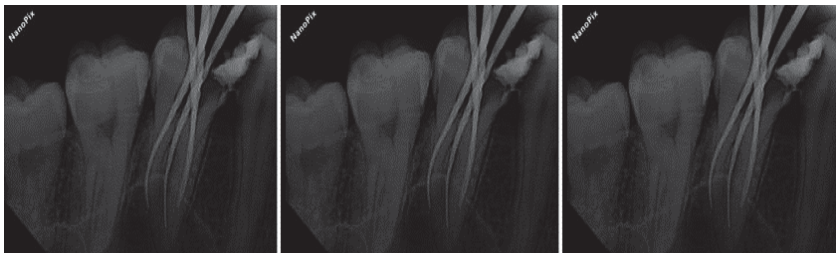		
$\frac{c}{c+d} * \frac{1}{2}$	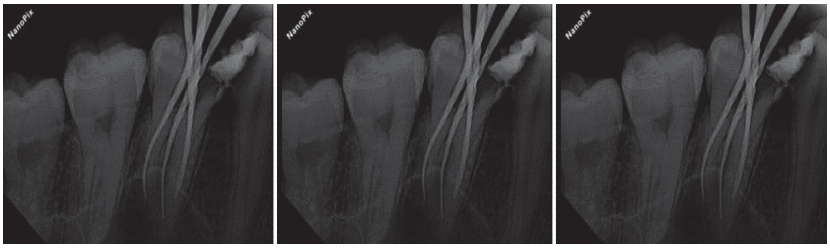		

Table 4. Extracting a watermark using *Algorithm 2Ex*($t = 0.99, x_1 = 0.9, x_3 = [c/(c+d)]/0.9$)

i_{wa}	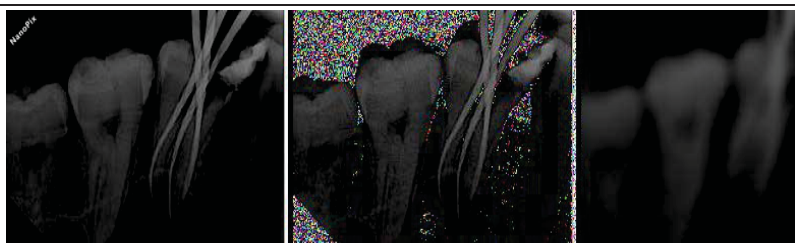		
w_a	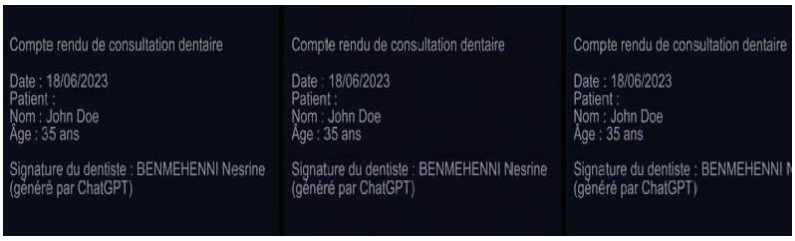		
	JPEG_50	**Noise_(0,5)**	**Gaussian blurr radius=5**

CONCLUSIONS

In this article, we focused on watermarking color and grayscale images, including Dicom images, and on extracting the watermark using domain transformations. Specifically, we transformed the RGB cube into a parallelepiped and a space similar to the YUV space. We then marked the images using both embedding methods and tested their robustness against some attacks. After any attack, we proceeded to extract the watermark. Numerous tests were performed, which demonstrate the strength of our algorithms, indeed, our methods demonstrate a high degree of resilience against attacks of the host watermarked image. This work is part of a larger ongoing project that involves developing models based on graph wavelets and data coding.

AUTHOR INFORMATION

Corresponding Author

*Nesrine Benmehenni

Email address: nesrine.benmehenni@univ-setif.dz

REFERENCES

1. N.K.Singh, N.J.Singh, W.K.Kumar, " Image classification using SLIC superpixel and FAAGKFCM image segmentation", IET Image ProcessingVolume 14, Issue 3 p. 487-494, 27 January 2020
2. Y.Guo, B.Z.Li, N.Goel, "Optimized blind image watermarking method based on firefly algorithm in DWT-QR transform domain", IET Image ProcessingVolume 11, Issue 6 p. 406-415 , 21 April 2017
3. Z.Yuan, Q.Su, D.Liu, X.Zhang, T.Yao , "Fast and robust image watermarking method in the spatial domain", IET Image Processing Volume 14, Issue 15 p. 3829-3838, 18 February 2021
4. W. Wan, K. Zhou, K. Zhang, Y. Zhan and J. Li, "JND-Guided Perceptually Color Image Watermarking in Spatial Domain," in IEEE Access, vol. 8, pp. 164504-164520, 2020, doi: 10.1109/ACCESS.2020.3022652.
5. Y. Zhang and G. Sun, "A Watermark Algorithm Based on Space-domain and Transform-domain," 2019 IEEE 9th International Conference on Electronics Information and Emergency Communication (ICEIEC), Beijing, China, 2019, pp. 41-44, doi: 10.1109/ICEIEC.2019.8784574.
6. Z.Yuan, Q.Su, D.Liu, X.Zhang, T.Yao, "Fast and robust image watermarking method in the spatial domain", IET Image Processing, Volume 14, Issue 15, 18 February 2021
7. R. K. Megalingam, M. M. Nair, R. Srikumar, V. K. Balasubramanian and V. S. V. Sarma, "Performance Comparison of Novel, Robust Spatial Domain Digital Image Watermarking with the Conventional Frequency Domain Watermarking Techniques," 2010 International Conference on Signal Acquisition and Processing, Bangalore, India, 2010, pp. 349-353, doi: 10.1109/ICSAP.2010.79.
8. F.A.P. Petitcolas, R.J. Anderson and M.G. Kuhn, "Attacks on copyright marking systems," Lecture Notes in Computer Science, vol. 1525, pp. 15–17, 1998
9. F. A. P. Petitcolas," Watermarking schemes evaluation" *IEEE Signal Process*., 2000, *17*(5): 58-64
10. D. Nashat and L. Mamdouh, "A Novel Least Significant Bit Steganographic Method Based on Hough Transform," in 2022 International Conference on Networking and Network Applications (NaNA), Urumqi, China, 2022 pp. 349-353, doi:10.1109/NaNA56854.2022.00066.
11. R. Sulaiman, B. Isnanto, Hengki and C. Kirana, "Cryptography in (LSB) Method Using RC4 Algorithm and AES Algorithm in Digital Image to Improve Message Security," in 2018 International Conference on Computing, Engineering, and Design (ICCED), Bangkok, Thailand, 2018 pp. 29-34, doi: 10.1109/ICCED.2018.00016.
12. K. Joshi and R. Yadav, "A new LSB-S image steganography method blend with Cryptography for secret communication," in 2015 Third International Conference on Image Information Processing (ICIIP), Waknaghat, India, 2015 pp. 86-90, doi: 10.1109/ICIIP.2015.7414745.
13. N. Bansal, V. Deolia, A. Bansal and P. Pathak, "Digital Image Watermarking Using Least Significant Bit Technique in Different Bit Positions," in 2014 International Conference on Computational Intelligence and Communication Networks (CICN), Bhopal, India, 2014 pp. 813-818, doi: 10.1109/CICN.2014.174.
14. R. R. Isnanto, R. Septiana and A. F. Hastawan, "Robustness of Steganography Image Method Using Dynamic Management Position of Least Significant Bit (LSB)," 2018 International Seminar on Research of Information Technology and Intelligent Systems (ISRITI), Yogyakarta, Indonesia, 2018, pp. 131-135, doi: 10.1109/ISRITI.2018.8864439.
15. T. Ejidokun, O. O. Omitola, I. Nnamah and K. Adeniji, "Implementation and Comparative Analysis of Variants of LSB Steganographic Method," 2022 30th Southern African Universities Power Engineering Conference (SAUPEC), Durban, South Africa, 2022, pp. 1-4, doi:10.1109/SAUPEC55179.2022.9730643.
16. F. A. Rafrastara, R. Prahasiwi, D. R. Ignatius Moses Setiadi, E. H. Rachmawanto and C. A. Sari, "Image Steganography using Inverted LSB based on 2nd, 3rd and 4th LSB pattern," 2019 International Conference on Information and Communications Technology (ICOIACT), Yogyakarta, Indonesia, 2019, pp. 179-184, doi:10.1109/ICOIACT46704.2019.8938503.
17. J. R. González Montero, A. R. Díaz, E. C. Rosillo and A. Conci, "Watermark Detection and Clearance in Video Using Simple Signal and Image Processing Techniques," 2020 International Conference on Systems, Signals and Image Processing (IWSSIP), Niteroi, Brazil, 2020, pp. 229-234, doi: 10.1109/IWSSIP48289.2020.9145376.
18. I.J. Cox and M. Miller, "A review of watermarking and the importance of perceptual modeling," Proc. SPIE Conf. on Human Vision and Electronic Imaging II, vol. 3016, pp. 92–99, 1997
19. N. V. Kumar, K. Sreelatha and C. S. Kumar, "Invisible watermarking in printed images," 2016 1st India International Conference on Information Processing (IICIP), Delhi, India, 2016, pp. 1-5, doi:10.1109/IICIP.2016.7975333.
20. P. Chotikawanid and T. Amornraksa, "Digital image watermarking against photo to cartoon effects," 2015 International Symposium on Intelligent Signal Processing and Communication Systems (ISPACS), Nusa Dua Bali, Indonesia, 2015, pp. 216-221, doi:10.1109/ISPACS.2015.7432768.
21. R. Feitosa, A. Soares and L. Pereyra, "A New Clustering-based Thresholding Method for Human Skin Segmentation Using HSV Color Space," in 2018 IEEE Symposium on Computers and Communications (ISCC), Natal, Brazil, 2018 pp. 639-1180, doi:10.1109/ISCC.2018.8538604.
22. A.Benhocine and L.Laouamer, "New Images Watermarking Scheme Based on Singular Value Decomposition", January 2013, Journal of Information Hiding and Multimedia Signal Processing, Volume 4, Number 1, Received July 2012; revised January 2013.
23. Z. Zhang, "Zero-watermarking algorithm based on DC component in DCT domain," 2021 International Conference on Electronic Information Engineering and Computer Science (EIECS), Changchun, China, 2021, pp. 475-478, doi: 10.1109/EIECS53707.2021.9588068.
24. N. Sangeetha and X. Anita, "Linear Weighted Multiple Watermarking in DWT-SVD Domain Through Covariance Analysis : (Linear weighted watermarking in DWT-SVD domain)," 2018 International Conference on Intelligent Computing and Communication for Smart World (I2C2SW), Erode, India, 2018, pp. 55-59, doi:10.1109/I2C2SW45816.2018.8997365.
25. S. E. Ghrare, A. Adim Mohamad Alamari and H. A. Emhemed, "Digital Image Watermarking Method Based on LSB and DWT Hybrid Technique," 2022 IEEE 2nd International Maghreb Meeting of the Conference on Sciences and Techniques of Automatic Control and Computer Engineering (MI-STA), Sabratha, Libya, 2022, pp. 465-470, doi: 10.1109/MI-STA54861.2022.9837586.
26. N. Jimson and K. Hemachandran, "DFT Based Coefficient Exchange Digital Image Watermarking," 2018 Second International Conference on Intelligent Computing and Control Systems (ICICCS), Madurai, India, 2018, pp. 567-571, doi: 10.1109/ICCONS.2018.8663122.
27. A. Chen and X. Wang, "An Image Watermarking Scheme Based on DWT and DFT," 2017 2nd International Conference on

Multimedia and Image Processing (ICMIP), Wuhan, China, 2017, pp. 177-180, doi: 10.1109/ICMIP.2017.51.
28. N. K. Yadav and S. Selvakumar, "An Optimized Transform Domain Watermarking Technique for Grayscale Images of Medical Applications," 2018 3rd International Conference for Convergence in Technology (I2CT), Pune, India, 2018, pp. 1-7, doi: 10.1109/I2CT.2018.8529356.
29. A. Tareef, A. Al-Ani, H. Nguyen and Y. Y. Chung, "A novel tamper detection-recovery and watermarking system for medical image authentication and EPR hiding," 2014 36th Annual International Conference of the IEEE Engineering in Medicine and Biology
30. Society, Chicago, IL, USA, 2014, pp. 5554-5557, doi: 10.1109/EMBC.2014.6944885.

2023

Innovative Deep Neural Network Models for Multilingual Translation Applied to Dyslexia

R. Bencheikh,[a, *] A. Moussaoui,[a]

[a] Computer Science Department, Faculty of Sciences, Ferhat Abbas-Setif1 University, Setif-19000, Algeria

ABSTRACT: Machine Translation is one of the most prominent-difficult topics in Natural Language Processing. It is based on building machine-learning models that can understand human languages and predict a target translation from a source expression. Actually, automation, as in different fields of our lives involving medicine, achieve prominent developments. Whatever the field that needs an automation solution, medical image can be used to recognize natural language processing. Dyslexia is a domain where such automation can be applied. Indeed, the diagnosis of this disorder brain disease implies the use of appropriate and standardized tests. This disease affects reading and language processing by making some challenge to some people to recognize and decode words and comprehend written text despite having average or above-average intelligence. This work presents a detailed comparative study between advanced approaches applied to natural language processing, mainly in machine translation task. Twelve (12) models and experiments in total were replicated, trained, and then validated on two types of datasets for both Language Support and Speech to Text Conversion in case of multilingual translation. Thus, many translation directions were considered (Turkish-English, English-Turkish, Spanish English, English Spanish, and Turkish-Spanish). The performed experiments show that Transformer based models tend to give better performance despite of linguistic complexities for natural languages translation task from Turkish, Spanish, or English. High accuracy models were applied for second data set by adding the speech-to-text task to make transcriptions that can help dyslexic individuals. Accuracy of 95% was achieved for whisper model.

Keywords: Machine translation; Deep-learning, Transformers; Dyslexia, Many-to-Many-100 models; Whisper model.

INTRODUCTION

Some learners fail to acquire the mechanisms involved in reading despite normal intelligence and the absence of any motor or sensory deficit. It is about dyslexia(originated from the Greek language)[1]. which is a neurological condition that also known until the 1960s as word blindness and it is believed to be caused by the interaction of genetic and environmental factors while its treatment involves adjusting teaching methods to meet the person's needs. by the way there are 9,000 cases of dyslexia in Algeria.

Developmental Dyslexia (i.e., dyslexia which is genetic, present from birth, and develops over time) is generally observed among the younger school-going population who performs poorly in schools and often faces difficulties during their studies. This ultimately results in negative emotions, such as anger, frustration, depression, anxiety, and low self-esteem [1].So, dyslexic people have specific difficulties in three areas: phonological processing, working memory and processing speed, From the definition

above, it becomes clear that conventional language teaching methods usually do not work for learners with dyslexia, but with the teacher's awareness and support, they might overcome their difficulties, Teacher awareness of dyslexia is very important to the success of affected children because many learners with reading difficulties report high levels of anxiety and fear for the reason that, their teachers have a poor understanding and insufficient awareness of this impairment.[2]

AI refers to the development of machines and systems to enable them to implement functions and tasks that demand human intelligence, such as translation, decision making, visual perception, and speech recognition. ML is considered a part of AI, which concentrates on the evolution of computer programs that use different datasets to learn for themselves.

In "phonological dyslexia", during the reading, fMRI(Magnetic Resonance Imaging) displays paralysis of three regions that are concerned with language production and grasping . Additionally, compared to controls, DTI(Diffusion Tensor Imaging) reveals white matter variation in the language area. In visual attentional dyslexia, when dyslexic participants are tasked to recognize congruous stimuli pairs, fMRI displays a separation between the temporal visual system and parietal attentional system as well as a disconnection, in the left hemisphere, of the temporal and occipital zones. In the "dyspraxia form of dyslexia", there is inactivation in the cerebellum–ventral frontotemporal and cerebellum–dorsal frontoparietal pathway. Besides fMRI, the surface measurement of brain potential, known as EEG(Electroencephalography), assists in identifying brain activation patterns (Fig.1). During spelling tests, phoneme deletion, the rapid naming of letters, and articulation, increased vigor is observed in the theta and delta EEG frequency bands in the frontal and right temporal zones in dyslexics [3].

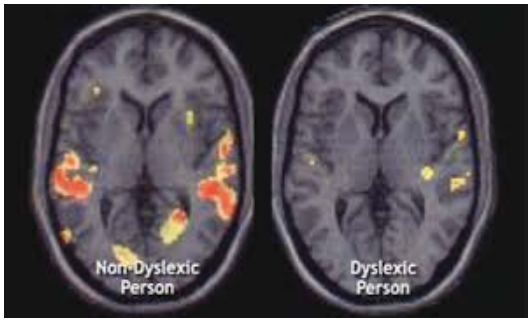

Fig. 1: How Dyslexia affects the Brain

Recently, machine-learning techniques have become popular in predicting Dyslexia from the data collected through online tests, such as reading and writing exercises, online games, tracking eye movement, or collecting EEG scans and MRI data while the participants engage in reading or writing tasks.[4]

However, Translation can help dyslexic individuals by translating written text into a basic language, other forms of support, such as specialized instruction or one-on-one tutoring (One-on-one tutoring is a type of educational support that involves a teacher or tutor working individually with a student or provide personalized instruction and support.), maybe necessary for dyslexic individuals to fully develop their reading skills.[-2]

To translate is to transpose a source-language text into a target-language text, this although seems like a simple answer, however it refers in fact to a dramatically complex problem.

Speech recognition, natural language interpretation, and natural language production are all common natural language processing challenges.

Machine translation has emerged as one of the most fascinating and difficult topics in Natural Language Processing (NLP) and Artificial Intelligence (AI). As the name implies, data-driven machine translation1 (DDM) is concerned with developing translation agents based on data. As a result, machine translation systems are now being created both in academia and industry and are being sold to end-users as commercial products.

EXPERIMENTAL

Neurological aspects have also been considered in modern technologies for diagnosing dyslexia, helping to increase detection accuracy and reliability. Medical devices enable dyslexia, helping to increase detection accuracy and reliability. Medical devices enable the observation of the brain structure of dyslexics[5].

From figure 2, we can consider that any disorder in the brain's left hemisphere would lead to important difficulties in a person's ability to read and write and some other skills. So the extended temporal processing deficit hypothesis of dyslexia", suggesting that a deficit in temporal processing could explain not only language-related peculiarities usually noticed in dyslexic children, but also a wider range of symptoms related to impaired

processing of time in general[6]. This means that if we want to solve the reading disorder we can do it by organizing other skills. Our Machine Translation models can provide assistance to Dyslexic individuals by: [3]

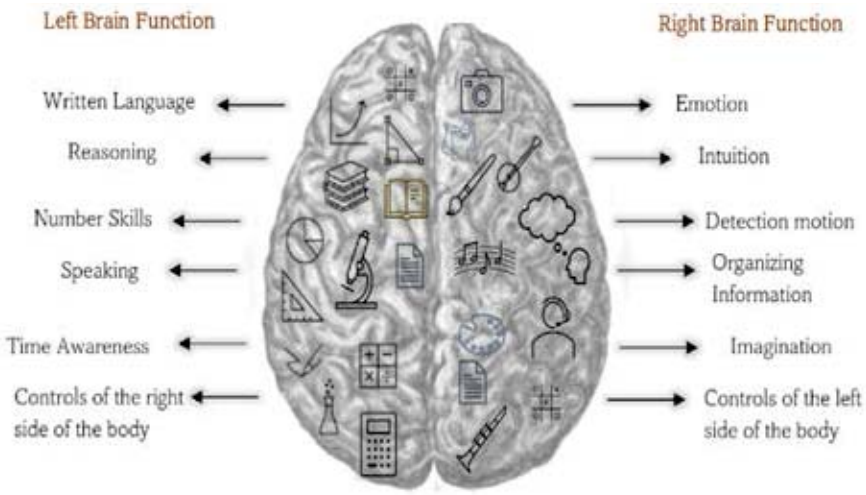

Fig. 2: Difficulties in brain's functions because of disordering

Language Support

Machine translation has a large history as we mentioned in the second chapter, in our work we tried to train different models using both of classical approaches and techniques based on Deep learning, for do a comparative study discussed later using the multilingual datasets (The OPUS-100 and The Tatoeba Corpus).

1- IBM Statistical Translation model

IBM (International Business Machines) alignment model which is a sequence of increasingly complex model used in statistical machine translation, we check a lexical translation probability computed using standard IBM model1 with English language (one to many).

2- Seq2Seq with RNN model

We move now to deep learning models, so for text treatment there is Recurrent Neural Networks, which are designed to take text sequences as inputs and return text sequences as outputs, or both. Fully recurrent neural networks (RNN) connect all neurons' outputs to all neurons' inputs. Because all other topologies can be represented by setting some connection weights to zero to simulate the lack of connections between those neurons, this is the most general neural network topology.

3- Seq2Seq with LSTM model

Sequence-to-sequence (seq2seq) models can help solve the translation problem with an input sequence and giving its translated sequence, we developed here a model with LSTM (long short term memory) cells, starting with an embedding layer at the top of the model.

4- Seq2Seq with GRU model

The GRU (gated recurrent unit) model is like a long short-term memory (LSTM) with a forget gate, but has fewer parameters than LSTM, as it lacks an output gate. in this experiment we exchanged the LSTM cells by GRU cells starting by the embedding layer.

5- Seq2Seq with BLSTM model

Bidirectional Long Short Term Memory is optimized LSTM, which can read input sequences from both ends. our idea behind this experiment is to develop our model such it can read bidirectionally where we used BLSTM cells.

6- Seq2Seq with Attention model

in this experiment we tried to train a sequence to sequence (seq2seq) model based on Effective Approaches to Attention-based Neural Machine Translation presented at and compare it with previous Seq2Seq models.

- The model consists of two parts:
  an **Encoder**: it takes a list of token IDs where an embedding layer generate a vector representing the input and feed it to a GRU layer, returning a sequence processed and its internal state.
- a **Decoder**: it receives the output of encoder and passes it by an attention layer and producing the context vector and feed it to a

GRU layer and finally, it generates logit predictions for the next token based on the "attention vector".

7- Transformer model

Here we replicate the same Transformer architecture as presented in [7]. The Transformer follows this overall architecture using stacked self-attention and pointwise, fully connected layers for both the encoder and decoder

8- Facebook many to many 100 418M model

We pretrained that model from Beyond English-Centric Multilingual Machine Translation (2020) [8] Many to Many 100 418M(parameters) is a multilingual encoder-decoder (sequence-to-sequence) model trained for Many-to-Many multilingual translation.
This model can directly translate between the 9,900 directions of 100 languages. To translate into a target language, the target language id is forced as the first generated token. To force the target language id as the first generated token, pass the forced id parameter to the generate method.

9- CTranslate2 m2m100 model

This model uses Many to Many -100 models converted to the CTranslate2 format. CTranslate2 is a fast inference engine for Transformer models. It supports models originally trained with (open neural machine translation) OpenNMT-py, OpenNMT-tf, and FairSeq. CTranslate2 is preferred for its high efficiency. It is cross-platform and can be used either on CPU (central processing unit) or GPU(graphics processing unit).

10- mBART-50 one to many model

This model is a fine-tuned checkpoint of mBART-large-50. mbart-large-50-one-to-many is fine-tuned for multilingual machine translation.it is a model developed by Facebook and built using huggingface's transformers. It was introduced in Multilingual Translation with Extensible Multilingual Pretraining and Finetuning paper. The model can translate English to other 49 languages. To translate into a target language, the target language id is forced as the first generated token. To force the target language id as
the first generated token, pass the forced id parameter to the generate method.

11- M2M100 418M model with pivot approach

In this experiment w tried to pretrain the Many to Many 100 418M model to translate from Turkish to Spanish using the pivot language English.

Speech to Text Conversion

This solution consists of using the technology to convert spoken language into written text. This technology can be highly beneficial for individuals with dyslexia, a learning disability that can make reading and writing more challenging. We used for this part the medical datasets (PxCorpus: A Spoken Drug Prescription Dataset in French for Spoken Language Understanding).

1-Whisper model

The Whisper architecture is a simple, implemented as encoder-decoder Transformer.

Input audios must be converted into spectrograms and then passed into the encoder; the decoder is trained to predict the corresponding text caption. Whisper checkpoints come in five configurations of varying model sizes. The smallest four are trained on either English-only or multilingual data, and because our PxCorpus is small and its recordings directory contains the 903 recording sessions. Each session can contain several recordings; we used the tiny version of whisper model.

RESULTS AND DISCUSSION

According to results displayed in Table 1 related to accuracy, and main metrics used to compare between models, the following statements and conclusions can be drawn.

Table 1. Studied Experimental for Turkish and French languages

N°	Model	Bleu scores[1]	Accuracy
1	IBM model 1	0.0102	/
		0.0446	
		0.0204 0.0257	
2	Seq2Seq with RNN	0.0028	/
		0.0091	

[1] Bleu score: the Bilingual Evaluation Understudy is a score for comparing a candidate translation of text to one or more reference translations.

		0.0135 0.016	
3	**Seq2Seq with LSTM**	**0.0029** **0.0093** **0.0137 0.0165**	**/**
4	Seq2Seq with GRU	0.0037 0.0115 0.0169 0.0202	/
5	Seq2Seq with BILSTM	0.0033 0.0111 0.0167 0.0202	/
6	Seq2Seq with Attention	0.3062 0.5534 0.6767 0.7439	/
7	Transformer	0.3505 0.0460 1 1	/
8	M2M100 418M	0.0275 1 1 1	/
9	CTranslate2 m2m100	0.0296 1 1 1	/
10	mBART-50	0.0296 1 1 1	/
11	Whisper Tiny-version	/	95%

- The Statistical Machine Translation experiment was not efficient comparing to Neural Machine Translation Models.
- In Neural Machine Translation experiments, there is an augmented progress of Bleu scores from simple RNN model to the Transformer.
- The addition of the attention mechanism to the Sequence to-Sequence model enhances the model performance in the support language part as illustrated by the arrow **A** in Figure 3. The model focuses only on the most important tokens.

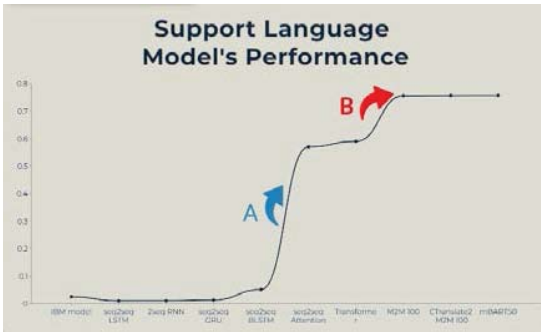

Fig. 3: Performance development for support language models

- The Transformer model starts increasing the model capacity and performance as illustrated by arrow **B** (Fig.3).
- The experiments show that the Transformer based models outperforms deep learning models in Neural Machine translation unlike the statistical machine translation approaches.
- Furthermore, the complexity of the problem is determined by the complexity of the vocabulary. A more complex vocabulary is a more complex problem. Therefore, the complexity of the dataset is very prominent and has a relation with the translation direction.
- The M2M 100 418M model has shown ideal scores of grams in both datasets and increased performance.
- Our pivot approach achieved good results for translation direction from Turkish to English. Tested examples on that model were successfully and correctly translated as shown in Figure 4.
- The Turkish translation dataset is less performant when compared to the spanish-english dataset. The poor performance of the translation models is due to the complexity of the Turkish language (Fig.4).

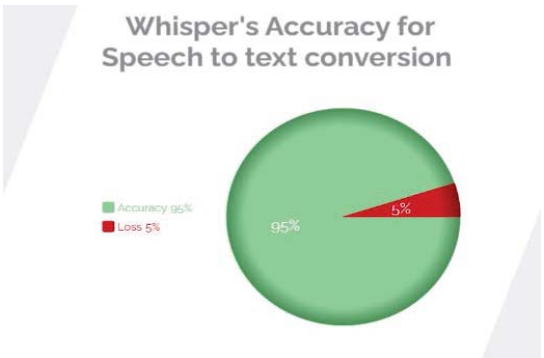

Fig. 4: Performance development for support language models

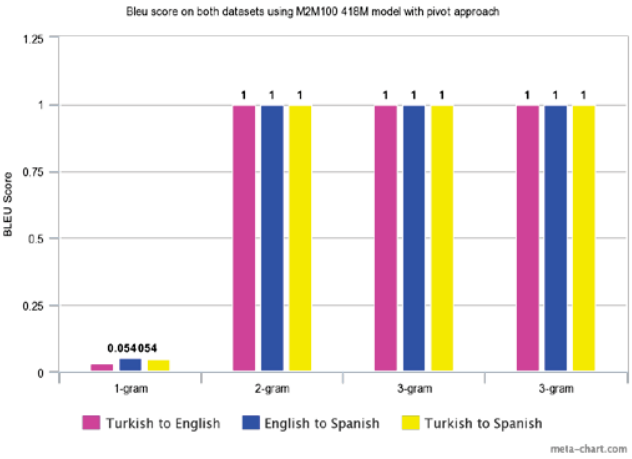

Fig. 5: Accuracy achieved for whisper model in speech to text conversion

- The version of Whisper model is less performant for a small dataset but achieves a high accuracy (Fig.5).
- To improve the accuracy of a speech-to-text model like Whisper, an iterative process of analysis and refinement is involved.

CONCLUSIONS

The actual study is related to the application of medical imaging neurological to diagnosis Dyslexia. This disease causes a reading disorder, affects language processing, and creates challenges to recognize and decode words and comprehend written text for some people. We are particularly interested in Machine Translation, one of the most fascinating and difficult topics in Natural Language Processing and Artificial Intelligence. Our objective was to develop and propose a performant translation model based on deep learning. This model must be a powerful language support despite of all linguistics complexities and constraints in translation between different languages. A second performance constraint for speech to text conversion is related to the mechanisms involved in reading despite normal intelligence and the absence of any motor or sensory deficit.

This work involves the translation task to be learned to a machine with all its complexities related to linguistics and psychology. Many machine learning principles and approaches were tested and compared to help dyslexic individuals. Thus, several models were studied and developed from statistical approaches to deep

learning techniques, such as IBM1, BLSTM, GRU, Transformer, BERT-based transformers models, and Whisper-Tiny model. The performance of all these models were validated on several datasets.

Results of our experiments demonstrate well that the SMT has less efficiency comparing to the NMT where the recent Transformer-based models outperform recurrent networks-based models in Translation tasks. The Transformer architectures using attention mechanism lead to improved training speed.

For the speech to text conversion, Whisper Open AI trained and open-source speech recognition model is used. Whisper is a neural net that approaches human level robustness and accuracy for speech recognition. A tiny version appropriated to our medical French dataset is considered to achieve our goal.

For future work, we propose to develop a new approach that can combine between all linguistics of several languages to achieve the desired goal by analyzing more deeply the performance of the neural translation models. We also aim to more effectively leverage the cross-lingual information in data augmentation settings to provide more data to the greedy neural translation models. Besides, we would like to find a solution for dyslexic brain using artificial intelligence techniques combined to neurological solution.

AUTHOR INFORMATION

Corresponding Author

*Rokia Bencheikh

Email address: bencheikhrokiag8@gmail.com

REFERENCES

1. Shahriar Kaisar and Abdullahi Chowdhury.Integrating oversampling and ensemble-based machine learning techniques for an imbalanced dataset in dyslexia screening tests.ICT Express volume8.p563,568.
2. Tobbi, S. (2020). Dyslexia between Reality and Misconception: Investigating Algerian EFL Teachers Awareness of Dyslexia. Case of EFL Teachers in Batna Middle Schools. Journal of Psychological and Educational Sciences. 6(3). Algeria: El-Oued University. 290-299.
3. Norah Dhafer Alqahtani et al. Deep Learning Applications for Dyslexia Prediction. Applied Sciences. *Appl. Sci*. 2023, *13*(5), 2804.
4. Kaisar S.Developmental dyslexia detection using machine learning techniques : A survey Elsevier ICT Express, 6 (3) (2020), pp. 181-184.
5. Jankovic, M.M. Biomarker-based approaches for dyslexia screening: A review. IEEE Zooming Innov. Consum. Technol. Conf. 2022,2022, 28–33.
6. Michel Habib. The Neurological Basis of Developmental Dyslexia and Related Disorders: A Reappraisal of the Temporal Hypothesis, Twenty Years on. Brain Sciences. 2021, *11*(6), 708.
7. A. Vaswani, et al., Attention is all you need, CoRR, vol. abs/1706.03762, 2017.
8. A. Fan, S. Bhosale, et al. “Beyond english-centric multilingual machine translation,” 2020.
9. T. Poibeau, Machine Translation The MIT Press Essential Knowledge series. MIT Press, 2017.
10. Zhixing Tan et al. Neural machine translation: A review of methods, resources, and tools.AI Open. Volume 1, 2020, Pages 5-21
11. C. Molnar, Interpretable Machine Learning. Lulu.com, 2020.

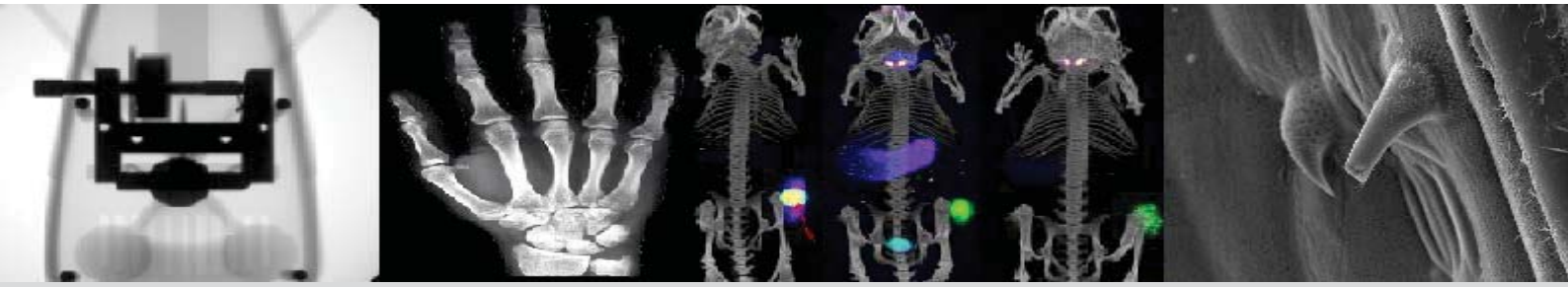

2nd International Conference and School on Radiation Imaging and Nuclear Medicine (ICSRI-2023)

11-15 June 2023, Setif, Algeria

2nd Call for Papers

With great pleasure, the Organizing Committee announces the second call for abstracts submission and school application for the second International Conference and School on Radiation Imaging and Nuclear Medicine (ICSRI-2023), to be held at Ferhat Abbas-Seitf1 University, in Setif, Algeria, from **11 to 15 June, 2023**. The conference is supported by the Algerian Atomic Energy Commission (COMENA).

The conference will include plenary sessions with conferences presented by eminent scientists, and orally and in poster sessions covering the different conference topics.

The invited talks are chosen to review recent advances in different areas covered by the conference.

The conference will be followed by ***a three (3) days school*** *for doctorate students and newly qualified academics and researchers in the field of radiation imaging and applications (20 participants max.). The program of the school will include lectures and practical sessions on four topics: 1. Monte Carlo simulations in molecular imaging and dosimetry, 2. Advanced anthropomorphic computational models, 3. Medical lasers-Physics, Clinical Applications and Safety Management, 4. Artificial intelligence in medical image processing, and 4. Transmission computed tomography.*

The conference proceedings will be published in a special issue via an academic publisher.

The conference will be held at Moloud Kacem Naït Belkacem Auditorium of Ferhat Abbas-Setit1 University, Algeria.

Important Dates

- **Registration and Abstract Submission Opening**
  1st December 2022
- **Abstract Submission Deadline**
  10th May 2023
- **Acceptance notification**
  20th March to 20th May 2023

Secretary of the ICSRI-2023

Mobile: +213(0) 557363347
Phone: +213(0) 36620136
Fax: +213(0) 36620136
E-mail: icsri@univ-setif.dz

Website:
https://ocs.univ-setif.dz/ICSRI/ICSRI

Conference Topics:

The 2nd International Conference and School on Radiation Imaging and Nuclear Medicine (ICSRI-2023) will held for the second time at the University of Sétif1 and will provide an international forum for discussing current research and developments in the domain of radiation imaging and applications that includes all kind of medical and industrial techniques.

- **Track 1: Non-medical radiation imaging (X-ray, γ-ray, neutrons, electrons...)**
- **Track 2: Radiation Imaging methods and systems development**
- **Track 3: Radiation Imaging Simulation and modeling**
- **Track 4: Molecular Imaging and Nuclear Medicine (SPECT, SPECT/CT, PET/CT, PET/MR, etc)**
- **Track 5: Medical Radiation Imaging (CT, Mammography, Fluoroscopy, MRI, US, etc)**
- **Track 6: Advanced Imaging Methods (Image Reconstruction, Artificial Intelligence, Radiomics, Theragnostics, etc)**
- **Track 7: Image Processing and Data Analysis Techniques**

Organizing Committee

General Chair: Pr. Fayçal Kharfi (UFAS1);
Deputy Chair: Dr. Layachi Boukerdja (CRNB);
Committee: Pr. Belkhiat Djamel Eddine Chouaib (UFAS1), Pr. Azizi Hacene (UFAS1), Pr. Moussaoui Abdelouahab (UFAS1), Pr. Boudaoud Khadidja (CLCC-Setif, Dz), Dr. Mosbah Ammar (UFAS1), Dr. Khelfi Djilali (COMENA), Dr. Sari Bilal (UFAS1), Dr. Chouaba Seif Eddine Allah (UFAS1), Mrs. Benachour Lilia (UFAS1), Mr. Benachour Nacim (UFAS1).

Ferhat ABBAS University of Setif

Commissariat à l'Energie Atomique

UFAS.1 Lab.DAC

CSR

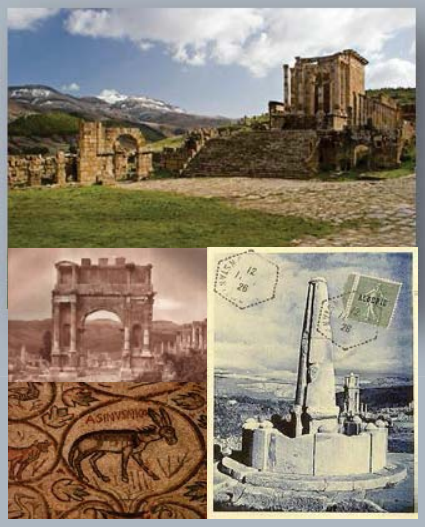

Cuicul (Djémila- 55 km from Setif city-) was built at 900 meters of altitude during the 1st century AD as a Roman military garrison. It became a UNESCO World Heritage Site for its unique adaptation of Roman architecture to a mountain environment. Significant buildings in ancient Cuicul include a theatre, two fora, temples, basilicas, arches, streets, fountain and houses. The exceptionally well preserved ruins surround the forum of the Harsh, a large paved square with an entry marked by a majestic arch.

International Program Committee

Atef El-Taher (Al-Azhar Univ, Eg)
Amrani Naima (UFAS1, Dz)
Azizi Hacene (UFAS1, Dz)
Babahenini Mohamed Chaouki (Biskra Univ, Dz)
Belkhiat Djamel Eddine Chouaib (UFAS1, Dz)
Benamrane Nacéra (USTO, Dz)
Bouchareb Yassine (Sultan Qaboos Univ, Om)
Boudaoud Khadidja (CLCC-Setif, Dz)
Bouyoucef Salahedine (Bab El Oued CHU, Dz)
Cherfa Yazid (SD-Blida Univ, Dz)
Djedi Noureddine (Biskra Univ, Dz)
Doghmane Noureddine (BM-Annaba Univ, Dz)
Drai Redouane (CRTI, Dz)
Guemmmaz Mohamed (UFAS1, Dz)
Guettoum Abderrahim (CRNA, Dz)
Hadid Abdenour (Oulu University, Fi)
Hachouf Fella (Constantine Univ, Dz)
Hamidatou Algham Lylia (CRNB, Dz)
Kambiz Shahnazi (PHIC, China)
Kharfi Fayçal (UFAS1, Dz)
Lounis-Mokrani Zohra (CRNA, Dz)
Maalej Nabil (KU, UAE)
Maouche Djamel (UFAS1, Dz)
Mansour Karim (Univ. Constantine 3, DZ)
Merouani Hayet Farida (Annaba Univ, Dz)
Meziane Abdelkrim (CERIST, Dz)
Mimi Malika (Mostaghanem Univ, Dz)
Mongy Tarek (ECAE, Eg)
Moussaoui Adelouahab (UFAS1, Dz)
Meriç Niyazi (Ankara University, Tr)
Oussalah Mourad (Oulu University, Fi)
Ounoughi Nabil (university of Jijel, Dz)
Saint-Gregoire Jean-pierre (ASCA, Fr)
Şahiner Eren (Ankara University, Tr)
Schillinger Burkhard (TUM, De)
Seghier Mohamed (ECAE, Abu Dhabi, UAE)
Seghour Abdessalem (CRNA, Dz)
Taleb-Ahmed Abdelmalik (Valencienns University, Fr)
Zaidi Habib (Geneva University Hospital, Ch)
Zidi Tahar (COMENA, DZ)

Welcome to Setif

Sétif (the capital of Sétif Province) is a town in north-eastern Algeria, 1096 meters above sea level. It is the second most populated Province after the country's capital. The streets are tree-lined with a fountain and theater, giving the town French feel. A large amusement park is located in the center of the city where the city Zoo can be found. The ruins from Roman, Byzantine, Islamic and colonial eras adorn the city center.

The local economy deals both with trade and industries. The trade is mainly in grain and livestock from the surrounding region. Sétif has become the commercial center of a region where textiles are made, phosphates are mined and cereals grown. Other industries are woodworking, manufacture of carpets and metal handicrafts.

Sétif is connected by rail as well as the main national highway. The city has also an international airport.

Registration Fees

- The registration fees include:
  - Lunch, banquet,
  - Conference proceedings and bag
  - City tour & Gala dinner
  - For the school participants diners are included in registration fees.
- Students are required to provide a copy of a valid ID that certifies their full-time student status.

The registration fees are:

Conference		
Regular scientists:	15000 DZD (100 Euro)	A I *
	7000 DZD (50 Euro)	ANI**
Doctorate students	10000 DZD (75 Euro)	AI
	6 000 DZD (40 Euro)	ANI
School	15000 DZD (100 Euro)	AI
	6000 DZD (40 Euro)	ANI
Industrial:	30000 DZD (200 Euro)	ANI

*: Accommodation included, **: Accommodation not included

Preliminary Conference and School Program

Day	Morning	Afternoon
Conference		
Day1	**Opening Ceremony** **Plenary Session**	**Session 1:** Non-medical radiation imaging (X-ray, γ-ray, neutrons, electrons…)
Day2	**Session 4:** Molecular Imaging and Nuclear Medicine (SPECT, SPECT/CT, PET/CT, PET/MR, etc)	**Session 5:** Medical Radiation Imaging (CT, Mammography, Fluoroscopy, MRI, US, etc)
School		
Day1	**Lecture 1:** The role of Monte Carlo simulations in molecular imaging and dosimetry	**Lecture 2:** Advanced anthropomorphic computational models
Day2	**Lecture 1:** Artificial Intelligence (AI) for medical image analysis	**Lecture 2:** Deep learning (DL) for medical image analysis
Day3	**Lecture 1:** Fundamental of Transmission Tomography	**Lecture 2:** Image Reconstruction Methods in Computed Tomography

Day	Afternoon
Conference	
Day1	**Session 2:** Radiation Imaging methods and systems development
Day2	**Session 6:** Advanced Imaging Methods (Image Reconstruction, Artificial Intelligence, Radiomics, Theragnostic, etc)
School	
Day1	**Lecture 3:** Medical lasers- Physics, Clinical Applications and Safety Management (Part1)
Day2	**Practical work 1:** Practical examples of machine learning for medical image analysis
Day3	**Practical work 1:** X-ray Tomography in Practice

Day	Afternoon
Conference	
Day1	**Session 3:** Radiation Imaging Simulation and Modelling
Day2	**Session 7:** Image Processing and Data Analysis Techniques
School	
Day1	**Lecture 4:** Medical lasers- Physics, Clinical Applications and Safety Management (Part2)
Day2	**Practical work 2:** Practical examples of DL for medical image analysis
Day3	**Practical work 2:** 3D Image Reconstruction and Analysis

Partners and Sponsors:

Proceedings of the ICSRI-2023 | ISSN 2800-1362

The second international conference and school on Radiation Imaging and Nuclear Medicine (ICSRI-2023), 11-15 June 2023, was organized for the second time by Ferhat Abbas-Setif1 University (UFAS1) in partnership with the Algerian Atomic Energy Commission (COMENA) and its different research centres. The conference brings together researchers, practitioners, and students from different universities and research centres to discuss the latest advances in radiation imaging and nuclear medicine.

The conference covers different topics related to radiation imaging and image processing methods and techniques.

The conference was followed by a practical school of three days for PhD students, medical physicists, and early-career researchers. The school provides an opportunity to learn about the fundamentals and practices of simulation and dosimetry in nuclear medicine, medical lasers, quality control in mammography, computed tomography, and deep-learning in medical image processing.

Organizing Committee

General Chair: Prof. Fayçal Kharfi (Ferhat Abbas-Setif1 University, Algeria)

Deputy Chair: Dr. Layachi Boukerdja (Nuclear Research Centre of Birine, Algeria)

Committee Members:

- Prof. Hacene Azizi (UFAS1, Algeria)
- Prof Djamel Edine Chouaib. Belkhiat (UFAS1, Algeria)
- Prof. Adelouahab Moussaoui (UFAS1, Algeria)
- Dr. Seif Eddine Allah Chouaba (UFAS1, Algeria)
- Dr. Ammar Mosbah (UFAS1, Algeria)
- Dr. Djilali Khelfi (COMENA, Algeria)
- Prof. Bilal Sari (UFAS1, Algeria)
- Prof. Khadidja Boudaoud (CLCC-Setif, Dz)
- Mrs. Lilia Benachour (UFAS1, Algeria)
- Mr. Benachour Nacim (UFAS1, Algeria)

Secretariat and Technical Staff:

Ms. Karima Bey and Mr. Ilyas Sekhri (UFAS1, Algeria)